Pontifícia Universidade Católica
do Rio de Janeiro

Fernanda Gonçalves Abrantes

Dalitz plot analysis of the decay $D^+ \to \pi^-\pi^+\pi^+$ and study of the $\pi^-\pi^+$ S-wave amplitude

Dissertação de Mestrado

Dissertation presented to the Programa de Pós–graduação em Física of PUC-Rio in partial fulfillment of the requirements for the degree of Mestre em Física.

Advisor: Profa. Carla Göbel Burlamaqui de Mello

Rio de Janeiro
April 2020

Pontifícia Universidade Católica
do Rio de Janeiro

Fernanda Gonçalves Abrantes

Dalitz plot analysis of the decay $D^+ \to \pi^-\pi^+\pi^+$ and study of the $\pi^-\pi^+$ S-wave amplitude

Dissertation presented to the Programa de Pós–graduação em Física of PUC-Rio in partial fulfillment of the requirements for the degree of Mestre em Física. Approved by the Examination Committee:

Profa. Carla Göbel Burlamaqui de Mello
Advisor
Departamento de Física – PUC-Rio

Prof. Diogo Rodrigues Boito
USP

Prof. Álvaro Gomes dos Santos Neto
UFTM

Profa. Jussara Marques de Miranda
CBPF

Rio de Janeiro, April 30th, 2020

Fernanda Gonçalves Abrantes

Received the title of Bachelor of Science degree in Physics from the Pontifícia Universidade Católica do Rio de Janeiro in 2017.

Bibliographic data

Abrantes, Fernanda Gonçalves

Dalitz plot analysis of the decay $D^+ \to \pi^-\pi^+\pi^+$ and study of the $\pi^-\pi^+$ S-wave amplitude / Fernanda Gonçalves Abrantes; advisor: Carla Göbel Burlamaqui de Mello. – Rio de janeiro: PUC-Rio, Departamento de Física, 2020.

v., 185 f: il. color. ; 30 cm

Dissertação (mestrado) - Pontifícia Universidade Católica do Rio de Janeiro, Departamento de Física.

Inclui bibliografia

1. Análise de amplitudes;. 2. Física de charme;. 3. Dalitz plot;. I. Mello, Carla Göbel Burlamaqui. II. Pontifícia Universidade Católica do Rio de Janeiro. Departamento de Física. III. Título.

CDD: 530

Acknowledgments

Firstly I would like to express my deep and sincere gratitude to my supervisor, Carla Göbel, for her support and guidance since my undergraduate times and during my master's. For her kindness in helping me in every step and being an inspiration to me, given her passion and dedication to research. For all the daily meetings with interesting discussions, not only limited to physics, and thoughtful advices that I will carry with me throughout my entire life.

To the Rio Charm group, for all the discussions and support that made this research possible. For the opportunity of joining such an active environment. To prof. Alberto dos Reis, Sandra Amato and Erica Polycarpo, thank you all for having taught me in these past years, contributing to my formation. To the "charmosinhos", for making this academic pursuit lighter with our silly backstage chats.

To my parents, Maria do Céu and Sergio Abrantes, for their support and effort towards my academic career, for always encouraging me to pursue my most ambitious dreams.

I want to lovingly thank Igor Weilemann for all the love, company and support in the hardest times. For always believing in me.

To all my friends at PUC Cíntia Pires, Lucianno Defaveri, Francisco Freitas, Antonio Galvão and João Gonçalves for all the support and our delighted nights at "cavernão" with the most nonsense conversations. To Ana Coquito, Matheus Borré and Rafael Flores for the long term friendship being present in every step of my life and for the tea times.

To the CNPq and CAPES for the financial support.

I would also like to thank the administrative staff of the physics department, Gizelda Dias da Silva, Eduardo da Silva Rodrigues, Marcia Arjona and Julinho for all their assistance.

This study was financed in part by the Coordenação de Aperfeiçoamento de Pessoa de Nível Superior - Brasil (CAPES) - Finance Code 001.

Abstract

Abrantes, Fernanda Gonçalves; Mello, Carla Göbel Burlamaqui (Advisor). **Dalitz plot analysis of the decay $D^+ \to \pi^-\pi^+\pi^+$ and study of the $\pi^-\pi^+$ S-wave amplitude**. Rio de Janeiro, 2020. 185p. Dissertação de mestrado – Departamento de Física, Pontifícia Universidade Católica do Rio de Janeiro.

Non-leptonic decays of heavy hadrons, such as B and D mesons, have proven to be a rich environment for the study of light meson spectroscopy and charge-parity violation. For decays of charm hadrons, due to their mass scale at about 2 GeV, many problems related to non-perturbative effects arise in the study of strong interactions. Therefore, the usage of hadronic decays to study weak interactions turns out to be also a great opportunity to study the dynamics of hadronic interactions in these processes.

This dissertation documents the study of the decay $D^+ \to \pi^-\pi^+\pi^+$ through an amplitude analysis in a data sample obtained from pp collisions with a centre-of-mass energy $\sqrt{s}$ =8 TeV, collected by the LHCb detector during 2012 (part of run I). The analysis is performed with around 200 thousand $D^+ \to \pi^-\pi^+\pi^+$ decays aiming to understand the decay dynamics. In particular, emphasis is given to the $\pi^+\pi^-$ $S-$wave amplitude, which is known to be the major contribution in this decay mode, but it is also very challenging to parametrise due to the presence of broad overlapping scalar resonances. To study this component, three different approaches are used: the Isobar Model, the K-Matrix formalism and a Quasi Model-Independent Partial Wave Analysis technique, in order to obtain the $S-$wave magnitude and phase. These results can be used as a reliable input for new phenomenological models.

Keywords

Amplitude Analysis; Charm physics; Dalitz Plot;

Resumo

Abrantes, Fernanda Gonçalves; Mello, Carla Göbel Burlamaqui. **Análise de Dalitz plot do decaimento $D^+ \to \pi^-\pi^+\pi^+$ e estudo da amplitude $\pi^-\pi^+$ de onda-S**. Rio de Janeiro, 2020. 185p. Dissertação de Mestrado – Departamento de Física, Pontifícia Universidade Católica do Rio de Janeiro.

Decaimentos não-leptônicos de hádrons pesados, como mésons B e D, têm se mostrado um ambiente rico para o estudo de espectroscopia de mésons leves e violação de carga-paridade. Para decaimentos hadrônicos charmosos, dada a escala de massa de cerca de 2 GeV, muitos problemas relacionados a efeitos não-perturbativos surgem no estudo das interações fortes. Portanto, o uso de decaimentos hadrônicos para o estudo de interações fracas se torna uma grande oportunidade para estudar a dinâmica das interações hadrônicas nesses processos.

Esta dissertação documenta o estudo do decaimento $D^+ \to \pi^-\pi^+\pi^+$ através da análise de amplitudes em uma amostra de dados obtida de colisões pp com energia de centro de massa $\sqrt{s}$ =8 TeV coletada pelo detector LHCb durante 2012 (parte do $runI$). A análise é feita com aproximadamente 200 mil decaimentos de $D^+ \to \pi^-\pi^+\pi^+$ com o objetivo de entender sua dinâmica. Em particular, é dada ênfase à amplitude $\pi^+\pi^-$ de onda$-S$, que é sabida ser a contribuição dominante, porém também a mais desafiadora para parametrizar devido à presença de ressonâncias escalares de grande largura superpostas. Para estudar essa componente, três métodos diferentes são usados: o Modelo Isobárico, o formalismo da Matriz$-K$, e a técnica Quasi Modelo-Independente de Análise em Ondas Parciais, com o objetivo de obter a magnitude e fase da onda$-S$. Tais resultados podem ser usados como um aporte confiável para novos modelos fenomenológicos.

Palavras-chave

Análise de amplitudes; Física de charme; Dalitz plot;

Table of contents

List of figures

"And so do all who live to see such times. But that is not for them to decide. All we have to decide is what to do with the time that is given us."

J. R.R. Tolkien, .

1
Introduction

The most successful model so far, representing our best understanding of the behaviour of all known particles and their interactions, is the so called *Standard Model* (SM). It describes the building blocks from which everything in the universe is made of - the fundamental particles - and the electromagnetic, weak and strong forces. The success of this model stems from its remarkable agreement with experimental measurements from high energy colliders, such as the anomalous magnetic dipole moment of the electron [1,2] with an agreement to experimental measurements of ten significant figures. Even though this model has proven its big success over the years, there are still a few questions that the SM does not address indicated by some physical observations that remain inconsistent with SM predictions such as the baryon asymmetry which requires CP violation as one of the conditions proposed by Sakharov [3], the origin of neutrino masses, searches for evidences of dark matter in the astrophysical sector and dark energy, and a quantum field prescription for gravity. The field of high energy physics aims to tackle the unsolved questions either by directly searching for particles that are not predicted by the SM or by high precision measurements looking for deviations from SM predictions.

In the past years, Charm Physics (dedicated to the study of hadrons containing the charm quark) has been a fruitful environment in particle physics in both experimental and theoretical frameworks, with exciting results such as the recent discovery of CP violation in charm decays [4]. One peculiar aspect of charmed particles is that, since the $c-$quark mass is around 1.2 GeV/c^2 and charmed hadrons around 2 GeV/c^2, nonperturbative effects represent a complicated problem in the treatment of strong interactions. Therefore, these charmed particles have demonstrated to be a very useful laboratory to understand weak interactions in the presence of strong interactions.

Charm hadronic decays predominantly proceed through processes in which intermediate resonant states are formed. The dynamics involved in producing the final state is determined by the decay of the resonance via strong interactions and, to determine the resonant structure, a full amplitude analysis is needed. This is done by fitting the distribution of events in the phase space from experimental data to a phenomenological model for the decay amplitude.

Three–body non–leptonic weak decays of heavy mesons are of special interest for several reasons: for light meson spectroscopy, to reveal and understand resonances in different final states, to search for and study CP violation, study lineshapes and interference patterns. In the case of three-body decays, the analysis of the decay amplitude is done by fitting the Dalitz plot, a bidimensional representation of the phase space.

This dissertation documents the study of the hadronic decay of the charmed meson D^+ into the final state $\pi^-\pi^+\pi^{+1}$, which proceeds through a quark level transition $c \to du\bar{d}$. Following the weak process, resonances can be produced which then decay strongly to $\pi^+\pi^-$ (plus a π^+ companion), creating particular signatures and interference patterns in the Dalitz plot. Given the complexity of the three-body decay, caused by the presence of many interfering resonant states, an amplitude analysis is required to understand the dynamics involved in such processes. In addition to the CP violation search performed by the LHCb [5], this decay channel has been previously studied [6–8] by other collaborations performing Dalitz plot analyses with limited statistics, thus a more detailed description of the data is still missing given all the features that this decay mode brings. With a large amount of data, the LHCb experiment presents a unique opportunity to study this decay mode in much more depth, being sensitive to details that previous analyses were not able to study.

The behavior of the $\pi^-\pi^+$ S–wave amplitude, that is known to be the major contribution in this channel, is very challenging to describe and the study of the dynamics underlying this component comprises one of our interests in this analysis. The $\pi^-\pi^+$ scalar sector is composed by several broad overlapping resonant states which poses a big challenge in describing the decay amplitude. To reveal and understand the structures observed in the Dalitz plot, besides the most traditional so-called Isobar Model, we also use the K–Matrix formalism as well as a quasi Model-Independent Partial Wave Analysis (MIPWA). We also try a phenomenological ansatz based in the parametrisation of a three-body decay amplitude in terms of mesonic form factors with an effective weak hamiltonian in the naive factorization approach. The results from the different approaches are compared and the extracted S-wave component, with the behavior of its magnitude and phase, can provide a reliable input for new phenomenological models aiming to describe this sector.

This dissertation is organised as follows. In Chapter 2 we present a brief description of the theoretical fundamentals related to the analysis. In Chapter 3 we provide a more specific discussion about the channel $D^+ \to \pi^-\pi^+\pi^+$, introduce the concept of the Dalitz plot and the kinematics involved in three-

[1]The CP conjugate process is implicit in this analysis.

body decays and present previous experimental results performed in this channel. We also present a phenomenological approach for the $P-$ and $S-$wave contributions.

The following chapters are dedicated to the experimental study involved. In Chapter 4 the LHCb experiment is outlined and the strategy used in the data selection of $D^+ \to \pi^-\pi^+\pi^+$ decays is discussed in Chapter 5. In Chapter 6, 7 and 8 we present the phenomenological concepts as well as the results from each method used to perform the Dalitz plot analysis and the S–wave extraction: Isobar Model, K–Matrix and MIPWA, respectively. Lastly, we present a detailed comparison between the models and our conclusions in Chapter 9.

2
Theoretical Fundaments

2.1
The Standard Model

The Standard Model (SM) of particle physics is a non-abelian gauge theory with spontaneous symmetry breaking that aims at describing the fundamental particles and their interactions [9]. They are divided into the following groups: the matter content constituted of fermions, the force carriers corresponding to the gauge bosons of the theory and the Higgs doublet. As a quantum field theory, the SM has to incorporate some features in order to make any physical sense: it needs to be Lorentz invariant, to be causal, to be unitary conserving probability and renormalizable. To obey the Lorentz symmetry, the fields must be representations of the Lorentz group and the gauge symmetry can be global or local, if the parameters depend or not on the position in the space-time. Regarding the algebra of the groups, they can also be defined as Abelian or non-Abelian, *i.e.* commutative or non-commutative. The local gauge symmetry group of the Standard Model is

$$G_{SM} = SU(3)_C \times SU(2)_L \times U(1)_Y \tag{2-1}$$

where $SU(3)_C$ represents the gauge group of the strong force between particles with colour charge, $SU(2)_L$ is the weak sector acting only on left-handed fermions and $U(1)_Y$ is hypercharge. The $SU(3)_C$ and $SU(2)_L$ are non-abelian groups while $U(1)_Y$ is abelian.

In these types of gauge theories, the vacuum does not necessarily need to be invariant under all symmetries of the Lagrangian. In that case, we say that there exists a spontaneous symmetry breaking (SSB). In the SM the G_{SM} is broken by the non-zero vacuum expectation value of the Higgs scalar. This is know as the Higgs mechanism which is responsible for mass generation of the gauge bosons in the electroweak sector and also for charged fermions. The unified electroweak sector $SU(2)_L \times U(1)_Y$ is broken[1], the generated gauge bosons $W^{\pm}$ and Z^0 acquire mass while the photon γ, from the invariant $U(1)_{EM}$

[1]For this theory, in 1979 the Nobel Prize was awarded to Abdus Salam, Steve Weinberg and Sheldon Glashow [10–12].

subgroup responsible for the electromagnetic interactions, remains massless. The electric charge is given by the Gell-Mann-Nishijima relation $Q = T_3 + Y/2$ [13,14] where Q is the electric charge, Y represents the hypercharge and T_3 the third component of the weak isospin. The Z^0 boson won't have the original structure vector-axial (V-A) from the $SU(2)_L$ group since it is mixed with the $U(1)_Y$ forming the $U(1)_{EM}$.

A general Lagrangian for this theory depends on the field and on the covariant derivatives with the form

$$\mathcal{L}(\phi(x), D_\mu\phi(x)), \quad D_\mu\phi = \partial_\mu\phi - iV_\mu^a T^a\phi. \tag{2-2}$$

Furthermore, for a non abelian theory

$$[D_\mu, D_\nu] \equiv -iF_{\mu\nu} = -iF_{\mu\nu}^a T^a, \tag{2-3}$$

where

$$F_{\mu\nu}^a = \partial_\mu A_\nu^a - \partial_\nu A_\mu^a + g f^{abc} A_\mu^b A_\nu^c, \tag{2-4}$$

in which the last term corresponds to a non abelian contribution with f^{abc} as the structure constant of the corresponding group and g the coupling constant.

The boson sector is composed by the following integer spin particles: eight massless gluon, mediating the strong force described by quantum–chromodynamics (QCD), one massless photon, for the electromagnetic interaction (EM) described by quantum–electrodynamics (QED), Z^0 and $W^\pm$ massive bosons for the weak interaction; and the spin-0 Higgs boson [15, 16]. In the fermion sector, there are half integer spin particles in three generations: six quarks (up (u), down (d), charm (c), strange (s), top (t), bottom (b)), three charged leptons (electron (e), muon (μ) and tau (τ)) and their respective neutrinos (ν_e, ν_μ and ν_τ). The quarks are not observed individually, only as bounded states such as a quark-antiquark pair called meson, three-quark states called baryons or excited states with four and five quarks called tetraquarks and pentaquarks respectively. See Fig. 2.1 for a representation of the particles in the SM coming in three generations.

The SM is a chiral theory in which each particle carries a representation of the gauge group where its chirality is naturally manifested. There are five fermionic representations in the Standard Model in which each one takes into account the three generations, labeled by the index i and the chirality left handed (L) or right handed (R) given by

$$Q_{L_i}(3,2)_{1/6}, \quad u_{R_i}(3,1)_{2/3}, \quad d_{R_i}(3,1)_{-1/3}, \quad \ell_{L_i}(1,2)_{-1/2}, \quad e_{R_i}(1,1)_{-1}. \tag{2-5}$$

The first represents the left-handed quarks being a triplet of $SU(3)_C$, a doublet of $SU(2)_L$ and the hypercharge given by Gell-Mann Nishijima formula [13,14].

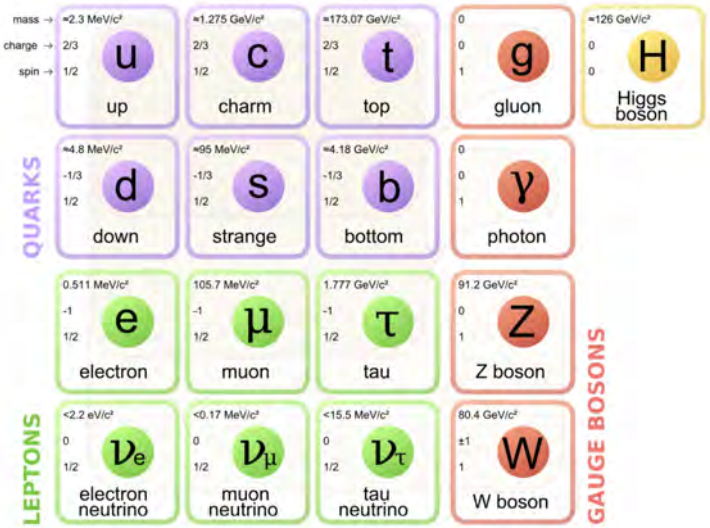

Figure 2.1: Fundamental particles of the Standard Model.

Then, the right-handed up and down quarks, also triplets of $SU(3)_C$ but singlets of $SU(2)_L$. In the leptonic sector, we observe the same behavior as quarks in the $SU(2)$ sector. The left-handed particles are $SU(3)_C$ singlets, since they don't have colour, and $SU(2)_L$ doublets while right-handed leptons are $SU(2)_L$ singlets. Furthermore, the scalar particle H carries the representation $(1,2)_{1/2}$.

2.2 The SM Lagrangian

The most general renormalizable Lagrangian is constituted of the terms:

$$\mathcal{L}_{\text{SM}} = \mathcal{L}_{Kin} + \mathcal{L}_{\text{Yukawa}} + \mathcal{L}_{H}, \tag{2-6}$$

where the first term concerns about the kinetic terms and gauge bosons interactions, the second corresponds to Yukawa interactions between fermions and the scalar field H where all fermions masses come from, and the last concerns about the Higgs field containing its kinetic and potential terms.

In the kinetic sector, the local symmetry of the SM implies gauge boson degrees of freedom which go under the representation:

$$G^{\mu}_{a}(8,1)_0, \quad W^{\mu}_{a}(1,3)_0, \quad B^{\mu}(1,1)_0, \tag{2-7}$$

where the index a indicates a non-abelian structure. G's are the gluon fields and the combination of the W's and B represents the $W^{\pm}$, Z^0 and the photon created after the spontaneous symmetry breaking. The corresponding field strengths are

$$\begin{aligned} G_a^{\mu\nu} &= \partial^\mu G_a^\nu - \partial^\nu G_a^\mu + g_s f_{abc} G_b^\mu G_c^\nu \\ W_a^{\mu\nu} &= \partial^\mu W_a^\nu - \partial^\nu W_a^\mu + g\epsilon_{abc} W_b^\mu W_c^\nu, \\ B^{\mu\nu} &= \partial^\mu B^\nu - \partial^\nu B^\mu \end{aligned} \tag{2-8}$$

where g and g_s correspond to the couplings, f_{abc} and ϵ_{abc} are the structure constants of $SU(3)_C$ and $SU(2)_L$ indicating the non–commutative algebra characteristic resulting in self–interactions for these gauge bosons. Furthermore, we can define the covariant derivative corresponding to SM group symmetry as

$$D_\mu = \partial_\mu - ig'YB_\mu - igW_\mu^a T^a - ig_s G_\mu^b L^b, \tag{2-9}$$

where g - SU(2), g_s - SU(3) and g' - U(1) are the couplings of the interactions of each corresponding gauge group, T^a denotes the generators of $SU(2)_L$, the set of Pauli matrices $\sigma^a/2$ in the fundamental representation, with $a = 1, 2, 3$ and L^b denotes the generators of $SU(3)_C$, Gell-Mann matrices with $b = 1, ..., 8$. The structure of the covariant derivative depends directly on the field that it is being applied to, on the field representation, and on how the fields transform under each symmetry group.

In the Higgs sector, the kinetic and potential terms are responsible for the mass generation of gauge bosons, for the Higgs couplings to gauge bosons and fermions, for the Higgs self couplings and for the Higgs mass. A more explicit expression is given by

$$\mathcal{L}_H = |D_\mu H|^2 - \mu^2 H^\dagger H - \lambda \left(H^\dagger H\right)^2. \tag{2-10}$$

where H is the Higgs field. In the Yukawa sector, the Lagrangian has the form

$$\mathcal{L}_{\text{Yuk}} = -Y_{ij}^d \bar{Q}_{L_i} H d_{R_j} - Y_{ij}^u \bar{Q}_{L_j} \widetilde{H} u_{R_j} - Y_{ij}^e \bar{\ell}_{L_i} H e_{R_j} + \text{h.c.} \tag{2-11}$$

where $Y^{d,u,e}$ are the Yukawa 3×3 matrices with complex entries, not necessarily hermitian, and $\tilde{H} = i\sigma_2 H^*$. This term is particularly interesting given that flavour physics is contained in it, therefore, a more detailed discussion about this term is provided in the next section.

A more explicit expression for the SM Lagrangian is given by

$$\begin{aligned} \mathcal{L}_{SM} &= -\frac{1}{4} G_{\mu\nu}^a G^{a\mu\nu} - \frac{1}{4} W_{\mu\nu}^a W^{a\mu\nu} - \frac{1}{4} B_{\mu\nu} B^{\mu\nu} \\ &+ i\overline{Q}_{L_j} \not{D} Q_{L_j} + i\bar{\ell}_{L_j} \not{D} \ell_{L_j} + i\overline{u}_{R_j} \not{D} u_{R_j} + i\overline{d}_{R_j} \not{D} d_{R_j} + i\overline{e}_{R_j} \not{D} e_{R_j} \\ &+ |D_\mu H|^2 + V(H) \\ &+ \bar{\ell}_L H Y_e e_R + \bar{Q}_L H Y_d d_R + \bar{Q}_L \tilde{H} Y_u u_R + h.c. \end{aligned} \tag{2-12}$$

where $\not{D} = \gamma^\mu D_\mu$. The first line corresponds to the kinetic terms and self-

interactions of the gauge bosons, the second line to the kinetic terms of fermions and their interactions with the gauge bosons, the third line to the kinetic and potential terms of the Higgs field and the last, to the Yukawa terms accounting the mass of quarks and leptons. The Yukawa terms are particularly interesting for this work given that flavour physics is contained in it and characteristics such as flavour changing between families arise from these terms.

2.3 Flavour physics

After the electroweak symmetry breaking, the vacuum is invariant under the gauge group $SU(3)_C \times U(1)_{EM}$. Both strong and EM interactions are flavour universal, meaning that there is no flavour mixing and the interactions have the same couplings, but the weak interactions don't behave in the same way.

Mediated by the charged bosons $W^{\pm}$ and the neutral boson Z^0, the weak interactions generate two types of weak currents. When the processs occurs mediated by the Z^0 boson, which couples diagonally in flavour space to all fermions, the current associated is the so called neutral current (NC) and no flavour changing has been observed at tree level. On the other side, for processes mediated by the charged $W^{\pm}$, we observe generation changing currrents, with a different behavior for leptons and quarks. The current associated is called the charged current (CC).

In the leptonic sector, the mass and interaction basis are the same[2]. The charged lepton couples to its corresponding neutrino, thus, there is no generation changing. On the contrary, in the quark sector, the interaction and mass basis are different with non-diagonal terms in the Lagrangian, thus generation changing is observed. The basis are related by a unitary matrix and each element of this matrix corresponds to a transition probability between quarks of different flavour including transitions between families.

Let's Consider the Yukawa terms for the quark sector after the SSB

$$\mathcal{L} = -\frac{v}{\sqrt{2}}\left(\bar{d}_L Y_d d_R + \bar{u}_L Y_u u_R\right) + \text{h.c.}. \tag{2-13}$$

To diagonalize these matrices, we can perform bi-unitary rotations written as

$$Y_d = U_d M_d U_d^{\dagger}, \quad Y_u = U_u M_u U_u^{\dagger}, \tag{2-14}$$

where $U_{u,d}$ are unitary matrices, thus $M_{u,d}^{\text{diag}} = U_{(u,d)}^{\dagger} Y_{u,d} U_{(u,d)} (v/\sqrt{2})$. In this

[2]In this case we are neglecting neutrinos masses.

basis, the Yukawa terms are

$$\mathcal{L} = -\frac{v}{\sqrt{2}}\left(\bar{d}_L U_d M_d U_d^\dagger d_R + \bar{u}_L U_u M_u U_u^\dagger u_R\right) + \text{h.c.} \tag{2-15}$$

Performing a change of basis for the left and righ-handed quarks ($d_R \to U_d d_R$, $u_R \to U_u u_R$, $d_L \to U_d d_L$ and $u_L \to U_u u_L$) we remove $U_{u,d}$ and the Yukawa terms are now diagonal. In the mass basis, the Lagrangian is written as

$$\mathcal{L} = -m_d \bar{d}_L d_R - m_u \bar{u}_L u_R + \text{h.c.} \tag{2-16}$$

where

$$m_d = \frac{v}{\sqrt{2}}(y_d, y_s, y_b), \qquad m_u = \frac{v}{\sqrt{2}}(y_u, y_c, y_t). \tag{2-17}$$

From the charged current interactions we have

$$\mathcal{L}_{W^\pm} = \frac{g}{\sqrt{2}} \bar{u}_L \gamma^\mu \left[(U_u)^\dagger (U_d)\right] d_L W_\mu^+ + h.c. \tag{2-18}$$

where the coupling only occurs for left-handed fermionic fields. The combination $V = (U_u)^\dagger (U_d)$ is the 3×3 unitary matrix known as the Cabibbo-Kobayashi-Maskawa (CKM) matrix [17,18]. Since V is non-diagonal, the gauge bosons $W^\pm$ couple to quarks mass eigenstates of different families, representing the mixing matrix for quarks. The transition amplitude probability between two quarks is proportional to the matrix element $V_{qq'}$. The explicit form of the CKM matrix is

$$V_{CKM} \equiv V_u V_d^\dagger = \begin{bmatrix} V_{ud} & V_{us} & V_{ub} \\ V_{cd} & V_{cs} & V_{cb} \\ V_{td} & V_{ts} & V_{tb} \end{bmatrix}. \tag{2-19}$$

There are several parametrisations for this matrix, the most used is the Wolfenstein parametrisation [19] making use of experimental measurements expanded in terms of $\lambda = \sin\theta_c$, where θ_c is the Cabibbo angle. The CKM matrix has the form:

$$V_{CKM} = \begin{pmatrix} 1 - \lambda^2/2 & \lambda & A\lambda^3(\rho - i\eta) \\ -\lambda & 1 - \lambda^2/2 & A\lambda^2 \\ A\lambda^3(1 - \rho - i\eta) & -A\lambda^2 & 1 \end{pmatrix} + O\left(\lambda^4\right). \tag{2-20}$$

Being unitary, there are only 4 independent parameters λ, A, ρ and η describing the matrix, where η express its complex nature responsible for CP violation in the SM. If we focus on the charm sector - the first two rows and columns - this sub-matrix is diagonal and real up to $\mathcal{O}(\lambda^2)$, the so-called Cabibbo matrix. A transition in which the amplitude depends only on elements on the diagonal

are called *Cabibbo-favored*; when it depends on one off-diagonal element, it is called *Cabibbo-suppressed* and for a transition which the matrix elements are both off-diagonal, are referred to as *doubly Cabibbo-suppressed*.

2.4 Hadronic Decays

The SM describes successfully the weak interactions between the fundamental particles via an exchange of bosons $W^{\pm}$ and Z^0. However, due to the strong interactions in the hadron sector, it is not easy to describe the weak process in terms of mesons and baryons.

Considering a meson decay mechanism, we can introduce the quark diagramatic approach by Chau [20]. The first two diagrams are characterised by the emission of a W boson either via an external emission as in Figure 2.2 (left) in which they are in a singlet state, or via an internal emission as in Figure 2.2 (right) in which the produced quarks have a defined colour state. The difference between both diagrams is the colour suppression of the second with respect to the first, the produced quark and antiquark must have their colour state defined such that the hadrons formed are colour singlets. In both diagrams the quark participating in the process is treated as a quasi-free particle inside the meson for the W emission diagrams while the light quark ($\bar{u}, \bar{d}$ or $\bar{s}$) would be a spectator during the decay, without producing any effects associated directly to the decay. The contribution of the light quarks should only appear later in the hadronization process. We call this the *Spectator Model*.

On the other side, diagrams in which both quarks contribute to the weak decay are called *non-Spectators* such as the *annihilation* of a W, as in Figure 2.3 (left), where a pair of quark-antiquark annihilates to produce a W boson that couples with another pair of quark-antiquark, or a W *exchange* processes, Figure 2.3 (right), which occurs only for neutral mesons.

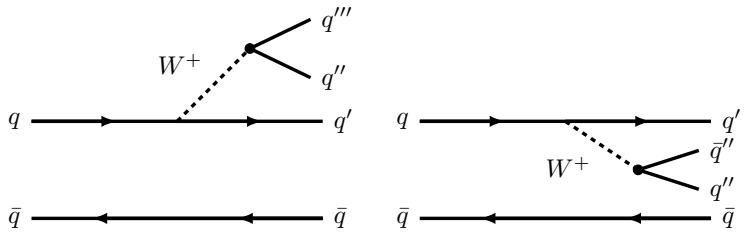

Figure 2.2: External (left) and internal (right) emission of W diagrams.

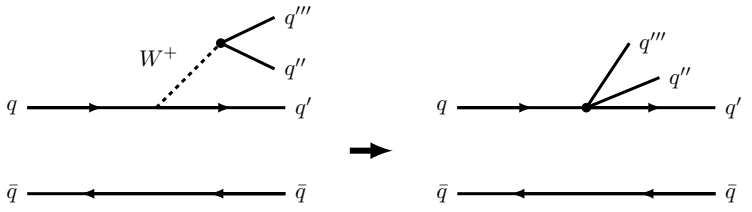

Figure 2.4: Schematic diagram illustrating the effective vertex.

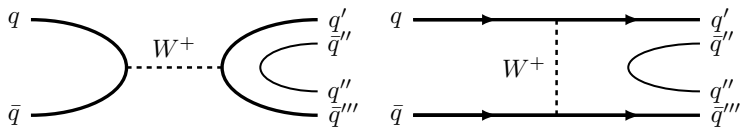

Figure 2.3: Annihilation (left) and W exchange (right) diagrams.

2.5 Effective Weak Hamiltonian and Factorization

One way to deal with hadronic decays, such as the decay of the D meson, is to work with an effective approach preserving the current–current structure in which the mesons are represented by effective hadronic currents. In this approach, the decay amplitude approximated into factorized terms of more simple amplitudes suggested by Cabibbo and Maiani [21] and Fakirov and Stech [22]. Considering the process in the limit $p^2 \ll m_W^2$, momentum smaller than the propagator mass, one can write the W propagator as:

$$\frac{1}{p^2 - m_W^2} \to \frac{1}{-m_W^2(1 - \frac{p^2}{m_W^2})} = \frac{-1}{m_W^2}\left(1 + \frac{p^2}{m_W^2} + ...\right) \tag{2-21}$$

Hence, looking at the first term of this expansion, it can be treated with an effective vertex since it is independent of p. A schematic diagram illustrating the effective vertex is shown Fig. 2.4. The effective weak Hamiltonian is obtained by integrating out the heavy degrees of freedom of the SM Lagrangian and has a structure given by [23, 24]

$$\mathcal{H}_{eff} = \frac{G_F}{\sqrt{2}} \sum_i V_{\rm CKM}^i C_i(\mu) \mathcal{O}_i, \tag{2-22}$$

where G_F is the Fermi constant, O_i are the relevant local operators governing the decay, V_{CKM} the Cabibbo–Kobayashi–Maskawa matrix elements [17], μ is the renormalization scale and C_i the Wilson coefficients [25] describing the contribution of a given operator in the Hamiltonian. Moreover the C_i coefficients depend on the renormalization scale μ which encode the short-distance effects above μ and are process independent. This series of effective vertices is known as operator product expansion (OPE) [25–27]. Since μ is

arbitrary, the scale dependence must be cancelled out or, in other words, the product of the coefficient and the operator must be scale independent

$$\frac{d}{d\mu}[C_i(\mu)\mathcal{O}_i(\mu)] = 0. \tag{2-23}$$

The value of μ is typically chosen to be the order of the mass of the decaying hadron ($\mathcal{O}(m_c)$ for D meson decays), serving as a way to separate physical contributions of the decay amplitude into long–distance contributions corresponding to scales lower than μ and short–distance contributions for scales higher than μ.

Let's consider a two-body process $D^+ \to h_1 h_2$, the effective hamiltonian is given by

$$\mathcal{H}_{eff} = \frac{G_F}{\sqrt{2}} V_{cd} V_{ud}^* [c_1 O_1 + c_2 O_2], \tag{2-24}$$

$$\begin{aligned} O_1 &= [(\bar{u}\gamma_\mu(1-\gamma_5)d)(\bar{d}\gamma_\mu(1-\gamma_5)c)] \\ O_2 &= [(\bar{u}\gamma_\mu(1-\gamma_5)c)(\bar{d}\gamma_\mu(1-\gamma_5)d)], \end{aligned} \tag{2-25}$$

where each term $\bar{q}\gamma_\mu(1-\gamma_5)q'$ corresponds to left-handed hadronic currents and the coefficients c_1, c_2 determine the influence of strong interactions in the QCD regime. The term containing $\mathcal{O}_1$ corresponds to the decay via the charged current describing the transition $c \to d$ while the later with $\mathcal{O}_2$ describes the transition $c \to u$. Applying the naive factorization method [3], we obtain

$$\begin{aligned} \langle h_1 h_2|\mathcal{H}_{eff}|D^+\rangle = \frac{G_F}{\sqrt{2}} V_{cd} V_{ud}^* [a_1 \langle h_2|(\bar{u}\gamma_\mu(1-\gamma_5)d)|0\rangle\langle h_1|(\bar{d}\gamma_\mu(1-\gamma_5)c)|D^+\rangle \\ + a_2 \langle h_1 h_2|(\bar{d}\gamma_\mu(1-\gamma_5)d)|0\rangle\langle 0|(\bar{u}\gamma_\mu(1-\gamma_5)c)|D^+\rangle], \end{aligned} \tag{2-26}$$

where the coefficients a_1, a_2, via perturbative QCD, are related to c_1, c_2. The factorization method applied to three body decays is more complicate and in the next chapter we will discuss this approach applied to the $D^+ \to \pi^-\pi^+\pi^+$ channel.

2.6 Resonances and the S−matrix

As a related topic to be seen later, this section is dedicated to define a resonance and its characteristics. In the study of elementary particles, the experiments which provide relevant information are scattering and decay processes. Instead of measuring transition amplitudes, we look at quantities

[3] From now on, we will refer simply as factorization.

such as rates and cross-sections to obtain information about what could have happened in the process. These observable quantities are related to the probability of observing a certain final state in the far future, *"out"*, given the initial state constructed in the far past, *"in"*, determined by their overlap, $\mathcal{P} = |\langle\phi_f(p)|\phi_i(p)\rangle|^2$.

In the scattering formalism, the unitary operator that connects asymptotic *in* and *out* states is called the $S-$matrix, defined as:

$$i(2\pi)^4\delta^4(p_1+p_2-p_3-p_4)\,\mathcal{M}(p_1,p_2;p_3,p_4) =_{\text{out}} \langle p_3p_4|S-\mathbb{1}|p_1p_2\rangle_{\text{in}} \quad (2\text{-}27)$$

where $|p_1p_2\rangle$ and $\langle p_3p_4|$ are asymptotic states of two non-interacting particles with momentum p_1,p_2 and p_3,p_4. The left side term describes deviations from the free theory. The $S-$matrix is responsible for encoding all physics underlying the process and is related to the scattering amplitude $\mathcal{M}$ which is strongly constrained by analyticity and unitarity principles of the $S-$matrix [1]. The scattering amplitude $\mathcal{M}$ can be written in terms of the Mandelstan variables s,t,u up to poles and kinematic singularities and can be distinguished from the decay amplitude $\mathcal{A}$ since unitarity puts different constraints on them. For the decay amplitude case, the unitarity relation for heavy state i into a channel a is given by

$$i\left[\mathcal{A}_a^i - \mathcal{A}_a^{i*}\right] = (2\pi)^4 \sum_c \int d\Phi_c \mathcal{M}_{ca}^* \mathcal{A}_c^i. \quad (2\text{-}28)$$

In the case where only a single channel contributes, the phase of $\mathcal{A}$ agrees to that of $\mathcal{M}$ according to Watson theorem [28].

The $S-$matrix is an analytic function up to its branch points, appearing when there is a channel opening, and poles, which can be bound states or resonances [1, 29, 30]. The location of such poles is an essential feature in defining these states. For bound states, the poles are located on the physical Riemann sheet, while for resonances, they are located on the unphysical Riemann sheet closest to the physical one, usually referred to as the second sheet. In the case of resonances in subsystems of multi–particle final states, branch points occur in the complex plane of the second sheet. Furthermore, from analyticity, a pole located at a complex value of s is accompanied by a pole located at its complex conjugate value, s^* [31]. At the threshold, both poles are equally relevant, but outside the threshold, the pole which has the negative imaginary part closer to the physical axis will plays a more important role, in the vicinity of the resonance region it influences more the observables.

An schematic plot of the imaginary part of a generic single–channel scattering amplitude with an isolated resonance is shown in Figure 2.5. The

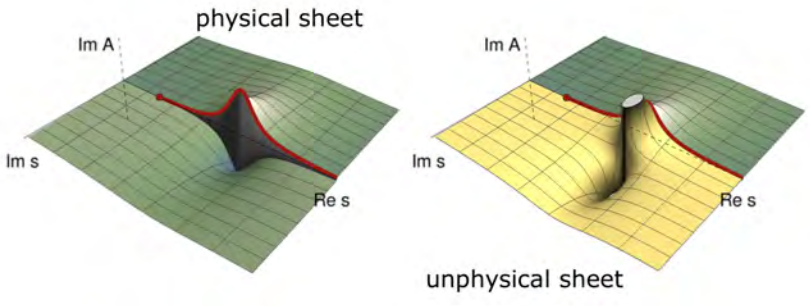

Figure 2.5: Imaginary part of a typical single–channel scattering amplitude with an isolated resonance [1,30].

solid red line illustrates the physical range of the real valued variable s in which the threshold is illustrated by the red dot. In the left plot, the imaginary part of the amplitude in the complex S–plane is illustrated and corresponds to the first physical sheet, ImA≥ 0 shown as the green surface, while the right plot shows analytic continuation of this amplitude to the lower plane of the unphysical sheet, ImA< 0 shown as the yellow surface, which contains the resonance pole.

Resonances can appear in decay processes of the form

$$A \to \mathbf{R} + S \to [P_1 + \ldots + P_n] + S, \tag{2-29}$$

where S is the spectator particle and R is the resonance which its properties can be studied via a Dalitz plot analysis. The main characteristics of a resonance are its pole position in the complex $s-$plane, s_R, and its residue [1,29,30]. The pole position is parametrised with its mass m_R and total width Γ_R introduced via the pole parameters $\sqrt{s_{\rm R}} = m_R - i\Gamma_R/2$ and it is independent of the reaction studied. Additionally, the residues are responsible for quantifying its couplings to the various channels and useful to define branching ratios. The residues can be calculated via an integration along a closed contour around the pole according to

$$\mathcal{R}_{fi} = \frac{i}{2\pi} \oint ds \mathcal{M}_{fi}, \tag{2-30}$$

where $\mathcal{M}$ denotes the scattering matrix written, in the close vicinity of a pole $\mathcal{M}$, as

$$\lim_{s \to s_R} \mathcal{M}_{fi} = -\frac{\mathcal{R}_{fi}}{s - s_{\rm R}}, \tag{2-31}$$

where s_R denotes the pole position of the resonance R and $\mathcal{R}$ the residue. If the structure is narrow and there are no other thresholds or other resonances nearby, the Breit-Wigner is the most common parametrisation.

3
The $D^+ \to \pi^-\pi^+\pi^+$ three body decay

The decay $D^+ \to \pi^-\pi^+\pi^+$ is a Cabibbo–suppressed mode with a quark level transition $c \to du\bar{d}$ that can proceed mainly at tree level by spectator and annihilation diagrams, which is suppressed with respect to the tree level diagram, from the current–current operators porportional to $V_{cd}V_{ud}^*$ of order $\mathcal{O}(\lambda)$ in Wolfenstein parametrisation [1,19], as can be seen in the top diagrams in Figure 3.1. A transition via a loop penguin type amplitude, as shown in the bottom diagram in Figure 3.1, is also possible, where the virtual quark being b would introduce a weak phase through V_{ub}, and potentially this would imply CP violation in this channel. Nevertheless, the penguin amplitude is $\mathcal{O}(\lambda^5)$ and, for the purposes of this work any CP-violation effect can be safely neglected. This process is observed with a branching fraction of $(3.29 \pm 0.2) \times 10^{-3}$ [1].

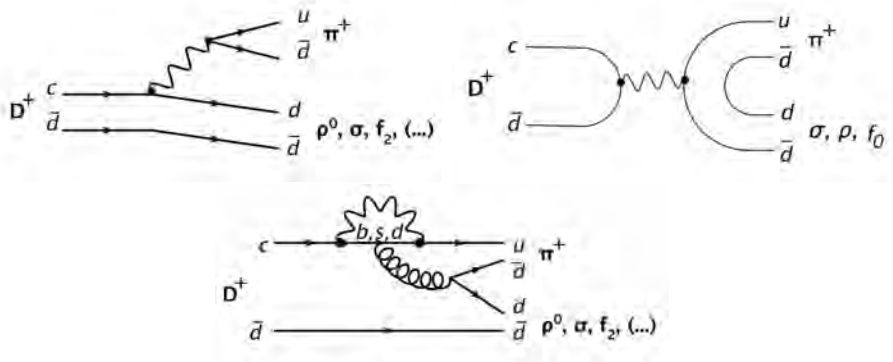

Figure 3.1: Tree level, annihilation and penguin diagrams of the $D^+ \to \pi^-\pi^+\pi^+$ decay.

Figure 3.1 also shows that the $d\bar{d}$ pair may form different resonances as intermediate states which decay to $\pi^-\pi^+$ creating a rich pattern in the phase space of the decay. From previous experimental analyses [6–8] we learned that the main resonances contributing for the $D^+ \to \pi^-\pi^+\pi^+$ channel are the spin 1 states $\rho^0(770)$ and $\rho^0(1450)$, the scalars $\sigma(500)$, $f_0(980)$, $f_0(1370)$, $f_0(1500)$ and the spin 2 contribution $f_2(1270)$. The distribution of events across the phase space provides important information about hadronic processes by revealing and allowing the understanding of the intermediate states dynamics. The study the resonance pattern and interferences in the $D^+ \to \pi^-\pi^+\pi^+$ decay is the

main objective of an amplitude analysis. From now on, we label the decay particles (pions) with the convention $D^+ \to \pi_1^-\pi_2^+\pi_3^+$, so particle 1 is always the pion with opposite charge with respect to the other decay products.

If a resonant state is produced in the $\pi_1^-\pi_2^+$ system, the third pion, π_3^+, is referred to as the companion. There are two π^+ in the final state so the same resonance can be formed in the $\pi_1^-\pi_3^+$ system with π_2^+ being the companion and, due to the pair of identical π^+, the process is symmetrical with respect to the systems $\pi_1^-\pi_2^+$ and $\pi_1^-\pi_3^+$. In this analysis, we label the π^- as particle 1 and the other two charged π^+ are randomly chosen as particles 2 and 3, to ensure that they have the same kinematic distributions.

3.1 Three-Body decay Kinematics

Consider a spinless particle with mass M and 4−momenta P that decays into three spinless particles with masses m_1, m_2 e m_3 with 4−momenta p_1, p_2 and p_3, as illustrated in Figure 3.2.

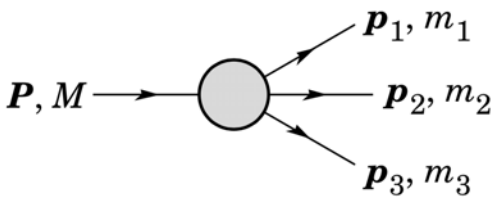

Figure 3.2: Schematic of a three-body decay from PDG [1].

In principle, there are 9 quantities to describe this decay, the three *tri-momentum* vectors of the final state particles. Considering energy–momentum conservation, $P^\mu = p_1^\mu + p_2^\mu + p_3^\mu$, we reduce the number of variables by 4. Recalling also that the decay is isotropic, it cannot depend on the three Euler's angles describing its orientation with respect to the parent reference frame, thus we end up with only two degrees of freedom [32]. The set of available configurations for any array of independent kinematics variables configures the *phase space* of the decay, therefore, in our case the phase space is bidimensional [33].

Looking at the decaying particle in the rest frame where $P^\mu = (M, \vec{0})$ for the initial particle and $p_i^\mu = (E_i, \vec{p}_i)$ for the three decay particles, we can

define the following Lorentz invariants:

$$\begin{aligned} s_{ij} = m_{ij}^2 &= (p_i + p_j)^2 = m_i^2 + m_j^2 + 2E_iE_j - 2\vec{p}_i\vec{p}_j \\ &= (P - p_k)^2 = M^2 + m_k^2 - 2ME_k, \end{aligned} \tag{3-1}$$

where $\{i, j, k\} \in \{1, 2, 3\}$ and $i \neq j \neq k$. Since only two of them are independent, the remaining one is determined by the relation

$$s_{23} + s_{31} + s_{12} = M^2 + m_1^2 + m_2^2 + m_3^2 \ . \tag{3-2}$$

The so called Dalitz plot (DP) is the three-body phase space represented by any pair among s_{12}, s_{13} and s_{23}, or by any related to these by a linear transformation with a constant Jacobian [34]. The boundaries of the DP are determined by the kinematics of the decay, limited by a maximum and minimum value of s_{ij} given by

$$(m_i + m_j)^2 \leq s_{ij} \leq (M - m_k)^2. \tag{3-3}$$

In the maximum limit, all the momenta is devoted to the m_{ij} system thus $\theta_{ij} = \pi$ where θ_{ij} is the angle between particles i and j, meaning that $\vec{p}_i = -\vec{p}_j$, collinear and in opposite direction, and $\vec{p}_k = 0$, at rest. On the other side, in the minimum limit, $\theta_{ij} = 0$ and $\theta_{ik} = \theta_{jk} = \pi$, meaning that i and j are collinear and in opposite direction to k. Another relevant quantity to define is helicity angle and the cosine defined as the angle between the bachelor particle and the resonance daughter with equal charge. The bachelor particle is the one that does not come from the resonance state, for instance, if the resonant state comes from the first and second daughter, we will call the third as the bachelor.

Given the invariant variables describing the process, the kinematic limits give rise to the upper and lower boundaries of the DP, corresponding to s_{13+} and s_{13-} respectively, given by

$$\begin{aligned} s_{13\pm} = m_1^2 + m_3^2 + \frac{1}{2\sqrt{s_{12}}}\Big[&(s_{12} - s + m_3^2)(s_{12} + m_1^2 - m_2^2) \\ &\mp \lambda^{1/2}(s_{12}, s, m_3^2)\lambda^{1/2}(s_{12}, m_1^2, m_2^2)\Big] \ , \end{aligned} \tag{3-4}$$

where the kinematic triangular function is given by $\lambda(x, y, z) = x^2 + y^2 + z^2 - 2xy - 2yz - 2zx$. A generic Dalitz plot with its boundaries is shown in Figure 3.3 in terms of the invariants $s_{12} = m_{12}^2$ and $s_{23} = m_{23}^2$.

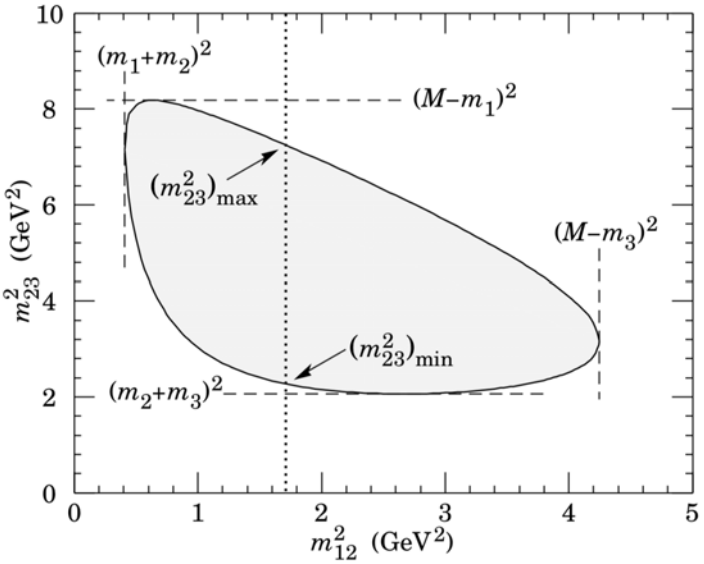

Figure 3.3: Generic Dalitz plot in (s_{12},s_{23}) from PDG [1].

The decay rate brings the dynamics of the decay. For the spinless three-body process, the decay rate is given by [1]:

$$d\Gamma = \frac{1}{2(2\pi)^5 M^5}\int |\mathcal{A}|^2\delta^4(P-p_1-p_2-p_3)\frac{d^4p_1}{2E_1}\frac{d^4p_2}{2E_2}d^4p_3\delta\left(p_3^2-m_3^2\right)\ , \quad (3\text{-}5)$$

in which $\mathcal{A}$ contains all the dynamic information, the four-dimensional delta function constrains the contour of the DP while the one-dimensional delta corresponds to on–shell (real) particles in the final state. Integrating over d^3p_3 and using the relation

$$\delta' = \delta\left(\cos\theta_{12} - \frac{M^2+m_1^2+m_2^2-m_3^2-2M\left(E_1+E_2\right)+2E_1E_2}{2p_1p_2}\right), \quad (3\text{-}6)$$

the integral in d^4p_3 can be solved and the decay rate can be reduced to a more compact form

$$d\Gamma = \frac{\pi^2}{2(2\pi)^5 M}\int |\mathcal{A}|^2\delta' dE_1 dE_2 d\cos\theta_{12}. \quad (3\text{-}7)$$

Also, we can write the decay rate in terms of the invariants s_{ij}, thus, after performing the cosine integral and rearranging the decay rate in terms of Dalitz variables, the expression is written as:

$$d\Gamma = \frac{1}{256\pi^3 M^3}\int |\mathcal{A}|^2 ds_{ij}ds_{jk}\ . \quad (3\text{-}8)$$

Given M, the density of events in the DP is proportional to $|\mathcal{A}|^2$, thus the dynamics is directly observed from the distribution in the phase space

$$\frac{d\Gamma}{ds_{ij}ds_{jk}} \propto |\mathcal{A}|^2 \ . \tag{3-9}$$

Each point in the DP corresponds to a possible configuration of the decay and with high statistics, the DP illustrates more explicitly its signatures and characteristics corresponding to the possible processes that occurred. If $|\mathcal{A}|^2$ is constant, meaning no dynamics, the DP will be distributed uniformly. However, if the processes occurs via an intermediate resonant state, the DP will be populated in bands with given features, such as its mass, width and spin. If there are more than one resonance sharing the same physical region in the phase space, interference effects will rise as a higher density of points for constructive interferences or almost no density of points for destructive interferences.

The use of a Dalitz Plot for amplitude analysis has many benefits since three-body decays usually proceed as quasi–two–body processes in which an intermediate resonant state is produced. Therefore, we can use this tool to understand and reveal resonances in different final states, and use for study of meson spectroscopy. It is an ideal place to study new and known states, lineshapes, to study interference patterns, and CP-violation since it is sensitive to phases.

3.2 The $\mathbf{D}^+ \to \pi^-\pi^+\pi^+$ phase space

The two Dalitz plot variables are chosen in order to better illustrate where the resonance contributions are expected. All states are formed in the $\pi^-\pi^+$ systems and, since there are two identical π^+, the Dalitz plot constituted as $s_{12} \times s_{13}$ presents a symmetric behavior with respect to the diagonal (remembering our choice $D^+ \to \pi_1^-\pi_2^+\pi_3^+$). At this point, for illustration only, we show the $D^+ \to \pi^-\pi^+\pi^+$ Dalitz plot in Figure 3.4 from our data sample containing approximately 900 thousand events (as discussed later in Chapter 5). The DP is a mass squared plot, thus a resonance with mass around 0.775 GeV$^2/c^4$ such as the $\rho^0(770)$ is expected to appear at $s_{12,13} \sim 0.6$ GeV$^2/c^4$. By a qualitative inspection, it can be seen a clear signature of a $f_0(980)$ contribution and a significant broad region corresponding to the $\sigma(500)$ state. Since the $f_0(980)$ is a scalar contribution, it should appear as a dense line, however, a destructive interference is cancelling part of the $f_0(980)$ region, at $s_{12,13} > 1.6$ GeV$^2/c^4$. In addition, an interesting effect can be observed in the corresponding

$\rho^0(770)$ region. The Dalitz plot illustrates in this region two lines providing evidence for an interference pattern between $\rho^0(770)$ and $\omega(782)$ contributions where the process $\omega(782) \to \pi^-\pi^+$ violates isospin [35]. Furthermore, given that the $\rho^0(770)$ is a spin 1 state, it is expected to have a distribution with two lobes considering the angular distribution for a spin-1 particle with a cosine behavior from the Legendre polynomials, but an interference between the $P-$ and low mass $S-$wave is observed producing an almost total cancellation of the highest lobe. We also observe a region at low $\pi^+\pi^+$, running along the diagonal axis, in which states such as $\rho^0(1450)$, $f_2(1270)$, $f_0(1500)$ and $f_0(1370)$ contribute. In addition, a thin line is observed at $s_{12,13} \sim 0.25$ GeV$^2/c^4$ which corresponds to decays into $K_S\pi^+$ but they will be vetoed as discussed in Chapter 5. The DP for each individual resonance can be found in Appendix 12. The complexity illustrated in the Dalitz plot shown in Figure 3.4 calls for the necessity of an amplitude analysis of this channel.

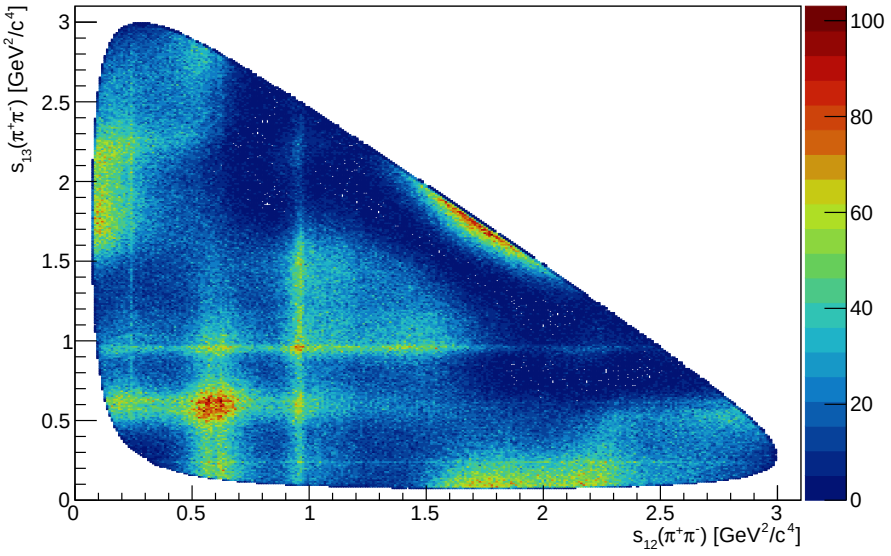

Figure 3.4: $D^+ \to \pi^-\pi^+\pi^+$Dalitz plot from LHCb data.

3.3 Previous analyses

Previous analyses of the $D^+ \to \pi^-\pi^+\pi^+$ decay were performed by E791, FOCUS and CLEO collaborations. In 2001, the E791 collaboration [6] performed a Dalitz plot analysis using the Isobar Model, discussed in Chapter 6, with a data sample consisting of approximately 1200 events. An evidence for a light and broad scalar resonance in $D^+ \to \pi^-\pi^+\pi^+$ decays was found in

this analysis indicating the existence of the scalar meson $\sigma(500)$ [1] with mass $478^{+24}_{-23} \pm 17\text{MeV}/c^2$ and width $324^{+42}_{-40} \pm 21\text{MeV}/c^2$ accounting approximately for half of the decays. This experimental evidence for the $\sigma(500)$ resonance provided a significant interest in understanding the underlying dynamics of this decay channel. The analysis also included the contributions $f_0(980)$, $f_2(1270)$, $f_0(1370)$, $\rho(770)^0$ and $\rho(1450)^0$. The $\pi^-\pi^+$ projection from E791 is shown in Fig. 3.5. Other analyses of $\pi\pi$ scattering data also claimed the presence of this state in the form of a pole close to the threshold with a significantly large imaginary part [37–39] but the E791 experiment was the first solid evidence for this resonant state.

FOCUS [7] and CLEO [8], have also performed a Dalitz plot analyses of this channel with more emphasis in studying the scalar sector. In FOCUS analysis the $S-$wave contribution was parametrised using a $K-$Matrix formalism using input from a global $\pi\pi$ analysis from scattering data; the data sample corresponded to approximately 1500 events, as illustrated in Fig. 3.6. In 2007, CLEO's analysis of the $S-$wave used different phenomenological approaches in addition to a Isobar approach with a data sample consisted of approximately 2600 events. The $S-$Wave was parametrised using Joseph Schechter [40] and co-workers model, based on the meson part of the chiral invariant linear sigma model Lagrangian, and the Achasov Model [41] in which treats the $\pi^+\pi^-$ $S-$wave via the sum of a number of amplitudes: a non resonant contribution, pointlike $\pi^-\pi^+\pi^+$ production, direct resonance production via the $D^+ \to \sigma(500)\pi^+$, $D^+ \to f_0(980)\pi^+$ and the rescattering terms from several intermediate states, $\pi^+\pi^-$, $\pi^0\pi^0$, and $K\bar{K}$ to the final $\pi^+\pi^-$ state and the other spin zero contributions were included via isobar. In the models contemplated by CLEO's analysis, the $S-$wave was composed of only a $\sigma(500)$ and $f_0(980)$ contributions. A summary of previous results is shown in Table 3.1.

From the available experimental analyses, it has become clear that the $S-$wave is the major contribution to the decay $D^+ \to \pi^-\pi^+\pi^+$ and the effort in parametrising this component is quite a challenging task due to the coexistence of several broad overlapping spin zero states at energies below 2 GeV$/c^2$.

[1] This important result was then followed by the observation of another scalar, the $\kappa(700)$, in $D^+ \to K^-\pi^+\pi^+$ decays [36].

Fit Fractions % (FF)			
	E791 [6]	CLEO [8]	FOCUS [7]
$\sigma(500)\pi^+$	46.3 ± 9.2	41.8 ± 2.9	
NR	7.8 ± 7.8	<3.5	
$f_0(980)\pi^+$	6.2 ± 1.4	4.1 ± 0.9	
$f_0(1370)\pi^+$	2.3 ± 1.7	2.6 ± 1.9	
$f_0(1500)\pi^+$		3.4 ± 1.3	
$(\pi^+\pi^-)_S\pi^+$	54.8 ± 9.5	51.9 ± 3.8	56.0 ± 3.9
$\rho(770)\pi^+$	33.6 ± 3.9	20.0 ± 2.5	30.8 ± 3.9
$f_2(1270)\pi^+$	19.4 ± 2.5	18.2 ± 2.7	11.7 ± 1.9
$\rho(1450)\pi^+$	0.7 ± 0.8	<2.4	
$\sum FF$	116.3	90.1	98.5

Table 3.1: Fit fractions (in %) from E791 [6] and CLEO [8] using Isobar Model and FOCUS [7] using $K-$Matrix. The $(\pi^+\pi^-)_S\pi$ estimates the fraction of the total $S-$wave being the sum of the scalar contributions in the Isobar analysis.

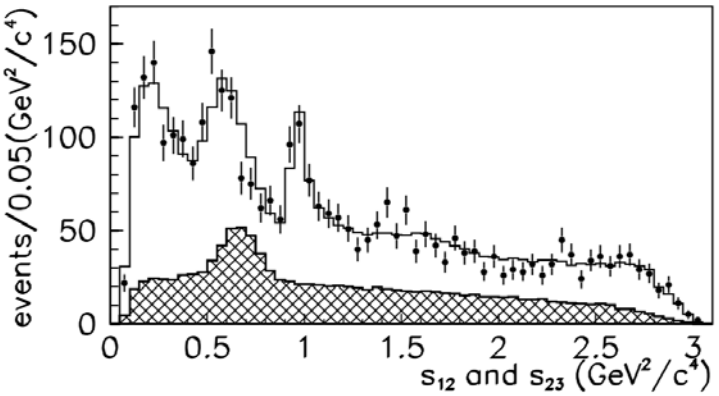

Figure 3.5: $\pi^+\pi^-$ mass projection from $D^+ \to \pi^-\pi^+\pi^+$ decays E791 analysis [6].

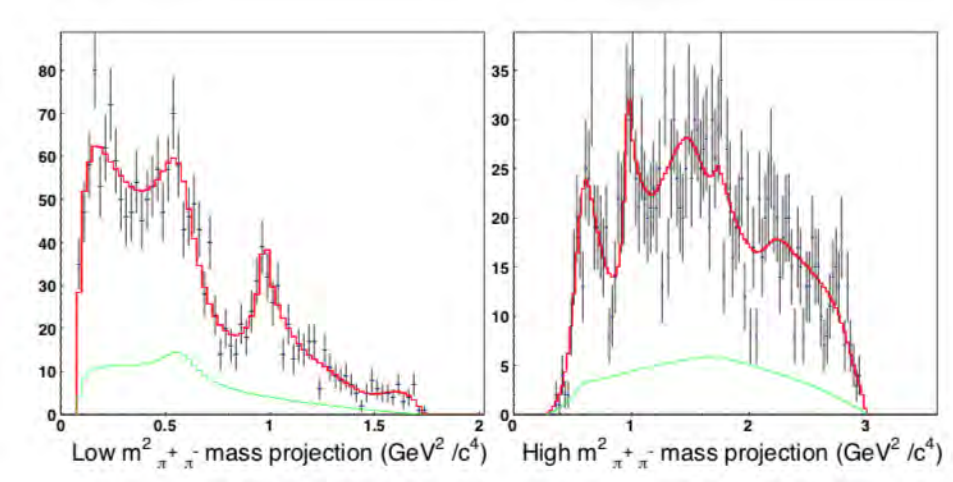

Figure 3.6: High and low $\pi^+\pi^-$ mass projections of $D^+ \to \pi^-\pi^+\pi^+$ decays using K-Matrix formalism form FOCUS analysis [7].

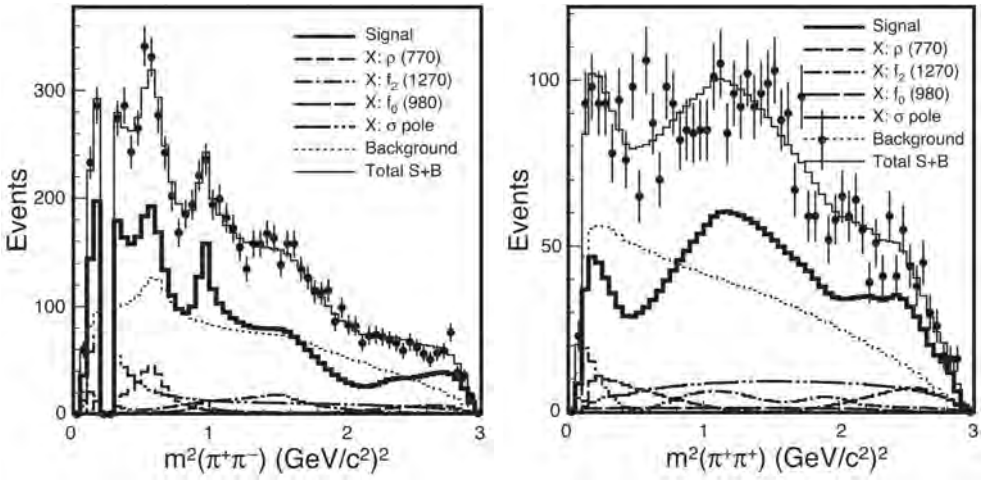

Figure 3.7: $\pi^+\pi^-$ and $\pi^+\pi^+$ mass projections of $D^+ \to \pi^-\pi^+\pi^+$ using Isobar model from CLEO analysis [8].

3.4 Towards the analysis with LHCb data

Although previous results [6–8] for this decay channel have provided significant contributions in understanding the dynamics involved in this process, the statistics were very limited and now, with larger samples from the LHCb experiment, a more detailed study can be done. In particular, the scalar sector remains as the biggest challenge in this decay mode. Composed by several broad overlapping resonant states, the $S-$wave contribution calls for a better description and phenomenological models to provide a satisfactory parametrisation able to explain the underlying behavior. Therefore, the Dalitz plot analysis, besides revealing and describing all the resonant substructures formed in

the process, is also used to extract the $S-$wave component that could be used as input for the development of new phenomenological models. To obtain the $\pi^+\pi^-$ $S-$wave amplitude, three different approaches are used: the traditional Isobar Model, the $K-$Matrix formalism and the quasi Model Independent Partial Wave Analysis. From the last approach, the $S-$wave magnitude and phase behavior are obtained in a model independent way. This quasi-model-independent analysis is particularly interesting in this work since it has never been previously performed in this channel.

The motivations for this analysis are manifold. Given the complexity and the variety of resonant states observed in the $D^+ \to \pi^-\pi^+\pi^+$ Dalitz plot, an amplitude analysis is quite challenging. Considering the huge amount of data collected by the LHCb experiment, an unique opportunity arises to study in more details the dynamics of this process, including features such as the $\rho-\omega$ mixing observed for the first time in this channel. Moreover, this scenario turns out to be well suited to study lineshapes and also to tackle the challenging parametrisation of the $\pi\pi$ $S-$wave. The results of this analysis can also be very useful for sensitivity studies for the search of CP violation in this channel using run II data from LHCb, which is a topic of great interest following the first observation of CP violation in charm [4].

No new amplitude analysis results have been obtained from about 13 years, since CLEO analysis. The last study for this channel was the CP violation search performed by the LHCb [5]. The final sample from LHCb data used in this work to perform all Dalitz fits is about 80 times larger than CLEO's sample, therefore, we are able to perform an analysis sensitive to different aspects of the dynamics of this decay.

3.5 Phenomenological approach

One possible phenomenological model to deal with hadronic decays is to work with an effective weak hamiltonian within the naive factorization approach, as discussed in Section 2.5, where the matrix elements can be parametrised in terms of form factors. In this approach, the effective weak Hamiltonian is written as an operator product expansion (OPE) and reads:

$$\mathcal{H}_{\text{eff}} = \frac{G_F}{\sqrt{2}} \sum_i V_{\text{CKM}} C_i(\mu) \mathcal{O}_i(\mu) + \text{h.c.} \tag{3-10}$$

From this model, the $D^+ \to \pi^-\pi^+\pi^+$ decay amplitude can be written through the following matrix element [42]:

$$\langle \pi^-\pi^+\pi^+|\mathcal{H}_{eff}|D^+\rangle = \frac{G_F}{\sqrt{2}} V_{cd}V_{ud}^* \sum_{i=1}^{2} C_i(\mu)\langle \pi^-\pi^+\pi^+|\mathcal{O}_i|D^+\rangle, \tag{3-11}$$

where $V_{CKM}^{tree} = V_{cd}V_{ud}^* = \mathcal{O}(\lambda)$ and

$$\mathcal{O}_1 = \bar{d}_i\gamma_\nu(1-\gamma_5)c_i\ \bar{u}_j\gamma^\nu(1-\gamma^5)d_j \tag{3-12}$$

$$\mathcal{O}_2 = \bar{u}_i\gamma_\nu(1-\gamma_5)c_j\ \bar{d}_j\gamma^\nu(1-\gamma^5)d_i, \tag{3-13}$$

where i, j are color indices. By writing the OPE, the problem now is separated in calculating the amplitude in two parts: perturbative short distance calculation of $C_i(\mu)$ and the usually non–perturbative long distance calculation of the matrix elements $\langle \mathcal{O}_i(\mu)\rangle$. The Wilson coefficients C_i can be evaluated in the renormalization group improved perturbation theory, meanwhile the matrix elements $\langle \mathcal{O}_i\rangle$ are more challenging to determine.

One possibility is to write the element $\langle \pi^-\pi^+\pi^+|\mathcal{O}_i|D^+\rangle$ within a factorization approach at leading order (in Λ_{QCD}/m_c and the coupling α_s). At leading order, the diagrams contributing to the decay are the W external emission and W internal emission, thus for the $D^+ \to \pi^-\pi^+\pi^+$ decay, the amplitude is given by [43]:

$$\begin{aligned}\langle \pi_1^-\pi_2^+\pi_3^+|\mathcal{H}_{eff}|D^+\rangle = \frac{G_F}{\sqrt{2}} V_{cd}V_{ud}^* \,[a(\mu)\langle \pi_2^+|\bar{u}\gamma_\nu(1-\gamma_5)d|0\rangle\langle \pi_1^-\pi_3^+|\bar{d}\gamma^\nu(1-\gamma^5)c|D^+\rangle \\ + b(\mu)\langle \pi_1^-\pi_3^+|\bar{d}\gamma_\nu(1-\gamma_5)d|0\rangle\langle \pi_2^+|\bar{u}\gamma^\nu(1-\gamma^5)c|D^+\rangle] + (\pi_2^+ \leftrightarrow \pi_3^+),\end{aligned} \tag{3-14}$$

where the two terms corresponds to a colour allowed and suppressed contributions multiplied by the coefficients $a(\mu)$, $b(\mu)$, which are related to the coefficients C_1 and C_2 via perturbative QCD according to

$$\begin{aligned} a(\mu) &= C_1(\mu) + \frac{1}{N_c}C_2(\mu) \\ b(\mu) &= C_2(\mu) + \frac{1}{N_c}C_1(\mu), \end{aligned} \tag{3-15}$$

where $N_c = 3$ is the number of colours. One phenomenological treatment of the factorised matrix elements is by using form factors [44–46].

In terms of the $\pi^-\pi^+$ $S-$ and $P-$waves, the decay amplitude can be written as

$$\left\langle \pi^-\pi^+\pi^+\,|\mathcal{H}_{\rm eff}|\,D^+\right\rangle = \mathcal{A}_S + \mathcal{A}_P, \tag{3-16}$$

in which $\mathcal{A}_S$ and $\mathcal{A}_P$ are the $S-$ and $P-$waves $\pi^+\pi^-$ amplitudes to be written

in terms of the scalar and vector form factors and given by [42]

$$\mathcal{A}_S\left(s_{12}, s_{13}\right) = e_1^S \left(m_D^2 - s_{12}\right) F_{0n}^{\pi\pi}\left(s_{12}\right) + \left(s_{12} \leftrightarrow s_{13}\right) \tag{3-17}$$

$$\begin{aligned}\mathcal{A}_P\left(s_{12}, s_{13}, s_{23}\right) = &\left[e_1^P + e_2^P F_1^{D\pi}\left(s_{12}\right)\right]\left(s_{13} - s_{23}\right) F_1^{\pi\pi}\left(s_{12}\right) \\ &+ \left(s_{12} \leftrightarrow s_{13}\right)\end{aligned} . \tag{3-18}$$

where the complex parameters e_1^S and $e_2^{S,P}$ assume any nonfactorizable corrections depending on the spin of the $\pi^-\pi^+$ pair, $F_{0n}^{\pi\pi}$ and $F_1^{\pi\pi}(s)$ are the scalar and vector $\pi\pi$ form factors, detailed in [42, 43] and $F_1^{D\pi}$ is the vector $D \to \pi$ form factor given by an analytical expression.

Generically, form factors $f(s)$ are analytic functions on the complex s plane except for a cut along the positive real axis starting from the two-particle threshold $s_{th} = (m_\pi + m_\pi)^2$. For $s > s_{th}$ the form factors have nonzero imaginary parts while for $s < s_{th}$ they are real functions. In addition, they obey the Schwartz principle, $f(s)^* = f(s^*)$ [31], where s is a complex variable and s^* denotes the complex conjugate of s. Using a Cauchy representation, $f(s)$ can be written as

$$f(s) = \frac{1}{2\pi i}\int_C ds' \frac{f\left(s'\right)}{s' - s}, \tag{3-19}$$

where the contour of integration is shown in Figure 3.8. In the limit where the radius goes to infinity we obtain

$$f(s) = \frac{1}{2\pi i}\int_{s_{\mathrm{th}}}^{\infty} ds' \frac{\Delta f\left(s'\right)}{s' - s}. \tag{3-20}$$

The contribution from the infinite circle is assumed to vanish and $\Delta f = f(s' + i\epsilon) - f(s' - i\epsilon)$ is the discontinuity across the cut proportional to the imaginary part of $f(s)$. More explicitly, from the Schwartz principle, one could write

$$f(s' - i\epsilon) = \mathrm{Re}\, f(s' + i\epsilon) - i\,\mathrm{Im}\, f(s' + i\epsilon), \tag{3-21}$$

thus the discontinuity is proportional to the the imaginary part of $f(s)$ on the upper rim of the cut

$$\Delta f = f(s' + i\epsilon) - f(s' - i\epsilon) = 2i\,\mathrm{Im}\, f(s' + i\epsilon) \tag{3-22}$$

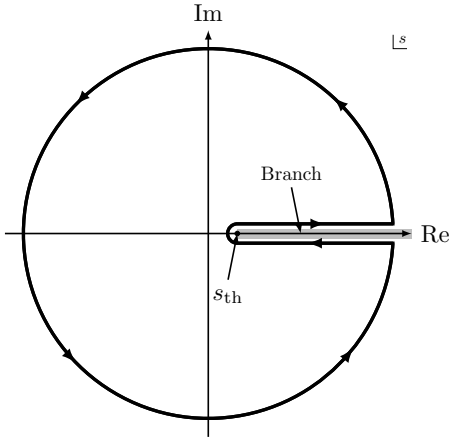

Figure 3.8: Contour of the integration.

Therefore, we can write the dispersion relation

$$f(s) = \frac{1}{\pi}\int_{s_{\rm th}}^{\infty} ds' \frac{\mathrm{Im}\, f\,(s'+i\epsilon)}{s'-s}. \tag{3-23}$$

The form factor above the threshold, *i.e* $s > s_{th} = (m_\pi + m_\pi)^2$, is obtained by approaching the real axis from above the cut $f(s) = \lim_{\epsilon\to 0^+} f(s+i\epsilon)$, yielding

$$f(s) = \frac{1}{\pi}\int_{s_{\rm th}}^{\infty} ds' \frac{\mathrm{Im}\, f\,(s')}{s'-s-i\epsilon}. \tag{3-24}$$

where $\mathrm{Im}\, f(s')$ is evaluated on the upper rim of the cut. From this equation we observe that the knowledge of $\mathrm{Im}\, f(s)$ for all values of s implies the knowledge of the full function $f(s)$. Recalling that the form factor is a complex function, it can be generally written as

$$f(s) = |f(s)|e^{i\delta(s)} \tag{3-25}$$

and, since $\delta(s)$ is real, Eq. 3-25 implies that $\mathrm{Im}\, f(s) = |f(s)|\sin\delta(s) = \tan\delta(s)\,\mathrm{Re}\, f(s)\Theta\,(s-s_{\rm th})$ where Θ is the Heaviside function ensuring that $f(s)$ is real on the real axis for $s < s_{th}$. By using this relation in Eq. 3-24, we obtain

$$f(s) = \frac{1}{\pi}\int_{s_{th}}^{\infty} ds' \frac{\tan\delta\,(s')\,\mathrm{Re}\, f\,(s')}{s'-s-i\epsilon} \tag{3-26}$$

which determines $f(s)$ up to a constant factor, the normalisation that can be calculated considering other conservation laws or by using effective field theories. Summarising all the discussion so far, the form factor $f(s)$ is analytic in the cut plane, it has a branch point at $s = s_{th}$, $f(s)$ is real for $s < s_{th}$, and, for $s > s_{th}$, on the upper rim of the cut the phase of $f(s)$ is $\delta(s)$.

The results derived so far have no precise knowledge of the phase $\delta(s)$, however, any information about the phase is required otherwise they are not useful. One important result, known as Watson's theorem [28], states that, within the elastic approximation, the phase of the form factor is equal to the corresponding scattering phase. Therefore, the discontinuity across the can be written as [45]

$$\text{disc}\, f(s) \;\; = \;\; f(s+i\epsilon) - f(s-i\epsilon) = f(s)e^{-i\delta}\sin\delta, \tag{3-27}$$

given the isospin and angular momentum. A solution to this unitarity relation, considering the analytic properties discussed before, is given by

$$f(s) = P(s)\Omega(s), \tag{3-28}$$

where $P(s)$ is a polynomial which is not fixed by unitarity and the Òmnes function $\Omega(s)$ [47], determined by the phase shift according to

$$\Omega(s) = \exp\left[\frac{s}{\pi}\int_{s_{\text{th}}}^{\infty}\frac{ds'}{s'}\frac{\delta\left(s'\right)}{s'-s-i\epsilon}\right], \tag{3-29}$$

with

$$\Omega(0) = 1 \quad \text{and} \quad \Omega(s) \neq 0 \quad \forall s \tag{3-30}$$

This phenomenological approach is used in this analysis as an alternative parametrisation for the $P-$wave as an attempt to describe the interference between the $\rho(770)$ and $\omega(782)$ via isospin violation. Considering the electromagnetic current

$$j^{\mu}_{\text{em}} = \frac{1}{2}\left(\bar{u}\gamma^{\mu}u - \bar{d}\gamma^{\mu}d\right) + \frac{1}{6}\left(\bar{u}\gamma^{\mu}u + \bar{d}\gamma^{\mu}d\right), \tag{3-31}$$

where the first term corresponds to an isovector and the second, an isoscalar component in which couples to the ω, in which its decay into $\pi^+\pi^-$ is suppressed by isospin. This effect of isospin violation is included with the following replacement [44, 48–50]

$$P_{F_\pi^V}(s)\Omega(s) \longrightarrow P_{F_\pi^V}(s)\Omega(s)\left(1 + \frac{\kappa_{\text{em}}s}{m_\omega^2 - im_\omega\Gamma_\omega - s}\right), \tag{3-32}$$

where m_ω and Γ_ω are the nominal mass and width of the ω contribution. The parameter κ_{em} is fitted to the KLOE data of $e^+e^- \to \pi^+\pi^-$ process [51] with $\kappa_{\text{em}} \approx 1.8 \times 10^{-3}$, obtained from a electromagnetic current, being responsible

to describe the strength of the mixing amplitude. From the $\bar{B}^0_d \to J/\psi\pi^+\pi^-$ analysis [45], the vector current from a $d\bar{d}$ source is given by

$$\bar{d}\gamma^\mu d = -\frac{1}{2}\left(\bar{u}\gamma^\mu u - \bar{d}\gamma^\mu d\right) + \frac{1}{2}\left(\bar{u}\gamma^\mu u + \bar{d}\gamma^\mu d\right), \tag{3-33}$$

where the relative strength of the isoscalar component differs from the electromagnetic case by a factor of -3, thus $\kappa_{\rm em} \to \kappa = -3\kappa_{\rm em}$. In principle κ could be obtained via a fit to the data but instead of setting it free in the fit model, we use as a fixed value of $\kappa \approx -5.4 \times 10^{-3}$ using the value of κ_{em} from KLOE. The pion vector form factor, $F_1^{\pi\pi}$ in Eq. 3-18 corresponding to the left side of Eq. 3-32, used was obtained from Hanhart [44] and the isospin violating effect is included according to the right side of Eq. 3-32. The pion vector form factor used in this analysis including the violating isospin effect is shown in Figure 3.9 and illustrates the general behavior of the $\rho - \omega$ mixing pattern as will be shown in Chapter 6. This phenomenological model will be used as an alternative parametrisation for the $P-$wave in Chapter 8.

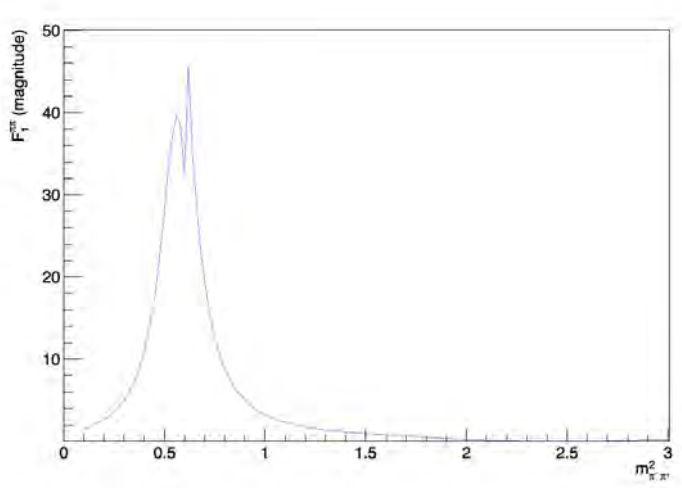

Figure 3.9: $F_1^{\pi\pi}$ magnitude including the isospin violating term.

4
The LHCb Experiment

The Large Hadron Collider (LHC) [52] is the last stage of the accelerator complex at CERN, located in Geneva, on the Franco-Swiss border. Constructed as two 27 km superconducting rings at an underground depth between 45 to 170 m, it is the world's largest and highest energy accelerator with the objective of colliding high-energy particle beams, *proton-proton*, travelling at almost speed of light. The two beams travel in opposite directions throughout the rings in ultrahigh vacuum, at a temperature of $-271^{o}C$, guided by a strong magnetic field created with dipole magnets to direct and quadruple magnets to focus the beams.

The LHC was designed to collide beams of protons at $\sqrt{s} = 14\text{TeV}$ in center-of-mass energy with a luminosity of $\mathcal{L} = 10^{-34}\ \text{cm}^{-2}\ \text{s}^{-1}$, which surpass the previous record of 1TeV per-beam held by the Tevatron accelerator at Fermilab in 2009. At four different interaction points, four detectors with specialised designs are placed giving birth to the four main experiments in the LHC which each one has its own purpose. When the beams collide, these detectors start their data taking to be analyzed. An schematic view of the LHC can be seen in Figure 4.1.

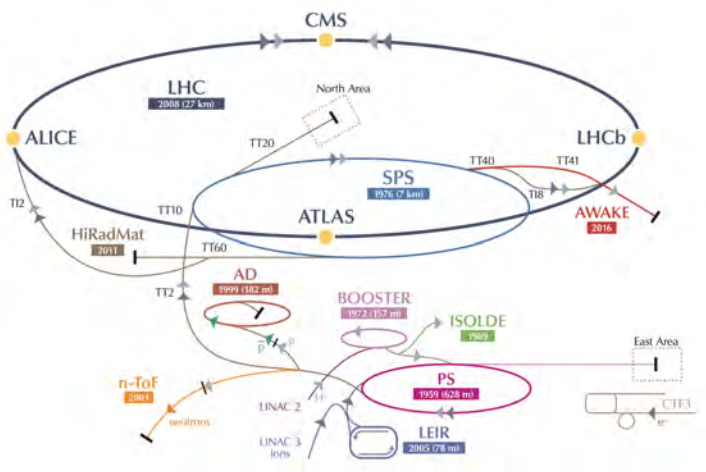

Figure 4.1: CERN accelerator complex [53].

An useful quantity to introduce when dealing with hadron colliders is the pseudorapidity. It has the important characteristic of being invariant

under boosts in the z direction, thus meaningful regardless of the longitudinal momentum fraction, and is defined in terms of the angle (θ) between the positive direction of the beam axis z and the particle momentum. The pseudorapidity is given by the following expression

$$\eta = -\ln\left[\tan\left(\frac{\theta}{2}\right)\right]. \tag{4-1}$$

The four main experiments are ALICE (A Large Ion Collider Experiment) [54], ATLAS (A Toroidal LHC ApparatuS) [55], CMS (Compact Muon Solenoid) [56] and LHCb [57].

ALICE is the experiment designed to study heavy-ion collisions (Pb-Pb or p-Pb) aiming to create the conditions in which matter passes to a dense quark-gluon plasma state of free partons and study the phenomenon of confinement in QCD [58].

ATLAS and CMS experiments lie on a energy frontier. Both detectors are designed with a segmented hadronic and electromagnetic calorimeters with precise energy resolution and a 4π solid-angle acceptance with the purpose to primarily study high-p_T physics in the central pseudorapidity region ($-2 < \eta < 2$). They are dedicated to analyze decay products of high-mass Standard Model (SM) and also to perform direct searches for beyond the Standard Model (BSM) particles such as supersymmetric and dark matter candidates by looking into missing energy signatures. The most successful contribution from these experiments was the observation of the Higgs Boson [15, 16] in 2011 and measurements of its spin and couplings [59–61]. Other noteworthy achievements from these experiments were the measurements of W, Z and t-quark couplings and cross-sections. Due to their lack of high-precision tracking close to the interaction point as well as a full instrumentation in the forward region, ATLAS and CMS are not suited to fully explore flavour physics studies.

The LHCb is the experiment dedicated to study decays of $b-$ and $c-$ hadrons. It is well suited to investigate the baryogenesis problem, understand the matter and antimatter difference in our universe, and study rare decays. Most of the LHCb studies comprises indirect BSM signatures via precision measurements of quark-flavour observables such as angular observables, CP asymmetries and CKM parameters [62].

4.1 The LHCb detector

The LHCb detector [63] is a single-arm spectrometer with forward angular coverage from 15 to 300 mrad in the bending plane and from 10 to 250 mrad in the non-bending plane of the magnet, equivalent to a pseudorapidity

of $1.9 < \eta < 4.9$, aiming to optimize the quantity of particles reconstructed in this angular acceptance. It is specially designed to efficiently detect $b-$ and $c-$hadrons, therefore, is well suited to investigate indirect BSM physics through precision measurements of CP violation, angular observables and rare decays. This angular range is motivated by the fact that, at high energies, the angular distribution from b and $\bar{b}$ (or c and $\bar{c}$) production is close to the beam pipe, thus, both tracks are produced predominantly in the same forward or backward direction. An schematic view of this angular distribution of $b-$quarks can be seen in Figure 4.2 with the LHCb acceptance in red.

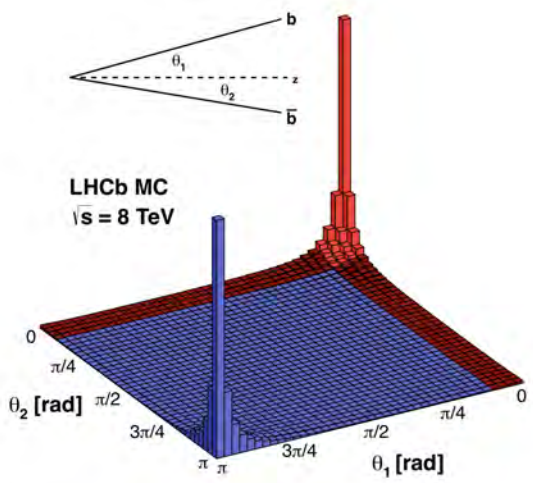

Figure 4.2: Distribution of b or $\bar{b}$ quarks produced using Pythia 8 [64] at the LHC ($\sqrt{s} = 8$TeV).

The general purpose of the LHCb experiment is to perform various precision measurements by working with heavy flavour physics. To distinguish $b-$ and $c-$hadrons, trigger and reconstruction algorithms rely drastically on a efficient reconstruction of primary (PVs) and secondary vertices (SVs), the point in which the meson is produced from the proton collisions and the point in which the meson decays into other particles displaced some distance from the PV, obtaining information about their flight distance, the distance between the PV and SV. As $b-$ and $c-$hadrons typically have a long flight-distance, the SVs are crucial signatures of a heavy flavour decays.

The LHCb was designed to operate with a luminosity of $\mathcal{L} = 10^{34}$ cm^{-2} s^{-1}, however, the LHCb operates with collisions at a constant reduced instantaneous luminosity of $\mathcal{L} = 2\times10^{32}$cm^{-2}s^{-1}, that is lower compared to ATLAS and CMS, shown in Figure 4.3, as a result of focussing the beams at the interaction point to a lesser degree. The motivation for the use of a lower luminosity is that LHCb is optimised for one visible interaction per bunch-

crossing on average and also to avoid any radiation damage in the VELO surrounding the interaction region, to be described in the next section.

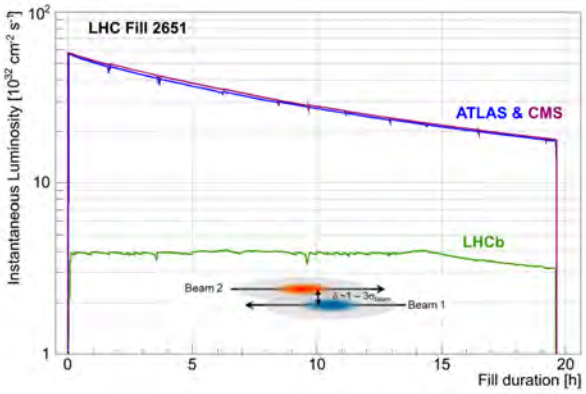

Figure 4.3: ATLAS, CMS, and LHCb integrated luminosity over fill 2651 of May 2012 [63].

The LHCb detector consists on a series of subdetectors each one with a different purpose from the interaction point up to an extension of 20m. An schematic view of the LHCb detector can be seen in Figure 4.4. To perform a full reconstruction of the process, the subdetectors need to provide information on the track and vertex reconstruction of $b-$ and $c-$hadrons, the primary vertex in which they are produced and the secondary vertex, the point that they decay, a good mass resolution, a reliable identification of the particle in the final states, high precision momentum measurements and a efficient online trigger system in order to be able to separate the events of interest from all the ones produced in a general pp collision.

In the following section, each subdetector will be described.

4.1.1 The Vertex Locator (VELO)

Located close to the interaction point surrounding the pp interaction region, the VELO [65] is responsible for providing information about the coordinate of tracks left by the particles produced in the PV and use them to localize and reconstruct the secondary vertex. As discussed before, this distance between primary and secondary vertex is extremely important to distinguish between beauty and charm hadrons due to their long lifetimes compared to decays from strong and electromagnetic processes.

The VELO comprises of 21 semi-circular modules with two identical sides positioned on opposite sides of the beam and a few centimeters space between each of the modules in the z axis ensuring that each track produced within the 300 mrad LHCb acceptance interacts with at least four VELO stations.

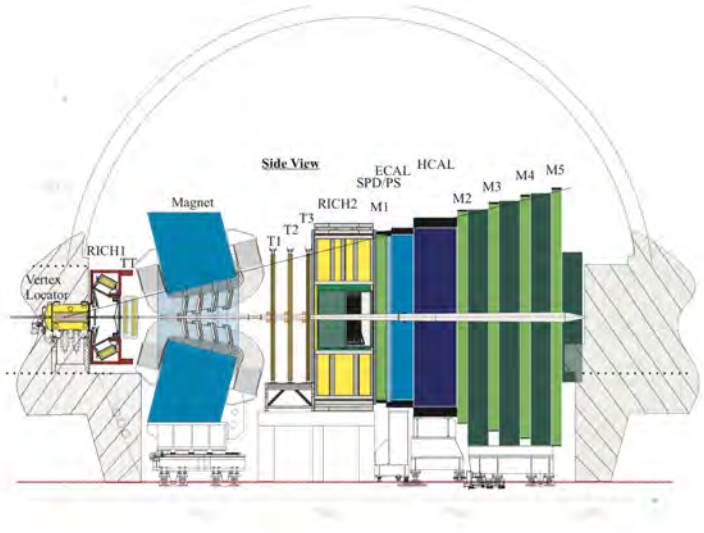

Figure 4.4: The LHCb detector layout with the subdetectors indicated [64 DOH]

Each module has two sets of silicon strip detectors, the radial R- sensor and a azimuthal $\phi-$ sensor, oriented orthogonal to each other proving a 3D spatial information for the reconstruction of vetices and tracks as illustrated in Figure 4.5. The z coordinate is obtained through the position of each modulus in the experiment. For the primary vertex, the spatial resolution is of 10μm in the ϕ direction and 40μm in the z axis, while for the secondary vertex is of 300μm and 150μm, respectively.

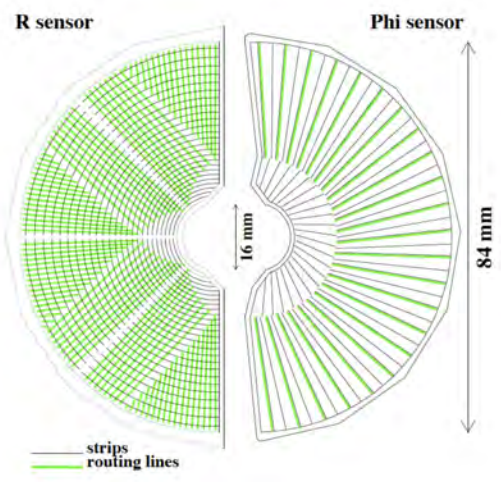

Figure 4.5: VELO R and ϕ sensor

4.1.2 The Magnet

The magnet [66] consists on a dipole generating an inhomogeneous magnetic field corresponding to an integrated bending power of 4 Tm over a track length of 10m. It is located downstream of the VELO, RICH1, and TT, and upstream of the rest of the sub-detectors and covers an angular distance of ±250 mrad in the vertical acceptance and ±300 mrad in the horizontal acceptance. A charged particle in the presence of this magnetic field experiences a perpendicular force depending on its momentum.

The magnet consists of two trapezoidal shape coils and allows measurements of charge and momentum of charged particles. The polarity of the magnet can be inverted, taking data either when the field is pointing up ("MagUp") or pointing down ("MagDown"). By varying this polarity, one can study and reduce systematic errors in the measurements. An schematic view of the magnet is shown in Figure 4.6.

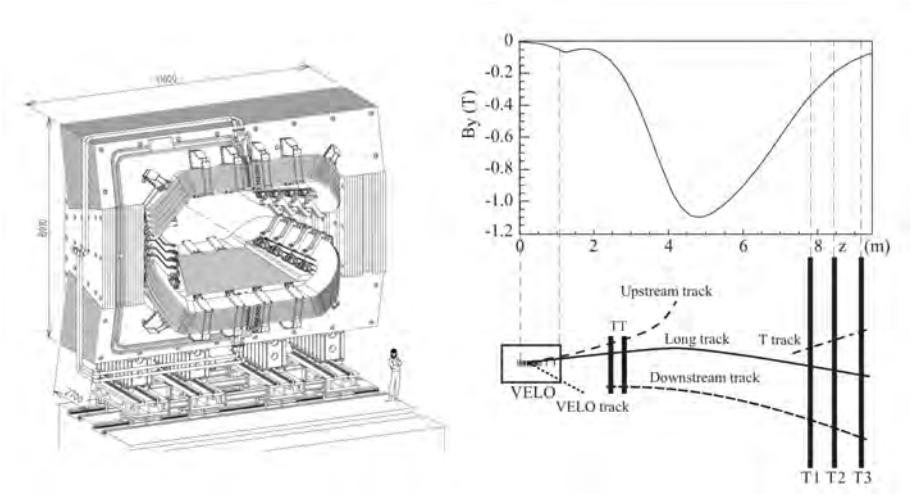

Figure 4.6: Schematic of the LHCb dipole magnet (looking upstream)(Left). Magnetic field along the z-axis of the detector (Right).

4.1.3 The tracking stations

The tracking system [67] is composed by the VELO and four additional tracking stations: the Tracker Turicensis (TT) before and upstream of the magnet, and three stations $T_1 - T_3$ downstream the magnet, each consisting of an inner (IT) [68] and outer (OT) [69] tracker. This system provides information about the trajectories of charged particles allowing their reconstruction.

Tracker Turicensis (TT)

With the purpose of providing information about tracks with low momentum, the TT is constituted of two stations covering a rectangular area and each station is composed of four layers of silicon microstrip sensors with the interior two layers rotated -5^o and $+5^o$ relative to the first and last vertically orientated layers as illustrated in Figure 4.7. Each sensor has a 50μm resolution in the position measurement. The Tracker Turicensis is located between the RICH1 and the magnet and all four layers are housed in a light-tight, thermally and electrically insulated volume, at a temperature of 5^oC, continually flushed with nitrogen to prevent condensation.

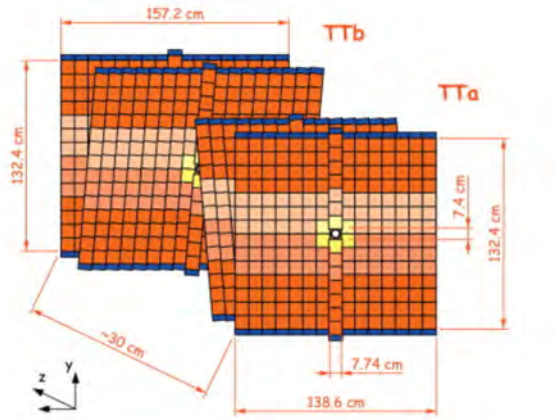

Figure 4.7: Schematic view of the four layers of the Tracker Turicensis stations.

Inner Tracker (IT)

Located in the tracking stations $T_1 - T_3$, the Inner Tracker sensors occupy the central region of the downstream tracking stations where the track multiplicity is expected to be the highest. Each of the three IT stations consists on four boxes around the beam axis and each box has four silicon layers arranged similarly to the TT layers configuration. All boxes have seven modules but in the upper and lower ones, each module has a single sensor while in the lateral boxes, each module has two sensors. The resolution on the position is around $50\mu m$. An schematic view of the IT can be seen in Figure 4.8.

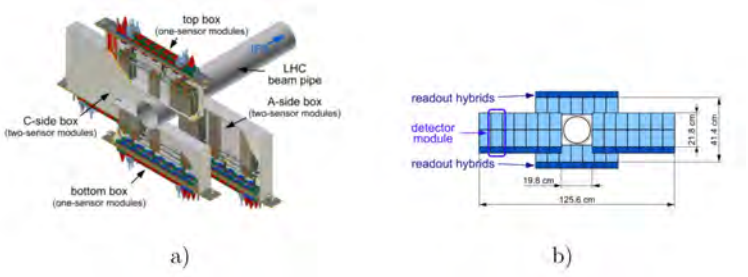

Figure 4.8: (a) The four boxes of a IT station arranged around the beam pipe. (b) The four modules comprising a Inner Tracker layer.

Outer Tracker (OT)

The outer tracker $T_1 - T_3$ consists of two staggered layers of straw-tube drift chambers [70]. In these regions the flux of particles is lower than in the inner tracker stations, designed for less than 10% occupancy at a luminosity of 2×10^{32} cm^{-2} s^{-1}. When a charged particle passes by, the gas contained in the tubes is ionised and the charge is collected by an anode in the centre of the tube. The time taken for the charge to reach the anode upon application of a current provides information of the trajectory of the charged particle measuring its relative position within the tube and, together with the magnet information, it is also possible to determine the momentum. Each tube has an inner diameter of 4.9mm filled with a gas mixture of Ar (70%), CO_2 (28.5%) and O_2 (1.5%) providing a drift-time under 50 ns and a resolution of 200μm.

Each station consists of four modules in which the first and last are vertically oriented, and the inner modules oriented at -5^o and $+5^o$ with respect to the vertical shown in Figure 4.9, as in the TT and IT stations. The entire OT detector is composed of four layers with 4608 cylindrical straw-tube.

The reconstruction the trajectories through the detectors is done with a software using all the information left and performing a fit based on the "Kalman-Filter" method updating the information periodically in order to improve the quality measured by the χ^2 of the fit.

The reconstructed tracks can be classified as: VELO tracks, the ones that passes only through the VELO exiting the detector acceptance; Downstream tracks, reconstructed tracks that pass through TT and $T_1 - T_3$ and in general correspond to particles that decay outside the VELO; Upstream tracks, the ones that passes through VELO and TT; Long tracks, reconstructed tracks that uses information from all the detectors (VELO, TT, $T_1 - T_3$), hence they have a good resolution; and T tracks, reconstructed using only information from $T_1 - T_3$, in general they are products of secondary interactions. A summary of

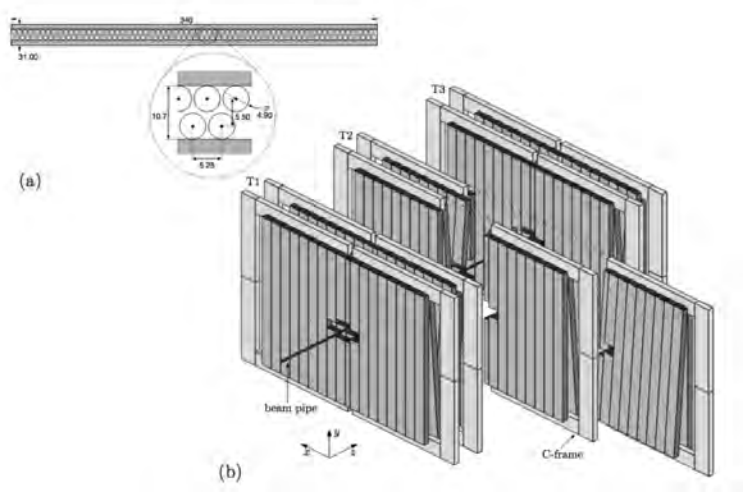

Figure 4.9: (a) Module cross section. (b) OT straw-tube detector four layers in the $T_1 - T_3$ stations.

the reconstructed tracks can be seen in Figure 4.6(right).

4.1.4 Ring-Imaging Cherenkov System (RICH)

One of the most important information provided by the LHCb detector is a good identification of particles in the final state like pions, kaons, protons, electrons and muons. The RICH detectors [71, 72] are responsible for differentiating these charged particles species allowing the reduction of the more produced pion backgrounds from kaons and proton final states, and the separation of final states that are topologically similar. The separation of pions and kaons is fundamental to study beauty and charm hadrons. A lateral view of the RICH detectors is shown in Figure 4.10

To correctly identify the particles, the LHCb has three subdetectors dedicated to this task: two RICH stations associated with a tracking system to perform the particle identification, the calorimeters to measure the energy deposited by the particles and identify neutral particles, and the muon stations to identify muons.

The RICH detectors utilise the Cherenkov radiation, therefore, when a charged particle passes through a dieletric material, with velocity greater than the speed of light in the medium, it causes a momentary polarizations and as the medium relaxes back to ground state, it emits photons (radiation). The emission of photons form a cone with an angle θ_c with respect to the trajectory given by:

$$\cos\theta_c = \frac{1}{v\beta}, \tag{4-2}$$

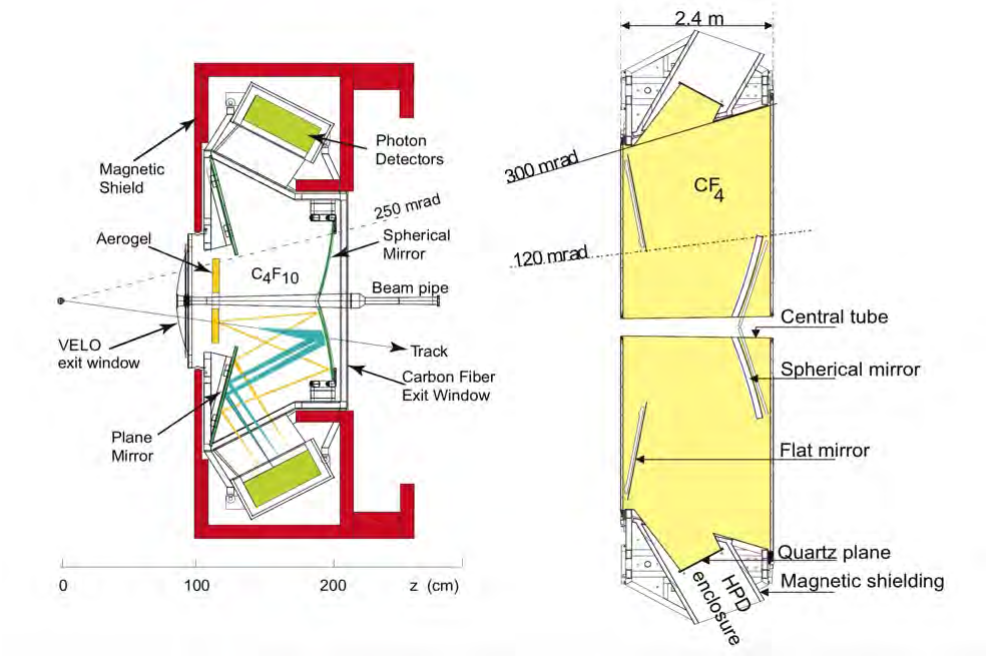

Figure 4.10: Schematic view of RICH1 (left) and RICH2 (right) subdetectors with the presence of spherical and plane mirrors.

where n is the refractive index of the material and $\beta = v/v_c$, the velocity of the particle (v) relative to the phase velocity of the light in the medium (v_c). For the particle identification, all information from the velocity of the particle and from the momentum measurement associated to the track is used. The momentum reconstructed by the tracking system together with the Cherenkov angle, can be used to discriminate particles of different masses.

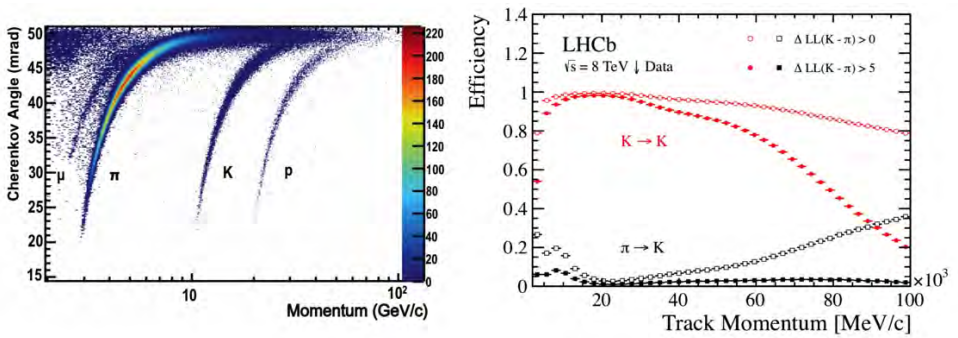

Figure 4.11: Left: Cherenkov light angle vs track momentum in RICH1 for isolated tracks. Right: Kaon identification and pion mis-identification efficiency as a function of track momentum for magnet down 2012 data for two requirements of the difference in the particle hypothesis log-likelihoods.

Two RICH detectors are used to cover the whole range of momentum spectra, one located between the VELO and TT (RICH1), and the other

between T_3 and the muon stations (RICH2). The RICH1 is composed by air gel radiators SiO_2 with $n = 1.03$ and C_4F_{10} with $n = 1.0014$ and projected to detect particles in a momentum range from 2 GeV to 70 GeV that emerge with large polar angles. The second, RICH2, contains gaseous CF_4 with $n = 1.005$ covering a momentum range from 16 GeV to 100 GeV that emerge with small angles. Both detectors use detectors of hybrid photons to focusses the Cherenkov light with a combination of spherical and plane mirrors.

4.1.5 Calorimeters

The electromagnetic (ECAL) and hadronic (HCAL) calorimeters [73], together with two stations SPD(Scintillator Pad Detector)/PS (Preshower Detector), are responsible to identify and measure the transverse energy E_T and position of the particles that produce electromagnetic or hadronic showers such as electrons, photons and hadrons when these particles interact with a dense material. They make the selection of the transverse energy of hadrons and electrons and photon candidates by communicating this information in the first trigger level (L0) making a decision 4μm after the interaction point. Both ECAL and HCAL can be observed in Figure 4.12.

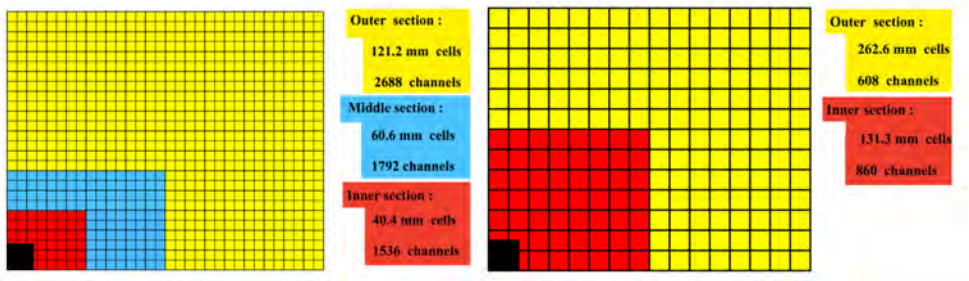

Figure 4.12: Left: SPD, PS and ECAL scintillating pads. Right: HCAL scintillating pads.

After travelling a certain distance, the particle produces new particles with lower energy creating a shower and the calorimeters can determine the energy of the particle responsible for that shower. The produced particle passes through the scintillators generating photons that can be collected by the photomultiplier tubes, SPD and PS detectors helping the identification process. The SPD contributes in rejecting electrons with high transverse momentum in neutral pion decays and in discriminating electron and photon showers. The PS is responsible to reject the background from charged pions.

The ECAL is constituted of alternating tiles of 2mm thick lead and 4mm thick scintillator material and a white layer to avoid reflection in the

scintillator. The purpose of this calorimeter is to measure the energy of electrons and photons and to reconstruct π^0. It is designed to give an energy resolution of $\sigma_E/E = 10\%\sqrt{E} \otimes \%1$.

The HCAL has the same operating principle than the ECAL, the similar scintillating tiles are used but oriented parallel to the beam axis, with the difference that the hadronic showers are determined by the interaction nuclear length that is greater than the radiation length, the depth of the HCAL is larger than the ECAL to accommodate the larger hadronic showers. Thus the HCAL is more dense and intercalates 4mm scintillator plates and 16 mm iron plates. The purpose of this calorimeter is to measure the energy of photons, neutrons, pions and kaons and the energy resolution is of $\sigma_E/E = 80\%\sqrt{E} \otimes \%10$.

4.1.6 The muon stations

Since many leptonic and semi-leptonic $b-$ and $c-$hadron decays are sensitive to BSM effects, the detection of muons is fundamental for LHCb analyses. Used to tag the decay flavour in oscillation studies, the muons system [74–76] requires a good offline performance in identifying muons and also provides online information to the L0 trigger level.

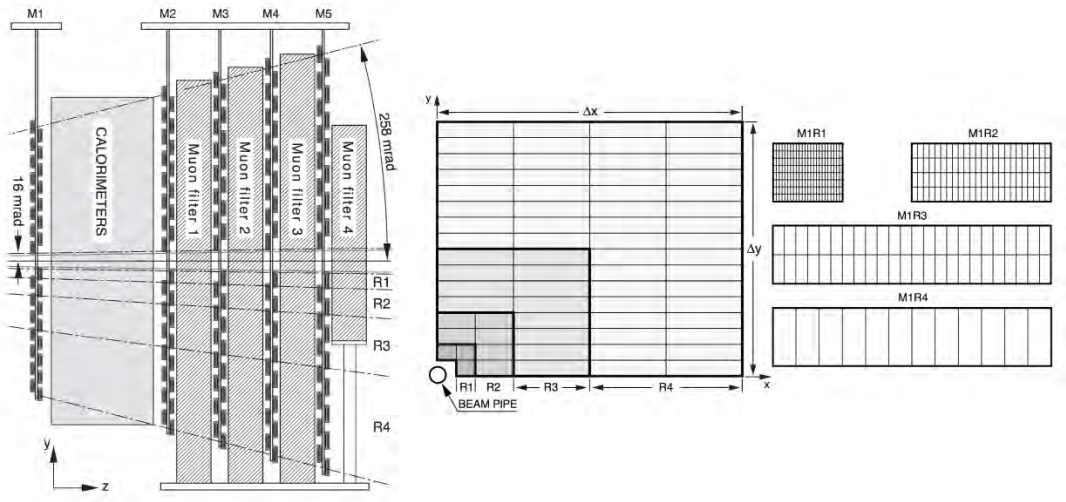

Figure 4.13: Left: Schematic view of the muons stations. Right: Four regions comprising each muon station.

The muon system is composed of five stations (M1-M5) which can be seen in Figure 4.13. The first station is located before the calorimeter in order to increase the precision in measuring the linear momentum of the muons identified in the trigger, it provides a higher resolution muon p_T measurements. The following stations are displaced at the end of the spectrometer, where

only muons can reach. The stations M2-M5 are intercalated with iron filter to avoid background from hadrons. M2 and M3 stations also have a high spatial resolution in x whereas M4 and M5 have limited spatial resolution and exist to indicate penetrating particles. The muon chambers are also divided in regions R1-R4 due to pile-up.

With the exception of the inner region of M1, which has the highest occupancy, using Gas Electron Multiplier (GEM), this detector system is constructed with the technology Multi Wire Proportional Chamber (MWPC). MWPCs use a gas mixture of Ar, CO_2 and CF_4 and this chambers produce an electron shower when a muon passes. The electrons are then taken to the anode producing an electric signal and the ions are taken to the cathode. GEMs use mixture of Ar, CO_2, CF_4 and three metal layers with a high density of holes to collect the ionized electrons, submitted to high voltage and intercalated between the anode and cathode.

4.2 The trigger

The LHCb detector uses a hardware L0-level trigger, operating with the LHC bunch-crossing rate of 40MHz, and two software high-level triggers (HLT1 and HLT2) [77, 78]. Since this rate cannot be all storage, the trigger system is responsible to reduce it to a few KHz order while selecting only interesting events.

The L0 trigger requires an event with high transverse energy, E_T, from one of the calorimeters, selecting electrons photons and hadrons, or high p_T from the muon system reducing the output rate to 1MHz at which the detector can be read out. This information is processed by the L0 decision unit (L0DU) that approves or not the event after 4μm after beam crossing. Also, high multiplicity events are rejected using the SPD system to avoid that the HLT overfull wit a large number of tracks.

One commom classification of the events that can fire the trigger is the following. If the signal track fires the trigger, it is classified as TOS (Trigger On Signal), otherwise is classified as TIS (Trigger Independent of Signal).

The transverse energy is given by:

$$E_{\mathrm{T}} = \sum_{i=1}^{4} E_i \sin\theta_i, \tag{4-3}$$

where E_i is the energy deposited in cell i and θ_i is the angle between the $z-$axis and a line passing from the mean position of the pp interaction to the centre of the cell. The L0DU computes the E_T deposited in 2×2 cell clusters using cells in the same region. These clusters form the `L0Hadron`, `L0Photon`

and `L0Electron` candidates. To select a muon candidate, the muon trigger needs a hit in all five stations to select a candidate and the highest and second highest p_T muons that passed to the L0DU are compared to the threshold for the highest p_T (`L0Muon`) or the product of highest and second highest p_T (`L0DiMuon`).

After this stage, the events pass to the software trigger level. The data is sent to an Event Filter Farm (EFF) to run algorithms for HLT. In the first stage, HLT1, a partial event reconstruction using information from the VELO and the tracking system can be performed and some requirements can be imposed to reduce the data rate entering HLT2 where the full event reconstruction will be done. VELO tracks are matched to tracks in the downstream tracking stations and a Kalman fit is performed and the quality of the fit is checked with the χ^2.

In HLT2, the HLT1 accepted events are fully reconstructed with more rigorous dedicated algorithms reducind the rate of accepted events to ~ 3 kHz in 2011 and two types of trigger lines are introduced: exclusive, which are optimised for specific final state; and inclusive, where only generic topological requirements are imposed on the final state.

4.3 Simulation

In addition to the trigger system and hardware of the LHCb detector, a fundamental part of the analysis is the simulation using Monte Carlo (MC). Given a physical process, the desired signal can be generated in order to be used in a series of important features of any LHCb analysis such as the determination of efficiencies, set limits on speculative processes, study systematic uncertainties, investigate biases and constrain background yields and shapes.

In the LHCb, the data is simulated using the framework *Gauss* using specialised programs [79, 80]. At first, the events are generated using *Pythia 8* [64] resulting in generic 7 and 8 TeV pp interactions. Starting from hard processes simulations using parton distribution functions that describe the relative composition of the protons as a function of the momentum of incoming proton, outgoing partons are generated. The outgoing simulated partons will produce showers that, due to QDC confinement, will be responsible to form colour neutral hadrons. This hadron is decayed using *EvtGen* [81] and the events generated pass to the GEANT4 [82, 83] detector simulating their propagation and interaction with the detector material. To reconstruct events, *Brunel* is used and to simulate the trigger stages (L0 and HLT), the *Moore*

package is used to simulate.

4.4 Operating conditions

For an accelerator, the two most important numbers are the collision energy and the luminosity. The energy determines what particles can be produced in the collisions while the luminosity says how often. Since the first data taking period, the LHCb operation conditions have been improving in response to the higher luminosity. During Run 1, protons were collided at a centre-of-mass energy of 7 TeV in 2011 and 8 TeV in 2012 [84]. The instantaneous luminosity $\mathcal{L}$ is a measure of the number of collisions that take place in a detector per cm^2 and per second [85] given by

$$\mathcal{L} = \frac{fN^2}{4\pi\sigma^2}, \tag{4-4}$$

where N is the number of protons in each bunch, σ is the width of the bunch at the interaction point and f is the bunch crossing frequency. This quantity can be also expressed in terms of the ϵ (emittance) and β (amplitude function) given that $\beta = \pi\sigma^2/\epsilon$. While ATLAS and CMS experiment operate at a instantaneous luminosity of $10^{34}\text{cm}^{-2}\text{s}^{-1}$ seeing an average of $\mathcal{O}(10)$ pp interactions per bunch crossing, the LHCb operates at $10^{32}\text{cm}^{-2}\text{s}^{-1}$ seeing $\mathcal{O}(1)$. High occupancy leads to difficulties in vertex reconstruction, flavour tagging and the increase in the combinatorial background levels. The LHCb luminosity is constant during the data-collection period [86] and Table 4.1 illustrates the luminosity and energies over time for each experiment.

Run	Year	$\sqrt{s}$ (TeV)	Integrated Luminosity (fb^{-1})		
			ATLAS	CMS	LHCb
I	2011	7	5.38	5.87	1.14
I	2012	8	23.2	23.2	2.19
II	2015	13	4.21	4.22	0.36
II	2016	13	38.5	41.0	1.88
II	2017	13	50.3	50.2	1.87
II	2018	13	64.9	66.8	2.46

Table 4.1: Centre-of-mass energy and integrated luminosity delivered by the LHC in pp collisions for each data-taking year.

5
Data Selection

In this chapter we describe the data selection process to obtain the final data sample used in the analysis, the determination of the efficiency across the Dalitz Plot and the parametrisation for the background. The information provided by the LHCb detectors is combined to reconstruct events. Since there will be events that are not of our interest some selection criteria are necessary to enrich the data sample with events containing true $D^+ \to \pi^-\pi^+\pi^+$ decays. This process starts during the data taking in the online event selection performed by the trigger systems [87] - hardware and software levels - then on offline selection performed in two stages - "stripping" then a multivariate analysis. In order to correct some introduced variations across the Dalitz from the selection process full LHCb simulations are used. The selection criteria are chosen to provide a high purity sample without causing too much distortions across the phase space. For this analysis we use just a fraction of 2012 data sample for Dalitz fits, of about 200 thousand decays. This is mainly because of two reasons: the analysis is systematic limited due to physics modeling - no gain in decreasing statistical uncertainties; the amount of simulation sample necessary to the efficiency corrections would be huge and again not justified given the systematic limitation. The data selection process is performed with the full sample and the subsample of the first 200 thousand events for Dalitz fits is taken as the last stage before performing fits. Even so, our data sample is still about 80 times larger than the antecessor analysis from CLEO [8]. Recall that we label the π^- as particle 1 and the other two charged π^+ are randomly chosen as particles 2 and 3, to ensure that they have the same kinematic distributions.

5.1
Dataset

The dataset used in this analysis consists on a data sample collected by the LHCb experiment in 2012 during Run I corresponding to an integrated luminosity of 2 fb^{-1} and a centre-of-mass energy of $\sqrt{s} = 8$ TeV of proton-proton, pp, collisions. Part of the data was taken with magnet polarity up and the other part with magnet polarity down, as indicated in Table 5.1, to avoid

biases due to the magnet polarity, reducing systematic effects associated to charge asymmetries.

	Luminosity (fb^{-1})
Magnet Up	1.000 ± 0.012
Magnet Down	0.988 ± 0.012

Table 5.1: Luminosity corresponding to the data sample used in this analysis.

5.2 Definition of variables

To identify D-meson decays there are several relevant variables, mostly based on their topological characteristics and particle identification, used to analyze the signatures left by the decay products in the detector. These variables are associated to physical quantities and requirements are imposed on them in the stripping and final selection in order to separate signal from background events. The D mesons are produced in the interaction point called the Primary Vertex (PV) and, after travelling a certain distance due to its significant lifetime $\tau = (1040 \pm 7) \times 10^{-15} s$ [1], they decay into its products in the Secondary Vertex (SV). The distance between the PV and SV is called flight distance (FD) and it is provided with a very good precision by the VELO detector being responsible to distinguish between B and D mesons. Some variables have a similar purpose, therefore, they can be divided into the following groups: variables of pointing, the ones that request that the direction of the reconstructed D meson point to the PV, variables requesting that the vertices are well separated, ensuring that for each decay product the trace won't point to the PV, and variables for particle identification. Some examples of variables are illustrated in Fig. 5.1.

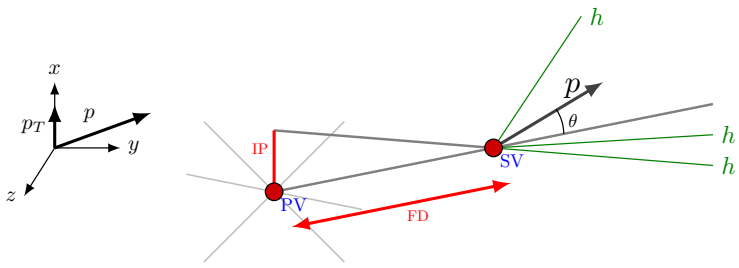

Figure 5.1: Topology of the decay $D^+ \to \pi^-\pi^+\pi^+$.

The relevant variables that characterize the decay are:

Mass: the invariant mass of the combination of three pion candidates to reconstruct the mass of a D^+ candidate. From 4-momentum conservation, the

D^+ invariant mass is reconstructed using $p_D^\mu = p_1^\mu + p_2^\mu + p_3^\mu$ where the left side represents the $D-$meson 4-momentum and the right side 4-momenta of the decay products. The invariant mass is given by

$$m(\pi^-\pi^+\pi^+) = \sqrt{(p_1^\mu + p_2^\mu + p_3^\mu)^2} = \sqrt{E^2 - \vec{p}\cdot\vec{p}} \tag{5-1}$$

Flight distance (FD): distance between the PV and SV.

$\chi^2_{\mathbf{FD}}$: ratio between the flight distance squared and the square of combined uncertainties of the primary and secondary vertex positions.

Impact parameter (IP): minimum distance between the primary vertex and the D^+ candidate flight direction.

$\chi^2_{\mathbf{IP}}$: difference in the vertex fit χ^2 of the primary vertex reconstructed with and without a given particle.

Transverse momentum (p_T): measurement of the momentum of a given particle in the transverse direction relative to the beam axis.

Momentum (p): modulus of the momentum of a given particle.

DIRA: cosine of the direction angle which is defined as the angle between the reconstructed tri–momentum vector of the D^+ candidate and the flight distance direction.

DOCA: the distance of closest approach between any two tracks. For a three-body decay there are three combinations (DOCA12, DOCA13, DOCA23) from the pion tracks.

DOCA max: highest DOCA from the previous combinations.

Vertex χ^2: χ^2 of the secondary vertex fit, to measure the quality of the vertex formed by the three tracks of the decay.

PTsum: scalar sum of transverse momentum of the three pions.

logIP: logarithm of the ratio between the product of the χ^2_{IP} of the three pions and the χ^2_{IP} of the D meson.

$$\log \mathrm{IP} = \log\left(\frac{\Pi_i \chi^2_{IP_{\pi_i}}}{\chi^2_{IP_D}}\right) \tag{5-2}$$

PIDK: From the RICH information, for each track the likelihood of being one of the possibilities is calculated: pion, kaon, proton, electron and muon. PIDK for a given track is the difference in likelihood for the hypothesis of kaon and pion.

Track χ^2/ndof: χ^2 per degree of freedom of the track fit, a measure of how good the track quality reconstruction is.

POINTING: weighted comparison of transverse momenta of the D candidate and its decay products. The transverse momentum of the mother is defined with respect to its flight direction, whereas for the decay products the transverse momentum is defined with respect to the z-axis:

$$\texttt{POINTING} = \frac{p \sin\theta}{p \sin\theta + \Sigma p_{T_i}} \tag{5-3}$$

5.3 Online selection: Trigger

To select hadronic decays, at the "online" stage, some trigger decision requirements are imposed during the data taking at hardware (L0) and then at the software level (HLT). The data collected in the LHCb experiment is filtered by trigger lines [88, 89] with some selection criteria in L0 and HLT trigger levels with the purpose of selecting interesting events while rejecting a huge amount of background events right away. The first is a hardware based, the L0 trigger, that collects information from the calorimeter and muon systems aiming to select muons with high transverse momentum and hadrons, photons and electrons with high transverse energy deposited in the calorimeters. To reject null events it uses information of the pile-up sub-trigger and to distinguish different candidates (hadrons, electrons, photons) signatures left in the detectors are used. The different transverse energy thresholds for each particle are given in Table 5.2. All information is collected in a Decision Unit (L0DU) and each particle gets a trigger decision depending on their specific threshold.

Offline, the events can be labeled as TOS (Trigger On Signal) if they are triggered by associating the information of the detector and the candidate signal itself or TIS (Trigger Independent of Signal) if they are triggered without the requirement to be associated to the candidate signal. At the L0

Candidate	2012
Hadron E_T (GeV)	3.7
Electron E_T (GeV)	3.0
Photon E_T (GeV)	3.0
muon p_T (GeV)	1.76
Dimuon ($p_{T1} \times p_{T2}$) (GeV$^2/c^2$)	$(1.6)^2$

Table 5.2: L0 thresholds in 2012

level, the candidates for the decay channel studied are required to be selected independently of the signal by a combination of L0 lines.

After the L0 level, the accepted L0 candidates are required to pass the software level trigger divided into HLT1 and HLT2. At the HLT1, a partial reconstruction and an inclusive selection of signal events is performed. The inclusive trigger line `Hlt1TrackAllL0`, described in Table 5.3, requires at least one of the decay product tracks to be a good quality track, to have a high χ^2_{IP} and high p_T. The reconstruction of tracks is performed at the HLT1 level using the information provided by the VELO detector and tracking systems with a three-dimensional pattern recognition. For HLT2, a full reconstruction of events based on topological characteristics [89, 90] is performed in which the candidates must pass the dedicated trigger line `Hlt2ChamHadD2HHH` that aims to select D^+ decays into three charged hadrons, with selection criteria described in Table 5.4, including requirements on variables for final state particles, three hadron hhh combination and variables related to the decaying particle. The trigger selection used is summarized in Table 5.5.

Cuts	**Value**
Track χ^2_{IP}	> 16
Track p_T (GeV/c)	> 1.6
Track p (GeV/c)	> 3
Track χ^2/ndof	< 2
Track IP (mm)	> 0.1
Number of VELO hits/Track	> 9
Number of missed VELO hits/Track	< 3
Number of OT + IT hits/Track	> 16
Number of VELO hits	< 6000
Number of IT hits	> 3000
Number of OT hits	< 15000
`L0_Decision_Physics`	

Table 5.3: `Hlt1TrackAllL0` trigger line requirements on at least one track.

	Cuts	Value
Global Event Cut	N. Long Tracks	< 180
final state particles	Track χ^2	< 3
	p_T (MeV/c)	> 300
	p (MeV/c)	> 3000
	χ^2_{IP}	> 6
hhh combination	PTsum (MeV/c)	> 2800
	min DOCA (mm)	< 0.08
$D^{\pm}$	χ^2_{FD}	> 175
	Vertex χ^2/ndof	< 15
	χ^2_{IP}	< 12
	Mass (MeV/c^2)	1800-2040
	TOS in any `Hlt1Track` Line	

Table 5.4: Dedicated `Hlt2ChamHadD2HHH` trigger line.

Trigger level	Condition required
L0	`D_L0HadronDecision_TIS` or `D_L0MuonDecision_TIS` or `D_L0ElectronDecision_TIS` or `D_L0PhotonDecision_TIS`
HLT1	`D_Hlt1TrackAllL0Decision_TOS`
HLT2	`D_Hlt2CharmHadD2HHHDecision_TOS`

Table 5.5: Trigger selection applied to the D^+ candidates.

5.4 Offline selection: Stripping

After triggered and collected online, the data passes through an offline selection to further separate events by the physics of interest and reduce background. The data is processed for reconstruction and the physical quantities are attributed in the event. The information from the energy measured by the HCAL and ECAL calorimeters, the hits associated to the track position, their momentum and the information related to the particle indentification are reconstructed.

In this stage, the so called stripping selection requirements are chosen to reduce events that can be identified as background and then improve the signal significance by applying cuts on the topological variables. This choice is a compromise between signal efficiency and retention. The $D^+ \to \pi^-\pi^+\pi^+$ decay mode is selected by the exclusive line `StrippingDhhh_PPPLine`, in which all particles are reconstructed as pions. Loose initial requirements are imposed and a summary of the stripping requirements is shown in Table 5.6. Figure 5.2 show the mass spectrum of three pions combination, $m(\pi^-\pi^+\pi^+)$, after trigger

and stripping selection where the first peak is centered at the D^+ mass and the second at the D_s^+ mass. Although the background has been reduced after these stages, we can still observe significant contaminations and to increase the purity, a further selection is required.

Variable	Selection requirement
Final state particles	
p_T(MeV/c)	> 250
p (MeV/c)	> 2000
PTsum (MeV/c)	> 2800
DOCA max (mm)	< 0.5
track χ^2_{IP}	> 4
PIDK	> 7 for all tracks
Combination cuts	
D p_T (MeV/c)	> 1000
D Vertex χ^2	< 30
DIRA	> 0.98
D χ^2_{IP}	< 12
D χ^2_{FD}	> 125
Mass (MeV/c^2)	1800-2040
Global Event Cut	
Number of tracks	< 500

Table 5.6: Stripping 20 cuts for `StrippingD2hhh_PPPLine`.

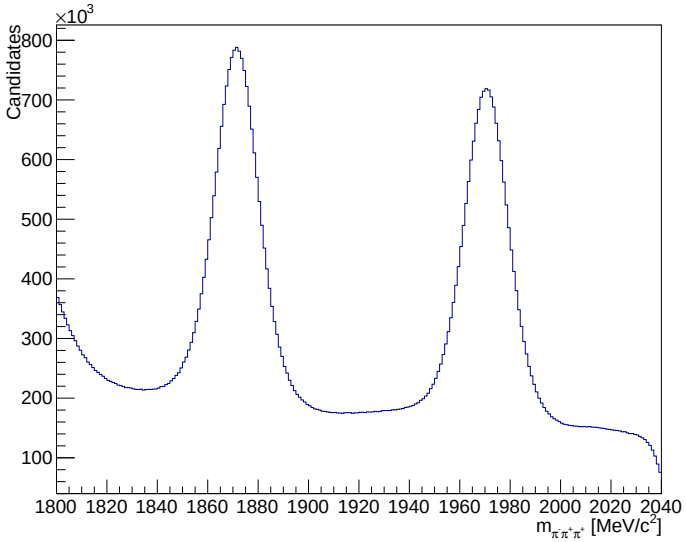

Figure 5.2: Invariant mass distribution of $\pi^-\pi^+\pi^+$ candidates after trigger requirements and stripping. The two peaks correspond to the $D^\pm$ at 1870 MeV/c^2 and $D_s^\pm$ at 1968 MeV/c^2 respectively.

Further offline selection

The remaining background may come from random three-track associations (combinatorial background) as well as from other charm decays (reflections) or partially reconstructed decays with misidentified particles such as $D^0 \to K^-\pi^+$, $D_s^+ \to \eta'\pi$, $\Lambda_c \to p\pi^+\pi^-$ and $D^+ \to K^-\pi^+\pi^+$. A further selection to remove semileptonic contributions such as $D^+ \to \pi^+\pi^-\mu^+\nu$ is applied by requesting the muon veto `isMuon=0` and to reduce combinatorial background as well as reflections, the particle identification is tightened to `PIDK<-2` for all pion candidates, however a contamination coming from $D_s^+ \to \eta'\pi^+$ is still not removed and a leaves a ρ structure in the background from $\eta' \to \rho^0\gamma$, as will be more explicitly seen in the Dalitz plot distribution of the background. The D^+ mass distribution after this stage is shown in Figure 5.3. From this plot, we observe that although we have managed to reduce the background even more, we still need a more sophisticated selection to obtain a higher purity sample and for that, we will need a simulation sample to perform a multivariate analysis technique.

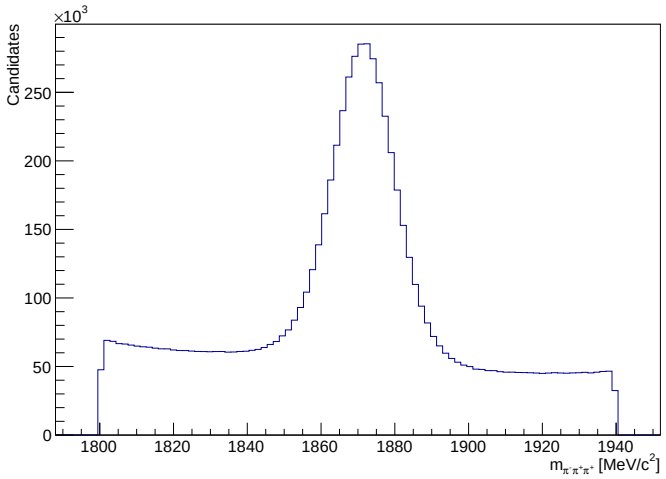

Figure 5.3: Invariant mass distribution of $D^+ \to \pi^-\pi^+\pi^+$ candidates after further selection.

5.5 Simulation

Simulated samples are used in this analysis to guide the selection criteria and to extract the efficiencies across the Dalitz plot, needed further on for the Dalitz fits. All samples were generated with constant matrix element, as phase space, i.e. with a uniform distribution through the Dalitz plot, using Pythia 8 [64, 91]. The simulation of the passage through detector is made by

GEANT [82, 83] and the reconstruction is processed by the same stages as the data. This is what is called a full LHCb simulation.

To generate large signal simulated samples, we have provided them with generator level cuts - loose restriction on the tracks and D candidates momenta and transverse momenta - shown in Table 5.7 and only stored events that passed the same dedicated trigger lines (`Hlt1TrackAllL0` and `Hlt2CharmHadD2HHH`). After that, simulated events are required to pass the selection criteria similar to data (`Stripping20` line), except the Particle Identification criteria [92] (PIDK), since the response of the RICH detectors is not well modelled in simulations, therefore, a method using calibration data is necessary.

In the simulated samples, factors such as non-linear effects like magnetic distortions in the detector, temperature variations, variations in the performance of the RICH detectors for different periods of data recording in the year are not considered. As a consequence of that, the simulation of the PID variables are not reliable. Instead, the PIDCalib package [92] is used, which is a data-driven technique, that uses a full set of calibration samples of pions, kaons and protons. This data-driven procedure provides a calibration to the particle identification likelihood distributions from a signal sample.

Variable	**Value (MeV/c)**
D candidate p_T	> 2100
D candidate p	> 14000
each daughter p	> 2000
each daughter p_T	> 250

Table 5.7: Generator level cuts for $D^+ \to \pi^-\pi^+\pi^+$ decay simulation.

As mentioned, the simulation sample is used in two stages: to guide the selection and for the efficiencies. In the first case, we need it to be as similar as possible to the data sample, therefore, the dynamics needs to be emulated and the kinematics well represented, so we apply dynamical and kinematical weights. In the second case, we just need to ensure that the kinematics is well represented, thus only a kinematical weight is applied.

Considering the large amount of available data, the data sample is divided into two reproducible subsamples, one used for the weighting of the simulation sample, that is not used for any subsequent stage, and the other half used for the analysis.

Fiducial cut

In addition to the stripping and trigger requirements, fiducial cuts are applied due to the use of the PIDCalib package [92]. Since the RICH has very limited discrimination above 100GeV/c, we exclude all the candidates in which any of the daughter tracks are out of the recommended momentum and pseudorapidity ranges as in Table 5.8.

Variable	Cuts
Track η	$1.5 < \eta < 5.0$
Track p	$3 < p < 100$ GeV/c

Table 5.8: Kinematically allowed regions of the p and η phase space as defined in PIDCalib Package.

PIDCalib

Particle identification (PID) efficiency is determined using the `PIDCalib` package [92], consisted on a data-driven technique that uses a full set of calibration samples of pions, kaons and protons, applied for each event. For any track, including pions, the PID efficiency is obtained through golden decays produced in the experiment and reconstructed only from their kinematics characteristics, without using the RICH detectors. In addition, a correlation between the kinematic variables of the tracks in the final-state illustrates that the identification of a track depends on its kinematics. Thus, the PID efficiency is obtained in bands of the kinematic variables: momentum, pseudorapidity and number of tracks. Therefore, the PID efficiency for a requirement on pions in the data sample is extracted by applying this cut on a distributions of pions in the calibration sample. For each simulated candidate, the PID efficiency is included via a weight, ϵ^{PID}.

5.6 Reweight Procedure

The simulation sample, as mentioned previously, is necessary for two purposes. First, to be used as signal input for a multivariate analysis training (MVA), as will be explained in the next section. Second, to construct the efficiency map across the Dalitz plot, as will be explained in Section 5.9 , as will be needed for the amplitude analysis fits. For the second purpose, it is necessary that the kinematics of the simulated decays is well described; for

the first both kinematics and dynamics need to be well represented by the simulation ensuring it to be alike the data.

As mentioned before, the simulated $D^+ \to \pi^-\pi^+\pi^+$ decays were generated with no dynamics. But it can be emulated by obtaining the Dalitz plot distribution from data, after subtracting the background and using it to weight the simulated sample. This is done through the sPlot technique [93]. Using these weights, the simulated sample is now compared to the data to check for differences in kinematics. If there are still differences between them, as observed in Figure 5.4, a second weight - "reweight" - needs to be performed to match these distributions. This second weight (kinematic weight) is expected to be independent of the first (dynamical weight).

Figure 5.5 illustrates the variables after the reweight process indicating that the simulated $D^+ \to \pi^-\pi^+\pi^+$ distributions are now equivalent to the data. A more detailed discussion about the reweight procedure is described in Appendix 10. An important comment is that the data used to provide the weight for the simulation sample is from half of the total data sample, and then is not used for further analysis to avoid potential biases.

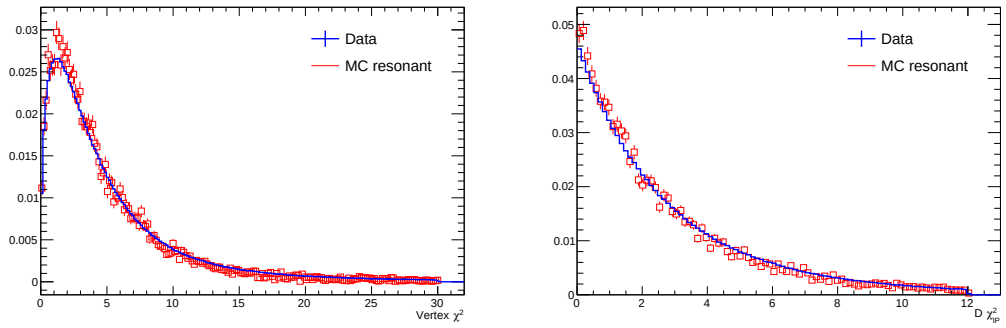

Figure 5.4: Vertex χ^2 and D χ^2_{IP} distributions for $D^+ \to \pi^-\pi^+\pi^+$ signal decays in blue and simulation with dynamical weight in red.

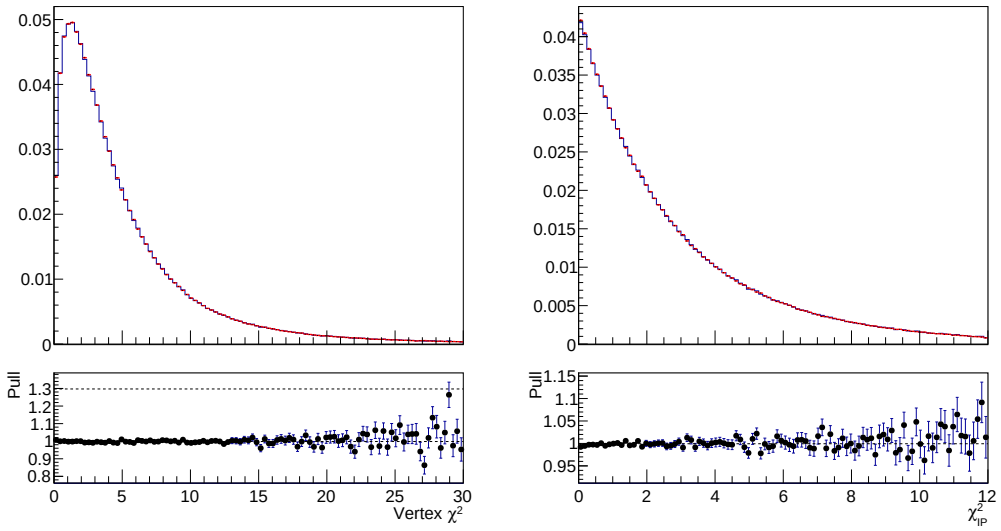

Figure 5.5: Vertex χ^2 and D χ^2_{IP} distributions for $D^+ \to \pi^-\pi^+\pi^+$ signal decays in blue and simulation after reweight (both dynamical and kinematic weights) in red.

5.7 Final Selection: Multivariate Analysis

In this stage the $D^+ \to \pi^-\pi^+\pi^+$ selection is further refined by an offline procedure aiming to reduce combinatorial background and to get a high purity sample, minimizing the effects of the eventual background misparametrisation in the Dalitz fits. Thus, events satisfying the criteria selection so far are additionally filtered using a multivariate analyser (MVA) based on a Boosted Decision Tree (BDT) technique [94]. In this analysis we used the framework called Toolkit of Multivariate Analysis [95] where the algorithms learn with supervision in the sense that the desired result is known. To determine a decision boundary in this multivariate space trained events are used. The strategy comes in two basic stages consisting on a training phase where from given signal and background samples, the decision boundary is determined and an application phase where the trained algorithm is applied to data and a discriminant variable is assigned to each event.

In the BDT the classifier structure consists on a binary tree making decisions on one variable at a time until the criteria is fulfilled aiming to provider a further refined classification for each event as signal or background. This method uses variables that exploit the differences between background and signal, its discriminant power, allowing a tree to be learned by recursively splitting the initial sample in many subsamples.

For each variable it is proposed a decision, a requirement on a value that maximizes the class separation (signal/background) and, based on the

information gained from the split, it builds regions of increasing purity stopping when there is no further improvement. The first node receives as input a full training sample and a requirement, determined by scanning the variable choosing the best separation of signal/background in N steps, is applied on one of the input variables creating two sub-samples that serves as input for the next node. This process goes on until it reaches the maximum number of requirements and the resulting nodes is classified as signal or background depending on whether they are primarily made up signal or background events. In the case of an misclassified event, a higher weight is assigned in the training of the next tree, making it more likely to make the correct classification. This procedure is called boosting and makes the stability and performance of the classifier better. Repeating this training process, we create a forest of decision trees.

In the training phase, half of the simulation sample is used as the signal together with kinematical and dynamical weights, as described in the previous section, while the other half will be used to test the MVA efficiency. The simulation sample has no PID cut, instead has the appropriate PIDCalib weights. For the background, data from the mass sidebands $[1810, 1830]$ and $[1910, 1930]$ MeV/c^2 are used. The variables choice is based on their discriminant power and, typically, variables associated to the pions are not good choices since they cause distortions in the Dalitz Plot. The variables request that the D^+ candidate points to the PV, a good separation between PV and SV, well defined trajectories and the decay products don't point to the PV. The set of variables used and their distributions are illustrated in Figure 5.6.

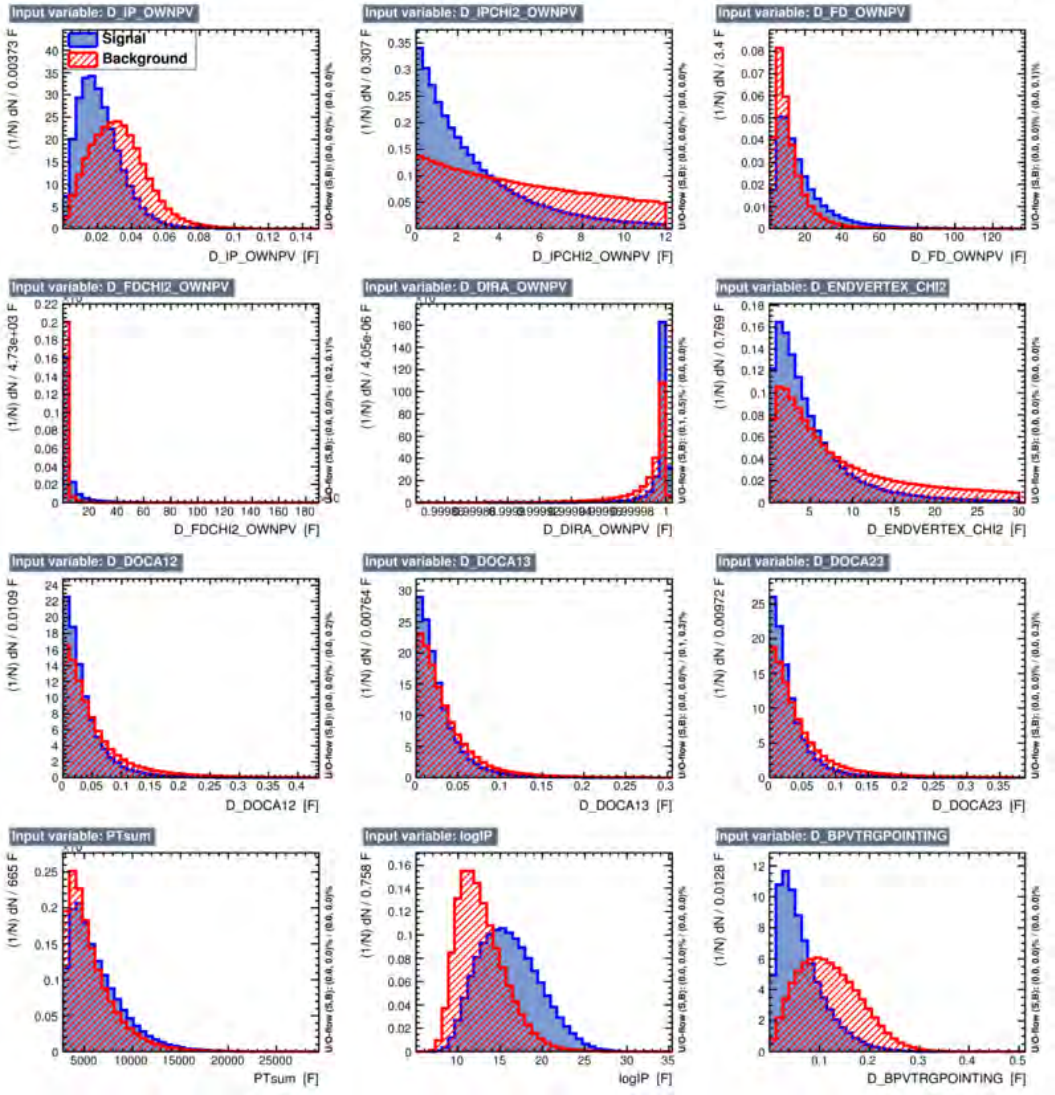

Figure 5.6: Set variables used as input for the MVA training given their distrimination power.

To perform the MVA selection, three classifiers were tested: `BDT` (Adaptative Boost), `BDTPCA`[1] (principal component analysis) corresponding to a BDT with PCA transformations on the input variables and `BDTG` (Gradient Boost). The output of the BDT for each classifier is shown is Figure 5.7 and the BDT response, `valBDT`, is used as a selection variable such that a requirement on this variable is chosen as a compromise between the efficiency and purity. To get a higher purity sample, a tighter value is required although it comes at a high cost in efficiency. A relevant information is the correlation between the variables, as in Figure 5.7, since if there were no correlation, linear requirements would provide a satisfying performance.

[1]BDTPCA consists on a linear transformation that rotates a sample of data points such that the maximum variability is visible.

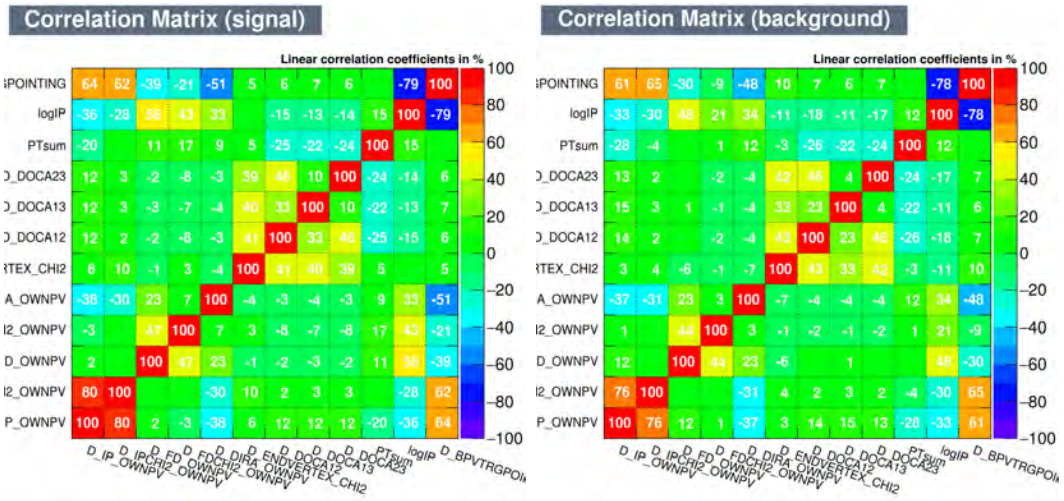

Figure 5.7: Correlation matrix for signal (left) and background (right).

The performance of each classifier is evaluated using the receiver operator characteristic (ROC) curves and is shown in Figure 5.8 displaying the signal efficiency against the background rejection. If the classifier provides an signal efficiency of 100% and 100% background rejection, the curve would be ideal and it would lie in the top–right corner. Comparing the ROC curves for the three classifiers, we observe that the performances of `BDT`, `BDTG` and `BDTPCA` were equivalent, therefore there is no specific motivation to choose a determined classifier. In this analysis we decided to use `BDTG` which provides a good separation between signal and background events.

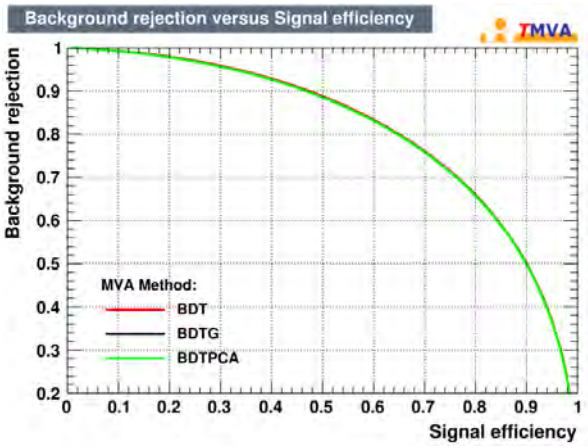

Figure 5.8: ROC curves for the `BDT`, `BDTG` and `BDTPCA` classifiers.

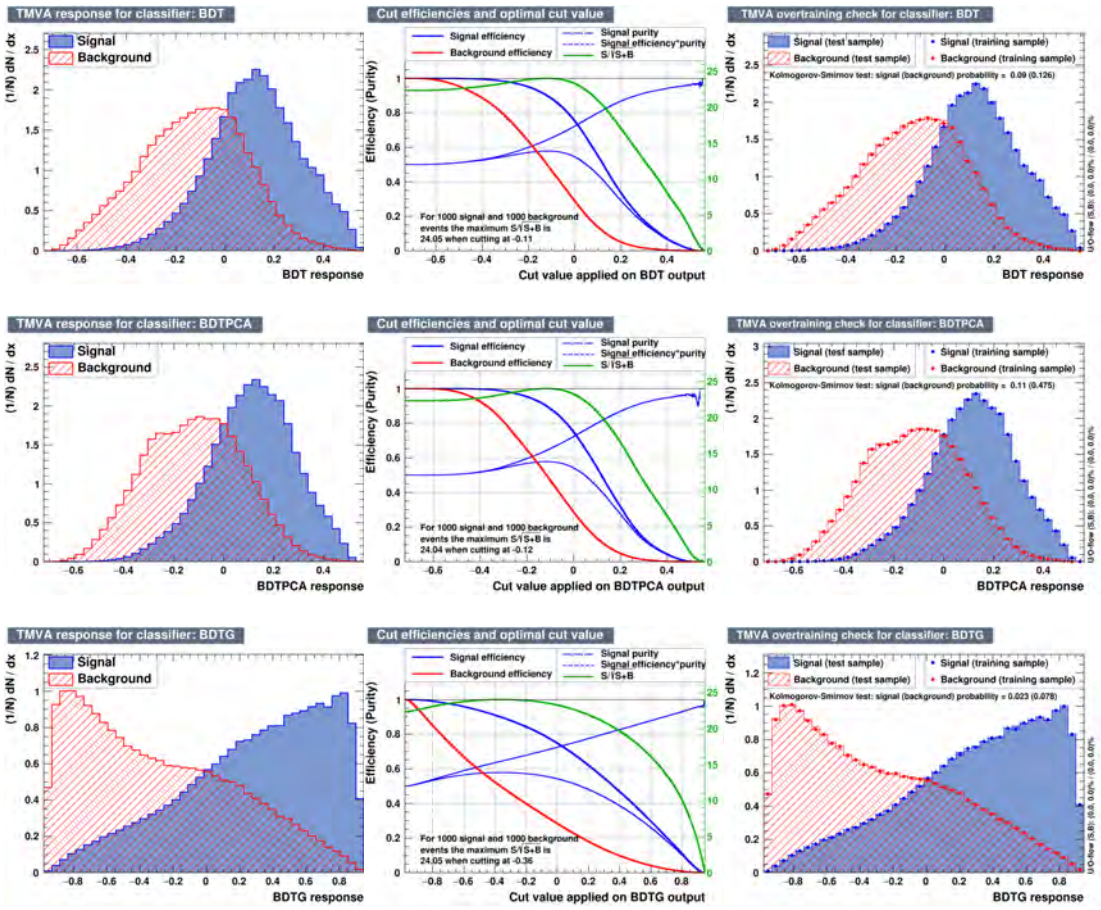

Figure 5.9: Output, efficiencies and overtraining performances of `BDT`, `BDTPCA` and `BDTG` respectively.

To test if two samples came from the same underlying distribution we used the Kolmogorov–Smirnov test in which has an output in the range [0,1]. If the test gets a result 0, it indicates that the samples are not compatible and if gets 1, the samples are identical.

In order to perform the Dalitz fits, a high purity sample is required. In this analysis, a sample with purity around 95% is chosen, thus, the requirement `BDTG` > 0.7 promotes the desired purity. For higher purities, the efficiency begins to drop sharply, also bringing stronger deformations in the Dalitz plot. The accurate yields are evaluated via an invariant mass fit, described in the next section. In Fig. 5.10 we show the D^+ mass spectrum before (left) and after (right) the `BDT` cut observing that the background level was significantly reduced.

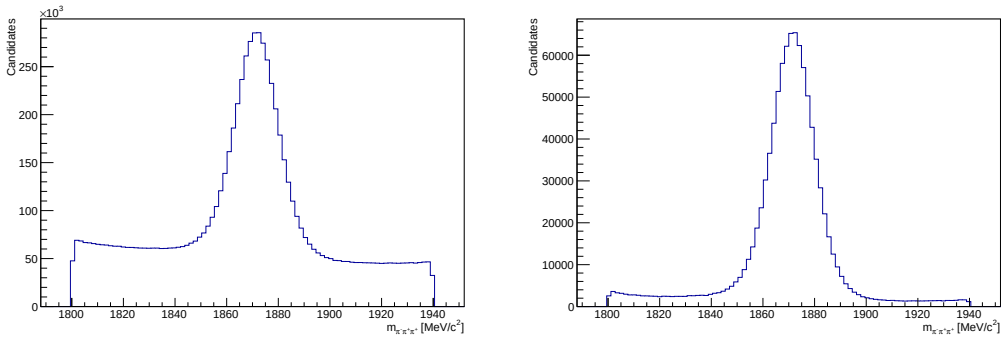

Figure 5.10: $\pi^-\pi^+\pi^+$ invariant mass distribution before (left) and after (right) the `valBDT`> 0.7 requirement applied.

5.8 $\pi^-\pi^+\pi^+$ invariant mass fit

To determine the signal yield and the estimation of the background, we perform a fit to the invariant mass spectrum after the final cuts using the data modeling package `RooFit` [96]. The mass fit is used to determine the signal region in which the Dalitz plot fit is to be performed, and is performed in two steps. At first, the simulation sample is fitted in order to obtain some signal shape parameters. Then, a invariant mass fit of the data sample is performed which the signal shape is derived from fixing some of the shape parameters from simulation sample fit and also including the background parametrisation. For this purpose we construct a total probability density function (PDF) that takes into account the signal and background individual parametrisations. For the simulated sample fit the signal PDF is composed of one Gaussian, which makes the core of the total PDF, plus two asymmetric Crystal-Balls [97] (Gaussian core with a power law tail), which make the left and right tails of the signal shape. The Crystal Ball (CB) function is parametrised by its mean μ, width σ, power of the tail n and α that indicate a distortion from a gaussian function according to the expression

$$CB(m|\alpha, n, \mu, \sigma) = N \begin{cases} \exp\left(-\frac{(m-\mu)^2}{2\sigma^2}\right) & \text{for } \frac{(m-\mu)}{\sigma} > -\alpha \\ A\left(B - \frac{(m-\mu)}{\sigma}\right)^{-n} & \text{for } \frac{(m-\mu)}{\sigma} \leq -\alpha, \end{cases} \tag{5-4}$$

where m is $m(\pi^-\pi^+\pi^+)$ (for short notation in the expressions) and

$$
\begin{aligned}
A &= \left(\frac{n}{|\alpha|}\right)^n \exp\left(-\frac{|\alpha|^2}{2}\right), \\
B &= \frac{n}{|\alpha|} - |\alpha|, \\
C &= \frac{n}{|\alpha|}\frac{1}{n-1}\exp\left(-\frac{|\alpha|^2}{2}\right), \\
D &= \sqrt{\frac{\pi}{2}}\left(1 + \mathrm{erf}\left(\frac{|\alpha|}{\sqrt{2}}\right)\right), \\
N &= \frac{1}{\sigma(C+D)}.
\end{aligned}
\tag{5-5}
$$

The means of the two CBs and the Gaussian are taken to be the same, the tails are constrained to be in opposite directions to accounts for both sides of the distribution and we defined ratios between the width of each CB and the gaussian (σ_{CB1}/σ_G and σ_{CB2}/σ_G). The gaussian function is parametrised by its mean and width given by

$$G(m|\mu,\sigma) = \frac{1}{\sqrt{2\pi}} e^{-\frac{1}{2}\left(\frac{m-\mu}{\sigma}\right)^2}. \tag{5-6}$$

The total signal parametrisation is then

$$\mathcal{P}_{sig}(m) = f_G G(m) + f_{CB1}\,CB1(m) + (1 - f_G - f_{CB1})\,CB2(m) \tag{5-7}$$

where f_G and f_{CB1} are the relative fractions of the gaussian and *CB1* functions and, the fraction of the second *CB2* is $(1 - f_G - f_{CB1})$. For the MC mass fit, the fit model is given by:

$$\mathcal{P} = \mathcal{N}_s \mathcal{P}_{sig}, \tag{5-8}$$

where $\mathcal{N}_s$ corresponds to the yield. The mass fit plots from simulation are shown in Fig. 5.11. The green line represents the gaussian function, the dashed red is the *CB1* and dashed magenta the *CB2*. The black dots are the simulation of the reconstructed mass spectrum of the of the $D^+ \to \pi^-\pi^+\pi^+$ decays, in which the both kinematical and dynamical weights are applied including the `BDTG`>0.7. The result of the simulated mass fit is shown in Table 5.9.

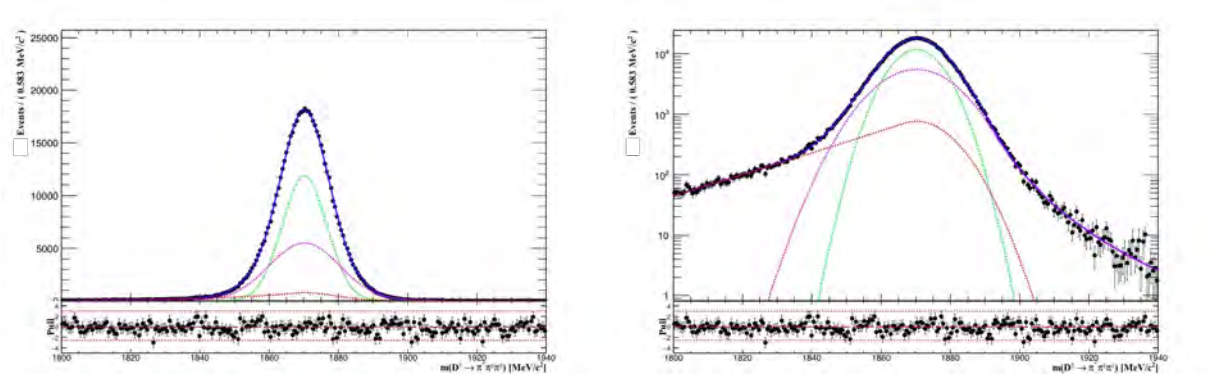

Figure 5.11: $\pi^-\pi^+\pi^+$ mass distribution of the true simulated sample after the final is applied. The PID, dynamical and kinematical weights are also applied. Plots with the fit superimposed in linear (left) and log (right) scale.

Parameter	Value
α_1	0.40 ± 0.01
α_2	-2.26 ± 0.03
σ_{CB1}/σ_G	1.42 ± 0.02
σ_{CB2}/σ_G	1.11 ± 0.02
σ_G (MeV/c^2)	6.48 ± 0.08
f_{CB1}	0.075 ± 0.002
f_G	0.53 ± 0.03
μ (MeV/c^2)	1870.22 ± 0.01
n_{CB1}	35.6 ± 11.4
n_{CB2}	4.0 ± 0.3
$\mathcal{N}_s$	619513 ± 787

Table 5.9: Invariant mass fit results for the simulated $D^+ \to \pi^-\pi^+\pi^+$ sample.

After obtaining a good description of the signal shape from the simulated mass fit, an invariant mass fit of the data including the background model is performed. The background model is given by

$$\mathcal{P}_{bkg}(m) = \exp[\lambda \cdot m], \tag{5-9}$$

where λ is a free parameter. The signal model used is the same as in the simulated sample mass fit with the parameters describing the tails of the CBs (α_1, α_2, nCB1, nCB2), the relative fraction (f_G, f_{CB1}) and the ratio between the width of the CBs and the width of the Gaussian (σ_{CB1}/σ_G, σ_{CB2}/σ_G) set fixed to the values obtained from the simulated sample mass fit. Only the common mass and width of the signal PDF and the exponential slope are left

to float. The fit model is then

$$\mathcal{P} = \mathcal{N}_s \mathcal{P}_{sig} + \mathcal{N}_{bkg} \mathcal{P}_{bkg}, \tag{5-10}$$

where $\mathcal{N}_s$ and $\mathcal{N}_{bkg}$ are the yields for signal and background, respectively (although not explicitly shown, $\mathcal{P}_{sig}$ and $\mathcal{P}_{bkg}$ are normalised such that their integrals are equal to one within the main range of the fit). The plots for the data mass fit are shown in Fig. 5.12 and Table 5.10 summarises the fit results.

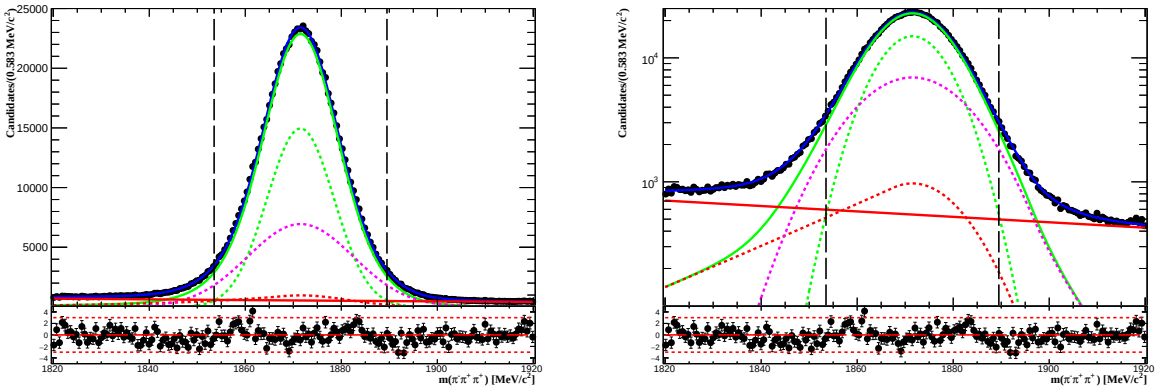

Figure 5.12: $\pi^-\pi^+\pi^+$ mass distribution of the data sample after final selection is applied. Plots with the fit superimposed in linear (left) and log (right) scales.

Parameter	**Value**
λ	-0.0050 ± 0.0001
μ (MeV/c^2)	1871.50 ± 0.01
σ_G (MeV/c^2)	6.99 ± 0.01
$\mathcal{N}_{bkg}$	134457 ± 766
$\mathcal{N}_s$	843779 ± 1026

Table 5.10: Invariant mass fit results for the data $D^+ \to \pi^-\pi^+\pi^+$ sample.

For the Dalitz Plot analysis only events within a $2\sigma_{eff}$ around the peak are considered where

$$\sigma_{eff} = \sqrt{f_G \sigma_G^2 + f_{CB1} \sigma_{CB1}^2 + [1 - (f_G + f_{CB1})]\, \sigma_2^2} = 9.0 \text{ MeV}/c^2. \tag{5-11}$$

The signal region is $[1853.51, 1889.51]$ MeV/c^2 and the purity in the signal region 95.28% within a $2\sigma_{eff}$ window and a total of 815981 candidates.

The Dalitz plot of the events within the signal region to be fitted is shown in linear and log scales, in Fig 5.13, defined in terms of the two invariants $s_{12} = s_{\pi_1^-\pi_2^+}$ and $s_{13} = s_{\pi_1^-\pi_3^+}$ computed such that the invariant mass of the candidate is constrained to be the nominal D^+ mass, by adjusting the

pion momenta within errors, using the DecayTreeFitter package. To perform all Dalitz fits, we used just a fraction of the total sample, consisting in the first 200 thousand events from the full sample of about 900 thousand events due to simulation size limitations (about 600 thousand events) and expected systematics from the amplitude model.

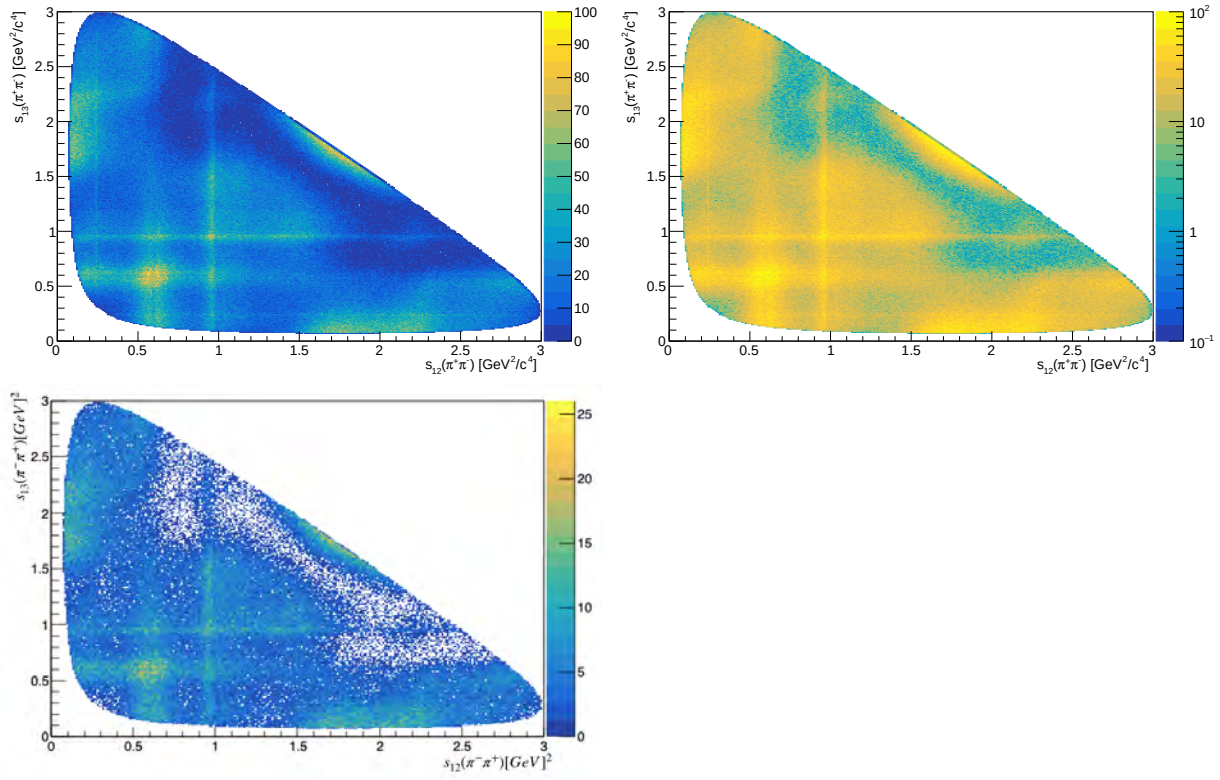

Figure 5.13: $D^+ \to \pi^-\pi^+\pi^+$ containing about 900k in linear, log scales, and 200k events respectively.

K_S veto

One non negligible contamination is the decay $D^+ \to K_S\pi^+$, with $K_S \to \pi^-\pi^+$ that can be visualised in the phase space as a thin line at s_{12} or s_{13} near 0.25 GeV$^2/c^4$. Instead of parametrising, its exclusion on each axis of the Dalitz Plot is done through the veto of candidates in the region $0.235 < s_{12,13}(\pi^-\pi^+) < 0.25$ GeV$^2/c^4$.

5.9 Efficiency

To perform any Dalitz plot fit, it is necessary to construct a signal efficiency map to account for acceptance effects introduced by the detector.

The efficiency is computed as a function of the Dalitz plot coordinates and determined from the simulation sample generated with a constant matrix element, as a uniform distribution across the Dalitz plot. If it presents any non-uniformity after the selection process, it stems from the selection and reconstruction process. Therefore, it needs to be considered in the adjustments. This correction is included via the efficiency map across the DP consisted on a histogram that is smoothed by a 2D cubic spline and determined by combining simulation and data-driven methods. The simulated events are restricted to lie in the same mass window as the data signal and with the same selection criteria - reconstruction, (L0+HLT1+HLT2) trigger and stripping requirements, reweight, tracking correction and MVA selection - with the exception of the PID, using instead the PID from the PIDCalib package [92]. Since it is known that the performance of PID requirements is not well described in the LHCb simulation, their efficiencies are computed directly from calibration samples.

The total efficiency is calculated as using $\epsilon^{\text{selection}}$, the offline selection efficiency, determined from full simulation sample in which the same selection criteria are applied, and ϵ^{PID} is the particle identification efficiency determined from calibration data using the `PIDCalib` tool. For each simulated candidate, the PID efficiency is included via a weight ϵ^{PID}.

The strategy to generate the acceptance is the following: a histogram is filled with the simulated events. Since the sample of full LHCb simulation was generated with a phase space distribution, the efficiency at a given position in the Dalitz plot is simply the height of the bin of the event. Bins near the border of the Dalitz plot may be only partially contained in the phase space, thus the efficiency in these bins is artificially lower. To deal with this, we divide the weighted histogram by a histogram from a very large simulated sample with uniform distribution. The final acceptance is the one obtained from the division of both histograms with same binning: the histogram containing all the selection criteria plus PID and kinematical weights divided by the one with the distribution of the unbiased generated events. This procedure is done with a 30×30 bins histogram. To deal with the statistical fluctuation, a 2D cubic spline is used to produce a high-resolution smoothed histogram, which is used in the fit. The spline procedure is based on the code LauCubicSpline from Laura++ [98].

The final efficiency map is shown in Fig. 5.14 and is the one used afterwards in Chapters 6,7 and 8. From the efficiency map we observe that it is mostly uniform with exception of regions in the corners corresponding to pions with low transverse momentum, events that the efficiency is low.

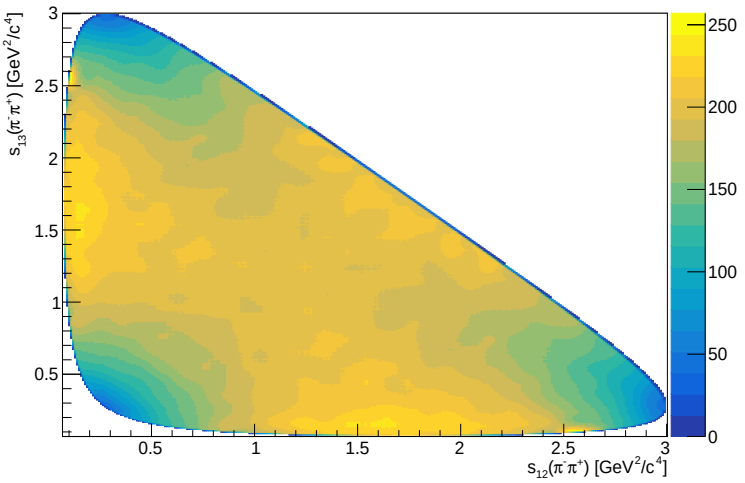

Figure 5.14: Final smoothed efficiency map of $D^+ \to \pi^-\pi^+\pi^+$ to be used in the Dalitz fits.

5.10 Background Model

After performing a MVA for final selection obtaining a high purity sample (95.28%), the remaining 4.72% of background events need to be parametrised and included in the Dalitz fit. The background model is expected to be mainly combinatorial and determined from the mass sidebands of the $D^+ \to \pi^-\pi^+\pi^+$ signal, [1810,1830] MeV/c^2 and [1910,1930] MeV/c^2 . By looking at the sidebands separately, one may observe that the left sideband has more structures while the right wing has a more smooth distribution, as illustrated in Fig. 5.15. We observe a structure corresponding to a $\rho^0(770)$ coming from the $D_s^+ \to \eta'\pi^+$ contamination in which $\eta' \to \rho^0\gamma$. The background within the signal region is assumed to be a composition of these two, so they are added. The exact proportion is not known and is assumed to be, in principle, 50% of each sideband. This unknown combination of sidebands is the main reason for asking such high purity (95%), such that the systematic uncertainties coming from the background are expected to be small. A spline procedure is used to obtain a smoothed histogram using LauCubicSpline from Laura++ [98]. The background histogram after the spline procedure is shown in Fig. 5.16, and it is the one to be used further on in Chapters 6,7, and 8.

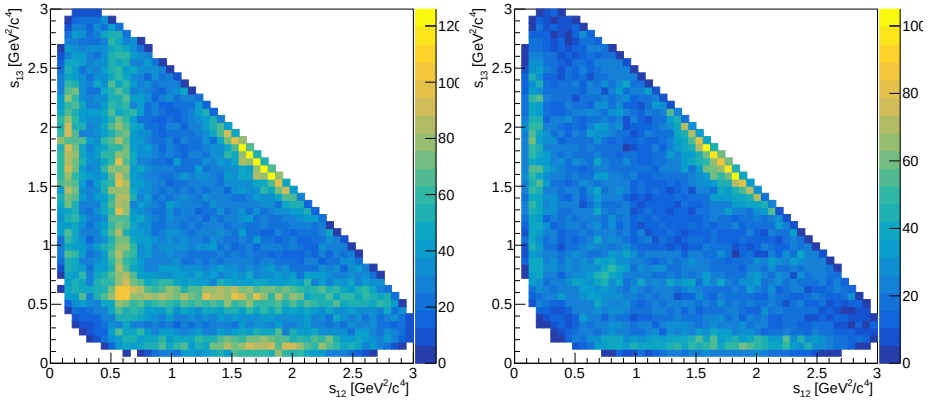

Figure 5.15: Dalitz plot distribution of the background from Left (left plot) and Right (right plot) sidebands.

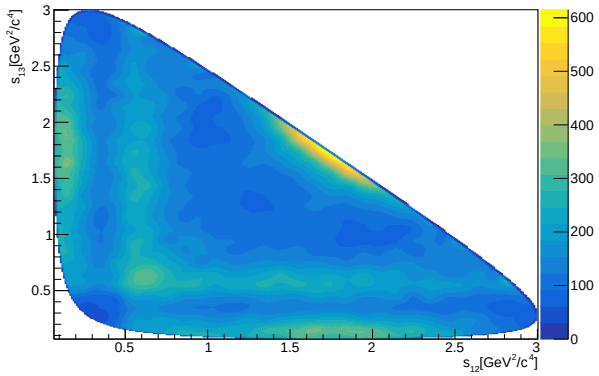

Figure 5.16: Dalitz plot distribution of the background from both wings after the spline procedure.

6
Isobar Model

Three-body non-leptonic decays usually proceed via short–lived intermediate resonant states and a way to understand the underlying dynamics and reveal the structures involved is via a Dalitz Plot analysis. A sketch of such processes is shown in the left plot in Figure 6.1, in which the D meson decays into a stable pseudoscalar meson p_3, referred to as the companion particle, and an intermediate resonant state R. The process $D \to Rp_3$ is what is called a quasi two-body state. The unstable resonant state subsequently decays, via strong interactions, into two pseudoscalar mesons, p_1 and p_2, forming, together with p_3, the three-particle final state. Furthermore, a contribution where the three mesons are directly produced, in which no resonant state is formed, is also possible and referred to as a non-resonant (NR) decay, shown in the right plot in Figure 6.1.

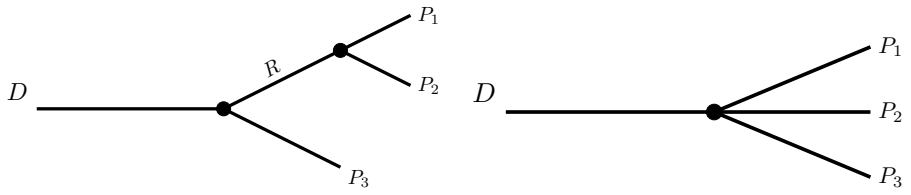

Figure 6.1: Representation of three-body resonant (left) and non–resonant (right) decays.

We aim to describe the transition amplitude of decays proceeding through intermediate resonant states in the form

$$D \to Rp_3 \qquad R \to p_1 p_2, \tag{6-1}$$

where R represents a resonant state that decays into particles p_1 and p_2.

To study and understand the possible resonant sub-structures of hadronic decays, the most traditional and simple framework is the so called *Isobar Model* [99, 100]. In this phenomenological approach, the total decay amplitude is written as a coherent sum of two successive two–body decay amplitudes given by:

$$\mathcal{A} = a_{NR} e^{i\delta_{NR}} + \sum_i a_i e^{i\delta_i} \mathcal{A}_i(s_{12}, s_{13}) \ , \tag{6-2}$$

in which the first term accounts for the non-resonant contribution (NR) assuming a constant amplitude (no dynamics), and the summed terms represent the possible resonant amplitudes that could be produced in the process. Each term in this expression contributes with a complex coefficient in which a_i is the magnitude of the i-th channel, and a phase δ_i, both extracted by a fit to the data. It is important to notice that this complex coefficient is fixed for one amplitude, typically we choose a dominant narrow peak, and we measure the other complex coefficients with respect to this reference choice.

To construct the amplitude for mode i, $\mathcal{A}_i(s_{12}, s_{13})$, that describes the properties of the i^{th} resonant contribution, some considerations are required. Given subsequent processes in Eq. 6-1, each two-body process is represented by a vertex in which momentum and angular momentum are conserved and a Lorentz invariant amplitude can be written by contracting the available four-momenta and polarization vectors. For each vertex we also include a form factor due to limitations in describing low-energy strong interactions, and for the resonance dynamics, we include a propagator term. In the most general way, the total three-body decay amplitude is written as:

$$\begin{aligned} \mathcal{A}_i\left(D \to (R_i \to p_1 p_2)\, p_3\right) &= \mathcal{A}(D \to R_i p_3) \times P_i^J \times \mathcal{A}(R_i \to p_1 p_2) \quad (6\text{-}3) \\ &= \langle R_i p_3 | D \rangle \times P_i^J \times \langle p_1 p_2 | R_i \rangle, \end{aligned}$$

where the factor $\mathcal{A}(D \to R_i p_3)$ is the amplitude from the D meson to $R_i p_3$, $P_R \equiv P_i^J$ accounts as the resonance propagator, usually taken to be a Breit–Wigner function, described in more details later in this chapter, $\mathcal{A}(R_i \to p_1 p_2)$ is the amplitude from the resonance state R_i to $p_1 p_2$ and J is the spin of resonance. Both $\mathcal{A}(D \to R_i p_3)$ and $\mathcal{A}(R_i \to p_1 p_2)$ processes incorporate angular information, considering angular momentum conservation in the transition, and energy dependence expressed with form factors.

For instance, consider a spin 1 resonant state. Recalling that the amplitude must be Lorentz invariant and linear in the spin function, we can construct the terms in Eq. 6-3 according the following strategy. For the amplitude $\langle R_i p_3 | D \rangle$, the available four-vectors are the four-momenta p_3^μ and the polarization vector of R, ϵ^μ, therefore a Lorentz invariant amplitude is obtained from the scalar product of these four-vectors given by the following expression:

$$\langle R_i p_3 | D \rangle = F_{D,R_i p_3}(p_3)_\mu \epsilon_i^{*\mu}, \quad (6\text{-}4)$$

where $F_{D,R_i p_3}$ is the form factor of this transition. For the amplitude $\langle p_1 p_2 | R_i \rangle$, the available four-vectors are: p_1, p_2 and the polarization vector $\epsilon^\mu(\lambda, p_R)$, where $\lambda = -1, 0, +1$ for $J = 1$ and $p_R = (p_1 + p_2)$. Considering that the

amplitude is linear in the spin function, only the scalar products $\epsilon \cdot p_1$ and $\epsilon \cdot p_2$ will contribute, moreover, $\epsilon_\mu p_R^\mu = 0$ since ϵ_μ does not have a time component. Therefore, the amplitude is is given by

$$\langle p_1 p_2 | R_i \rangle \quad = \quad F_{R_i,p_1p_2}(p_1 - p_2)_\nu \epsilon_i^\nu, \tag{6-5}$$

where F_{R_i,p_1p_2} is the form factor of this transition.

Summing the contributions and over all the possible λ values, for a spin-1 resonance, the decay amplitude is given by

$$\mathcal{A}_i\left(D \to (R \to p_1 p_2)\, p_3\right) = F_{R,p_1p_2} F_{D,Rp_3} \sum_\lambda \epsilon_\lambda^{*\mu} \epsilon_\lambda^\nu \left(p_1 - p_2\right)_\nu \left(p_3\right)_\mu \times P_R, \tag{6-6}$$

In addition, we can use the following relation for polarization vectors

$$\sum_\lambda \epsilon_\lambda^{*\mu} \epsilon_\lambda^\nu = -g^{\mu\nu} + \frac{p_R^\mu p_R^\nu}{p_R^2}, \tag{6-7}$$

where $g_{\mu\nu}$ is the Minkowski metric tensor. In the reference frame of R, one can recall the projection operator $P_1^{\mu\nu} = \delta^{ij}$ and $\vec{p}_1 = -\vec{p}_2$, rewriting the amplitude as:

$$\mathcal{A}_R\left(D \to (R \to p_1 p_2)\, p_3\right) = F_{R,p_1p_2} F_{D,Rp_3} \left(-2\overrightarrow{p_3} \cdot \overrightarrow{p_1}\right) \times P_R. \tag{6-8}$$

The generalization of resonance states in terms of their spin can be done by using the Zemach tensor formalism [101–103]:

$$\mathcal{A}_R\left(D \to (R \to p_1 p_2)\, p_3\right) = F_{R,p_1p_2} F_{D,Rp_3} \left(-2\left|\overrightarrow{p_3}\right| \left|\vec{p}_1\right|\right)^J P_J\left(\cos\theta_{13}\right) \times P_R, \tag{6-9}$$

where θ_{13} is the angle between the particles p_1 (π_1^-) and p_3 (π_3^+) in the rest frame of R, ($\pi_1^-\pi_2^+$) system, $P^J(\cos\theta_{13})$ is the Legendre polynomial of order J and J is the spin of the resonance. The spin dependent factor, $\left(-2\left|\overrightarrow{p_3}\right| \left|\vec{p}_1\right|\right)^J P_J\left(\cos\theta_{13}\right)$, represents the angular part of the decay amplitude and the expressions for $J = 0, 1, 2, 3$ are shown in Table 6.1. In all what was written above, the resonance was assumed to be formed in the (p_1, p_2) system, but similarly it could have been formed in the (p_1, p_3) system.

6.1 Angular distributions

The angular information is described using Zemach tensors formalism [101–103] resulting from the angular momentum conservation between the companion meson, p_3, and the resonance, therefore, it depends on the spin

of the resonance. This Lorentz invariant function is defined using the Legendre polynomial of order J in terms of the angle θ_{13} in the rest frame of R and is summarized in Table 6.1.

Resonance Spin	Angular Distribution
0	1
1	$-2\vec{p_1}\cdot\vec{p_3}$
2	$\frac{4}{3}\left[3(\vec{p_1}\cdot\vec{p_3})^2-(\lvert\vec{p_1}\rvert\lvert\vec{p_3}\rvert)^2\right]$
3	$-\frac{24}{15}\left[5(\vec{p_1}\cdot\vec{p_3})^3-3(\vec{p_1}\cdot\vec{p_3})(\lvert\vec{p_1}\rvert\lvert\vec{p_3}\rvert)^2\right]$

Table 6.1: Angular Distributions from Zemach tensor formalism.

6.2 Blatt–Weisskopf barrier factors

The factors F_{D,Rp_3} and F_{R,p_1p_2} in Eq. 6-9 represent penetration effects due to the finite extend of the particles involved in the process. While fundamental particles are considered as pointlike, bound states of quarks must have a finite spatial extent creating a potential well that limits the maximum angular momentum.

These factors are parametrised by Blatt–Weisskopf barrier form factors [104] defined in terms of $z = |\vec{p}|\,r$ that depend on the effective radius r of the barrier and the decay momentum $|\vec{p}|$ in the rest frame of the parent D. Considering that we have two form factors, one accounting for the transition $D \to Rp_3$ and the other for the transition $R \to p_1p_2$, the values for the barrier radius can be different and are taken to be $r_{F_{D,Rp_3}} = 5.0\ \text{GeV}^{-1}$ in the parent form factor case and $r_{F_{R,p_1p_2}} = 1.5\ \text{GeV}^{-1}$ for the daughter form factor. The expressions for $J = 0, 1, 2, 3$ are given by

$$
\begin{aligned}
F_r(z)_{J=0} &= 1\ , \qquad (6\text{-}10)\\
F_r(z)_{J=1} &= \sqrt{\frac{1}{1+z^2}}\ ,\\
F_r(z)_{J=2} &= \sqrt{\frac{1}{z^4+3z^2+9}}\ ,\\
F_r(z)_{J=3} &= \sqrt{\frac{1}{z^6+6z^4+45z^2+225}}\ .
\end{aligned}
$$

6.3 Dynamical functions for resonance propagators

Recalling Eq. 6-9, P_R corresponds to the resonance propagator, usually described by a relativistic Breit–Wigner function, but other possible parametrisations are also used. For the $D^+ \to \pi^-\pi^+\pi^+$ decay, the expected contributions are: $\rho(770)^0$, $\omega(782)$, $f_0(980)$, $f_2(1270)$, $\rho(1450)^0$, $f_0(1500)$, $\sigma(500)$, $f_0(1370)$. The most relevant lineshapes used in this analysis are described below.

Breit–Wigner Lineshape

From Feynman rules for a massive intermediate resonance, the propagator can be written as

$$BW = \frac{i}{s - \Sigma(s)}, \tag{6-11}$$

where $\Sigma(s) = m_0^2(s) + im_0(s)\Gamma_0(s)$ is the self-energy of the intermediate state, m_0 is the mass of the propagator and $s = m^2$ is the invariant mass squared of the two-body system to which the resonance decay. In the case of narrow and isolated resonances $m_0(s)$ is well approximated by a constant. The relativistic Breit-Wigner lineshape (RBW) [105] is the most commonly used to describe resonances and it is well suited for narrow intermediate states. Its expression is given by

$$P_R(m) = \frac{1}{(m_0^2 - m^2) - im_0\Gamma(m)}, \tag{6-12}$$

where m_0 is the nominal mass of the resonance, m^2 is the two-body invariant mass corresponding to the two particles to which the resonance decays, for instance, in the case of $D^+ \to \pi^-\pi^+\pi^+$, it corresponds to the $\pi^+\pi^-$system. For a resonance decaying into spin-0 particles, the dependence of the decay width on $m = \sqrt{s}$ is expressed by

$$\Gamma(m) = \Gamma_0 \left(\frac{p}{p_0}\right)^{2J+1} \left(\frac{m_0}{m}\right) \frac{F_r^2(z)}{F_r^2(z_0)}, \tag{6-13}$$

where Γ_0 is the nominal width of the resonance, J is the quantum number of angular momentum, that due to angular momentum conservation the two-body final state must have angular momentum equal to the spin of the resonance, p is the resonance's daughter momentum, p_0 is the momentum calculated when $m = m_0$ and $F_r^2(z_0)$ is the Blatt–Weisskopf barrier factor, also calculated at p_0.

Within the Isobar approach, the sum of RBW functions is well suited when the resonances are narrow and isolated. In the case of broad overlapping resonances, this sum violates two-body unitarity [29].

Flatté Lineshape

The Flatté lineshape [106] is commonly used for resonances whose invariant mass distribution lies close to a two-particle threshold, such as the light scalar $f_0(980)$ whose mass is close to the K^-K^+ threshold. To account for this effect the parametrisation of the Breit–Wigner function is modified into the following expression:

$$P_R(m) = \frac{1}{m_0^2 - m^2 - im_0(g_{\pi\pi}^2\rho_{\pi\pi} + g_{KK}^2\rho_{KK})}. \tag{6-14}$$

The coupling constants $g_{\pi\pi}$ and g_{KK} are the $f_0(980)$ couplings to $\pi^+\pi^-$ and K^+K^- final states respectively ($g_{\pi\pi} = 0.165$ GeV^{-1}, $g_{KK} = 4.21 g_{\pi\pi}$ GeV^{-1} [107]). The phase-space factors ρ are given by Lorentz-invariant phase space

$$\rho_{\pi\pi} = \frac{2}{3}\sqrt{1 - \frac{4m_{\pi^\pm}^2}{m_{\pi^+\pi^-}^2}} + \frac{1}{3}\sqrt{1 - \frac{4m_{\pi^0}^2}{m_{\pi^+\pi^-}^2}}, \tag{6-15}$$

$$\rho_{KK} = \frac{1}{2}\sqrt{1 - \frac{4m_{K^\pm}^2}{m_{\pi^+\pi^-}^2}} + \frac{1}{2}\sqrt{1 - \frac{4m_{K^0}^2}{m_{\pi^+\pi^-}^2}}. \tag{6-16}$$

Complex Pole Lineshape

In addition to the Breit–Wigner parametrisation, the $\sigma(500)$ resonance can be also described by a complex pole lineshape given by [108]:

$$P_R(m) = \frac{1}{m_\sigma^2 - m^2}, \tag{6-17}$$

where $m_\sigma = (0.47 - i0.22)$ GeV/c^2 is a pole located in the complex $s = m(\pi^-\pi^+)$ plane [109].

Nonresonant term

A non-resonant term consists in the process where the mother particle, in this case the D meson, decays directly into the three-body final state without producing intermediate states. The simplest approximation is to parametrise this contribution using a flat function that populates the whole phase space

in a homogeneous way, therefore usually assumed to be a constant and set to 1. However, more sophisticated models for the non-resonant amplitude have been studied [32].

Gounaris–Sakurai lineshape

Commonly used to describe broad resonances decaying into two pions, such as $\rho^0(770)$ and $\rho^0(1450)$, this lineshape is a modification to the Breit–Wigner with a width depending on the di–pion invariant mass calculated according to Gounaris and Sakurai (GS) [110] given by

$$P_R(m) = \frac{1 + \Gamma_0 d/m_0}{(m_0^2 - m^2) + f(m) - i m_0 \Gamma(m)}, \tag{6-18}$$

where

$$f(m) = \Gamma_0 \frac{m_0^2}{p_0^3} \left[p^2 \left(h(m) - h(m_0)\right) + \left(m_0^2 - m^2 \right) p_0^2 \left.\frac{dh}{dm}\right|_{m_0} \right], \tag{6-19}$$

The function $h(m)$ is given by

$$h(m) = \frac{2}{\pi} \frac{p}{m} \ln\left(\frac{m + 2p}{2m_\pi}\right) , \tag{6-20}$$

with

$$\left.\frac{dh}{dm}\right|_{m_0} = h(m_0) \left[(8p_0^2)^{-1} - (2m_0^2)^{-1}\right] + (2\pi m_0^2)^{-1} , \tag{6-21}$$

From the normalization condition at $P_R(0)$, the parameter $d = f(0)/(\Gamma_0 m_0)$ is given by

$$d = \frac{3}{\pi} \frac{m_\pi^2}{p_0^2} \ln\left(\frac{m_0 + 2p_0}{2m_\pi}\right) + \frac{m_0}{2\pi\, p_0} - \frac{m_\pi^2 m_0}{\pi\, p_0^3} . \tag{6-22}$$

$\rho - \omega$ mixing lineshape

Usually, the $\rho(770)$ contribution is well parametrised with a GS or RBW function, however from the $\pi^+\pi^-$ invariant mass spectrum shown in the right plot in Figure 6.2, it is clear that not only we observe a significant contribution of $\rho(770)^0$, but an interesting effect arises from isospin–violating interactions allowing a decay via the $\omega(782)$ into $\pi^-\pi^+$ [111]. This effect causes a distortion in the lineshape creating an interference pattern in the $\rho - \omega$ region and the observation of this effect occurs either if both amplitudes are included separately as individual contributions or if the $\omega(782)$ is introduced in the $\rho(770)^0$ amplitude via a mixing lineshape [112]. In the case where they are included as individual contributions, we use a RBW lineshape for the $\omega(782)$ and a GS or RBW for the $\rho(770)$. On the other hand, by using a mixing lineshape both contributions are accounted and the interference pattern is

governed by a complex mixing parameter. The mixing amplitude is given by:

$$P_{\rho-\omega} = P_\rho \left[\frac{1 + P_\omega \Delta |B| \exp(i\phi_B)}{1 - \Delta^2 P_\rho P_\omega} \right], \tag{6-23}$$

where P_ρ corresponds to $\rho(770)^0$ using a GS lineshape, P_ω to $\omega(782)$ using a RBW lineshape, $|B|$ and ϕ_B are the parameters, magnitude and phase respectively, responsible to reproduce the interference pattern obtained by a fit to data to avoid any theoretical biases, and $\Delta = \delta(m_\rho + m_\omega)$, with δ governing the electromagnetic mixing of $\rho(770)$ and $\omega(782)$ [35]. Since Δ^2 is small, this term can be ignored in the denominator. From previous analyses it has been found $|\delta| = 2.15 \pm 0.35$ MeV/c^2 [113], $|\delta| = 1.57 \pm 0.16$ MeV/c^2, and arg $\delta = 0.22 \pm 0.06$ [35], illustrated in the left plot in Figure 6.2 from the $e^+e^- \to \pi^+\pi^-$ analysis.

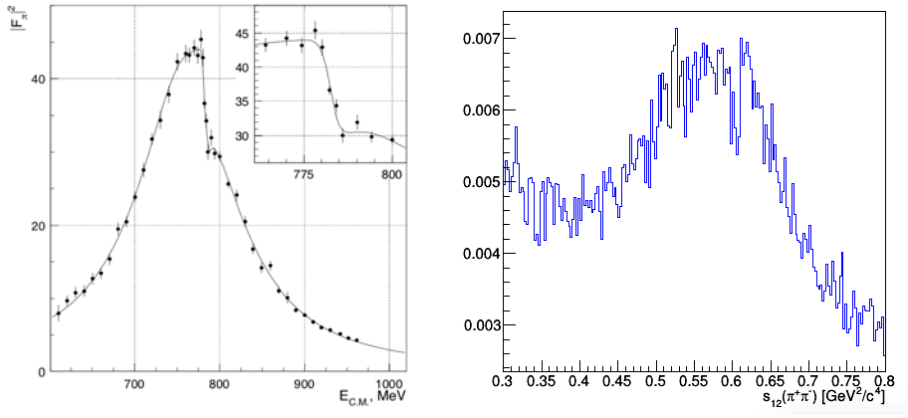

Figure 6.2: $\pi^-\pi^+$ invariant mass in the $\rho - \omega$ region from $e^+e^- \to \pi^+\pi^-$ from CMD [35] analysis (left) and from $D^+ \to \pi^-\pi^+\pi^+$ candidates from LHCb data (right).

This interference pattern depends on the decay channel, therefore the mixing parameters are not expected to be the same in all cases. From the $\pi^+\pi^-$ invariant mass spectrum of $D^+ \to \pi^-\pi^+\pi^+$, the mixing pattern does not look as that from the e^+e^- case in which, instead of a GS distorted with a sudden decrease, it seems to have more of a two peak profile; therefore, the mixing parameters are expected to be different. By ploting the lineshape from Eq. 6-23 and varying the mixing parameters, by inspection, we could in principle expect them to have values close to the ones indicated in Figure 6.3. An alternative approach is to include both $\rho(770)$ and $\omega(782)$ contributions independently via Isobar model and observe the interference effect. Given that the mixing profile is related to the decay channel, in addition to the CMD result, other channels have been studied by the LHCb in which different interference patterns for the $\rho - \omega$ have been observed [114–116].

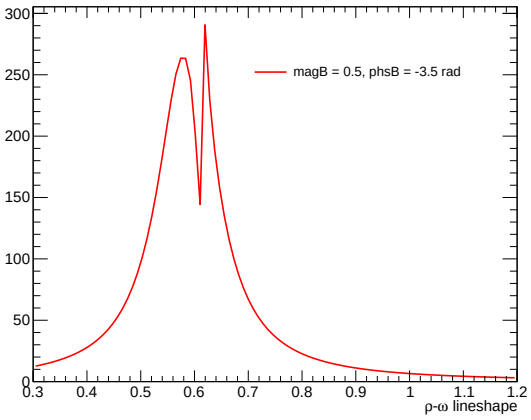

Figure 6.3: $\rho - \omega$ lineshape from Equation 6-23 for the values of $|B|$ and ϕ_B given in the legend.

6.4 Fit strategy

The purpose of perfoming an amplitude analysis is to determine the resonant structure in multi-body decays. The total amplitude is written as

$$\mathcal{A}\left(s_{12}, s_{13}\right) = \mathcal{A}_{S-Wave}\left(s_{12}, s_{13}\right) + \sum_{spin1,spin2} a_i e^{i\delta_i} \mathcal{A}_i\left(s_{12}, s_{13}\right) + \left(s_{12} \leftrightarrow s_{13}\right), \tag{6-24}$$

where the summed terms correspond to $P-$ and $D-$waves included via Isobar Model and $\mathcal{A}_{S-Wave}$ is the amplitude of the $S-$wave to be parametrised using Isobar Model, $K-$Matrix or QMIPWA. For each approach, the amplitude model depends on a set of parameters and their optimum values are obtained using a maximum likelihood fit method.

The maximum likelihood fit provides a parameter estimation given a set of data points $x : x_1, x_2, ..., x_N$. The model describing the distribution of the data points is called a probability dentisity function (PDF) $PDF_{tot}(\vec{x}; \vec{\theta})$ that depends on a set of variables $\vec{x}$ and the parameters $\vec{\theta} : \theta_1, \theta_2, ..., \theta_{npars}$. Based on $\vec{x}$, this method provides an estimation of the optimum set of values for θ. Defining the likelihood function:

$$\mathcal{L}(\vec{\theta}) = \prod_{i=1}^{N} PDF_{tot}\left(\vec{x}; \vec{\theta}\right), \tag{6-25}$$

the optimum set of parameters is such that maximizes $\mathcal{L}(x; \theta)$. Alternatively,

we can define the quantity FCN to be minimized as:

$$FCN = -2\log\mathcal{L} = -2\sum_{i=1}^{N}\log PDF_{tot}(\vec{x},\vec{\theta}) \tag{6-26}$$

For the Dalitz plot fit, the variables $\vec{x}$ are the s_{12} and s_{13}, and the parameters θ will depend on the model being tested. The total PDF is a sum of the signal and the background PDFs. Each term comes with their relative fraction as a multiplicative factor. For the signal PDF, one has to consider the variation of the efficiency across the Dalitz plot. The total PDF is written as

$$PDF_{tot}(s_{12},s_{13},\vec{\theta}) = f_s\mathcal{P}_{sig}(s_{12},s_{13}) + (1-f_s)\mathcal{P}_{bkg}(s_{12},s_{13}), \tag{6-27}$$

where $\mathcal{P}_{sig}(s_{12},s_{13})$ represents the signal PDF and $\mathcal{P}_{bkg}(s_{12},s_{13})$ corresponds to the normalised background PDF. The expression for the $\mathcal{P}_{sig}(s_{12},s_{13})$ is given by

$$\mathcal{P}_{\text{sig}}(s_{12},s_{13}) = \frac{|\mathcal{A}(s_{12},s_{13})|^2\,\epsilon(s_{12},s_{13})}{\iint_{\text{DP}}|\mathcal{A}(s_{12},s_{13})|^2\,\epsilon(s_{12},s_{13})\,ds_{12}ds_{13}}, \tag{6-28}$$

where $\epsilon(s_{12},s_{13})$ is the efficiency map, as obtained in section 5.9. The denominator represents the normalization factor performed needed for $\mathcal{P}_{sig}$ to be a proper PDF.

The free parameters in the fit will be the magnitude a_i, phases δ_i and shape parameters for spin 1 and 2 contribution, meanwhile, for the $S-$wave, when parametrised with Isobar model, the free parameters will be a_i's and δ_i's for each resonant contribution, similarly to the higher spin waves. The parameters for the $K-$matrix and QMIPWA approaches are discussed in Chapters 7 and 8, respectively.

Fit quality and comparison between models

To measure the fit quality we can define the statistical quantity χ^2 as:

$$\chi^2 = \sum_{i=1}^{n_{bins}}\chi_i^2 = \sum_{i=1}^{n_{bins}}\frac{(N_i^{obs}-N_i^{est})^2}{\sigma_i^2}, \tag{6-29}$$

where the Dalitz plot is divided in n_{bins} bins and for each the number of observed events, N_i^{obs}, and the number of events estimated from the fit model, N_i^{est}, are obtained. The number of degrees of freedom (ndof) given by $n_{bins}-n_{par}-1$, in which n_{par} is the number of free parameters of the fit, is used to calculate the quantity χ^2/ndof. We can also define the χ^2/ndof range in which the limits are calculated as $[\chi^2/(n_{bins}-n_{par}-1),\ \chi^2/n_{bins}-1]$. A value

of χ^2/ndof near to 1 indicate a good fit. The binning of the Dalitz plot can be made uniformly - the n_{bins} bins with the same size - or adaptively, where the Dalitz plot is divided such as all n_{bins} bins have the same number of events. This last one is what we use here. The distribution of χ^2 across the Dalitz plot serve for visual inspection of the regions where the fit model describes better or worse the data. Although χ^2 is positive defined, in the plots, for better visualization, we attribute $\chi^2 < 0$ when the fit model exceeds the data in bin i. In addition, a residual distribution across the Dalitz plot, illustrating the Fitted-Data/σ quantity, is used for visual inspection of how the discrepancies between the model and the data are distributed. Furthermore, the FCN value obtained in each fit is used to provide a comparison between the models such that given two fits, the one that has the lowest FCN value indicated a better solution.

Fit Fractions

The general output of a fit is the returned values of the parameters that minimizes $FCN = -2\log\mathcal{L}$ describing the relative contribution of each resonant state. However, the values of these complex amplitude coefficients depend on the amplitude formalism, choice of normalisation and phase convention used in the analysis. Hence, it is not so trivial to compare the values of these parameters from different analysis using different fit programs. Thus, a quantity based on convention–independent method can be used to make such comparisons, the fit fraction (FF_i) defined for each component i:

$$FF_i = \frac{\int\int_{\mathrm{DP}} \left|c_i\mathcal{A}_i\left(s_{12},s_{13}\right)\right|^2 ds_{12}ds_{13}}{\int\int_{\mathrm{DP}} \left|\sum_j c_j\mathcal{A}_j\left(s_{12},s_{13}\right)\right|^2 ds_{12}ds_{13}}. \tag{6-30}$$

Due to presence of interferences, these fit fractions do not necessarily sum 100%. The sum of fit fractions and interference fit fractions is, by construction, 100%. The interference fit fractions between two intermediate processes, symmetrizing i, j and taking $i < j$, are defined as

$$FF_{ij} = \frac{\int\int_{DP} 2\,\mathrm{Re}\left[c_ic_j^*\mathcal{A}_i\left(s_{12},s_{13}\right)\mathcal{A}_j^*\left(s_{12},s_{13}\right)\right] ds_{12}ds_{13}}{\int\int_{\mathrm{DP}} \left|\sum_i c_i\mathcal{A}_i\left(s_{12},s_{13}\right)\right|^2 ds_{12}ds_{13}}. \tag{6-31}$$

6.5 Results

We now present the results of the $D^+ \to \pi^-\pi^+\pi^+$ fits using the Isobar Model performed using the Dalitz plot fit package `LAURA++` [98]. Several challenges are found in the analysis given the variety of resonant states

presented in this channel. In particular the scalar sector where difficulties are encountered due to the presence of many possible contributions which do not have clear signatures given the absence of angular distribution and broad structures. Therefore, the inclusion of scalar states needs to be cautious and one possible approach is to allow many contributions to obtain a better fit however, this strategy can produce unrealistic interference scenarios. The strategy to perform the fits is to identify characteristic resonances that are expected to appear and add/remove them into the model based on the change in FCN observing the physical content of the solution. Typically, decreases in FCN of more than ≈ 30 units are considered significant.

As discussed in Chapter 5, the fits are performed using a fraction of the final samples consisting in 200 thousand events with 95.28% purity. The fit model is constructed including known resonances by previous analyses for this channel, however more contributions are tested. Lineshapes are also studied by allowing mass and width of some resonances to float. According to Equation 6-24, the fitted parameters in this model are the magnitudes and phases for each contribution. Furthermore, in all fits the $\rho(770)^0\pi^+$ is chosen as reference, fixing its magnitude to 1 and phase to zero. The lineshapes and parameters used for each resonance are summarised in Table 6.2 and for resonances which more than one lineshape is listed, the one used in each model is specified. The fit fractions are calculated according to the previous discussion, however, the error of the fit fractions have not been calculated yet.

The goodness of the fit is estimated using the χ^2/ndof range and, since there are two identical pions in the final state, a residual plot is computed using the folded Dalitz plot represented as $s^{high}_{\pi^-\pi^+} \equiv s_{hi}$ versus $s^{low}_{\pi^-\pi^+} \equiv s_{lo}$, which are respectively the higher and the lower values among s_{12} and s_{13}. The results are shown together with the s_{lo}, s_{hi}, $\pi^+\pi^-$, $\pi^+\pi^+$ projections and residual distribution. In addition, to ensure that the best minimum was found and to verify the possibility of multiple solutions, we perform 100 fits starting from random input parameters and observing the possible solutions, thus, only the solution with the lowest FCN is shown.

Once the fit is performed, and the optimal set of parameters is found, a large simulation sample (toy sample) is generated and weighted by the full PDF, with the parameters from the fit. This toy sample includes simulation of the background and is also weighted by the efficiency used in the signal fit. The projections illustrate the data as the black dots, the fit result in blue and the background in gray.

Resonance	Spin	Lineshape	$m(\mathrm{MeV}/c^2)$	$\Gamma(\mathrm{MeV}/c^2)$
$\sigma(500)^\dagger$	0	Pole/RBW	475	550
$f_0(980)$	0	Flatté	990	70
$f_0(1500)$	0	RBW	1505	109
$f_0(1370)$	0	RBW	1370	350
$f_0(1710)$	0	RBW	1722	135
$\rho(770)^{0\dagger}$	1	$\rho-\omega$ mixing/GS/RBW	775.26	149.1
$\omega(782)^\dagger$	1	$\rho-\omega$ mixing/RBW	782.65	8.49
$\rho(1450)^0$	1	GS/RBW	1465	400
$\rho(1700)$	1	RBW	1720	250
$f_2(1270)$	2	RBW	1275.1	185.1
$f_2'(1525)$	2	RBW	1525	73
$\rho_3(1690)$	3	RBW	1688.8	161

Table 6.2: List of resonant contributions including their spin, lineshape used and parameters of mass and width set in `Laura++`. The contribution indicated with † can be parametrised with either of the lineshapes indicated. The lineshape used is specified in each model. RBW indicates a relativistic Breit-Wigner and GS a Gounaris-Sakurai lineshape.

Model I-1

We begin our Dalitz plot analysis by attempting to reproduce results previously obtained. This first model is composed by resonances according to the fit model used in E791 analysis: $\rho(770)^0$ included with a GS lineshape, $f_2(1270)$, $\sigma(500)$ parametrised with a RBW lineshape, $f_0(980)$ as a Flatté, $f_0(1370)$, a non resonant term (NR) and $\rho(1450)$ included with a GS lineshape. All lineshape parameters are fixed, with masses and width set according to PDG values, while the complex coefficients are free in the fit. The resulting magnitudes, phases and fit fractions are shown in Table 6.3. In Figures 6.4, we show the $\pi^+\pi^-$ and $\pi^+\pi^+$ projections with the fit result indicated by the blue line and the residuals distribution.

Although the fit projections illustrates clearly some contributions such as the $\rho(770)^0$, $\sigma(500)$ and $f_0(980)$, the fit quality is very poor, specially at high masses. The low mass region shows a qualitative agreement, specially the $\sigma(500)$ and $\rho(770)^0$ contributions with a reasonable description, while regions after 1.2 GeV^2/c^4 present a very low fit quality. Regarding the $\rho(770)^0$ region, we observe a pattern in the data that a simple GS lineshape is not sufficient to describe, better seen in the bottom left plot of Figure 6.4. To better describe

this region the $\omega(782)$ must be included. A clear $f_0(980)$ signature is also observed, however, it appears to be centered at a shifted $s_{12}(\pi^-\pi^+)$ value, possibly due to interferences, thus it is also does not provide a good description of this resonant state given the large discrepancies between the data and the fit result. Altogether this model does not describe the data well and the fit fractions shown in Table 6.3 agree qualitative with E791 result.

Resonance	**Magnitude**	**Phase** [rad]	**Fit Fraction (FF)** (%)
$\rho(770)^0$	1 [fix]	0 [fix]	26.4
$f_0(980)$	0.547 ± 0.006	3.12 ± 0.02	7.9
$\sigma(500)$	0.836 ± 0.013	3.82 ± 0.02	18.4
$f_2(1270)$	0.621 ± 0.005	1.45 ± 0.02	10.2
$f_0(1370)$	0.604 ± 0.011	2.61 ± 0.02	9.6
$\rho(1450)$	0.222 ± 0.012	7.68 ± 0.03	1.3
NR	0.655 ± 0.014	-0.96 ± 0.02	11.3
$\sum$ FF (%)	85.2		
χ^2/ndof (range)	[8.44 - 8.27]		
			FCN = -1908208

Table 6.3: Model I-1 (E791): component parameters and fit fractions. Uncertainties are statistical only.

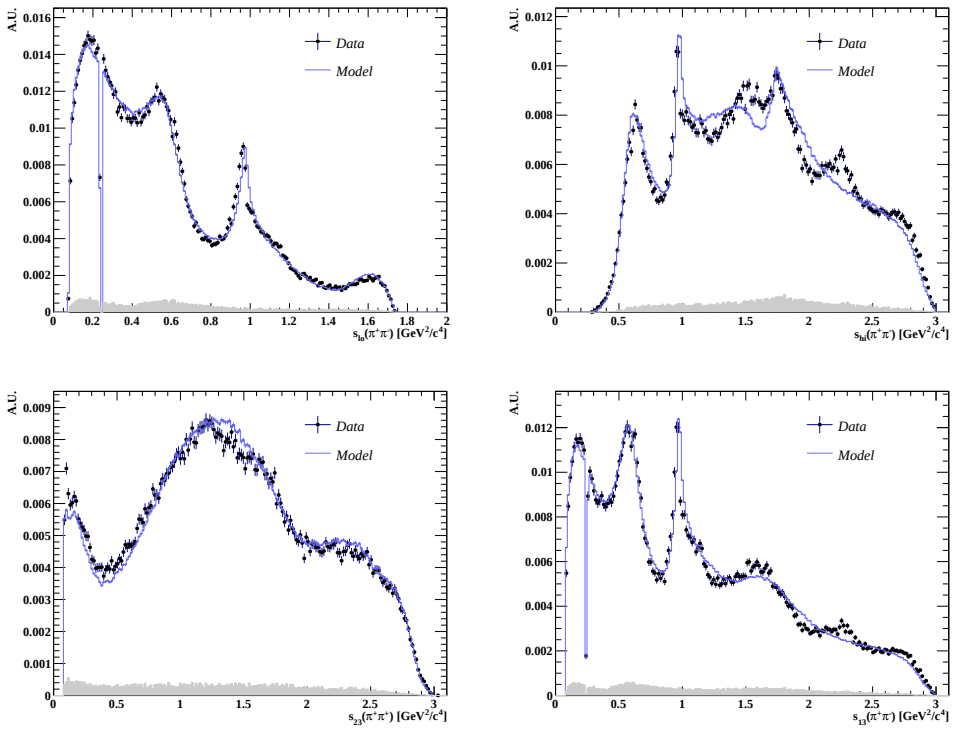

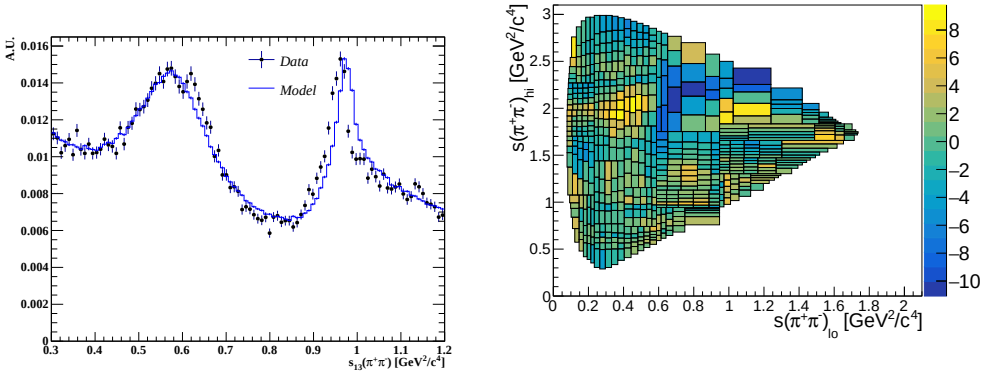

Figure 6.4: Fit results from Model I-1 (E791): s_{lo}, s_{hi}, s_{23} and s_{12} projection. In addition, a zoomed plot in the $\rho^0(770)$ region to better visualize the $\rho - \omega$ interference and the residual plot.

Model I-2

Several fits were performed including different combinations of resonances in order to achieve a better solution and the best fit, the one with the lowest FCN, is the following. The progress in starting from Model I-1 until we reach this best FCN value is shown in Appendix 13 where we present other fit models tested with a worse FCN compared to Model I-2 but with some regions better adjusted. In this model we attempt to improve the fit quality at high masses. We include the $\omega(782)$ contribution, in order to produce the observed interference effect, and in the $f_0(980)$ region that was slightly shifted in the previous result, we allow its mass free in the fit. This model is composed by $\rho - \omega$ included with a mixing lineshape, $f_2(1270)$, $\sigma(500)$ parametrised with a RBW lineshape, $f_0(980)$ with its mass set as free in the fit, $f_0(1370)$, $f_0(1500)$, $\rho(1450)^0$ included with a GS lineshape and $f_0(1710)$. All other lineshape parameters not mentioned are set as PDG values and fixed in the fit. The resulting magnitudes, phases and fit fractions are shown in Table 6.4. In Figures 6.5 we show the $\pi^+\pi^-$ and $\pi^+\pi^+$ projections with the fit result indicated by the blue line and the residuals distribution.

At first, we observe that the $\pi^-\pi^+$ high mass region is better adjusted compared to Model I-1 but it still present significant issues comparing to the data. The inclusion of the $f_0(1710)$ promoted a significant improvement in this region but it compromised the description at low masses. Since the phase space of this decay is tight, the inclusion of the $f_0(1710)$ promotes interferences that improve the high mass part but worsens the low mass region that was better described before. The result still illustrates qualitative $\rho(770)^0$, $\sigma(500)$

and $f_0(980)$ contributions but the fit quality is worse, specially in the $\sigma(500)$ region. The $\rho-\omega$ interference presents now the form of the interference pattern with the mixing lineshape, however, it still shows large discrepancies between the result and the data. The $f_0(980)$ is centered at a $s_{12}(\pi^-\pi^+)$ value with a better agreement and converged to $m_{f_0(980)} = 911.7 \pm 2.0$ MeV/c^2 but it still requires a more precise description. When the $f_0(980)$ mass was fixed in the fit, the results showed the previous shifted behavior. In addition, the region $1.1 < s_{12}(\pi^-\pi^+) < 1.7$ GeV$^2/c^4$ presents a very poor agreement with the data. The $\pi^+\pi^+$ projection shows a significant improvement compared to Model I-1 but it still illustrates the same misparametrised region at $s_{23}(\pi^+\pi^+) < 0.3$ GeV$^2/c^4$.

Many other tests were performed including different contributions and allowing lineshapes parameters free in the fit but this result is the one that provides the lowest FCN value, thus, the best description of the data with the Isobar Model.

Resonance	**Magnitude**	**Phase** [rad]	**Fit Fraction (FF)** (%)
$\rho - \omega$	1 [fix]	0 [fix]	22.7
$f_0(980)$	0.541 ± 0.006	-3.50 ± 0.03	6.6
$\sigma(500)$	1.031 ± 0.026	3.57 ± 0.03	24.1
$f_2(1270)$	0.685 ± 0.013	1.49 ± 0.02	10.7
$f_0(1500)$	0.326 ± 0.023	-2.83 ± 0.06	2.4
$f_0(1370)$	0.274 ± 0.027	3.68 ± 0.06	1.7
$\rho(1450)$	0.220 ± 0.012	1.78 ± 0.06	1.1
$f_0(1710)$	0.359 ± 0.012	-1.54 ± 0.07	2.9
$m_{f_0(980)}$	911.7 ± 2.0 MeV/c^2		
$\|B\|$	0.627 ± 0.036		
ϕ_B	-3.26 ± 0.06		
$\sum$ FF (%)	72.2		
χ^2/ndof (range)	[5.12 - 4.98]		
			FCN = -1909144

Table 6.4: Model I-2: component parameters and fit fractions. Uncertainties are statistical only.

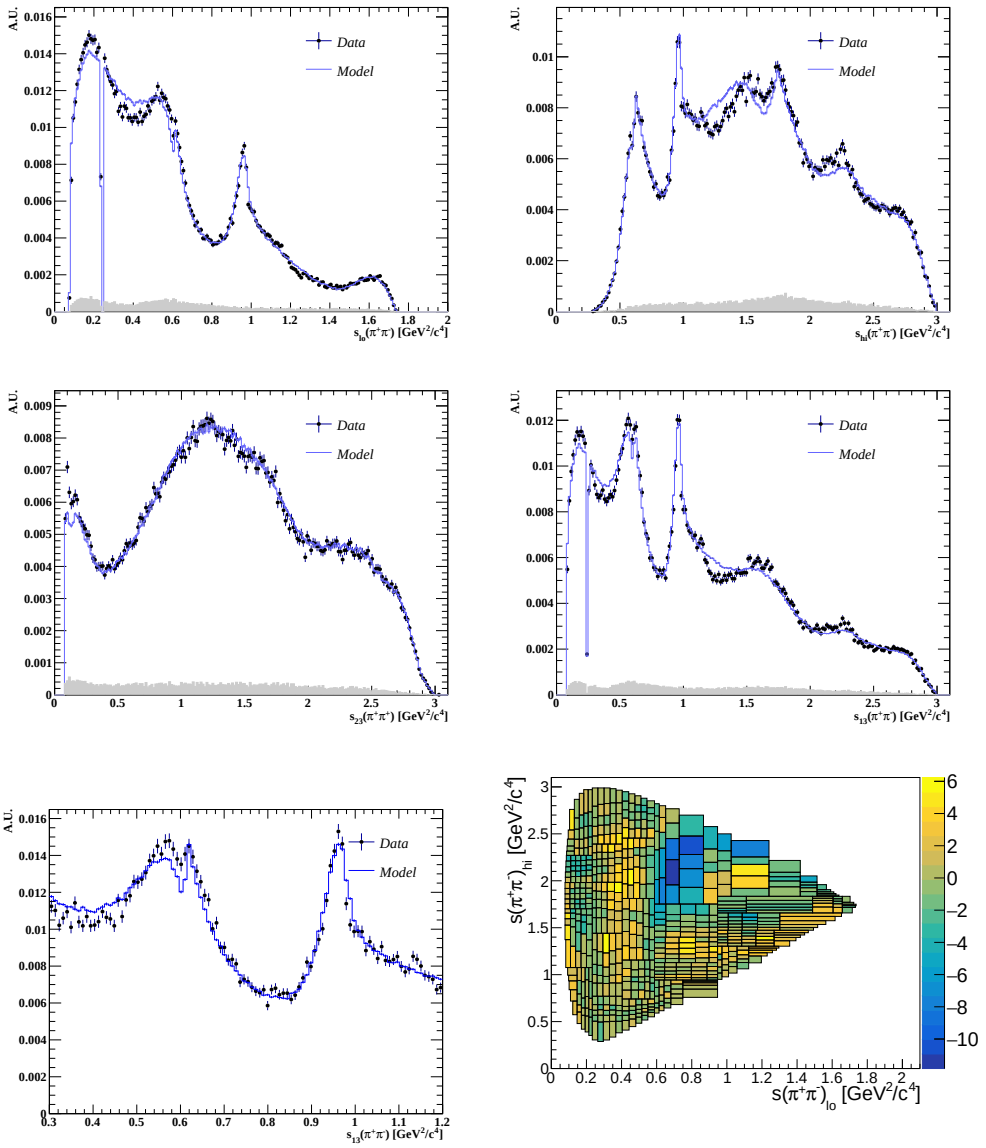

Figure 6.5: Fit results from Model I-2: s_{lo}, s_{hi}, s_{23} and s_{12} projection. In addition, a zoomed plot in the $\rho^0(770)$ region to better visualize the $\rho - \omega$ interference and the residual plot.

Additional tests

As an attempt to improve the fit quality, other contributions were tested instead of including the $f_0(1710)$ such as a non resonant (NR), $\rho_3(1690)$, rescattering and allowing the $f_0(1370)$ lineshape parameters free in the fit. More details about some of the relevant additional tests can be found in Appendix 13.

– **Model I-3**: In this model we include a non resonant (NR) contribution. The model consists in $\rho - \omega$ (free mixing parameters), $f_2(1270)$, $\sigma(500)$

using a RBW, $f_0(980)$ (free mass), $f_0(1500)$, $f_0(1370)$, $\rho(1450)^0$ using GS lineshape and NR. The solution converged to FCN=-1908882 and the fraction of the NR was 5.8%. The inclusion of this contribution did not provided any improvement in the description of the spectrum at high masses.

– **Model I-4**: In this model we include a spin 3 contribution, $\rho_3(1690)$. The model includes $\rho - \omega$ (free mixing parameters), $f_2(1270)$, $\sigma(500)$ using a RBW lineshape, $f_0(980)$, $f_0(1500)$, $f_0(1370)$, $\rho(1450)^0$ using GS lineshape and $\rho_3(1690)$. The solution converged into a FCN=-1908678 and the fraction of $\rho_3(1690)$ was 0.2%, therefore, it did not provide any significant change in the fit.

– **Model I-5**: In this model we include a rescattering amplitude [117–119] $\pi\pi \to KK$ in a two-body interactions context in which a pair of mesons produced in one channel will appear in the final state of a coupled channel. The model included $\rho - \omega$ (free mixing parameters), $f_2(1270)$, $\sigma(500)$ using a RBW, $f_0(980)$, $f_0(1500)$, $\rho(1450)^0$ using GS lineshape and rescattering. The solution converged to FCN=-1908625 and the fraction of rescattering was 0.05%. Compared to the previous results, the inclusion of the rescattering amplitude did not promote any increase in the fit quality.

– **Model I-6**: In this test we allowed the mass and width parameters of the $f_0(1370)$ contribution free in the fit. The model includes $\rho - \omega$ (free mixing parameters), $f_2(1270)$, $\sigma(500)$ using a RBW, $f_0(980)$, $f_0(1500)$, $f_0(1370)$ (free mass and width) and $\rho(1450)^0$ using GS lineshape. The fitted $f_0(1370)$ mass shifted to a higher value while the width decreased. This solution provided a significant improvement at high mass regions, compared to Model I-1, with the fitted parameters of the $f_0(1370)$ equal to $m_{f_0(1370)} = 1696.9 \pm 3.6$ MeV/c^2 and $\Gamma_{f_0(1370)} = 150.8 \pm 9.6$ MeV/c^2. The solution converged to a FCN= -1909083, with a fit fraction of 4.3% for the $f_0(1370)$ contribution. Comparing to Model I-2, the inclusion of the $f_0(1710)$ still promotes a better solution than setting the $f_0(1370)$ lineshape parameters free.

– σ **considerations**: The same tests have also been performed with a RBW using with a mass dependent width for the $\sigma(500)$ resonance given by

$$\Gamma(m) = \sqrt{1 - (m_1 + m_2)^2 / m} \left(\frac{m - s_A}{M^2 - s_A} \right) (b_1 + b_2 m)\, e^{-(m - M^2)/A} \quad (6\text{-}32)$$

in which M is the mass where the phase shift goes through 90^o for real $s \equiv m^2$, the square-root term is the phase space factor, m_1 and m_2 the invariant masses of the daughter particles, s_A is the Adler-zero constant and b_1, b_2 and A are additional constants parametrised according to BES data [120]. This choice of parametrisation did not provide any significant improvement in the fit compared to a RBW. In addition, tests with a pole lineshape presented a worse fit quality than using RBW, therefore, only the tests with RBW parametrisation have been shown.

– $\rho-\omega$ **considerations**: We also included both contributions individually. The $\rho(770)^0$ was parametrised with a GS and the $\omega(782)$ contribution with RBW. The fit result illustrates that the inclusion of each contribution individually is equivalent to include with a mixing lineshape.

The Isobar model is extensively used in Dalitz plot analyses, however, one has to consider its limitations specially regarding final state interactions, three-body unitarity and any discrepancy between RBW and true $S-$Matrix poles. Given the coexistence of several broad overlapping resonances in the scalar sector, all the results shown in this section illustrate the problems arising from this sum of RBW approach. Within the Isobar model, a somewhat qualitative description of the $D^+ \to \pi^-\pi^+\pi^+$ Dalitz plot is obtained, however none of the fit results provided a good description of the data and other alternatives must be considered to better describe the underlying dynamics this channel, specially the scalar sector. The $P-$ and $D-$ waves fit fractions were consistent in all fits but the $S-$wave components presented a large variation in the fit fraction depending on which resonant states are included. As expected, the $\sigma(500)$ is all tests was the major contribution in the scalar sector. Several models were tested including different scalar contributions but no reasonable fit was obtained.

7
K-Matrix Model

The Isobar Model may provide a good description of the dynamics of three-body decays only under certain limits, when the quasi two-body resonances are relatively narrow and isolated (from other amplitudes with the same spin). However, in this analysis we have the opposite case since we are dealing with a huge amount of charm decays from LHCb data and the $\pi^-\pi^+$ S-Wave contribution is composed of many broad overlapping resonant states coexisting at energies below 2 GeV/c^2 as indicated in Table 7.1.

Resonance	**Mass (MeV/c^2)**	**Width (MeV/c^2)**
$f_0(980)$	990 ± 20	$10 - 100$
$f_0(1370)$	$1200 - 1500$	$200 - 500$
$f_0(1500)$	1504 ± 6	109 ± 7
$\sigma(500)$	$400 - 550$	$400 - 700$

Table 7.1: $\pi^-\pi^+$ S-Wave components obtained from PDG [1].

Under this scenario, the Isobar model violates two-body unitarity, *i.e.* violates the conservation of quantum mechanical probability current and other models to describe the $\pi^-\pi^+$ scalar sector must be considered. One alternative is to use the $K-$Matrix formalism [98, 121], in principle developed in the framework of two-body scattering [122] and resonances in nuclear reactions [123] but it was extended to study resonance production more generically [124]. This approach based on the idea of writing the physical amplitude $\mathcal{A}_{S-wave}$ as a pole part and a non-pole part, often called slowly varying part

$$\mathcal{A} = \mathcal{A}_{pole} + \mathcal{A}_{SVP}.$$

By using this approach, unitarity is naturally obeyed assuming that the $\pi^-\pi^+$ $S-$Wave does not interact with the rest of the products in the final state. This is far from obvious in the $D^+ \to \pi^-\pi^+\pi^+$ decay. Although here we have a D meson as the initial state and three pions in the final state, from this stage on we assume that once the state $\pi^+\pi^-$ is created what follows that is, the transition $\pi\pi \to \pi\pi$, the initial state $\pi^+\pi^-$ can rescatter into $\pi^+\pi^-$ and into other final states in a unitary transition and the total $\pi^+\pi^-$ amplitude

is a sum over all possible rescattering channels. This chapter is dedicated to describe the formalism and fit results using the $K-$matrix approach.

7.1 Basic Formalism

In the scattering formalism, a general transition between a given initial to a final state can be written in terms of the scattering S-Matrix according to

$$\mathcal{S} = \langle f| S |i\rangle = I + 2i \langle f| T |i\rangle \tag{7-1}$$

where the first term represents the case in which there is no interaction between the initial and final states and the second when there is any interaction represented by the transition matrix T. The factor $2i$ is conventionally used such that the transition amplitude for a single resonance channel corresponds to a circle in the complex plane centered at $(0,i/2)$ and diameter 1 such that the physically allowed possibilities of T for inelastic scattering lie inside the circle while elastic scattering processes lie in the boundary. The $S-$Matrix is unitary ($SS^\dagger = S^\dagger S = I$) therefore, it conserves scattering probability and from Equation 7-1 we can define a Hermitian $K-$matrix ($K = K^\dagger$) operator according to:

$$K \equiv \left(T^{-1} + iI\right)^{-1} \longrightarrow\ T = (I - iK)^{-1}K, \tag{7-2}$$

where K is real and symmetric given the time-reversal invariance of S and T and in the right side we have the expression of T written in terms of K. To produce a Lorentz invariant transition amplitude, we include phase-space factors for initial and final states in the normalisation of two-body functions producing the Lorentz invariant $T-$Matrix written as

$$T_{ij} \equiv \left\{\rho_i^\dagger\right\}^{\frac{1}{2}} \hat{T}_{ij} \left\{\rho_j\right\}^{\frac{1}{2}}, \tag{7-3}$$

where i and j are channel indices, running from 1 to n, and ρ is the normalised diagonal $n \times n$ phase-space matrix given by

$$\rho = \begin{pmatrix} \rho_1 & 0 \\ 0 & \rho_2 \end{pmatrix} \tag{7-4}$$

and

$$\rho_1 = \frac{2p_1}{m} \quad \text{and} \quad \rho_2 = \frac{2p_2}{m} \tag{7-5}$$

with p_k as the magnitude of the momentum of the daughter k in the rest-frame of the two–body state with invariant mass $m = \sqrt{s}$. The phase-space element of a channel i is in general parametrised as:

$$\rho_i = \sqrt{\left(1 - \frac{(m_{1i} + m_{2i})^2}{s}\right)\left(1 - \frac{(m_{1i} - m_{2i})^2}{s}\right)}, \tag{7-6}$$

where m_{1i} and m_{2i} are the rest masses of the two daughter particles. The Lorentz–invariant form of the $K-$Matrix is then defined as

$$\hat{K}^{-1} = \hat{T}^{-1} + i\rho, \tag{7-7}$$

being also real and symmetric. From this expression we can then obtain the Lorentz–invariant transition amplitude depending on the $K-$Matrix

$$\hat{T} = (I - i\hat{K}\rho)^{-1} \cdot \hat{K}, \tag{7-8}$$

which can be used to obtain the generalised amplitude of the production of overlapping resonant states according to the expression

$$\mathcal{A}_i = \sum_{j=1}^{n} [I - i\hat{K}\rho]^{-1}_{ij} \cdot \hat{P}_j \tag{7-9}$$

describing the amplitude of a given channel i in terms of a initial $\hat{P}$-vector preparation of channel states j (from 1 to n, being n the number of channels) scattering into a final state i through the propagator $(I - i\hat{K}\rho)^{-1}$ [125]. The $\hat{K}$-matrix is written as a sum of N poles with real bare masses m_α with $g_i^{(\alpha)}$ and $g_j^{(\alpha)}$ real coupling constants to respective channels, and non–resonant slowly–varying parts (SVPs) with a $1/s$ dependence with real coupling constants f_{ij}^{scatt} symmetric in i and j [121, 126] illustrating all possible rescattering channels j from a given initial state i

$$\hat{K}_{ij}(s) = \left(\sum_{\alpha=1}^{N} \frac{g_i^{(\alpha)} g_j^{(\alpha)}}{m_\alpha^2 - s} + f_{ij}^{\text{scatt}} \frac{m_0^2 - s_0^{\text{scatt}}}{s - s_0^{\text{scatt}}}\right) f_{A0}(s). \tag{7-10}$$

It is important to notice that the masses m_α in the pole terms correspond to the so-called bare states that are not directly the resonances from the complex poles in the physical T matrix, instead, a physical resonance can even be a mixture of bare states. The factor

$$f_{A0}(s) = \left(\frac{1\text{GeV}^2 - s_{A0}}{s - s_{A0}}\right)\left(s - \frac{1}{2} s_A m_\pi^2\right) \tag{7-11}$$

is the Adler zero term [127] responsible to suppress the false kinematic singularity when s goes below the $\pi\pi$ production threshold. The remaining parameters m_0^2, s_0^{scatt}, s_A and s_{A0} are real constants. For $\pi\pi$ systems, five channels are available: $\pi\pi$, $K\bar{K}$, 4π, $\eta\eta$, $\eta\eta'$ (above the open charm threshold) mutimeson states and all parameters were taken from a global analysis of $\pi\pi$ scattering data by Anisovich and Sarantsev [126] for five channels ($n = 5$) and five poles ($N = 5$) summarized in Table 7.2.

α	m_α (GeV/c^2)	$g_1^{(\alpha)}[\pi\pi]$	$g_2^{(\alpha)}[K\bar{K}]$	$g_3^{(\alpha)}[4\pi]$	$g_4^{(\alpha)}[\eta\eta]$	$g_5^{(\alpha)}[\eta\eta']$
1	0.65100	0.22889	-0.55377	0.0	-0.39899	-0.34639
2	1.20360	0.94128	0.55095	0.0	0.39065	0.31503
3	1.55817	0.36856	0.23888	0.55639	0.18340	0.18681
4	1.21000	0.33650	0.40907	0.85679	0.19906	-0.00984
5	1.82206	0.18171	-0.17558	-0.79658	-0.00355	0.22358
	s_0^{scatt}	f_{11}^{scatt}	f_{12}^{scatt}	f_{13}^{scatt}	f_{14}^{scatt}	f_{15}^{scatt}
	-3.92637	0.23399	0.15044	-0.20545	0.32825	0.35412
	s_0^{prod}	m_0^2	s_A	s_{A0}		
	-1.0	1.0	1.0	-0.15		

Table 7.2: $K-$Matrix parameters for the $\pi^-\pi^+$ $S-$wave [126]. Masses m_α and couplings $g_u^{(\alpha)}$ are given in GeV/c^2 while s related quantities in GeV$^2/c^4$.

The parameter $s_0^{\rm prod}$ could in principle be a free parameter in the fit. Instead, it is taken from FOCUS analysis from the $D^+ \to \pi^-\pi^+\pi^+$ decay [7] to be $s_0^{\rm prod} = -1.0^{+0.4}_{-5.5}$ GeV$^2/c^4$. This choice was made after varying this parameter systematically from -1 to -5 and verifying that the fit is relatively insensitive to the value of this parameter. The production vector, $\hat{P}$, has the same parametrisation as the $\hat{K}$ matrix with the exception of the Adler zero factor since previous analysis have shown that the consideration of this factor does not improve the description of $S-$Wave amplitudes [7,128]. The $\hat{P}$-vector is given by

$$\hat{P}_j(s) = \sum_{\alpha=1}^{N} \frac{\beta_\alpha g_j^{(\alpha)}}{m_\alpha^2 - s} + f_j^{\rm prod} \frac{m_0^2 - s_0^{\rm prod}}{s - s_0^{\rm prod}}, \tag{7-12}$$

where β_α and $f_j^{\rm prod}$ are complex production constants for poles and SVPs to be extracted by a fit to data. The mass poles m_α in the $\hat{P}$–vector must be the same as the scattering process in order for the transition amplitude to not diverge at the $\hat{P}$–vector hence vanishing at the $\hat{K}$–matrix poles. The total amplitude for the $\pi\pi$ S–Wave is given by $\mathcal{A}_1(s)$, in which $i = 1$ corresponds to $\pi^-\pi^+$, meaning that only the first row of the propagator matrix needs to be used. The SVP production amplitude, separated for each individual channel, is given by

$$\mathcal{A}_{{\rm SVP},j}(s) = \frac{m_0^2 - s_0^{\rm prod}}{s - s_0^{\rm prod}} [I - i\hat{K}\rho]^{-1}_{1j} f_j^{\rm prod}, \tag{7-13}$$

and for each production pole, summing the propagator contributions over all channels j,

$$\mathcal{A}_\alpha(s) = \sum_{j=1}^{n} [I - i\hat{K}\rho]^{-1}_{1j} \frac{\beta_\alpha g_j^{(\alpha)}}{m_\alpha^2 - s} \equiv \frac{\beta_\alpha}{m_\alpha^2 - s} \sum_{j=1}^{n} [I - i\hat{K}\rho]^{-1}_{1j} g_j^{(\alpha)}. \tag{7-14}$$

Then the S–Wave amplitude is

$$\mathcal{A}_{S-wave} = \sum_{\alpha=1}^{N} \mathcal{A}_{\alpha} + \sum_{j=1}^{n} \mathcal{A}_{SVP,j} \tag{7-15}$$

to be combined with the Isobar Model to include spin 1 and 2 resonances according to Eq.6-24.

7.2 Results

We now present the results of the $D^+ \to \pi^-\pi^+\pi^+$ Dalitz plot fits using the $K-$Matrix formalism using the Dalitz plot fit package `LAURA++` [98]. Higher spin contributions such as $f_2(1270)$, $\rho(1450)^0$, $\rho(770)^0$ and $\omega(782)$ are included via isobar model while the $S-$Wave is described using the $K-$Matrix formalism determined from a global fit to scattering data by Anisovich and Sarantsev from Table 7.2 with $s_0^{\rm prod} = -1.0{\rm GeV}^2$ from FOCUS analysis. In the $P-$ and $D-$waves, all resonant contributions have the radius parameter in the Blatt-Weisskopf barrier factor fixed to $r_{F_{D,Rp_3}} = 5.0$ GeV^{-1} and $r_{F_{R,p_1p_2}} = 1.5$ GeV^{-1} and the lineshapes used for each contribution are summarized in Table 6.2. In addition, lineshape parameters are set to fixed PDG values unless specified. The $S-$wave is accounted with: $K-$matrix model including all five poles in the $P-$vector, and three slowly varying parts.

The free parameters in the fit are the magnitudes and phases for higher spin contributions in which the $\rho(770)^0$ is chosen to be the reference with magnitude 1 and phase zero, thus, the parameters of all other components are measured relative to this one. In particular, the $\rho - \omega$ interference is included as individual contributions using a GS lineshape for the $\rho^0(770)$ and a RBW for the $\omega(782)$ contribution. Regarding the $S-$wave component, the fitted parameters are the complex production parameters β_α, in case of a pole term, and f_v^{prod} for a SVP term. The goodness of the fit is estimated by the χ^2/ndof range and the residual distribution computed using a folded Dalitz plot. The results are shown together with the s_{lo}, s_{hi}, $\pi^+\pi^-$, $\pi^+\pi^+$ projections, residual distribution across the Dalitz plot and the χ^2/ndof range. To ensure that a good minimum has been found by the fit, for each model configuration the fit runs 100 times with randomised initial coefficients making also possible the study of multiple solutions, *i.e.* more than one solution with similar FCN. The parameters that correspond to the fit with the most negative FCN within the ensemble are taken to be the final result of the fit. In some cases, the results required to be vetoed by hand in the case where they presented the most negative FCN but the parameters corresponded to 'unphysical' values (such as masses, widths, or other parameters, hitting the limit of their range, or fit fractions incoherent to expected values).

In the following results we present the set of parameters from the relevant fits and also the $\pi^+\pi^-$ $S-$wave magnitude and phase extracted from the fit with the best FCN value with its main features interpreted. At the moment, only the central values of fit fractions are given.

SVP inclusion strategy

In principle, the $S-$wave can be parametrised with 10 complex parameters, according to Tabel 7.2 but in this analysis we use it with three of the five SVP terms due to the convergence and stability of the fit result. We also tried to include more SVP terms but in all results, the convergence was lost or the solutions corresponded to unphysical scenarios, for instance unrealistic fit fractions such as components with more than 100%. The inclusion of these terms is done until convergence is lost.

Two strategies of including these terms are tested: α ordered according to Table 7.2, i.e including the first three SVP terms ($\alpha = 1, 2, 3$) or including one at a time based on the change of the FCN. According to the second strategy, the optimum order to include the SVP term corresponds to $\alpha = 1, 3, 4$. In this way we have a result with all five poles and SVP's 1,2 and 3, and the other with the same poles with SVP's 1,3 and 4.

Model KM-1

In Model KM-1 we use the strategy of including the SVP term according to the order presented in Table 7.2, α ordered. This model is composed in the non-$S-$wave part by $\rho^0(770)$ and $\rho^0(1450)$ included with a GS lineshape, $\omega(782)$ and $f_2(1270)$ as a RBW. In this model both $\rho(770)^0$ and $\omega(782)$ are included as individual contributions instead of a mixing lineshape. The $S-$wave is composed of five poles and the three SVP terms corresponding to $\alpha = 1, 2, 3$ included following the mass order. The resulting magnitudes, phases (for spin 1 and 2 contributions), production parameters (for the $S-$wave) and fit fractions are shown in Table 7.3. In Figures 7.1, we show the $\pi^+\pi^-$ and $\pi^+\pi^+$ projections as well as the projections onto the highest and lowest invariant masses squared of the two $\pi^-\pi^+$ combinations, the $s^{lo}_{\pi^-\pi^+} = s_{lo}$ and $s^{hi}_{\pi^-\pi^+} = s_{hi}$, with the fit result superimposed indicated by the blue line and the residuals distribution.

Model KM-1 is in a qualitative agreement with the data. The Swave is the major contribution as expected. The $\omega(782)$ contribution has a very low fit fraction but it is sufficient to produce the interference pattern although

it requires a better adjustment. Furthermore, a more accurate description of the interference between the $\sigma(500)$ region and $\rho^0(770)$ is needed. The high mass region presents a reasonable agreement with the data but also requires improvement while the $\pi^+\pi^+$ projection describes the data with a good quality with exception of $s_{23}(\pi^+\pi^+) < 0.2$ GeV$^2/c^4$. Starting from this solution, when more SVP terms are included no convergence is found.

This result is already much better than all of the Isobar results with a FCN=-1909696 indicating that the $K-$Matrix approach deals with the scalar sector better than the Isobar Model. From the $\pi^+\pi^-$ projection, we also observe that it describes the high $\pi^-\pi^+$ mass region more easily compared to the Isobar results.

Component	Magnitude	Phase [rad]	Fit Fraction (%)
$\rho^0(770)$	1.0 [fixed]	0.0 [fixed]	26.6
$\omega(782)$	0.063 ± 0.004	-1.61 ± 0.07	0.1
$f_2(1270)$	0.673 ± 0.006	1.52 ± 0.02	12.1
$\rho^0(1450)$	0.093 ± 0.009	2.78 ± 0.12	0.2

$S-$wave

Component	β/f_{prod} Magnitude	β/f_{prod} Phase [rad]	Fit Fraction (%)
Pole1	0.543 ± 0.030	-3.19 ± 0.05	7.9
Pole2	0.423 ± 0.035	-1.69 ± 0.09	4.8
Pole3	1.194 ± 0.036	-0.48 ± 0.02	37.9
Pole4	1.088 ± 0.044	-0.46 ± 0.03	31.5
Pole5	1.027 ± 0.034	-9.07 ± 0.04	28.0
SVP1	0.876 ± 0.020	-2.47 ± 0.04	20.4
SVP2	0.265 ± 0.051	2.35 ± 0.17	1.9
SVP3	0.248 ± 0.039	-4.74 ± 0.14	1.6
$S-$wave			61.2
χ^2/ndof (range)	[4.06 - 3.92]		
$\sum$ FF (%)	173.0		
FCN			-1909696

Table 7.3: Model KM-1: component parameters and fit fractions. Uncertainties are statistical only and fit fractions without errors.

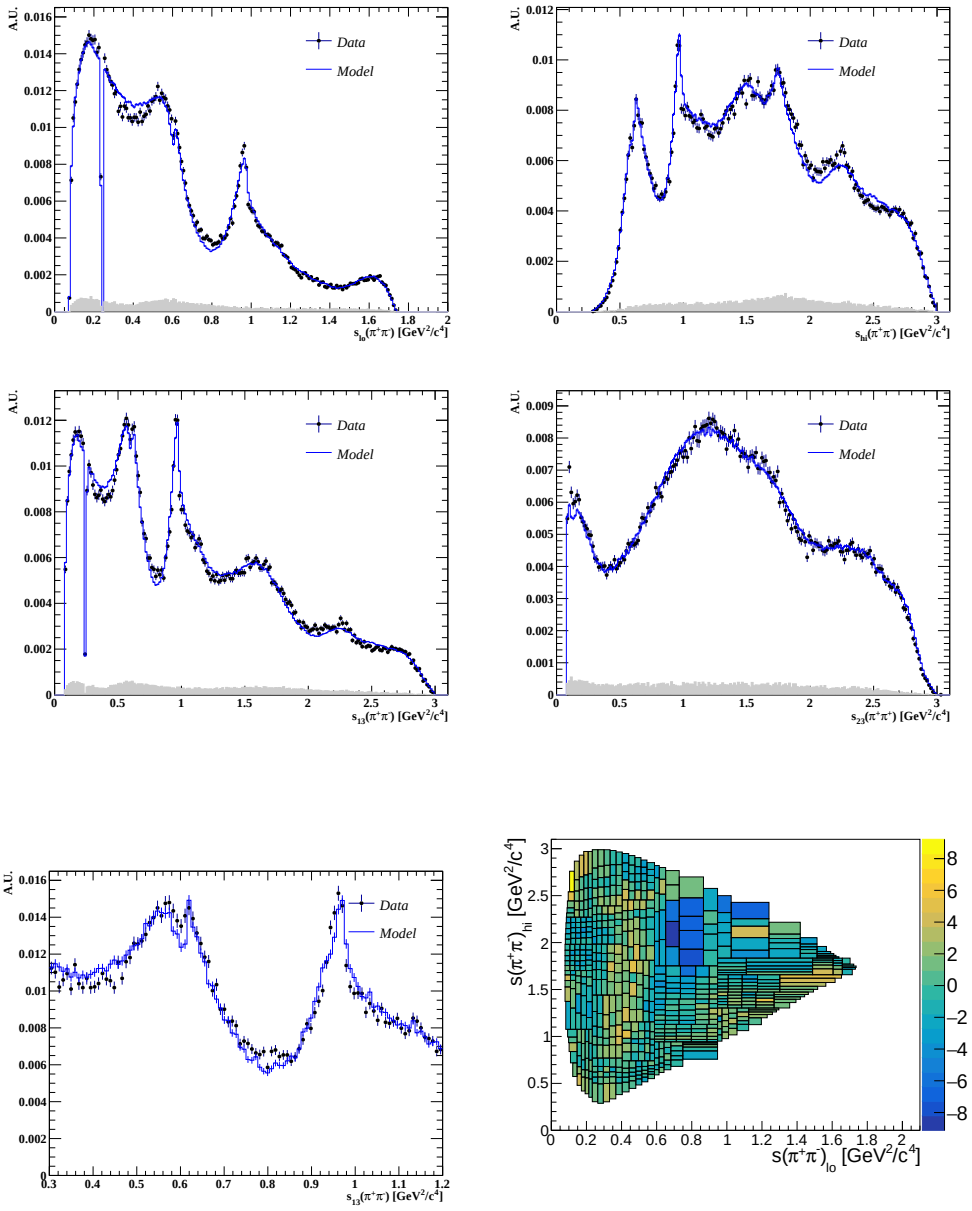

Figure 7.1: Fit results from Model KM-1: s_{lo}, s_{hi}, s_{23} and s_{12} projection. In addition, a zoomed plot in the $\rho^0(770)$ region to better visualize the $\rho - \omega$ interference and the residual plot.

Model KM-2

In Model KM-2, both $P-$ and $D-$waves consider the same contributions as the previous model but a different strategy in the definition of the $S-$wave is tested. The inclusion of the SVP terms is now based on the change in the FCN in order to investigate if there is any freedom in defining the $S-$wave component, *i.e.* define it using different SVP terms. In this strategy, the order considered for the inclusion of the SVP term is $\alpha = 1, 3, 4$. The resulting

magnitudes, phases (for spin 1 and 2 contributions), production parameters (for the $S-$wave) and fit fractions are shown in Table 7.4, the $\pi^+\pi^-$ and $\pi^+\pi^+$ projections with the fit result indicated by the blue line as well as the residuals distribution are shown in Fig. 7.2.

No significant improvement is observed, the fit fractions are similar to those in Model KM-1 in the $P-$ and $D-$waves as well as the total $S-$wave fit fraction. The FCN presents a difference in 52 units, therefore, Model KM-2 corresponds to a solution slighlty better than that of Model KM-1. The fractions within the composition of the $S-$wave differs from the solution with SVP 1,2,3 therefore, it indicates some freedom in defining the scalar sector in the sense that we can have a different set of SVP terms that produce a result with the similar features.

As in Model KM-1, after including the third SVP term, we can no longer include the fourth and fifth without losing convergence. Therefore, the final result for this strategy considers the five poles and SVP corresponding to $\alpha = 1, 3, 4$.

Component	Magnitude	Phase [rad]	Fit Fraction (%)
$\rho^0(770)$	1.0 [fixed]	0.0 [fixed]	26.7
$\omega(782)$	0.063 ± 0.004	-1.64 ± 0.07	0.1
$f_2(1270)$	0.672 ± 0.006	1.49 ± 0.02	12.1
$\rho^0(1450)$	0.076 ± 0.007	-3.73 ± 0.15	0.2

$S-$wave

Component	β/f_{prod} Magnitude	β/f_{prod} Phase [rad]	Fit Fraction (%)
Pole1	0.953 ± 0.031	-3.33 ± 0.03	24.3
Pole2	0.394 ± 0.014	-2.16 ± 0.04	4.2
Pole3	0.873 ± 0.045	-0.70 ± 0.05	20.4
Pole4	0.934 ± 0.042	-0.57 ± 0.04	23.3
Pole5	0.665 ± 0.044	-2.76 ± 0.06	11.8
SVP1	0.601 ± 0.055	-1.58 ± 0.11	9.7
SVP3	0.257 ± 0.035	6.53 ± 0.15	1.8
SVP4	0.523 ± 0.045	-0.10 ± 0.07	7.3
$S-$wave			60.6
χ^2/ndof (range)	[3.91 - 3.77]		
$\sum$ FF (%)	141.8		
NLL			-1909748

Table 7.4: Model KM-2: component parameters and fit fractions. Uncertainties are statistical only and fit fractions without errors.

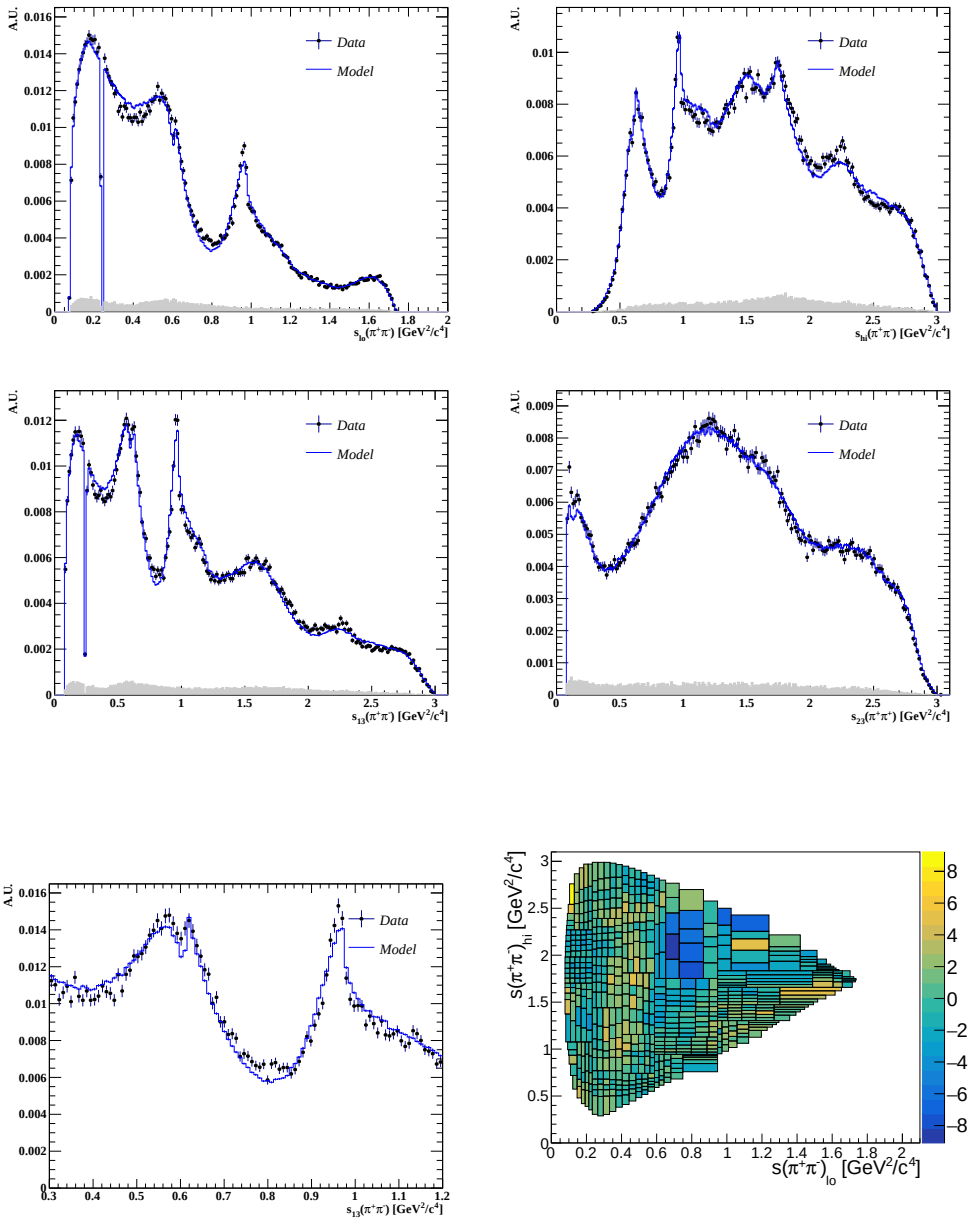

Figure 7.2: Fit results from Model KM-2: s_{lo}, s_{hi}, s_{12} and s_{23} projection. In addition, a zoomed plot in the $\rho^0(770)$ region to better visualize the $\rho - \omega$ interference and the residual plots.

In addition to this solution with around 26% of $\rho^0(770)$, another minimum was found with a ΔFCN of 31 units worse than the previous result, with the $\rho^0(770)$ contribution as approximately 13%, shown in Fig. 7.3 and Table 7.5. We will refer to this solution as Model KM-2'. Although the FCN difference indicates that both solutions are equally good to describe the data, a solution with 13% of $\rho^0(770)$ does not provide a proper physical content as it can be seen in Fig. 7.3, in which the $\pi^-\pi^+$ projection clearly illustrates that at low masses the solution provides a poorly description of the data compared to

the Fig. 7.2 with 26% of $\rho^0(770)$, thus we take KM-2 solution to be the better one, with more physical content and exclude Model KM-2'. Moreover, as the solution from Model KM-1, the $\pi^+\pi^+$ projection present similar features.

Component	Magnitude	Phase [rad]	Fit Fraction (%)
$\rho^0(770)$	1.0 [fixed]	0.0 [fixed]	13.2
$\omega(782)$	0.072 ± 0.006	-1.63 ± 0.08	0.1
$f_2(1270)$	0.996 ± 0.014	1.48 ± 0.02	13.1
$\rho^0(1450)$	0.235 ± 0.013	-3.20 ± 0.06	0.7

$S-$wave

Component	β/f_{prod} Magnitude	β/f_{prod} Phase [rad]	Fit Fraction (%)
Pole1	1.535 ± 0.047	-3.22 ± 0.03	31.2
Pole2	0.586 ± 0.025	-1.47 ± 0.04	4.5
Pole3	0.676 ± 0.066	-1.22 ± 0.11	6.0
Pole4	0.655 ± 0.057	-1.65 ± 0.11	5.7
Pole5	0.916 ± 0.080	-0.79 ± 0.07	11.1
SVP1	0.714 ± 0.093	-1.13 ± 0.12	6.7
SVP3	0.873 ± 0.064	5.30 ± 0.07	10.1
SVP4	0.782 ± 0.066	0.33 ± 0.08	8.1
$S-$wave			72.2
χ^2/ndof (range)	[4.01 - 3.87]		
$\sum$ FF (%)	110.6		
NLL			-1909717

Table 7.5: Model KM-2': component parameters and fit fractions. Uncertainties are statistical only and fit fractions without errors.

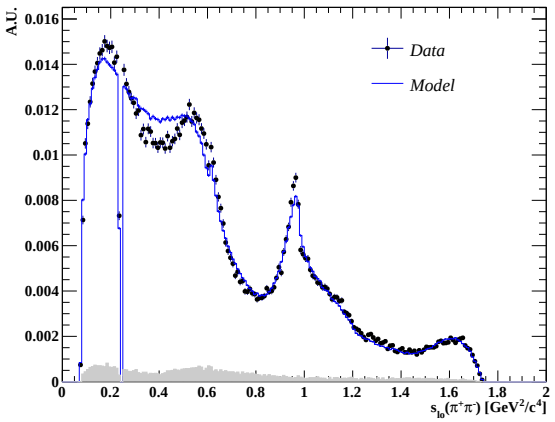

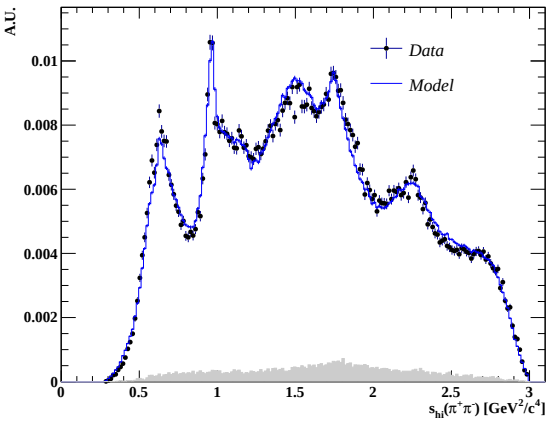

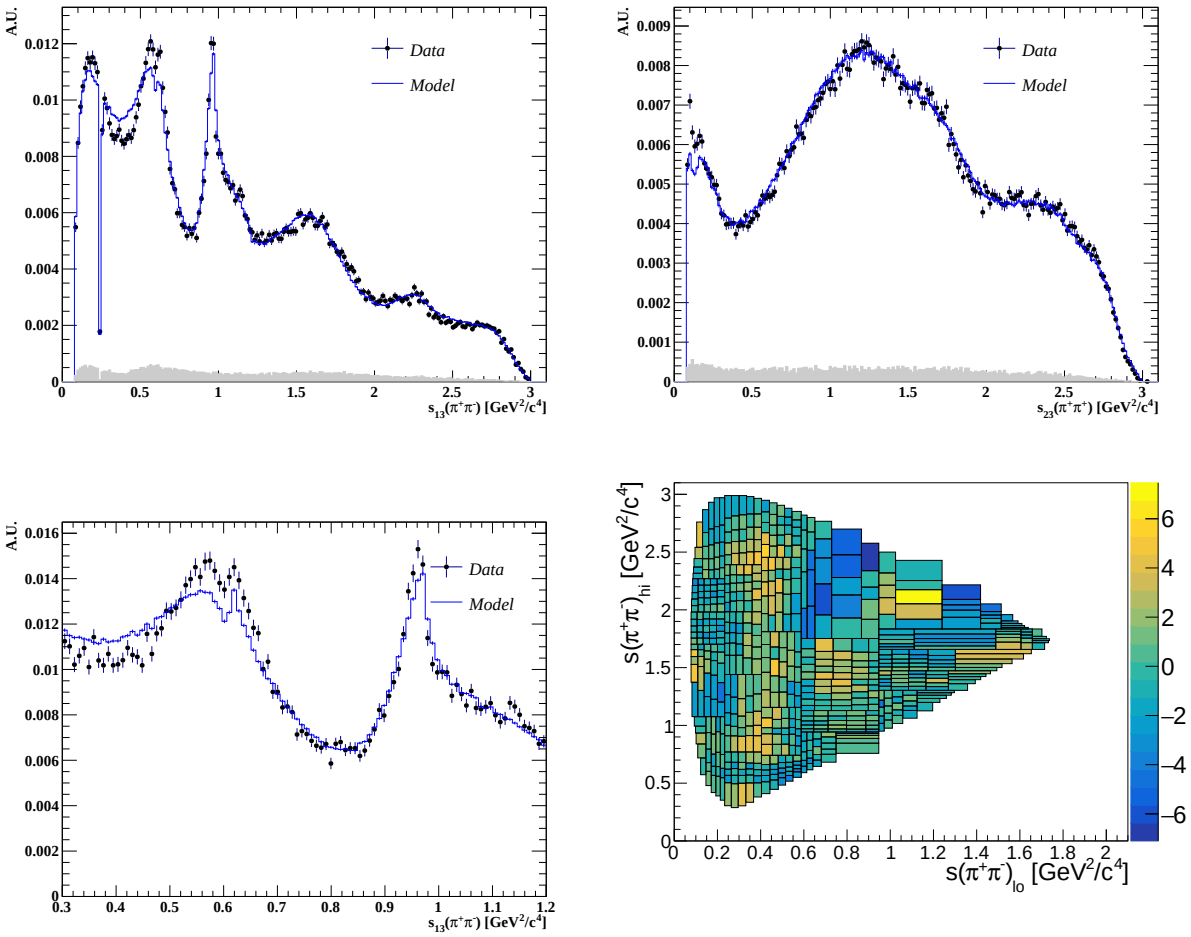

Figure 7.3: Fit results from Model KM-2': s_{lo}, s_{hi}, s_{12} and s_{23} projection. In addition, a zoomed plot in the $\rho^0(770)$ region to better visualize the $\rho - \omega$ interference and the residual plots.

Model variations

Starting from the best result, the one with the lowest FCN, Model KM-2, we made some model variations as an attempt to improve the fit quality. For contributions which present an obvious structure such as the $\rho(770)^0$, $\omega(782)$, and $f_2(1270)$, no model without these components is considered so we tried to include further contributions. In all tests, parameters such as masses and widths are fixed to PDG values, otherwise stated, and the lineshapes used are the ones in Table 6.2. In addition, since the construction of the $S-$wave component is not trivial, we also test variations in the definition of the $S-$wave. More details about some of the relevant additional tests can be found in Appendix 13.

Results for the variation of the initial model can be found in Table 7.6 with their respectives FCN values, ΔFCN compared to Model KM-2 and fit fractions for each included contribution. In general, the inclusion of each additional state improved the FCN but it was not sufficient to solve the problems presented in the baseline model. The result which presents the most significant change in the FCN is the inclusion of the spin-2 state $f_2'(1525)$, although it is mainly expected in KK systems, with 0.4%. Furthermore, the inclusion of an additional higher spin state increases the number of free parameters to 24. Even with this large number, the $K-$Matrix formalism presents difficulties in describing the whole spectrum. An inclusion of a spin-3 state is also tested. The inclusion of $\rho_3^0(1690)$ slightly improves the FCN but its corresponding fit fraction is tiny, 0.03%, therefore, it is not a significant contribution to include in the baseline model. Additionally, we also verified if there is any difference in including the $\rho - \omega$ interference using a mixing lineshape or including as individual contributions but, given the ΔFCN, both strategies promote an equally good solution.

Regarding the construction of the $S-$wave component which is not so obvious, additional tests are performed in order to explore any freedom in defining the parameters that contribute to the scalar sector. Since the last pole ($\alpha = 5$) is above the charm threshold, one test performed is to remove this pole. The results illustrate a worse description in comparison with solutions including all five poles and the fit fractions of each component within the $S-$wave represented a non physical scenario with values of fit fractions above 100%.

After removing Pole5, we also tried to include more SVP terms but the fit converged to a different minimum with a fit fraction of the $\rho^0(770)$ contribution corresponding to 10%. Therefore the result of variations with four SVP terms are all rejected due to physical reasons.

Given that no significant improvements are found from the many variations tested, Model KM-2 is chosen as the main result using the $K-$Matrix approach. Although it describe qualitatively the main structures presented in the Dalitz plot (and projections) it fails to describe important details such as the $\pi^-\pi^+$ $S-$wave at low mass and the region of the $\rho - \omega$ resonances.

Table 7.6: Model components and the changes in the log-likelihood when they are included in the baseline model.

Component	FCN	ΔFCN	Fit Fraction (%)
Baseline (SVP 1,3,4)	-1909748	—	—
Add $f_2'(1525)$	-1909992	-244	0.40
Add $\rho_3(1690)^0$	-1909764	-16	0.03
No Pole5	-1896566	+13182	—
Add SVP2 and remove Pole5	-1909260	+488	10.0 ($\rho^0(770)$)
$\rho-\omega$ mixing lineshape	-1909749	-1	—

In general, the $K-$Matrix fits provided a better description of the data compared to those from the Isobar fits. The high mass region is dealt more easily within this approach but it still requires improvement. On the other hand, the low mass region, although the fit was able to identify the components such as the $\sigma(500)$, $\rho-\omega$ and $f_0(980)$, there still remain relevant misfitted regions in all results. We observed that there seems to be some freedom in defining the SVP terms contributing to the $S-$wave given that two possible solutions were found (with very similar FCN values). Another interesting feature of this model is that the rescattering $KK \to \pi\pi$ is already included while in the Isobar approach it needs to be "manually" included as one of the contributions. Even though this approach provides a qualitative description with the data, considering the poorly described regions, it is still not sufficient to describe the whole spectrum and requires a large amount of free parameters. From Table 7.2 we could in principle have 20 parameter just for the $S-$wave and in our best result, it includes a total of 22 parameters in which 16 are used to define the $S-$wave. Considering a purely Isobar analysis, this would correspond to include eight scalar contributions in the model and even with this large amount of parameters, the fit was not able to provide a good solution. Another important topic to discuss is the physical interpretation behind this formalism, which is not as trivial as the usual coherent sum of Breit-Wigner functions, therefore, the physical interpretation behind our best $S-$wave with 16 parameters is complicated. In summary, both Isobar and $K-$Matrix are not able to described the data and other approaches should considered.

From the best result, Model KM-2, we extracted the $\pi^-\pi^+$ $S-$wave amplitude shown in Figure 7.4. The magnitude plot illustrates two clear contributions, the $f_0(980)$ peak with a phase transition in the corresponding $m_{\pi^-\pi^+}$ value and $\sigma(500)$ appearing as a more spread contribution in the magnitude and a slower phase movement, as expected from previous analysis [129] due to its large width. In addition, we observe an interesting behavior of a

sudden decrease in the transition between the $\sigma(500)$ and $f_0(980)$ also observed in CLEO's analysis [8]. Although all KM fits present some misfitted regions, the qualitative behavior of the $\pi^-\pi^+$ $S-$wave amplitude can be extracted and compared with the results from Isobar and QMIPWA.

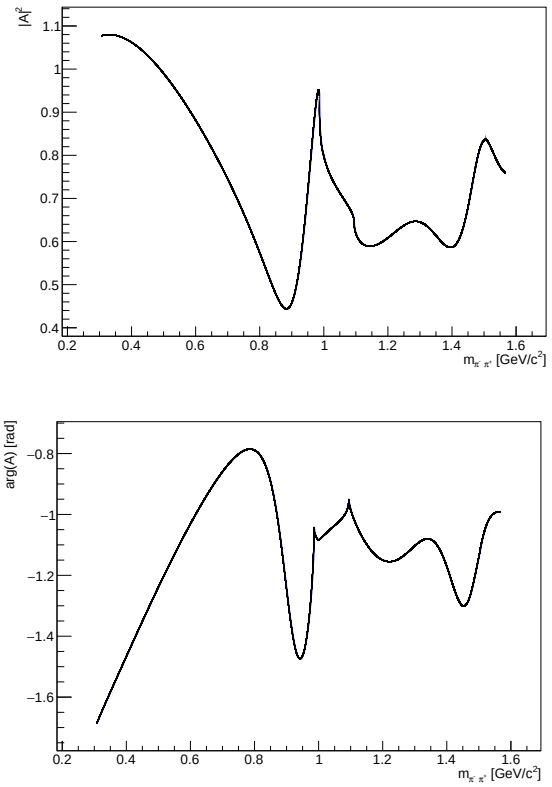

Figure 7.4: $S-$wave magnitude and phase extracted from Model KM-2.

8
Quasi Model Independent Partial Wave Analysis

Considering the relatively unknown and complicated structure of the $\pi^-\pi^+$ $S-$wave, an alternative method to extract its amplitude consists in a quasi-model-independent way in which the $S-$wave is modelled bin by bin in a non parametric form and a cubic spline is performed to obtain the $S-$wave at any point of the spectrum. Although this method provides a way to extract the $S-$wave component, the interpolation between points in a spline is a construct based on a smoothing algorithm, possibly resulting in structures that may not necessarily represent to real physical effects but it still present a mathematically viable solution. Within this approach, the $S-$wave is fitted through a model independent lineshape and as such can be used as a reliable input for new phenomenological models aiming to better understand its behaviour.

8.1
Basic Concepts

From previous discussions, the $\pi^-\pi^+$ $S-$wave is poorly described via Isobar Model, considering its deep limitations when dealing with disentangling individual contributions from broad components in the scalar sector. Given the results from both the Isobar and $K-$Matrix methods, although we have observed that the $S-$wave dominates over other contributions and it is constituted mainly of $\sigma(500)$ and f_0 states, both approaches have not provided a satisfactory description of the data. One alternative method to deal with this problem is to describe the scalar sector with a quasi Model Independent Partial Wave Analysis technique (QMIPWA), first employed by the Fermilab E791 Collaboration [130], which attempts to alleviate the model dependency of the Isobar Model. As a quasi–model–independent approach, the higher spin waves, in this case the $P-$ and $D-$Waves, are assumed to be well modelled in the Isobar approach, with relatively well separated resonances, in order to guarantee that the the QMIPWA is responsible to fit only the $S-$Wave contribution, assuming no leakage from these higher spin contributions. The

total amplitude is written as

$$\mathcal{A}\left(s_{12}, s_{13}\right) = \mathcal{A}_{S-Wave} + \sum_{spin1,spin2} c_i \mathcal{A}_i + \left(s_{12} \leftrightarrow s_{13}\right), \tag{8-1}$$

where c_i are complex coefficients. The summed terms account for higher spin waves while $\mathcal{A}_{S-Wave}$ accounts for the $S-$wave. In this approach, the $\pi^-\pi^+$ mass spectrum is divided in slices (bins) and in each bin edge k the amplitude, $\mathcal{A}^k_{S-wave}$, is modelled by two constants, a magnitude a^k and a phase ϕ^k, to be extracted from the fit

$$\mathcal{A}^k_{S-wave}\left(m_{\pi^+\pi^-}\right) = a^k e^{i\phi^k}. \tag{8-2}$$

Then, a cubic spline interpolation is used to get the $S-$wave amplitude at any point in the spectrum. Since this is a quasi-model-independent approach, any limitation of the Isobar approach to describe the higher-spin components will be tried, by the fit, to be compensated by the binned $\pi^-\pi^+$ $S-$wave, resulting in leakage of these higher waves onto the $S-$wave. Altogether, the fitted parameters are the coefficients c_i for spin 1 and 2 contributions and the coefficients assigned to each $m_{\pi^+\pi^-}$ slice. Note that the $S-$wave amplitude is bose symmetrized, so in a given k bin in $m_{12} = \sqrt{s_{12}}$ and l bin in $m_{13} = \sqrt{s_{13}}$, the amplitude is given by $\mathcal{A}^{k,l}_{S-wave}(s_{12}, s_{13}) = \mathcal{A}^k_{S-wave}(m_{12}) + \mathcal{A}^l_{S-wave}(m_{13})$.

We typically divide the spectrum in order of 48 bins, the final set of parameter has the order of 102 parameters. To perform a fit of 200 thousand events with so many free parameters, with the PDF normalization evaluated at each iteraction, a high computational cost is required. The GooFit framework for maximum likelihood fit is based on GPU with a parallel process thus it performs the fits in a reasonable amount of time. It would be not feasible, for instance, to use `Laura++`.

At first, the mass spectrum is binned creating input points for the $S-$wave. The strategy to create these input points, the binning method, is a relevant feature to consider. For each bin, an magnitude and phase values are assigned and a cubic interpolation is performed providing the value of the $S-$wave at any point of the spectrum. It is important to note some differences between `Laura++` (used in the Isobar and K-Matrix approaches) and GooFit. In `Laura++`, each amplitude is individually normalised, and magnitudes and phases are fitted. In GooFit, there is no individual normalization, and real and imaginary parts are fitted. Therefore, the FCNs obtained using `Laura++` (Isobar and $K-$Matrix results) cannot be directly compared to the FCNs obtained using GooFit (QMIPWA results) and the comparison between the

fits can by done by looking to the χ^2/ndof range.

Due to the large number of free parameters, during the minimization process several minima can be found. Since this approach relies on mathematical techniques, the physical content of the solution needs to be analyzed in the sense that given all the possible solutions, not all of them will provide a physical meaning. The expected behaviour should be illustrated in the $S-$Wave amplitude, for instance the $f_0(980)$ should appear as a peak in the amplitude with its corresponding phase transition, also the $\sigma(500)$ contribution it is expected to appear as a more spread contribution due to its large width with a slow phase movement [129]. If the $S-$wave presents a unrealistic behavior even though the fit is in a good agreement with the data, the solution is vetoed by hand since it represents only a mathematical solution without the physical content.

8.2 Binning scheme

The bin boundaries are determined in s_{12} (and s_{13}) in an ad-hoc way. Previous studies [8] illustrate the main features of the $S-$wave composed of low mass states ($\sigma(500)$ and $f_0(980)$) and high mass components such as $f_0(1370)$ and $f_0(1500)$. Initially the bins are uniformly distributed throughout the spectrum and more bins are added/removed according to the necessity of improving the description in a determined region. The fit stability also depends on the binning scheme. Bins lying in characteristic regions of the $P-$wave components, in particular $\rho^0(770)$, may inherit some of their features - a leakage from the $P-$wave to the $S-$wave. The following results include 48 bins non-uniformly distributed, for which the amplitude and phase of each bin is fitted. The $\sigma(500)$ and $f_0(980)$ regions contains more bins, in order to obtain more information of the $S-$wave in these regions, the region after 1 GeV$^2/c^4$ presents a more uniform distribution and the $\rho(770)^0$ region contains one bin centered in its mass. More bins in the $\rho(770)^0$ region promoted an instability to the fit and contamination from the $P-$wave in the $S-$wave component. The binning scheme used in the results is shown in Fig. 8.1, illustrated for s_{12} only.

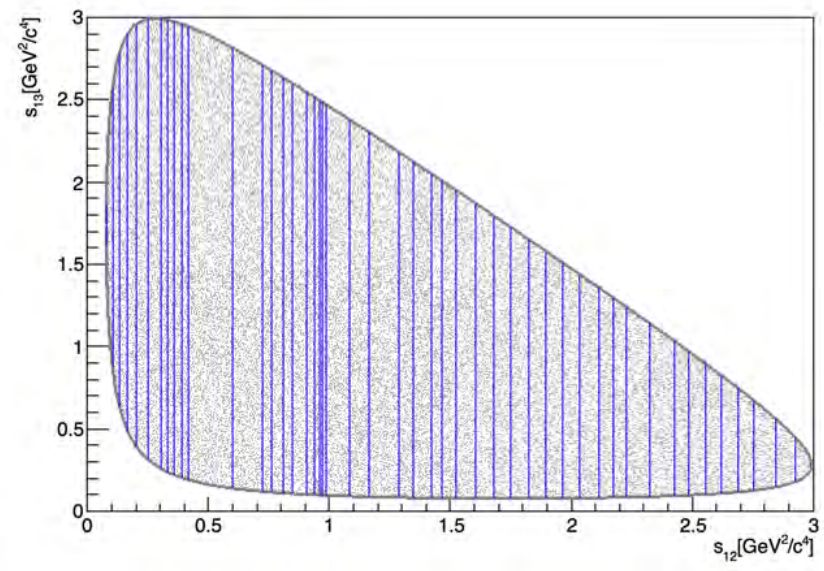

Figure 8.1: Binning scheme used for the $\pi^-\pi^+$ $S-$wave.

8.3 Results

We now present the results of the $D^+ \to \pi^-\pi^+\pi^+$ Dalitz plot fits using the QMIPWA approach. At the moment, all results don't present the fit fraction errors but in the future these will be evaluated. The baseline fit is constructed including known resonances for the $P-$ and $D-$waves included via Isobar Model while the scalar sector is parametrised with the model independent technique as described previously. Both $\rho^0(770)$ and $\omega(782)$ resonances are included as a individual contribution instead of using the mixing lineshape for the $\rho-\omega$ interference. Furthermore, in all fits the $\rho^0(770)\pi$ is chosen as reference fixing the real part equal to 1 and imaginary to zero. The other coefficients are relative to the reference one. The baseline model is composed of $\rho^0(770)$, $\omega(782)$, $\rho(1450)^0$, $f_2(1270)$ and the $S-$wave. All higher spin contributions are parametrised with a RBW lineshape with their masses and widths set fixed to PDG values, otherwise stated. The results are shown together with the s_{lo}, s_{hi}, $\pi^+\pi^+$, $\pi^+\pi^-$ projections, residual distribution across the Dalitz plot and the χ^2/ndof range.

Model PWA-1

The model is composed by $\rho^0(770)$, $\omega(782)$, $f_2(1270)$, $\rho^0(1450)$, in the non-$S-$wave part, and the $S-$wave using the QMIPWA approach with 48 points. The fit results for the QMIPWA approach with the non-$S-$wave

components are given in Table 8.1. In Figures 8.2, we plot the s_{lo}, s_{hi}, $\pi^+\pi^-$ and $\pi^+\pi^+$ projections with the fit result indicated by the red line and the data in blue, the residual distribution across the Dalitz plot and the fitted $S-$wave. The interference fractions between each component in the model are shown in Table 8.2. Overall, the projections illustrate a very good agreement with the data with a χ^2/ndof significantly better compared to that from the $K-$Matrix and Isobar results.

Resonance	**Real**	**Imaginary**	**Fit Fraction (FF)** (%)
$\rho^0(770)$	1 [fix]	0 [fix]	25.1
$\omega(782)$	-0.003 ± 0.001	-0.014 ± 0.001	0.1
$f_2(1270)$	-0.528 ± 0.029	-1.684 ± 0.023	10.9
$\rho^0(1450)$	0.283 ± 0.082	1.141 ± 0.056	1.0
$S-$Wave	48 points		60.7
$\sum$ FF			97.8
χ^2/ndof (range)	[1.86-1.55]		**FCN = 272947**

Table 8.1: Model PWA-1: component parameters and fit fractions. Uncertainties are statistical only and fit fractions without errors.

	$\omega(782)$	$\rho^0(770)$	$\rho^0(1450)$	$f_2(1270)$	$S-$wave
$\omega(782)$	0.09	-0.21	0.00	0.04	0.02
$\rho^0(770)$		25.11	2.62	-0.52	-0.52
$\rho^0(1450)$			1.03	0.23	-0.11
$f_2(1270)$				10.90	-0.44
$S-$wave					60.70

Table 8.2: Model PWA-1: Interference fractions between amplitude components for the QMIPWA approach.

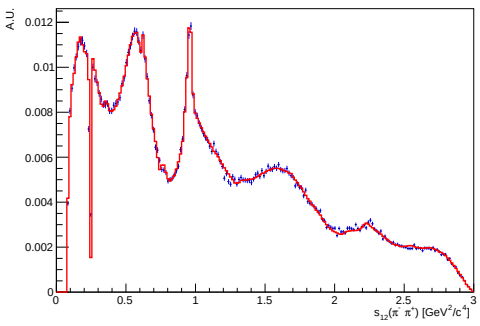

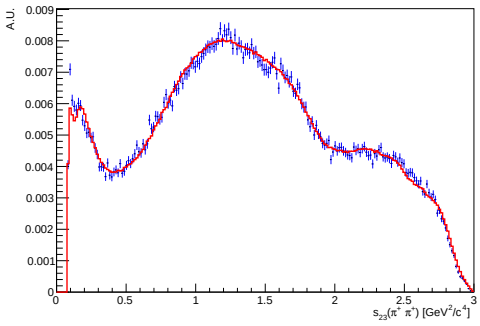

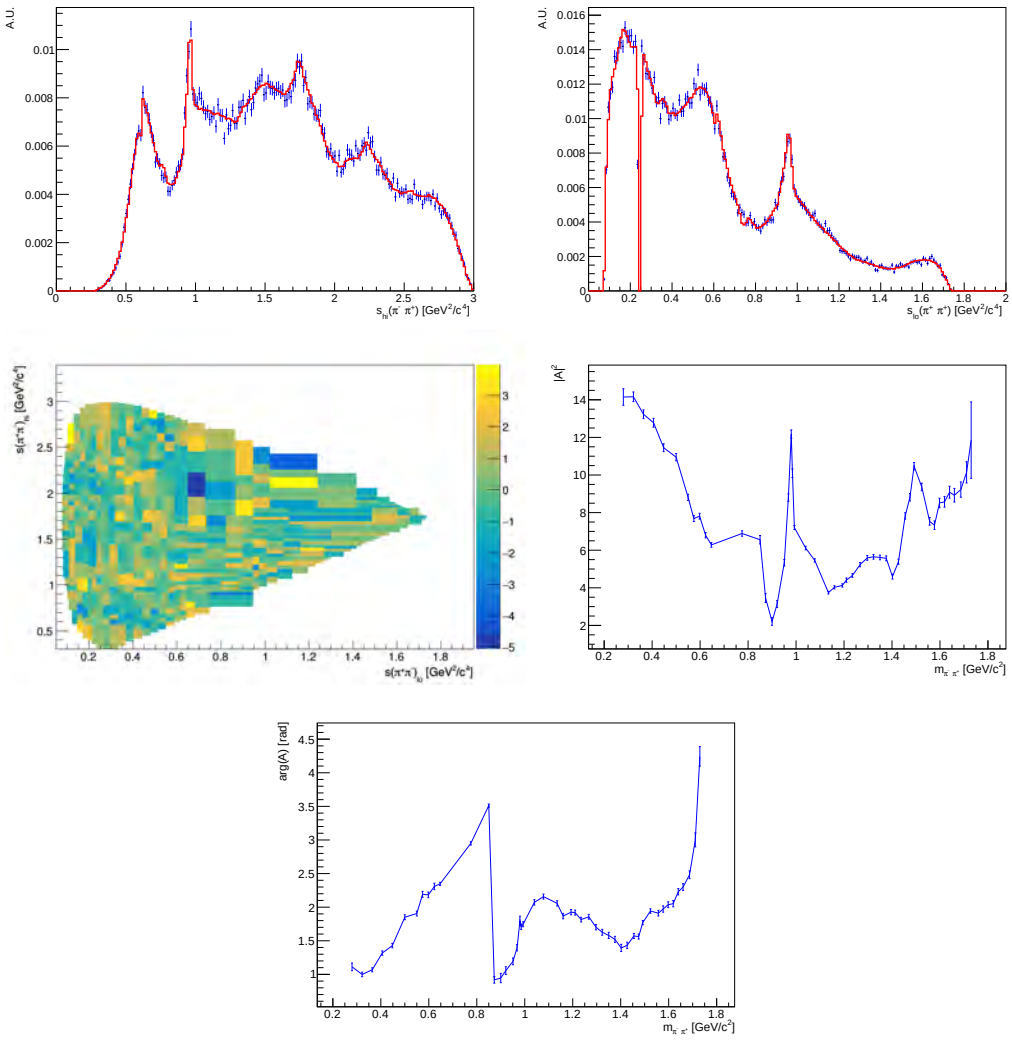

Figure 8.2: Fit results from Model PWA-1: s_{12}, s_{23}, s_{hi} and s_{lo} projections, residual distribution and fitted $S-$wave.

From the $\pi^-\pi^+$ projection, we observe that the fit quality in both high and low $\pi^-\pi^+$ mass regions shows a very good description of the data, which was not possible using other approaches. The region where the $\sigma(500)$ and $f_0(980)$ states lie are well parametrised as well as the $\rho-\omega$ mixing, in contrast with the previous results in which the low mass region presented only a qualitative solution. The $\pi^+\pi^+$ projection illustrates a good description of the data with the exception of $s_{23} < 0.2$ GeV$^2/c^4$, as observed in the previous Isobar and $K-$Matrix results. This result shows that the $S-$wave accounts for the largest fit fraction, 60% and the extracted $\pi^-\pi^+$ $S-$wave lineshape shows a consistency with the $S-$wave extracted from the $K-$Matrix approach with a clear $f_0(980)$ peak in the magnitude with its corresponding phase transition, the $\sigma(500)$ as a spread out contribution with a slower phase movement and the sudden decrease in the phase between these states. In the $S-$wave magnitude

plot, near the $\rho^0(770)$ mass region, we can observe a "bump" which may indicate a leakage of the $P-$wave to the $S-$wave. In principle, this spin 1 resonance should be well parametrised in the Isobar Model and the QMIPWA should take care just of the scalar sector. To study in more details the presence of any leakage in the $S-$wave, a variation in the number and position of the bins in this region is required.

Model PWA-2

In this model we start from the previous result and include one more spin-2 contribution, $f_2'(1525)$, which is mainly expected in the KK channel, as an attempt to improve the $\pi^+\pi^+$ low mass region. This model is composed by $\rho(770)^0$, $\omega(782)$, $f_2(1270)$, $\rho(1450)^0$, $f_2'(1525)$ and the $S-$wave with the same 48 points. The resulting real and imaginary parts (for spin 1 and 2 contributions) and fit fractions are shown in Table 8.3. In Figures 8.3, we see the s_{lo}, s_{hi}, $\pi^+\pi^-$and $\pi^+\pi^+$projections with the fit result indicated by the red line and the data in blue, the residual distribution across the Dalitz plot and the fitted $S-$wave. All masses and widths are fixed to PDG values and all lineshapes used for the non-$S-$wave components are RBW. In addition the interference fit fractions are shown in Table 8.4.

By including this spin-2 resonance, the FCN improved by 80 units as well as the χ^2/ndof with a fit fraction of 0.3% for the $f_2'(1525)$ contribution. The low mass $\pi^+\pi^+$ region presents a better fit quality however, it still requires improvement. In the $\pi^+\pi^-$ projection we still observe a very good agreement with the data as the previous result. A comparison between the $S-$waves obtained from Models PWA-1 and PWA-2 is shown in Figure 8.4 where we can observe that the general behavior is similar for both solutions but the inclusion of this spin-2 contribution promoted some changes in the details of the $S-$wave, specially in its magnitude.

Resonance	**Real**	**Imaginary**	**Fit Fraction (FF)** (%)
$\rho^0(770)$	1 [fix]	0 [fix]	24.6
$\omega(782)$	-0.002 ± 0.001	-0.014 ± 0.001	0.1
$f_2(1270)$	-0.519 ± 0.029	-1.652 ± 0.025	10.3
$\rho^0(1450)$	0.434 ± 0.086	1.032 ± 0.088	0.9
$f_2'(1525)$	0.501 ± 0.041	0.396 ± 0.063	0.3
$S-$Wave	48 points		59.1
$\sum$ FF			95.2
χ^2/ndof (range)	[1.72 - 1.43]		**FCN = 272867**

Table 8.3: Model PWA-2: component parameters and fit fractions. Uncertainties are statistical only and fit fractions without errors.

	$\omega(782)$	$\rho^0(770)$	$\rho^0(1450)$	$f_2(1270)$	$f_2'(1525)$	$S-$wave
$\omega(782)$	0.08	-0.18	0.01	0.04	0.00	0.02
$\rho^0(770)$		24.60	2.38	-0.50	0.32	0.10
$\rho^0(1450)$			0.91	0.26	0.01	0.04
$f_2(1270)$				10.28	-0.08	-0.26
$f_2'(1525)$					0.29	0.23
$S-$wave						59.05

Table 8.4: Model PWA-2: Interference fractions between amplitude components for the QMIPWA approach.

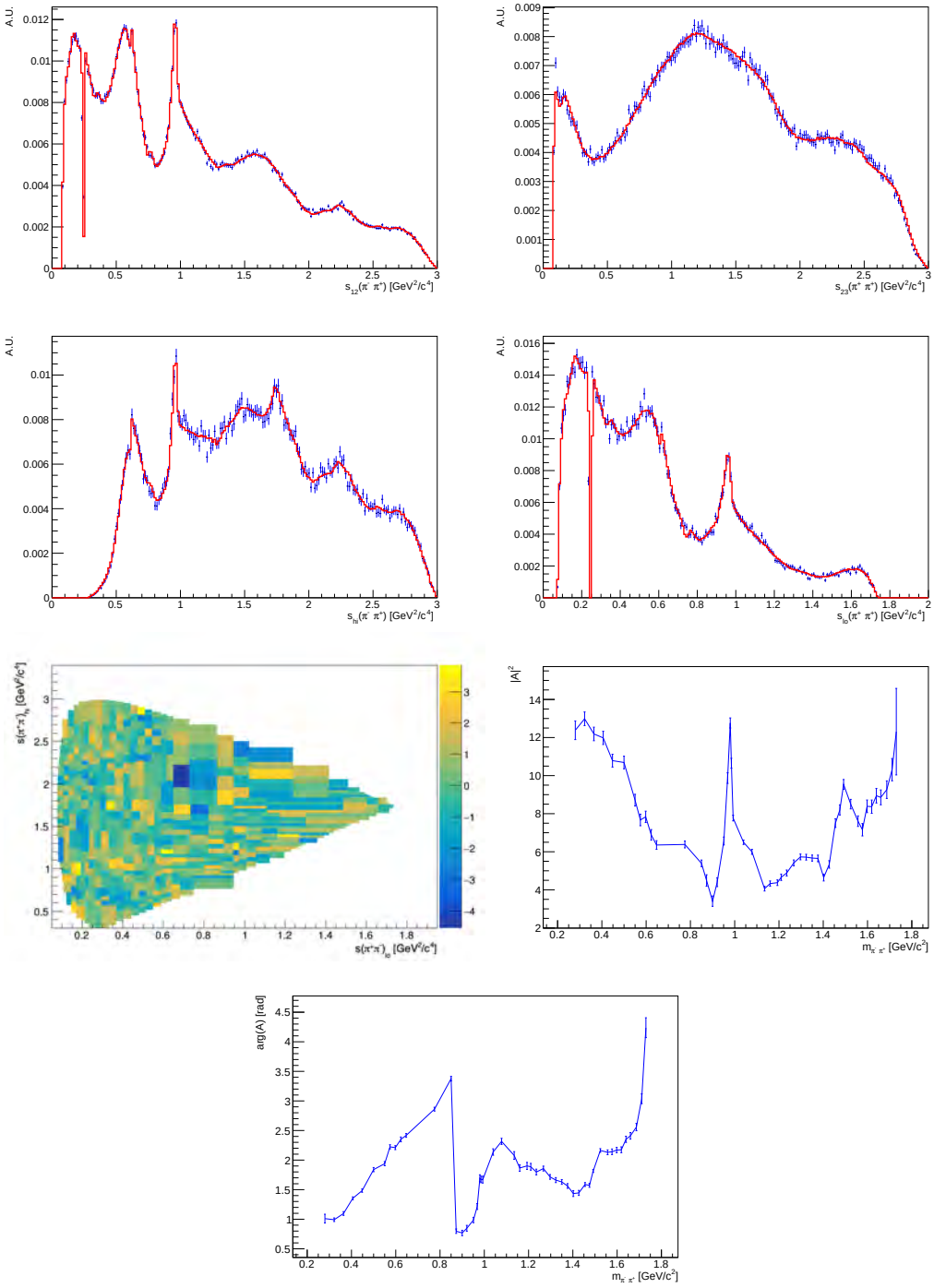

Figure 8.3: Fit results from Model PWA-2: s_{12}, s_{23}, s_{lo} and s_{hi} projections, residual distribution and fitted $S-$wave.

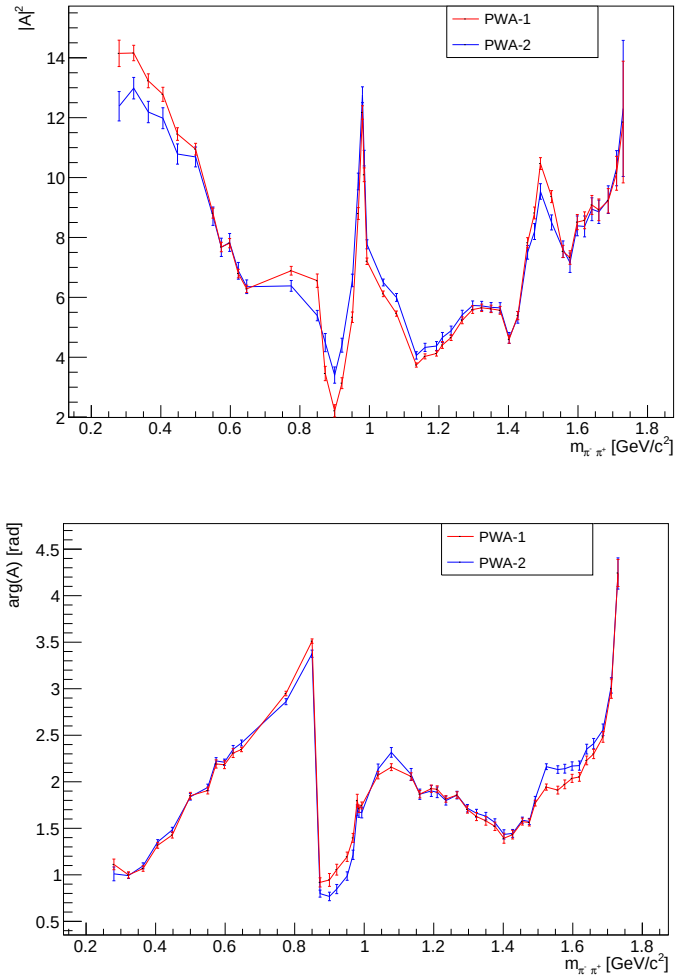

Figure 8.4: $S-$wave comparison between Models PWA-1 and PWA-2.

Interpretation

From Fig. 8.4 we observe that the general behavior of both solutions is quite similar. The differences lie on details of the $S-$wave specially in the magnitude. In both cases we observe the clear $f_0(980)$ and $\sigma(500)$ contributions with their expected characteristics as already discussed. By including the $f_2'(1525)$ as in Model PWA-2, the bump in the $\rho^0(770)$ region is reduced, and we observe some shifts in the magnitude in the $\sigma(500)$ and $f_0(980)$ regions without losing their general trends.

The suspected contamination from the spin-1 $\rho(770)^0$ may be present in the $S-$wave amplitude and phase plots for these models. Any defect in the parametrisation of the non-$S-$wave components will manifest in this way, as a leakage indicating that the QMIPWA is fitting not only the $S-$wave but also other misparametrisation of non-$S-$wave components. The reason for

this effect is the inherent freedom of fitting each $m_{\pi\pi}$ bin with a magnitude and phase. The possible sources by which this could arise are: an incomplete $S-$wave model, meaning that the $S-$wave is not well described, any interference between the $S-$ and $P-$waves that are also not well fitted, the spin-1 and 2 waves are not well modelled in the Isobar, and any misparametrisation of the background model. Although there are several possibilities, the identification of the exact source is not trivial.

Model PWA-3

In this model we use the $P-$wave amplitude from the phenomenological approach discussed in Chapter 3 instead of a $\rho - \omega$ amplitude as an attempt to better describe the mixing pattern. This model is composed by a $P-$wave included with the phenomenological form factor approach, $f_2(1270)$, $\rho^0(1450)$, both using a RBW function with masses and widths fixed, and the $S-$wave with 48 points. The reference contribution is taken to be the $f_2(1270)$ and the resulting real and imaginary parts (for spin 1 and 2 contributions) and fit fractions are shown in Table 8.5. In Figures 8.5, we plot the s_{lo}, s_{hi}, $\pi^+\pi^-$and $\pi^+\pi^+$projections with the fit result indicated by the red line, the residual distribution, χ^2/ndof range and the fitted $S-$wave. This result is preliminary and illustrates a qualitative solution. A more detailed study of this phenomenological approach, also a set of parameters corresponding to a more physical solution is required.

Resonance	**Real**	**Imaginary**	**Fit Fraction (FF)** (%)
$f_2(1270)$	1 [fix]	0 [fix]	16.6
$\rho^0(1450)$	0.063 ± 0.038	-0.695 ± 0.023	1.7
$S-$Wave	48 points		80.1
c_{P-wave}	-57.800 ± 13.416	97.309 ± 1.216	7.6
e_1^P	1 [fix]		
e_2^P (mag)	$0.002 \pm 9.800 \times 10^{-5}$		
e_2^P (phase)	$-0.003 \pm 6.486 \times 10^{-5}$		
$\sum$ FF			106.1
χ^2/ndof (range)	[1.93 - 1.61]		**FCN = 273036**

Table 8.5: Fit results from Model PWA-3.

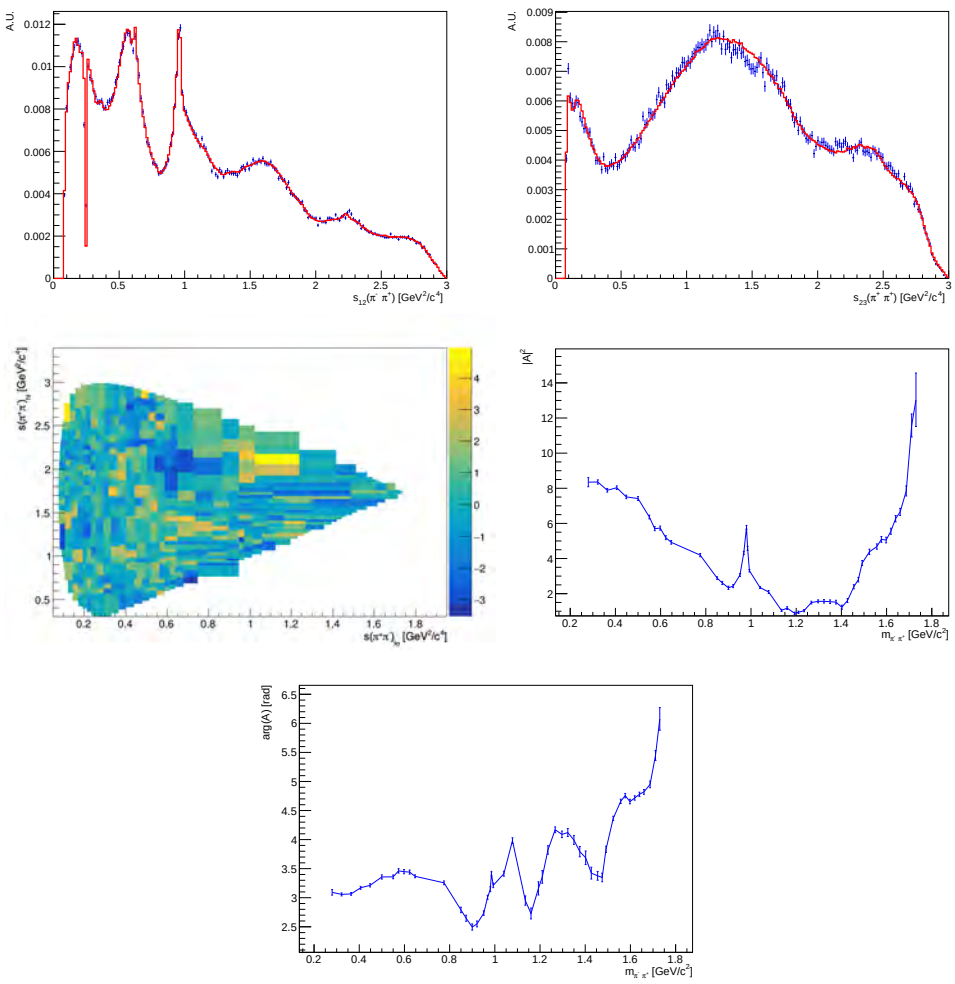

Figure 8.5: Fit results from Model PWA-3.

By including the $\rho-\omega$ contribution using the form factor approach, both the FCN and χ^2/ndof increased showing that this solution is worse than the ones obtained in the previous fits. We observe a reasonable description at high $\pi^-\pi^+$ mass illustrated in the s_{12} projection while, in the low $\pi^-\pi^+$ region we observe some regions such as the $\rho-\omega$ in which it appears to be slightly worse compared to the previous results. Furthermore, the $\pi^+\pi^+$ projection illustrates clearly that the fit result is significantly worse than Models PWA-1 and PWA-2, not only at low $\pi^+\pi^+$ mass, but also around 1.5 GeV$^2/c^4$. The set of parameters describing the $P-$wave does not promoted a realistic scenario in which the fitted e_2^P parameter indicates that this contribution could be neglected compare to the contribution multiplied by e_1^P, thus it shows that the form factor $F^{D\pi}$ does not promote any significant improvement compared to the other term.

The $f_2(1270)$ accounted for approximately 16%, a fit fraction higher than in the previous results and the $P-$wave, accounting for the $\rho-\omega$ in the

previous models, has a fit fraction that is inconsistent and nonphysical given the expected fit fraction at the order of 20%, according to the previous results obtained in this work and in previous analyses. The $S-$wave still presents the highest fit fraction but it also shows a value that is not realistic given our expectations and results obtained. For the $\pi^-\pi^+$ $S-$wave we observe that, in the magnitude plot, we still observe the main features but the overall behavior is not consistent with the previous results and in the phase plot, the solution does not seem to have any physical content, being rather a mathematical viable solution. The parameters obtained for the $P-$wave are significantly high with small uncertainties compared to $f_2(1270)$ and $\rho^0(1450)$ contributions and do not provide physical meaning, thus, more tests using this approach will be performed in order to search for a better physical solution. The fit converged but it struggled in stabilizing the parameters, therefore, this result is preliminary.

Model variations

Instead of including the $f_2'(1525)$ as in Model PWA-2, other variations are tested and the results are shown in Table 8.3, where various components are individually removed from the model and the change in log-likelihood with respect to Model PWA-1 (ΔFCN) computed. Among the possibilities, other higher spin contributions are tested such as $\rho(1700)^0$ and $\rho_3(1690)$, inclusion of a Bose Einstein correlation effect (BEC) as an attempt to improve the misparametrised $\pi^+\pi^+$ low mass region and variations on the $\rho^0(770)$ lineshape. In the $S-$wave, the inclusion of more bins is also tested. More details about some of the relevant additional tests can be found in Appendix 13.

Regarding studies of the $\rho^0(770)$, the use of a Breit-Wigner lineshape instead of a Gounaris-Sakurai, and also the inclusion of the interference pattern with a mixing lineshape did not promote any relevant difference in the FCN. Considering the large fit fraction of this component, a fit with both mass and width free configures an interesting laboratory to study its lineshape parameters, and the results illustrate that both fitted mass and width increase compared to PDG values, $m_{\rho^0(770)} = 778.7 \pm 1.3$ MeV/c^2 and $\Gamma_{\rho^0(770)} = 151.9 \pm 2.3$ MeV/c^2, with a negligible difference in the FCN. However the extracted $S-$wave amplitude lost the stability from Model PWA-1 result in the sense that the phase behavior of this component did not correspond to the solution obtained in the previous tests, thus we exclude this solution. The FCN reached a similar value compared to Model PWA-1 even though we included two more parameters in the model and two bins in the $S-$wave phase

lost stability from the previous solution indicating that this solution is not reliable.

Considering the inclusion of the $\rho(1700)$ contribution, the FCN improved resulting in a χ^2/ndof range of [1.74 - 1.45] but it was not sufficient to solve the low $\pi^+\pi^+$ mass region. A second attempt to tackle this problem is to include a BEC contribution as an additional term in the total amplitude due to the presence of two identical final state particles with equal charge. This effect has been intensively studied [131, 132] in which the amplitude can be written as

$$\mathcal{A}_{BEC}(Q) = (1 + \lambda e^{(-rQ)^\alpha})(1 + \delta Q), \tag{8-3}$$

where r is a parameter related with the source spacial dimension, λ is the coherence parameter and $\alpha = 1$ for an exponential or $\alpha = 2$ for a gaussian function but according to CMS analysis [133], an exponential function provides a better fit. By including this component, total amplitude is now given by $\mathcal{A} = \mathcal{A}_{S-Wave} + \sum_{spin1,spin2} c_i\mathcal{A}_i + c_{\text{BEC}}\mathcal{A}_{\text{BEC}}$ where in Eq. 8-3, the constant term, "1", accounts as a non resonant contribution and will not be included, the λ parameter is absorbed by c_{BEC} such that the BEC amplitudes can be simplified into a decreasing exponential function $\mathcal{A}_{BEC} = e^{-Qr}$ where $Q = \sqrt{s_{23} - 4m_\pi^2}$ and r corresponds to the slope of this function set as fixed in the fit ($r = 1$). We included it in Model PWA-1 and the solution converged to a better FCN with χ^2/ndof range of [1.69 - 1.41]. The $\pi^+\pi^+$ projection improved significantly in this region. However, since both BEC and S-wave don't include any angular information and barrier factors, they compete and the result for this model compromised the fitted S-wave, which decreased to an unphysical fit fraction of around 40% while the BEC accounted as around 38%. In fact, the $S-$wave itself, given its freedom, should be enough to incorporate such an effect, if enough bins are allocated. This solution does not qualify as a good physical solution, even though the fit quality seems to be very good. Therefore, this solution comprises as a mathematical solution and it was excluded.

Component	FCN	ΔFCN	Fit Fraction (%)
Baseline	272947	—	
Add $\rho(1700)^0$	272898	-49	1.3
Add BEC	272833	-114	38.1
$\rho^0(770)$ GS mass and width free	272944	-3	25.1

Table 8.6: Model components and the changes in the log-likelihood when they are included in the baseline model.

9
Discussions and perspectives

9.1
Discussions

This work is dedicated to the analysis of the Cabibbo-suppressed decay $D^+ \to \pi^-\pi^+\pi^+$ using about 200 thousand events from the LHCb experiment. In the analysis three phenomenological approaches for the decay amplitude are used: Isobar model, $K-$matrix formalism and QMIPWA. At first, for the most traditional Isobar model, we started with an attempt to reproduce the results from E791 analysis [6]. The fit Model I-1 showed a very poor quality indicating that the model used in this analysis is not sufficient to describe the data collected by the LHCb experiment. Then, after extending the Isobar Model to include different states, the best model (Model I-2) included $\rho(770)^0$, $\omega(782)$, $f_2(1270)$, $f_0(980)$, $f_0(1500)$, $f_0(1370)$, $\rho(1450)^0$ and $f_0(1710)$. The scalar contributions are found to dominate the decay.

Although the final Isobar Model is composed by many resonant states, the fit still presents significant disagreements with the data. The high $\pi^-\pi^+$ mass region is better parametrised with the inclusion of the $f_0(1710)$, however, the low mass region illustrated a very low quality in describing the $\rho - \omega$ mixing, $\sigma(500)$ and $f_0(980)$ regions. Given the tight phase space and the spread behavior of the $f_0(1710)$, the inclusion of this state as an attempt to improve the high mass region in the $\pi^+\pi^-$ projection also interfered the low mass region, thus the cost of improving one region affected the others by worsening the fit quality significantly. The interference pattern in the $\rho(770)^0$ region is adjusted with the inclusion of the $\omega(782)$ but still requires improvement. Given the poor descriptions obtained from isobar results, we find this scenario as a strong motivation for the use other phenomenological parametrisations to describe the $D^+ \to \pi^-\pi^+\pi^+$ decay.

As a first alternative to parametrise the $\pi^-\pi^+$ $S-$wave component, the $K-$matrix approach is used [121]. The model is composed of $\rho(770)^0$, $\omega(782)$, $f_2(1270)$, $\rho(1450)^0$ and the $S-$wave consisted of five poles and three SVP terms. This formalism, using input from a global $\pi\pi$ scattering data [126] and provided a significant improvement in the high $\pi^-\pi^+$ mass region compared

to that from Isobar Model results. Nevertheless, the low $\pi^-\pi^+$ mass region still presents significant issues in describing the known contributions and interferences illustrating only an agreement on a qualitative level. From the two strategies of including SVP terms - based on the change of the FCN and in the mass order as provided in the parameter table - both solutions presented a similar fit quality given that the small difference in their ΔFCN indicating some freedom in defining the scalar sector. Compared to the Isobar fits, the FCNs of all tests performed with the $K-$matrix formalism were significantly better indicating that this model provides a better parametrisation of the data although it also illustrates difficulties in dealing with the low mass region. Moreover, while the rescattering contribution needs to be included manually in the isobar model, it is already considered in the $K-$matrix formalism given that both $\pi\pi$ and KK channels are included. As in Model I-2, the $\pi^+\pi^+$ projection presents a very good agreement with the data with the exception of the region $s_{23}(\pi^+\pi^+) < 0.2$ GeV$^2/c^4$.

The $S-$wave again appears as the major contribution with around 60%. The fraction of the $\rho(770)^0$ contribution appears with around 27% and the $f_2(1270)$ with approximately 12% and $\rho^0(1450)$ with 0.2%. Although the $\omega(782)$ fit fraction was 0.1%, it is sufficient to create the distortion in the lineshape necessary to reproduce qualitatively the mixing pattern. Therefore, the $K-$Matrix formalism represents better the data given the lower FCN and χ^2/ndof values, but the number of free parameters describing the $S-$wave is larger than that of the Isobar Model, so it relies on more degrees of freedom to achieve a better parametrisation and it still presents difficulties in providing a good description of the data, thus, other phenomenological approaches should pursued. Other relevant topic within this model is the complicated physical interpretation behind the definition of the $S-$wave in which we use 16 parameters to describe the scalar sector but the interpretation is not as trivial as the usual coherent sum from the Isobar model.

The second alternative to parametrise the scalar sector consisted in a quasi model independent approach where the $S-$wave can be modelled bin by bin in a non parametric form providing a way to extract $\pi^-\pi^+$ $S-$wave which could serve as a reliable input for new phenomenological models. The use of the QMIPWA is particularly interesting since it is being performed in this channel for the first time and, with the large amount of data collected by the LHCb experiment, these results provide a more accurate description of the $\pi^+\pi^-$ $S-$wave amplitude. In this approach, both $P-$ and $D-$ waves are included via isobar model while the scalar sector is parametrised with a QMIPWA. The model is composed of $\rho(770)^0$, $\omega(782)$, $f_2(1270)$, $\rho(1450)^0$

and the $S-$wave parametrised through 48 points non-uniformly distributed in $m(\pi^-\pi^+)$. From the results, we observed that the fit quality increased significantly compared to both Isobar and $K-$matrix approaches. The high mass region presents a very good agreement with the data as well as the low mass region, not possible with the other approaches, with the exception of the low $\pi^+\pi^+$ mass region that could not be well described in all three models. The lowest FCN was achieved by including the $f_2'(1525)$ in the model.

One important feature of this approach is the binning method which is very sensitive. Not only the number of bins is a relevant feature but also their positions in the sense that slightly shifts in some bins may lead to instabilities in the fit. The strategy behind the binning method was to distribute the bins uniformly throughout the $m_{\pi^-\pi^+}$ spectrum and add and/or remove bins when required. In the $\rho^0(770)$ region we verified that if there are too many points, a leakage is observed by the fact that the QMIPWA tries to fit this region even though it was not supposed to. The contamination of the $P-$wave onto the $S-$wave appears as a peak in the $S-$wave magnitude in the region of the $\rho^0(770)$ contribution. To avoid the leakage, one could carefully study the best position for each bin in this region promoting a compromise between reducing the leakage as possible without losing to much information of the $S-$wave in this region. As in the $S-$wave extracted from the Isobar and $K-$matrix models, the $f_0(980)$ appears as a significant peak in the magnitude plot with its corresponding phase transition in the same mass region. The $\sigma(500)$ appears as a more spread contribution, showing a phase movement slower than that of the $f_0(980)$. The other scalar contributions are not as trivial to identify as these ones, due to their overlap and large widths.

Additionally, a phenomenological model based on a effective weak hamiltonian within a naive factorization approach and form factors [42] was used as an alternative for the $P-$wave parametrisation but a more detailed study is still needed to obtain a result for which the set of parameters constitutes a more realistic scenario.

In summary, the QMIPWA provided the best fit result among the three approaches given its best χ^2/ndof range. The extracted $\pi^-\pi^+$ $S-$wave behavior presents features in both magnitude and phase that provide an understanding of the $S-$wave and the result obtained can be used as input for phenomenological models aiming to provide a better description of the scalar sector.

9.2 Model discussion and $S-$wave comparison

This section contains the discussion and comparisons between the Isobar, $K-$matrix, and QMIPWA approaches modelling the $\pi^-\pi^+$ $S-$wave. The qualitative agreement between the models is verified by observing important features such as the fit fractions of the contributions and the general behavior of the extracted $\pi^+\pi^-$ $S-$waves. To perform this comparison, the best Isobar, Model I-2, $K-$Matrix, Model KM-2, and QMIPWA, Model PWA-1, results. In these tree models, the same contributions in spin 1 and 2 waves are used: $\rho(770)^0$, $f_2(1270)$, $\rho(1450)^0$ and $\omega(782)$, plus the $S-$wave contribution, which the parametrisation is different for each approach. Table 9.1 summarizes the results from the models to be compared.

Model	Contribution	Fit Fraction (%)
Isobar (Model I-2)	$\rho - \omega$	22.7
	$f_2(1270)$	10.7
	$\rho(1450)^0$	1.1
Isobar $S-$wave	$\sigma(500)$,$f_0(980)$,$f_0(1500)$, $f_0(1370)$,$f_0(1710)$	37.7
$K-$Matrix (Model KM-2)	$\rho(770)^0$	26.7
	$\omega(782)$	0.1
	$f_2(1270)$	12.1
	$\rho(1450)^0$	0.2
$K-$Matrix $S-$wave	—	60.6
QMIPWA (Model PWA-1)	$\rho(770)^0$	25.1
	$\omega(782)$	0.1
	$f_2(1270)$	10.9
	$\rho(1450)^0$	1.0
QMIPWA $S-$wave	—	60.7

Table 9.1: Fit fractions for the various components included in each baseline model, Model I-2, KM-2 and PWA-1. Fit fraction errors still need to be implemented. For the Isobar result, the $S-$wave fit fraction is the sum of the fit fractions of the scalar components included in the model.

For the Isobar result, the composition of the $S-$wave includes five scalar states summed coherently while in the $K-$Matrix model, it consists of all five production poles, and the three production slowly-varying parts, corresponding to the index $\alpha = 1, 3, 4$. In the QMIPWA approach, the $S-$wave is constructed with 48 points non-uniformly distributed fitted by two real parameters for each

bin. As discussed previously, no reliable fit with the Isobar model has been found given the limitations within this approach in dealing with a large number of broad overlapping states, the unitarity violation problem. For the non-$S-$wave components the obtained fit fractions are in a reasonable agreement between the Isobar, $K-$Matrix and QMIPWA approaches. In all results the $\rho^0(770)$ has a fraction of the order of 22 to 26%, the $\omega(782)$ of 0.1% and the $f_2(1270)$ around 10 to 12%. The main difference lies in the $\rho^0(1450)$ which appears around 1.0% in the QMIPWA and Isobar results in contrast with 0.2% in the $K-$Matrix approach. Regarding the $S-$wave component, a fit fraction of around 60% is obtained in both $K-$Matrix and QMIPWA solutions, also in qualitative agreement with the results from previous analyses [7, 8] however in the Isobar Model the total $S-$wave fit fraction presented a significant lower value. Considering the poorly fitted $\pi^+\pi^-$ and $\pi^+\pi^+$ projections within this approach, we expect that even for our best Isobar result, the fit fraction of this component as well as the extracted magnitude and phase of the $\pi^+\pi^-$ $S-$wave don't present a reasonable description of the true $S-$wave behavior but we can still look for main features and compare with results from the other approaches.

All results from the $K-$Matrix approach are worse than the results from QMIPWA but significantly better compared to Isobar results, thus we expect the $K-$Matrix $S-$wave to be more accurate than the $S-$wave from the Isobar Model but the most precise description is obtained from the QMIPWA result. Although the fit results of these two approaches present significant issues, the main features of the $S-$wave are clear making this comparison possible with the $S-$wave from the QMIPWA and also from other collaborations [8]. For both Isobar and $K-$Matrix, we used `Laura++` while the QMIPWA performed in `GooFit`. As discussed, since we cannot look for the FCN values of these different fitting packages, the comparison is through χ^2/ndof and for the $S-$wave, the agreement is observed in the general form of the magnitude and phase of the $S-$wave regardless the scales of the plots.

$\pi^-\pi^+$ $S-$wave comparison

From Figs. 9.1 one can see that the general trends of the shapes for the amplitude and phase for the three approaches are similar, however the QMIPWA presents the most accurate description since it has the best χ^2/ndof. From previous results [6, 8], the $\sigma(500)$ contribution accounts as the largest fraction in the scalar sector, therefore, a significant $\sigma(500)$ is expected to appear in the $S-$wave plots. Given its large width, it's presented as a broad contribution in the magnitude plot with a corresponding slow phase movement

[129] in contrast with the $f_0(980)$, the second highest fit fraction in the scalar sector, that appears as a sharp peak, thus an abrupt phase movement in the correspondent region. In both results these features are explicit while the other scalar contributions expected to contribute such as $f_0(1500)$ and $f_0(1370)$ don't appear as clear. Another interesting characteristic in the $S-$wave phase plot is the movement between the $\sigma(500)$ and $f_0(980)$ for which the phase suddenly decreases, also observed in CLEO's analysis [8], which could be related to the superposition of the $f_0(980)$ and the opening KK channel creating a discontinuity. Usually discontinuities in the phase are signatures of resonances but in the case of the $f_0(980)$ it is enhanced by the opening KK channel. Another possible reason for such behavior is any interference between the low mass $\pi^-\pi^+$ $S-$wave with the $\rho^0(770)$.

Regarding the number of free parameters, the QMIPWA approach deals with a large number since each bin includes two real parameters but, the more number of bins included, more information about the $S-$wave can be extracted. Therefore, the main strategy is to include as much bins as possible until the fit loses stability or we start having leakages from higher spin waves in the $S-$wave. For regions where we expect clear contributions, such as the $\sigma(500)$ and $f_0(980)$, we want more information about the $S-$wave, thus the we have a higher number of bins. On the other hand, in the $K-$Matrix formalism, the $S-$wave could be in principle described with 20 parameters however we used 16 due to convergence of the fit. By writing the $S-$wave with 5 poles and 3 SVP terms, it would correspond to include 8 scalar resonances in a purely Isobar analysis but, instead of a usual coherent sum, the physical interpretation behind the $K-$Matrix formalism is not so trivial.

In top Figures 9.1, we plot the extracted $S-$wave amplitude from the Isobar fit, Model I-2, including five scalar components, the middle plots illustrate $K-$Matrix $S-$wave amplitude including with all five poles and three SVP terms ($\alpha = 1, 3, 4$), Model KM-2. The main features are present in these two approaches but the fit quality of both results is low, therefore the $S-$wave contains less details and also interferences with non-$S-$wave components are poorly parametrised. In the bottom plots we show the $S-$wave amplitude extracted from the QMIPWA fit, Model PWA-1. The three solutions share the main features but the QMIPWA descriptions is much more accurate.

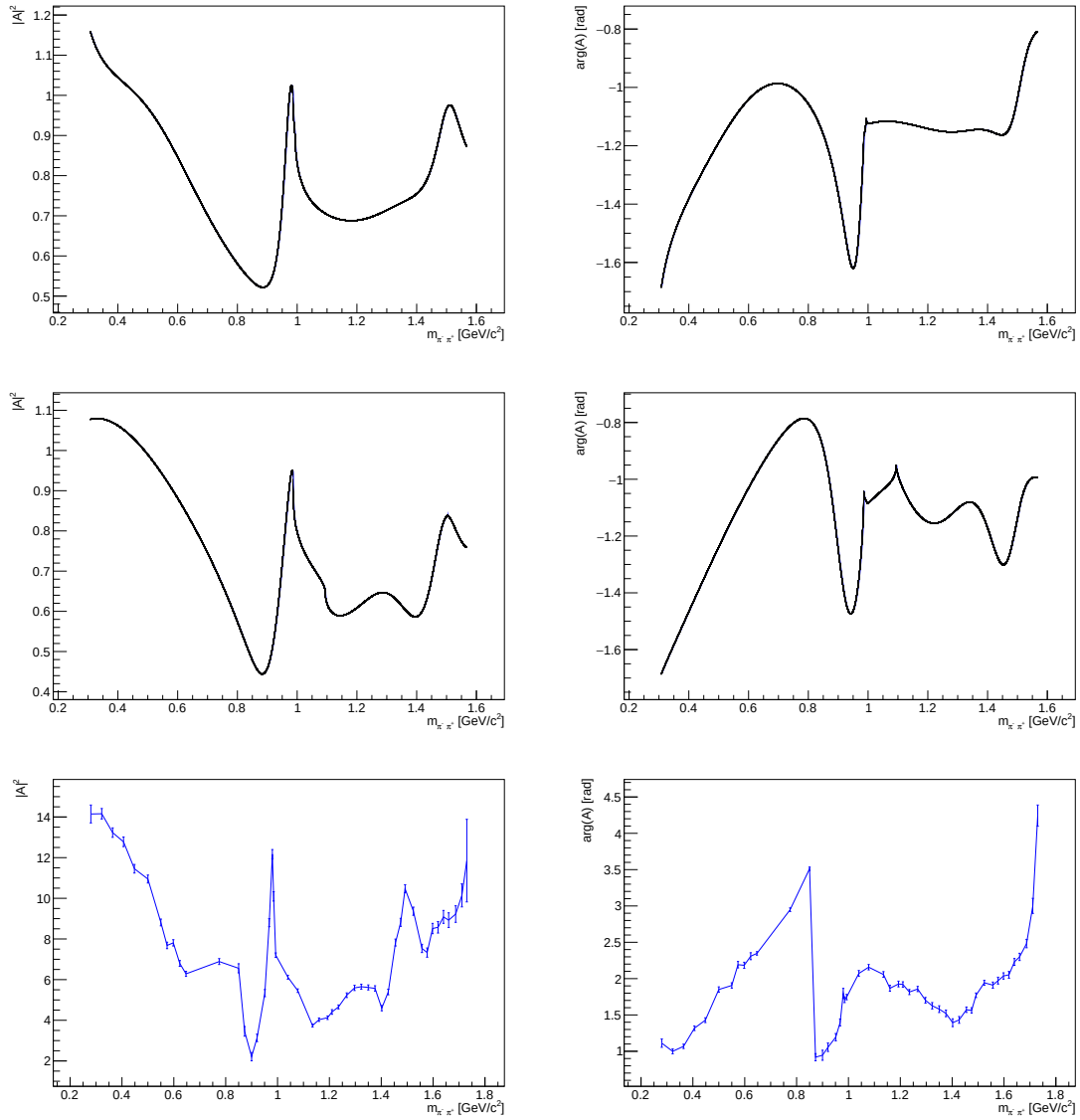

Figure 9.1: $S-$wave extracted from the best Isobar (top), $K-$Matrix (middle) and QMIPWA (bottom) model respectively.

9.3 Discussion on possible systematic uncertainties

Although the systematic uncertainties have not been evaluated yet for this analysis, we discuss here the sources to be considered from now on. They are divided into two categories: the ones that come from the impact on the fit results from experimental aspects such as efficiency correction, background parameterisation, selection, finite detector resolution; and the second, referred to as model systematics, corresponds to the uncertainties in resonance lineshape parameters such as masses, widths and couplings.

From the experimental side, the main sources of systematic uncertainties are the efficiency correction and the background parameterisation which are common for all Isobar, $K-$Matrix and QMIPWA fits. Let's first discuss the systematic uncertainties from the efficiency. The efficiency map is obtained from a series of steps and the outcome of each stage is a 2D histogram. The final efficiency accounts both selection, determined from simulated events with no PID applied, $\epsilon^{\text{selection}}$, and PID, ϵ^{PID}, determined from the PIDCalib tables where weights – the per track efficiency – are applied to the simulated events that passed the MVA selection. Therefore, final efficiency map is obtained using the projections from the simulated sample including the same stages for the selection, $\epsilon^{\text{selection}}$, weighted by the PID, ϵ^{PID}, which is fitted using a 2D cubic spline yielding a smoothed, high-resolution histogram used in the analysis. The possible sources of systematic uncertainty associated to the efficiency map are: the finite size of the simulated sample; the uncertainty on the PID efficiency; and the binning scheme of the efficiency map before the smoothing procedure.

Uncertainties related to the PID efficiency are due to the size of the calibration samples. The PID efficiency table is a histogram which contains the average efficiency in the corresponding bin and its uncertainty. The PID efficiency is given as function of the particle momentum, pseudo-rapidity and track multiplicity of the event and to evaluate the systematics, one could generate a set of histograms with PID efficiency tables with the values of efficiencies and correction factors fluctuating according to a Gaussian centred in the nominal value and width equal to the uncertainty. Then the efficiency maps are produced, smoothed by the 2D cubic spline and used to fit the data. For each fit parameter, the r.m.s. of the distribution of fitted values is assigned as systematic uncertainty. The PID calibration samples are large and the uncertainty on the PID efficiency is expected to be small, thus the resulting systematic uncertainties due to the PID efficiency are also expected to be very small compared to those due to other sources.

The finite size of the simulated sample is also a source of systematic uncertainty. One could generate a set of histograms from the selection efficiency histogram, $\epsilon^{\text{selection}}$, in which the bin content is varied according to its uncertainty .For each of histograms, an efficiency map can be produced and used to fit the data. For each parameter, the r.m.s. of the distribution of fitted values can be assigned as a systematic uncertainty.

To account for biases from the efficiency correction, one should vary the binning schemes of the 2D smoothed histogram of simulated candidates, weighted according to efficiency numbers extracted from tables provided by the PIDCalib [92] and observe the difference in the fit result given the binning

scheme variation.

The background corresponds to approximately 5% of the sample within the mass interval. The uncertainties related to the background come from both level and shape. For the first, the background level can be varied according to the uncertainty from the mass plot fit. The data can be fitted changing the background level by $\pm 1\sigma$ observing the direct shift of the central values of the parameters. For the second, the background model is built from both mass sidebands of the $D^+ \to \pi^-\pi^+\pi^+$ signal and, as we observed, the background structure is different between the left and right $\pi\pi\pi$ wings. In principle we assume it to be 50% of each wing but the exact proportion is unknown and variations can be also included as a source of systematics. In addition, the background can be assumed to be one or the other and the impact on the fit parameters evaluated.

Systematic uncertainties assigned to biases in the fit algorithm could be included. To evaluate it, ensembles large toy samples are required. For the three approaches: Isobar, $K-$Matrix and QMIPWA, the toys can be generated using with the fitted values of the parameters from the best result of each model. The simulations include background and efficiency and each toy is fitted independently. The result are distributions of fitted values of the parameters and their respective uncertainties. For each parameter, the mean of the distribution of fitted values is compared to the input. The difference is assigned as the systematic uncertainty due to the fit bias. As a sanity check, the statistical uncertainties from MINUIT are compared to the mean value of the distribution of fitted parameter uncertainties. If there is any bias, it should be included in the systematics.

Regarding model systematics, uncertainties related to lineshape parameters also need to be included. In this analysis, for both $K-$Matrix and QMIPWA models, masses and widths of spin 1 and 2 components can be varied by $\pm 1\sigma$ observing the effect while for Isobar results, the lineshape parameters from all resonances (spin 0,1 and 2 states) can be also varied by $\pm 1\sigma$ observing the effects in the fitted parameters and including in the model systematics. Furthermore, Blatt-Weisskopf radius, $r_{F_{D,Rp_3}}$ and $r_{F_{R,p_1p_2}}$, are also varied for higher spin states in the $K-$Matrix and QMIPWA models and for all resonant states in the Isobar model observing any shifts of the central values of the parameters. In the QMIPWA, the choice of number of points in which the mass spectrum is binned is also a source of uncertainties. A variation of the number of bins in the $S-$wave needs to be considered.

9.4 Conclusions

In this dissertation it was presented the amplitude analysis of a sample of 200 thousand $D^+ \to \pi^-\pi^+\pi^+$ Cabibbo-suppressed decays from the LHCb experiment aiming to understand the resonant intermediate structures for this decay and to extract and interpret the $\pi^+\pi^-$ $S-$wave. Model dependent parametrisations - Isobar and $K-$Matrix approaches - were not good enough to describe the data. The best result was accomplished by using the QMIPWA method, where the $S-$wave is obtained in bins of $m(\pi^+\pi^-)$, while $P-$ and $D-$waves are described by Isobar approach.

The results presented in this dissertation are still preliminary and they do not include systematic uncertainties. The analysis is well advanced and the results presented here are being discussed within the collaboration and final results will be presented in the full analysis note, towards publication.

10
Appendix: Reweight Procedure

In this appendix, the reweight procedure using half (containing only odd events) of the total sample is described.

The overall steps required in the reweight procedure are the following:

- At first, the data sample with PIDK< -2 for all pion cadidates is splitted into two reproducible sub samples. The first sample is reserved for further analysis while the second sample proceeds into the next steps.
- For each polarity a mass fit within the range $[1810, 1930]\mathrm{MeV}/c^2$via sPlot technique [93] is performed in which the signal weight is saved. The signal PDF is composed of a Gaussian and a Crystal Ball function with positive parameter α and width related to the Gaussian width ($\sigma_{CB} = \sigma_G \times CB_{ratio}$). The background PDF is given by an exponential function.
- Since the MC sample is generated as phase space and weighted by the PIDCalib, the dynamics is emulated by applying a resonant structure weight. Furthermore, a tracking correction to equalize the track multiplicity between data and MC is provided as a function of particle momentum, transverse momentum and event track multiplicity is applied as a weight. Both corrections are saved and we will refer to the tracking correction as $MC_{nTracks}$ and the resonant structure weight to as MC_{DP}.
- Once both data and MC samples have the tracking correction and resonant structure weights, we construct the ratio between the MC and data to be stored in the MC sample.

$$hist_{DP} = \frac{MC_{DP}}{Data_{DP}}, \tag{10-1}$$

$$hist_{nTracks} = \frac{MC_{nTracks}}{Data_{nTracks}}. \tag{10-2}$$

- Then, merging Up and Down polarities for both data and MC, the samples together with their respective weights, will proceed as inputs for the reweight code.

To perform the mass fit, the signal was modelled by one Gaussian function and one Crystal Ball function (CB) with α_{CB} positive. The Crystal Ball parameter σ_{CB} was constructed as a product of the Gaussian width and the CB σ ratio

$$\sigma_{CB} = \sigma_G \times CB_{ratio}. \tag{10-3}$$

For the background model, it was used an exponential function parametrised with a negative τ dislocated by a fix value, an offset

$$\mathcal{PDF}_{bkg} = e^{-\tau(x-1810)}. \tag{10-4}$$

The signal PDF is written as

$$\mathcal{PDF}_{sig} = frac_G f_G(x) + (1 - frac_G) f_{CB}(x), \tag{10-5}$$

thus the fit model can be written as

$$\mathcal{PDF} = \mathcal{N}_{sig}\mathcal{P}_{sig} + \mathcal{N}_{Bkg}\mathcal{P}_{Bkg}. \tag{10-6}$$

The plot and fit result for MagUp polarity is shown in Figure 10.1 and Table 10.1.

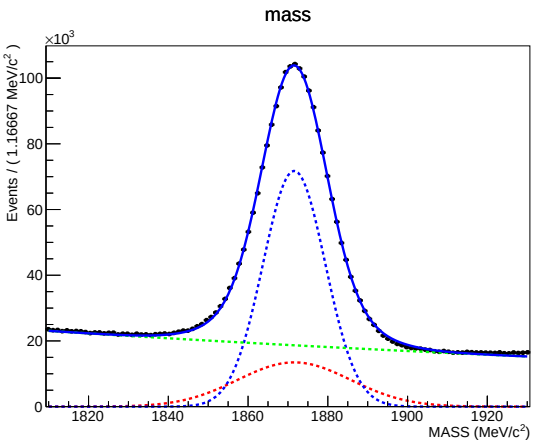

Figure 10.1: Mass Fit for MagUp sample.

Parameter	Value
Nbkg	2142570 ± 14297.6
Nsig	1734200 ± 13721.0
α_1	0.491 ± 0.040
σ^{CB}_{ratio}	1.838 ± 0.043
μ_G	1871.58 ± 0.011
σ_G	8.132 ± 0.023
n_{CB}	19.99 ± 14.03
frac	0.7700 ± 0.0038
τ_{bkg}	-0.00222 ± 0.00010

Table 10.1: Invariant mass fit parameters.

The blue full line represents the fit result, red dashed line the Gaussian function, green dashed line the background and blue dashed line the Crystal Ball

function. The fit parameters in the output were used to calculate the signal weight via sPlot as a technique for background subtraction.

The reweight is created on a multivariate analysis based code with the following inputs: MC sample (MagUp+MagDown), true ID and weights (PID, tracking correction and phase space dynamics) and the data sample (MagUp+MagDown) with background subtracted from sPlot. The input variables are:

- D IP
- D χ^2_{IP}
- D FD
- D χ^2_{FD}
- DIRA
- POINTING
- tCM
- D p_T
- PTsum
- D Vertex χ^2
- logIP
- for each daughter χ^2_{IP}, IP, p and p_T

The output is the "reweight" which matches the distributions ensuring that the MC kinematics is well described. Figure 10.2 illustrates the variables after the reweight process indicating that the simulated $D^+ \to \pi^-\pi^+\pi^+$ distributions are now equivalent to the data. The blue line corresponds to the data with background subtracted and in red the simulated sample with all weights applied (kinematical, dynamical and reweight).

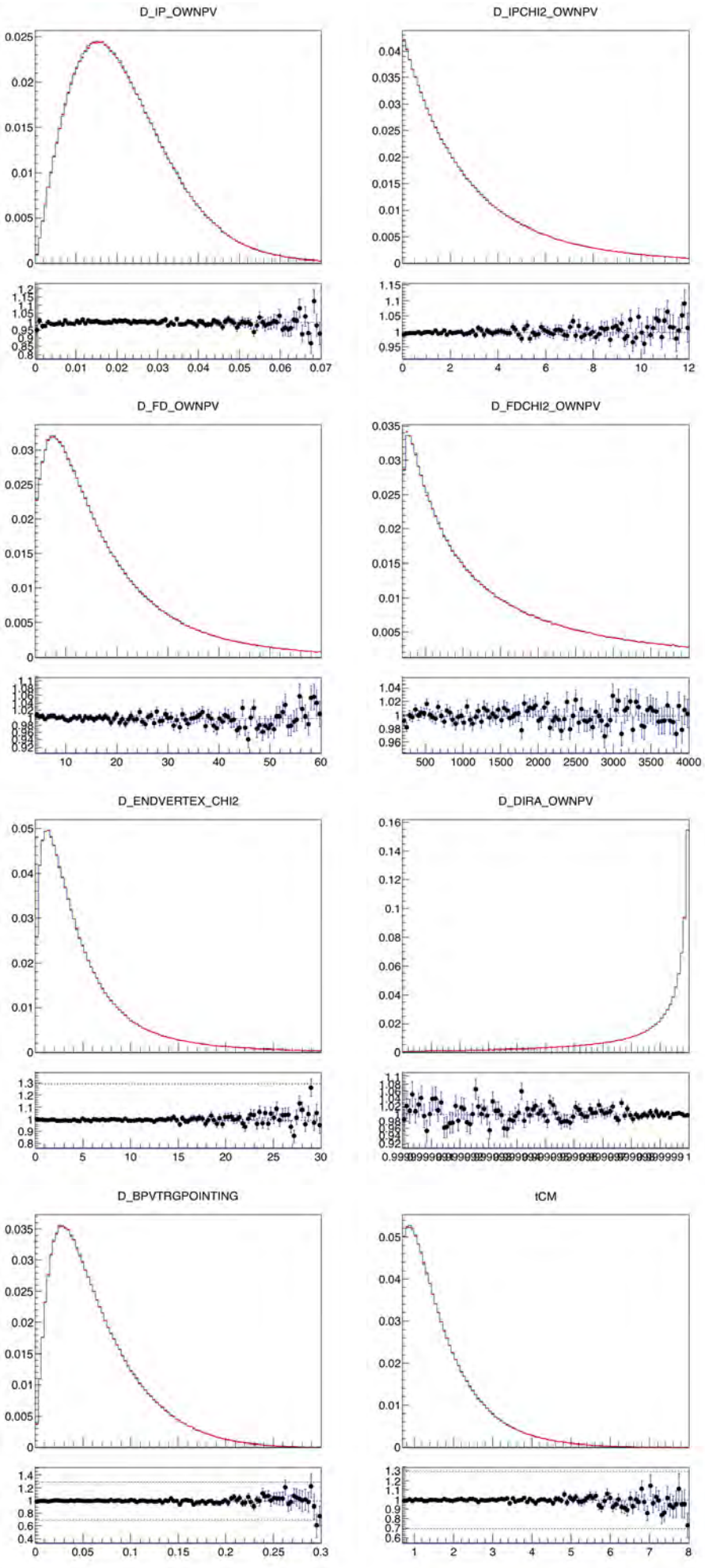

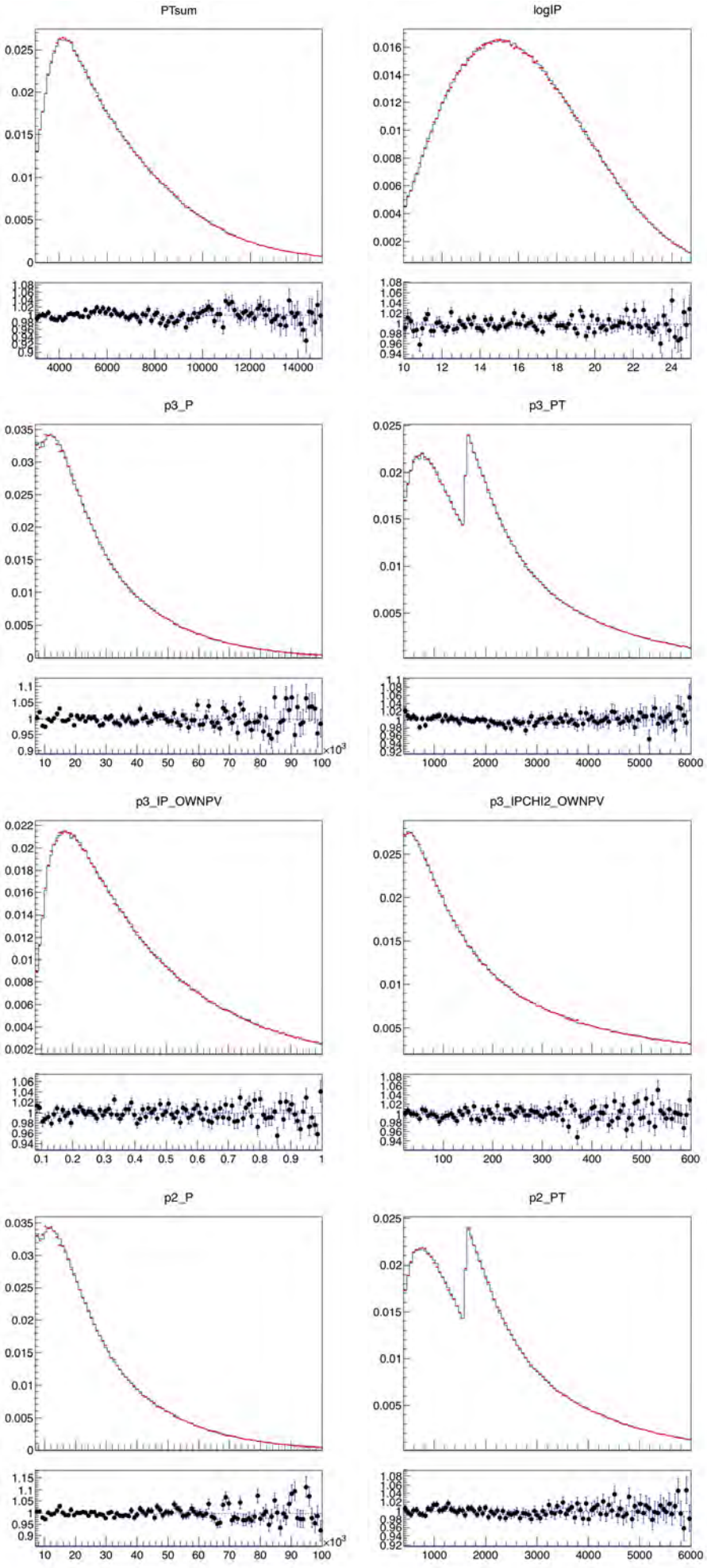

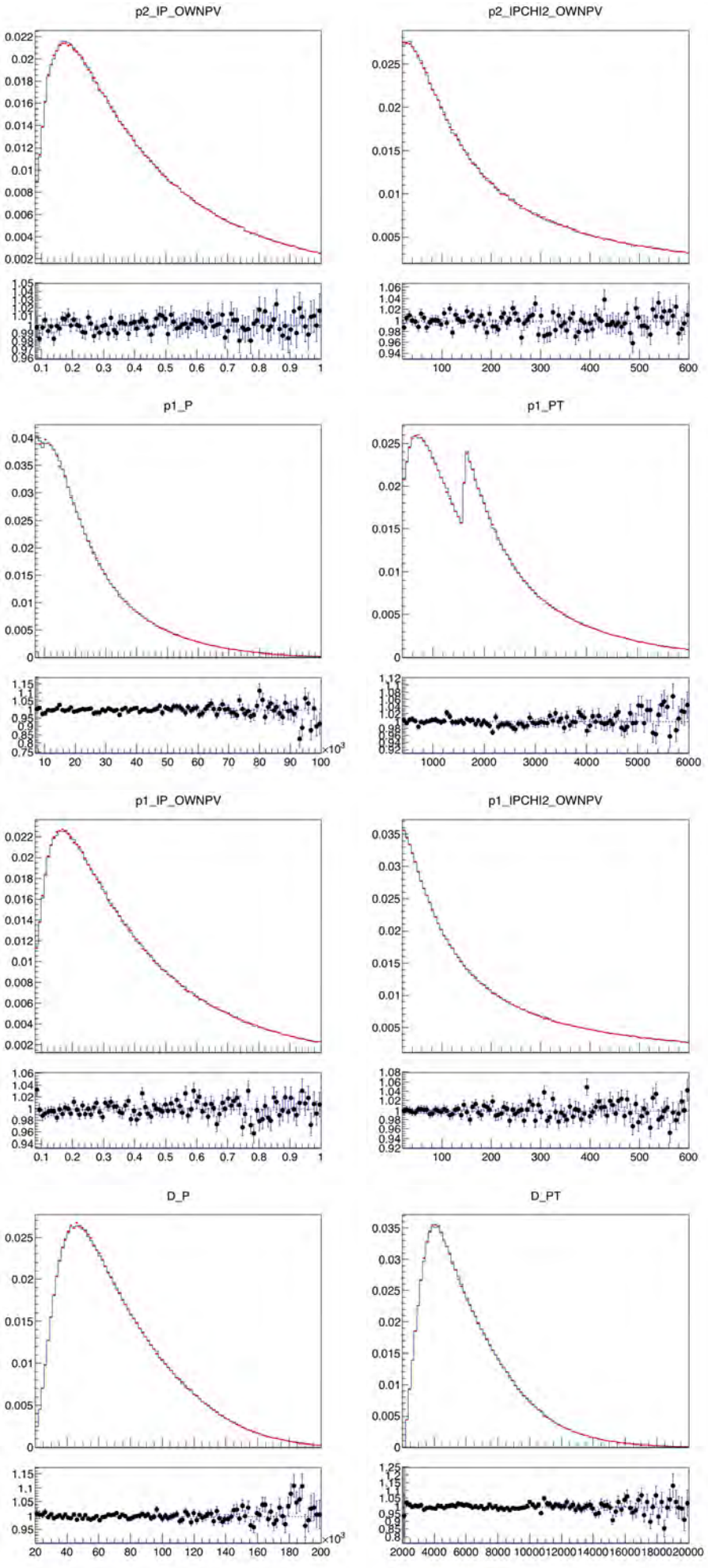

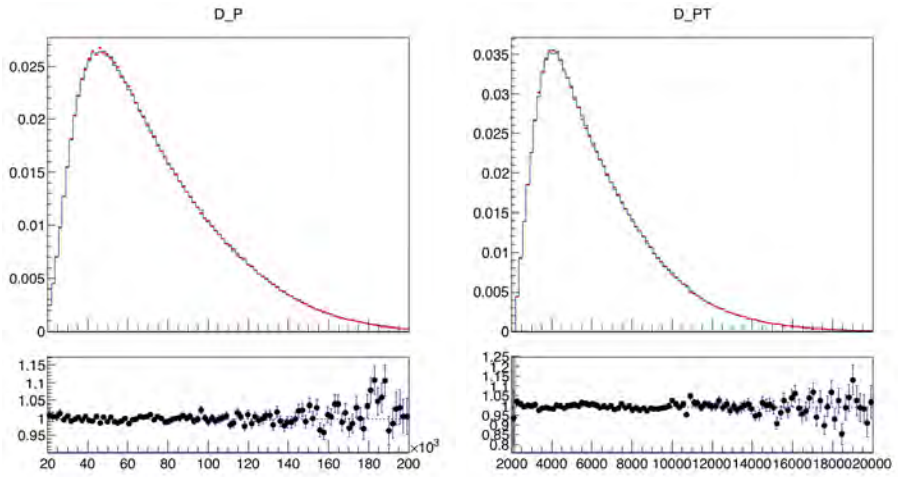

Figure 10.2: Variables after the reweight procedure.

11
Appendix: GooFit validation

In this appendix we present a code validation for the GooFit software. The purpose is to verify the performance of the fitter via a *genfit* procedure.

To perform the genfit, we first generate a large number of simulation samples according to a determined model such that the contributions and the input parameters are chosen. Then we perform a fit for each simulated sample in order to compare the inout values with the ones obtained from the MINUIT. The distributions for each fitted parameter are created and expected to have a gaussian behavior centered at the input value and the width compatible with the distribution of the mean errors.

The model consists on four resonances: $\rho(770)$ in the reference, $f_0(980)$, $f_2(1270)$ and $\rho(1450)$. Each sample has 200 thousand events and the genfit procedure was performed with 1000 samples. Background and efficiency histograms were considered and all widths and masses are set free in the fit. The $\rho(770)$ was fixed at real equal to 1 and imgaginary equal to 0. The results and the parameters distributions are shown in Table 11.1. The compatibility tests from the input values are given by:

$$\text{Compatibility1} = \frac{|\text{gen} - \mu|}{\text{error}}, \tag{11-1}$$

$$\text{Compatibility2} = \frac{|\sigma - \text{error}_\mu|}{\text{error}}, \tag{11-2}$$

where, in the compatibility 1, gen corresponds to the generated input value, μ is the mean of the gaussian adjustment of the parameter distribution and in the denominator, the error associated to the mean. In the compatibility test 2, σ corresponds to the width of the gaussian adjustment, error_μ is the mean of the error distribution and, in the denominator, the error associated with the width adjustment.

Resonance	**Generated**	**Fit mean μ**	**μ error**	**Fit σ**	**σ error**	**Fit μ Error**
$f_0(980)$ real	-0,4891	-0,4901	0,0010	0,02982	0,00075	0,02996
$f_0(980)$ img	-0,3265	-0,3262	0,0008	0,02427	0,00066	0,02517
$f_2(1270)$ real	-0,2487	-0,2464	0,0005	0,01442	0,00036	0,01516
$f_2(1270)$ img	0,7447	0,7435	0,0003	0,00767	0,00019	0,00783
$\rho(1450)$ real	0,00251	-0,00046	0,00072	0,02184	0,00054	0,02227
$\rho(1450)$ img	-0,0937	-0,09762	0,00065	0,01959	0,00053	0,02001

Resonance	**Compatibility 1**	**Compatibility 2**
$f_0(980)$ real	1	0,19
$f_0(980)$ img	0,38	1,36
$f_2(1270)$ real	4,6	2,06
$f_2(1270)$ img	4	0,84
$\rho(1450)$ real	4,13	0,80
$\rho(1450)$ img	6,03	0,79

Table 11.1: Genfit results.

12
Appendix: Individual Resonances

In this appendix, the Dalitz plot of each individual resonance is shown in order to observe the region where each one contributes.

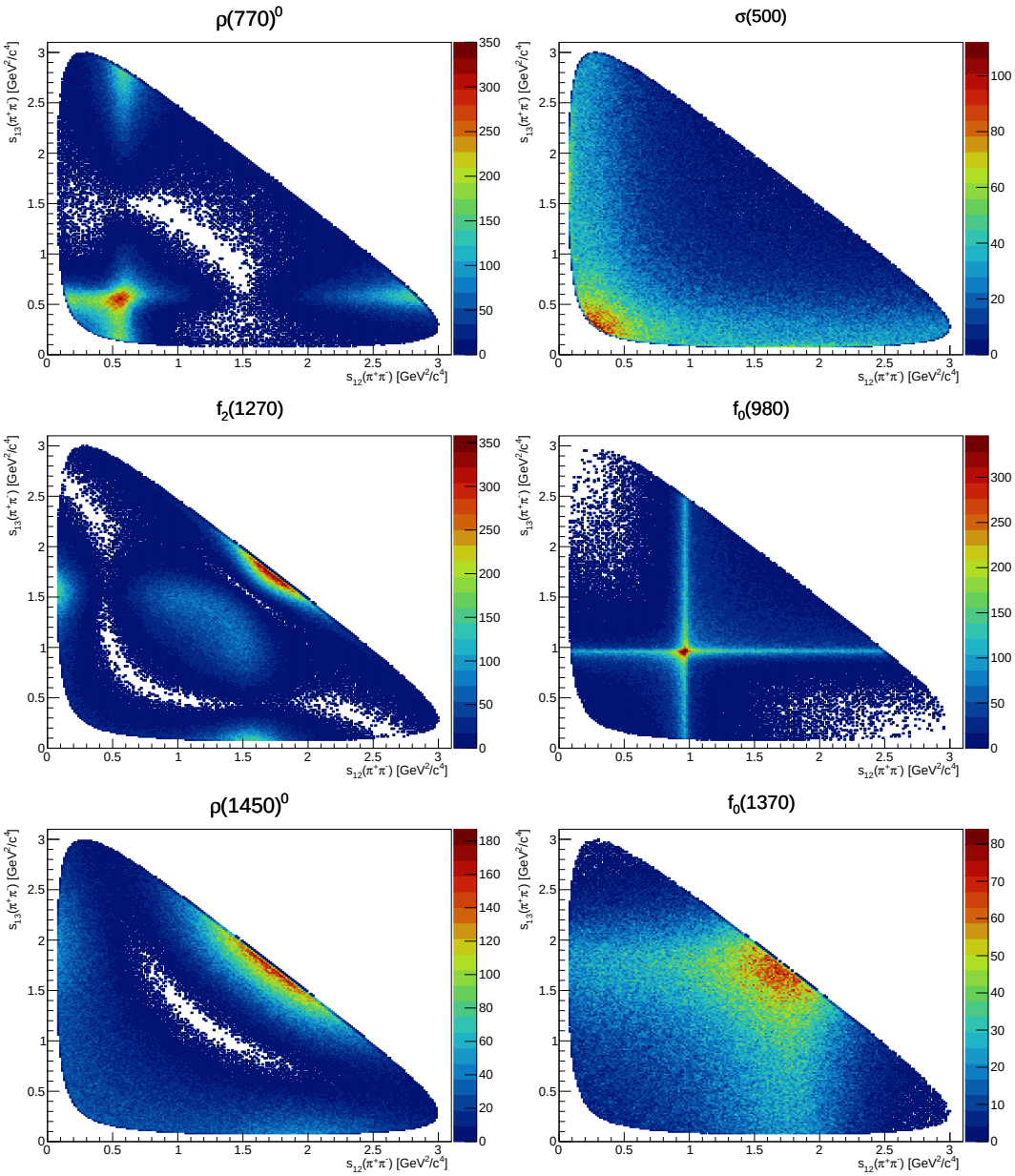

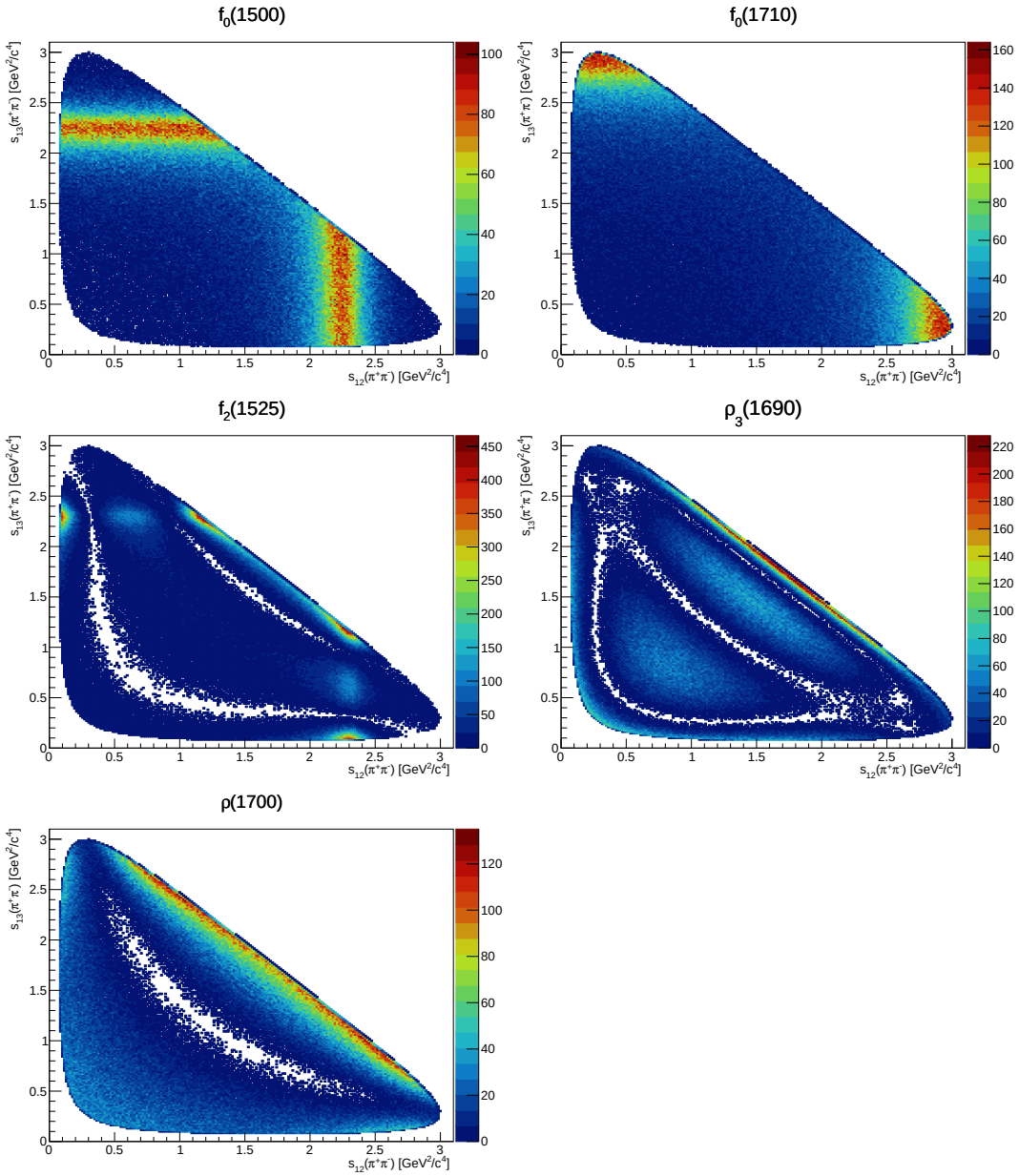

Figure 12.1: Dalitz plot of each individual resonance.

13
Appendix: Additional Results

In this Appendix we present some additional results mentioned in the previous chapters. In all of the following, all masses and widths are fixed to PDG values unless any parameter is explicitly said to be free and all lineshapes used for each contribution are according to Table 6.2.

Isobar Model

Considering an initial model composed of $\rho^0(770)$, $\omega(782)$, $f_2(1270)$, $\sigma(500)$, $f_0(980)$, $\rho^0(1450)$, $f_0(1500)$ and $f_0(1370)$. From now on, we will refer this model to as Model I-0. In Model I-2 we presented the result of this model including the $f_0(1710)$ in Model I-0 and in the following results we show the inclusion of other contributions instead the $f_0(1710)$. In all results the masses and widths are set fixed to PDG values unless it is specified in the fit result. In addition, for fits which the $\rho - \omega$ is included via a mixing lineshape, the parameters responsible for the mixing are $|B|$ and ϕ_B and in all cases they are set as free.

Model I-0

Resonance	**Magnitude**	**Phase [rad]**	**Fit Fraction (FF)** (%)
$\rho - \omega$	1 [fix]	0 [fix]	24.8
$f_0(980)$	0.550 ± 0.005	-3.34 ± 0.02	7.5
$\sigma(500)$	1.165 ± 0.015	3.63 ± 0.01	33.7
$f_2(1270)$	0.680 ± 0.005	1.42 ± 0.02	11.5
$f_0(1500)$	0.404 ± 0.008	-3.36 ± 0.03	4.1
$f_0(1370)$	0.553 ± 0.018	3.67 ± 0.02	7.6
$\rho^0(1450)$	0.171 ± 0.010	1.99 ± 0.08	0.7
$m_{f_0(980)}$	924.8 ± 2.0 MeV/c^2		
$\|B\|$	0.525 ± 0.034		
ϕ_B	-3.37 ± 0.07		
$\sum$ FF (%)	89.8		
χ^2/ndof (range)	[6.62 - 6.46]		**FCN = -1908561**

Table 13.1: Fit results from Model I-0.

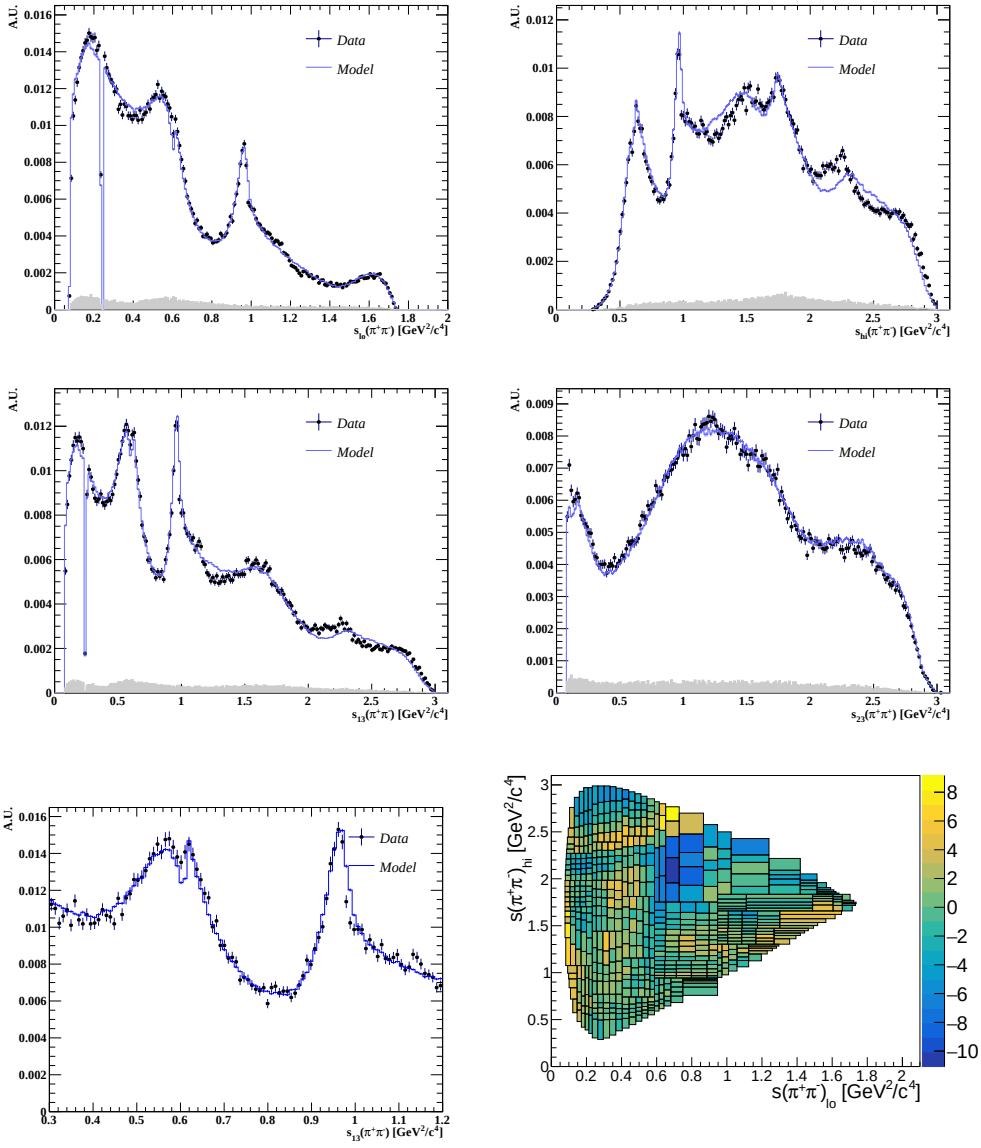

Figure 13.1: Fit projections from Model I-0 and residuals distribution.

Model I-0 plus a non resonant (NR) contribution

Resonance	**Magnitude**	**Phase [rad]**	**Fit Fraction (FF)** (%)
$\rho - \omega$	1 [fix]	0 [fix]	25.6
$f_0(980)$	0.539 ± 0.006	-3.60 ± 0.02	7.4
$\sigma(500)$	0.955 ± 0.020	3.60 ± 0.02	23.3
$f_2(1270)$	0.654 ± 0.005	1.48 ± 0.02	10.9
$f_0(1500)$	0.272 ± 0.010	-3.48 ± 0.04	1.9
$f_0(1370)$	0.417 ± 0.018	3.14 ± 0.04	4.4
$\rho^0(1450)$	0.176 ± 0.012	1.61 ± 0.06	0.8
NR	0.478 ± 0.021	-0.68 ± 0.04	5.8
$m_{f_0(980)}$	906.8 ± 2.0 MeV/c^2		
$\|B\|$	0.567 ± 0.034		
ϕ_B	-3.34 ± 0.06		
$\sum$ FF (%)	80.2		
χ^2/ndof (range)	[5.87 - 5.71]		**FCN = -1908882**

Table 13.2: Fit results from Model I-0 plus NR.

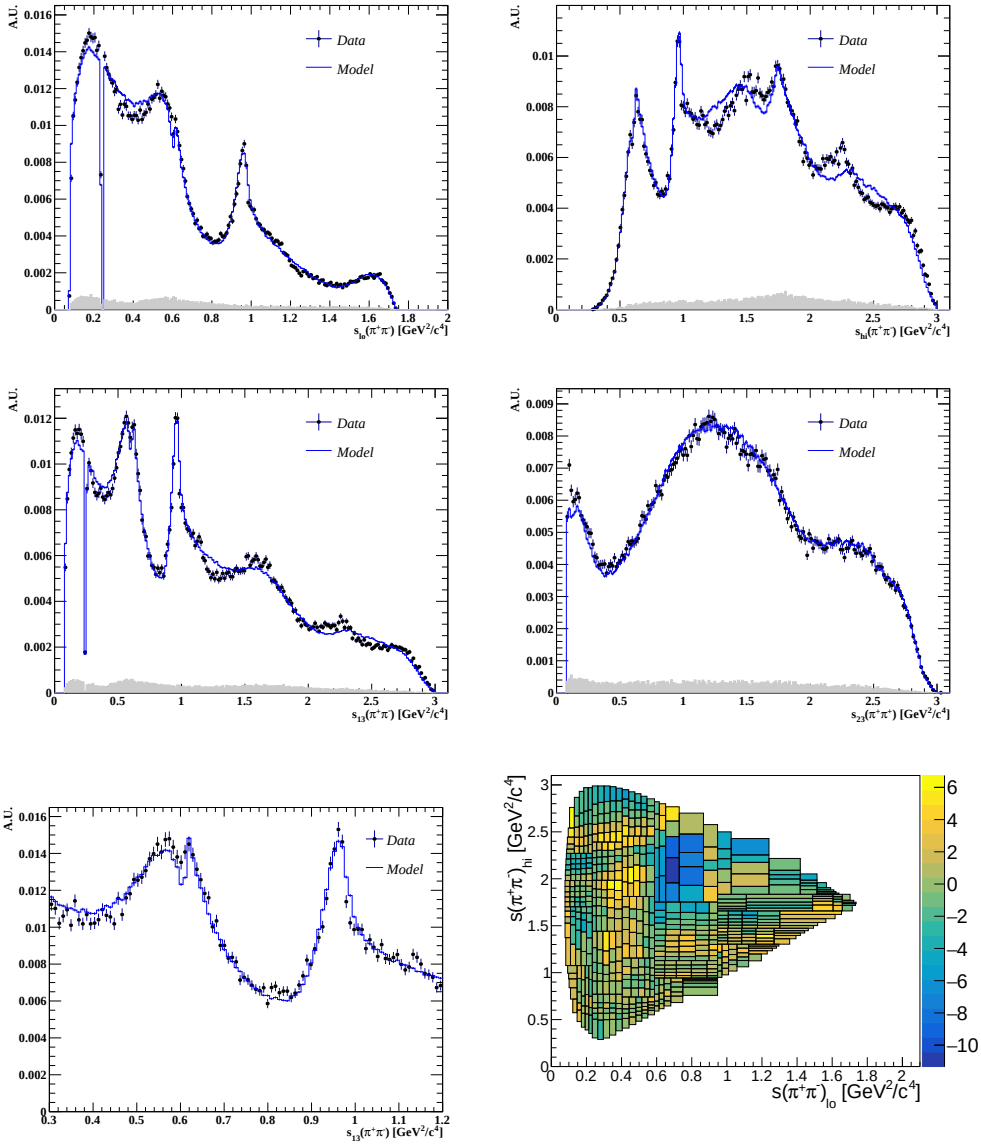

Figure 13.2: Fit projections from Model I-0 plus NR and residuals distribution.

Model I-0 with $f_0(1370)$ mass and width free

Resonance	**Magnitude**	**Phase [rad]**	**Fit Fraction (FF)** (%)
$\rho - \omega$	1 [fix]	0 [fix]	20.3
$f_0(980)$	0.552 ± 0.006	-3.56 ± 0.02	6.2
$\sigma(500)$	1.168 ± 0.020	3.44 ± 0.01	27.7
$f_2(1270)$	0.742 ± 0.008	1.51 ± 0.02	11.2
$f_0(1500)$	0.408 ± 0.014	-2.43 ± 0.03	3.4
$f_0(1370)$	0.459 ± 0.015	4.66 ± 0.05	4.3
$\rho^0(1450)$	0.180 ± 0.009	2.06 ± 0.07	0.7
$m_{f_0(980)}$	903.0 ± 1.7 MeV/c^2		
$\|B\|$	0.610 ± 0.037		
ϕ_B	-3.30 ± 0.06		
$m_{f_0(1370)}$	1696.9 ± 3.6 MeV/c^2		
$\Gamma_{f_0(1370)}$	150.8 ± 9.6 MeV/c^2		
$\sum$ FF (%)	73.7		
χ^2/ndof (range)	[5.45 - 5.30]		**FCN = -1909083**

Table 13.3: Fit results from Model I-0 with $f_0(1370)$ free.

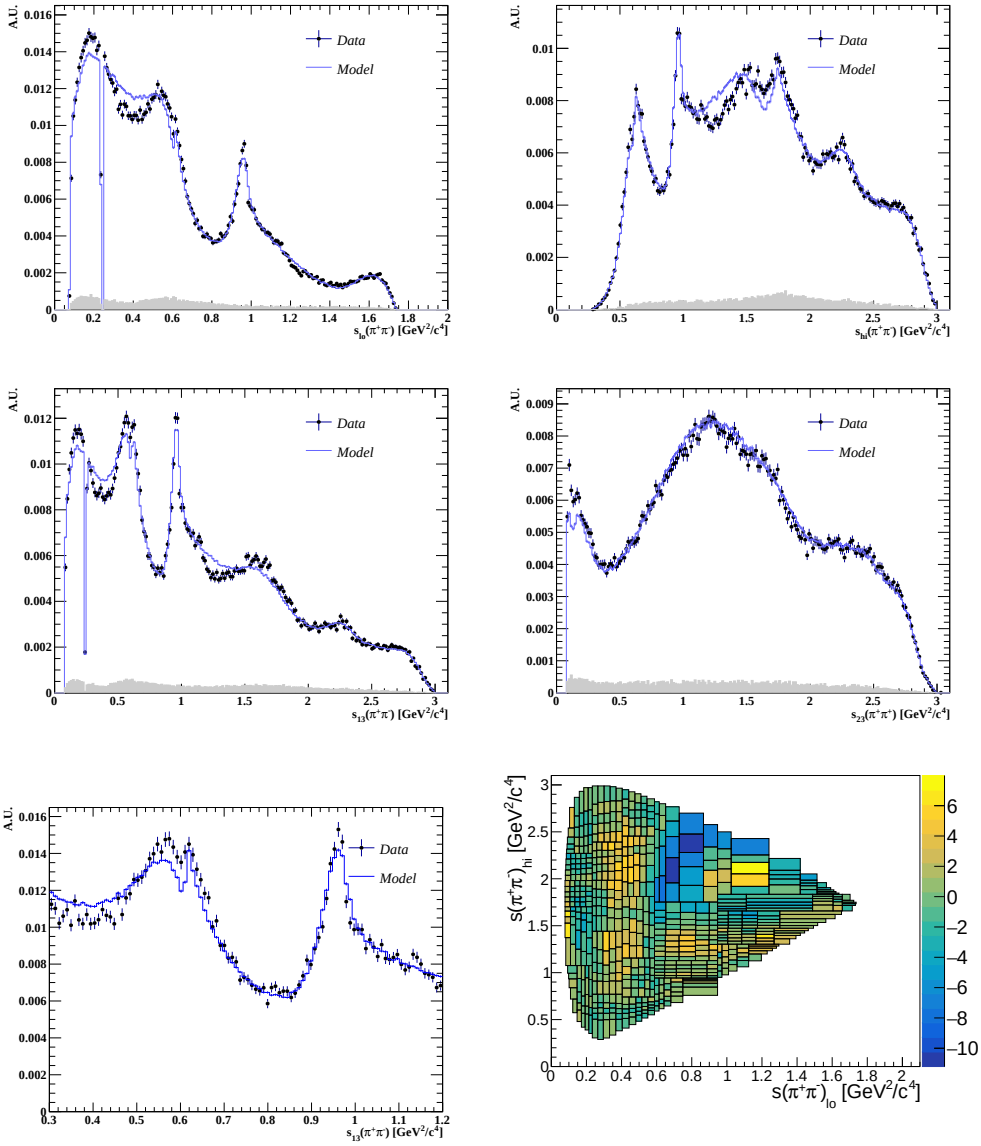

Figure 13.3: Fit projections from Model I-0 with $f_0(1370)$ free and residuals distribution.

Model I-0 plus a $\rho_3(1690)$

Resonance	**Magnitude**	**Phase [rad]**	**Fit Fraction (FF)** (%)
$\rho - \omega$	1 [fix]	0 [fix]	25.4
$f_0(980)$	0.552 ± 0.005	-3.47 ± 0.02	7.8
$\sigma(500)$	1.214 ± 0.016	3.59 ± 0.01	37.5
$f_2(1270)$	0.662 ± 0.005	1.39 ± 0.02	11.2
$f_0(1500)$	0.351 ± 0.009	-3.41 ± 0.03	3.1
$f_0(1370)$	0.567 ± 0.020	3.56 ± 0.02	8.2
$\rho^0(1450)$	0.108 ± 0.011	2.11 ± 0.15	0.3
$\rho_3(1690)$	0.084 ± 0.006	-2.12 ± 0.06	0.2
$m_{f_0(980)}$	917.8 ± 2.1 MeV/c^2		
$\|B\|$	0.540 ± 0.034		
ϕ_B	-3.40 ± 0.06		
$\sum$ FF (%)	93.6		
χ^2/ndof (range)	[6.26 - 6.09]		**FCN = -1908678**

Table 13.4: Fit results from Model I-0 plus $\rho_3(1690)$.

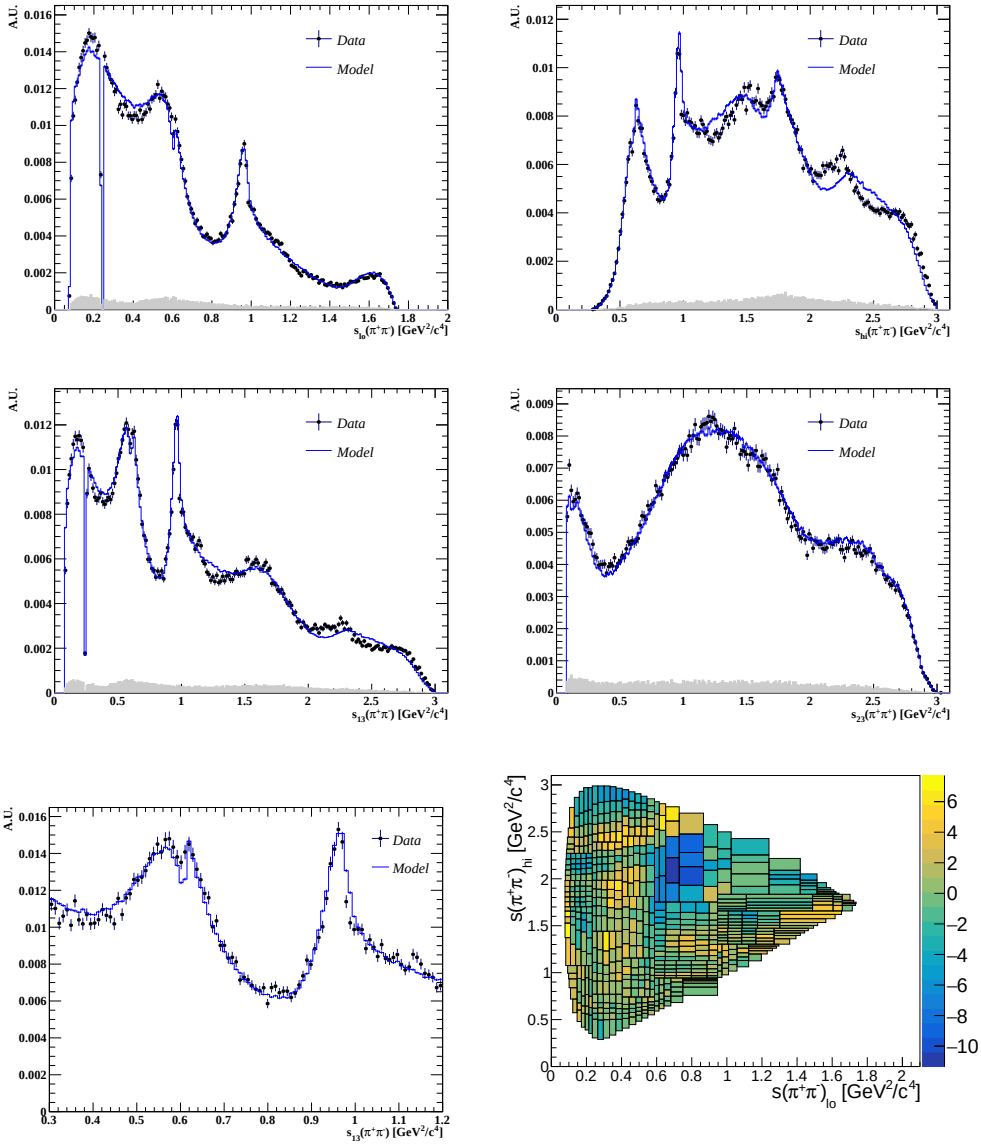

Figure 13.4: Fit projections from Model I-0 plus $\rho_3(1690)$ and residuals distribution.

Model I-0 plus rescattering

Resonance	**Magnitude**	**Phase [rad]**	**Fit Fraction (FF)** (%)
$\rho - \omega$	1 [fix]	0 [fix]	24.9
$f_0(980)$	0.549 ± 0.005	-3.33 ± 0.02	7.5
$\sigma(500)$	1.132 ± 0.015	3.66 ± 0.01	32.0
$f_2(1270)$	0.671 ± 0.005	1.41 ± 0.02	11.2
$f_0(1500)$	0.406 ± 0.008	-3.40 ± 0.03	4.1
$f_0(1370)$	0.596 ± 0.018	3.67 ± 0.02	8.9
$\rho^0(1450)$	0.191 ± 0.011	1.85 ± 0.07	0.9
Rescattering	0.043 ± 0.004	0.51 ± 0.09	0.05
$m_{f_0(980)}$	927.6 ± 2.1 MeV/c^2		
$\|B\|$	0.533 ± 0.034		
ϕ_B	-3.37 ± 0.07		
$\sum$ FF (%)	89.5		
χ^2/ndof (range)	[6.61 - 6.43]		**FCN = -1908625**

Table 13.5: Fit results from Model I-0 plus rescattering.

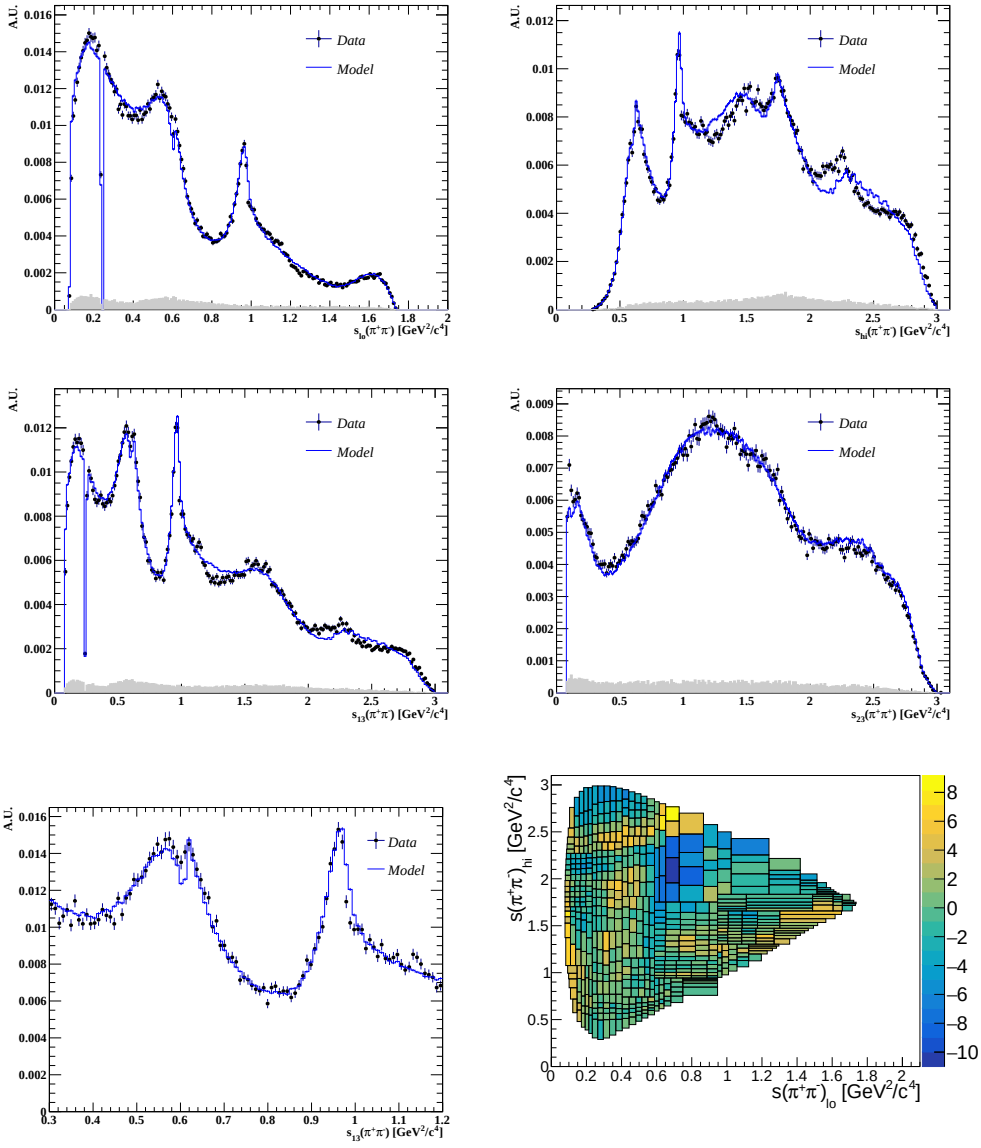

Figure 13.5: Fit projections from Model I-0 plus rescattering and residuals distribution.

K-Matrix

Model KM-2 plus $f_2'(1525)$

Component	Magnitude	Phase [rad]	Fit Fraction (%)
$\rho^0(770)$	1.0 [fixed]	0.0 [fixed]	26.5
$\omega(782)$	0.060 ± 0.004	-1.61 ± 0.07	0.1
$f_2(1270)$	0.672 ± 0.006	1.48 ± 0.02	12.0
$\rho^0(1450)$	0.075 ± 0.009	-4.31 ± 0.14	0.1
$f_2'(1525)$	0.123 ± 0.006	-1.98 ± 0.05	0.4

$S-$wave

Component	β/f_{prod} Magnitude	β/f_{prod} Phase [rad]	Fit Fraction (%)
Pole1	0.975 ± 0.031	-3.47 ± 0.03	25.2
Pole2	0.427 ± 0.014	-2.07 ± 0.04	4.8
Pole3	0.769 ± 0.045	-0.78 ± 0.05	15.7
Pole4	0.841 ± 0.041	-0.70 ± 0.05	18.7
Pole5	0.531 ± 0.044	-2.57 ± 0.09	7.5
SVP1	0.631 ± 0.060	-1.31 ± 0.10	10.5
SVP3	0.301 ± 0.035	6.00 ± 0.13	2.4
SVP4	0.556 ± 0.045	-0.18 ± 0.07	8.2
$S-$wave			58.4
χ^2/ndof (range)	[3.26 - 3.13]		
$\sum$ FF (%)	132.1		
FCN			-1909992

Table 13.6: Model KM-2 plus $f_2'(1525)$: component parameters and fit fractions. Uncertainties are statistical only and fit fractions without errors.

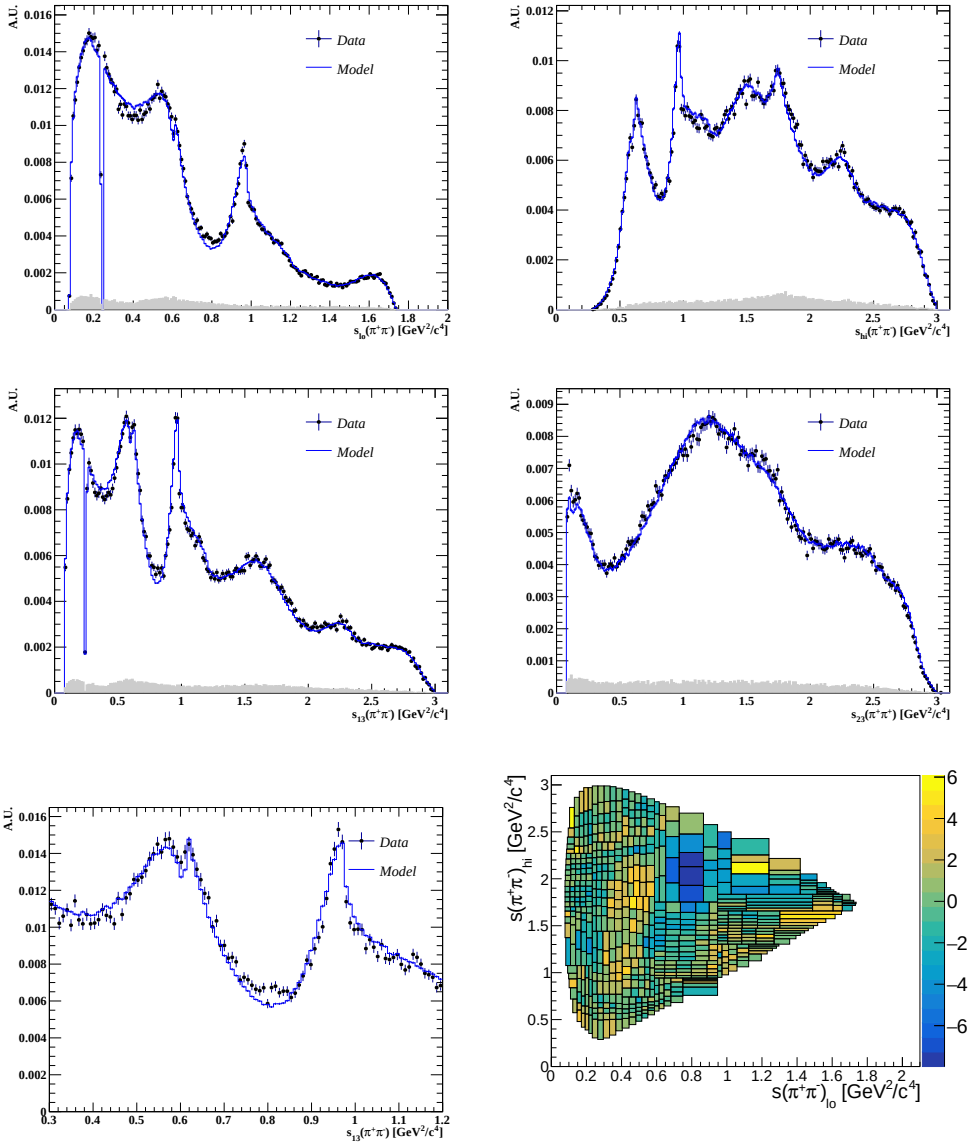

Figure 13.6: Fit results from Model KM-2 plus $f_2'(1525)$.

Model KM-2 plus $\rho_3(1690)$

Component	Magnitude	Phase [rad]	Fit Fraction (%)
$\rho^0(770)$	1.0 [fixed]	0.0 [fixed]	26.4
$\omega(782)$	0.063 ± 0.004	-1.66 ± 0.07	0.1
$f_2(1270)$	0.667 ± 0.006	1.53 ± 0.02	11.8
$\rho^0(1450)$	0.062 ± 0.008	-3.54 ± 0.21	0.1
$\rho_3(1690)$	0.034 ± 0.006	3.01 ± 0.21	0.03

$S-$wave

Component	β/f_{prod} Magnitude	β/f_{prod} Phase [rad]	Fit Fraction (%)
Pole1	0.989 ± 0.033	-3.29 ± 0.03	25.8
Pole2	0.376 ± 0.014	-2.12 ± 0.05	3.7
Pole3	0.928 ± 0.050	-0.76 ± 0.05	22.8
Pole4	0.983 ± 0.046	-0.64 ± 0.04	25.6
Pole5	0.631 ± 0.049	-2.84 ± 0.07	10.5
SVP1	0.519 ± 0.059	-1.55 ± 0.13	7.1
SVP3	0.335 ± 0.038	6.50 ± 0.12	3.0
SVP4	0.533 ± 0.046	-0.03 ± 0.07	7.5
$S-$wave			61.4
χ^2/ndof (range)	[3.84 - 3.69]		
$\sum$ FF (%)	144.5		
FCN			-1909764

Table 13.7: Model KM-2 plus $\rho_3(1690)$: component parameters and fit fractions. Uncertainties are statistical only and fit fractions without errors.

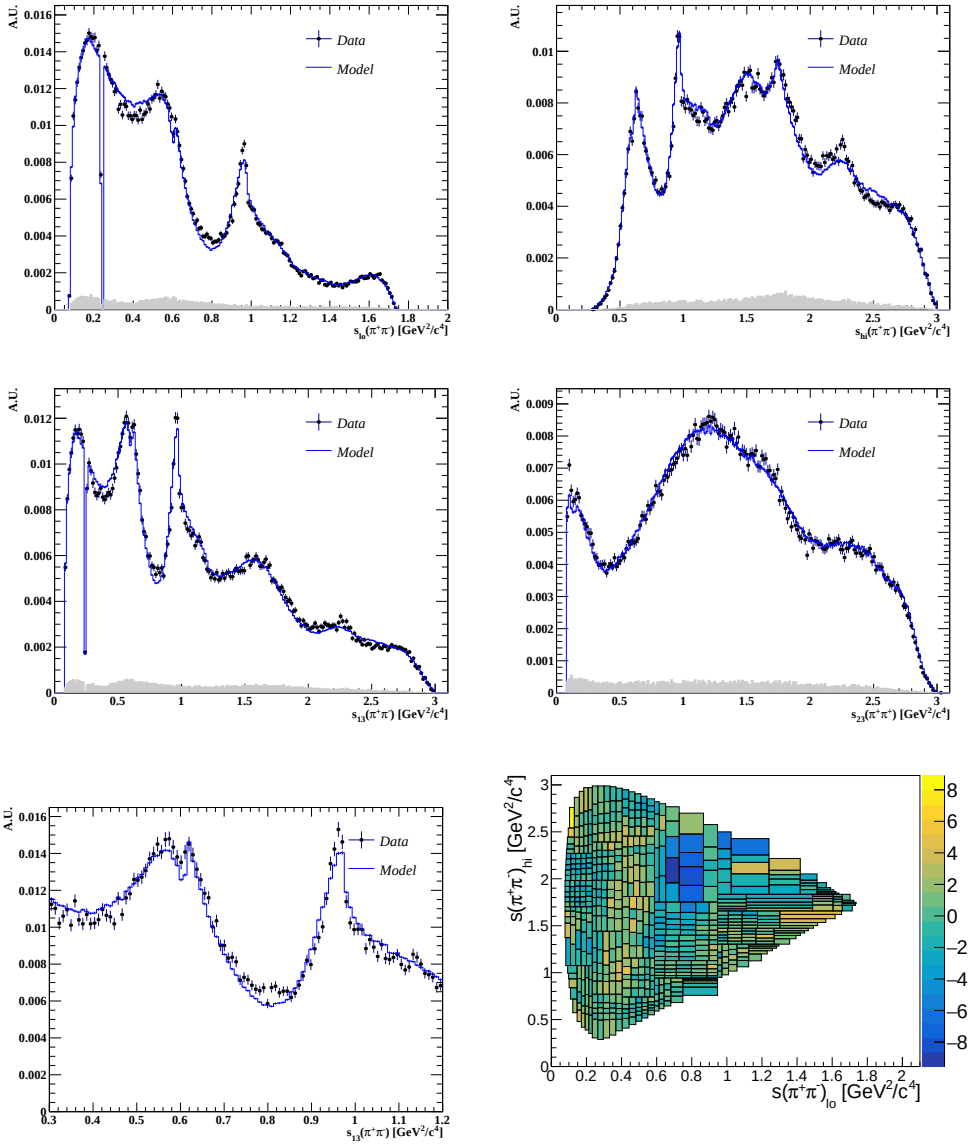

Figure 13.7: Fit results from Model KM-2 plus $\rho_3(1690)$.

QMIPWA

Model PWA-1 plus $\rho(1700)$

Resonance	**Real**	**Imaginary**	**Fit Fraction (FF)** (%)
$\rho^0(770)$	1 [fix]	0 [fix]	25.8
$\omega(782)$	-0.003 ± 0.001	-0.014 ± 0.001	0.1
$f_2(1270)$	-0.406 ± 0.036	-1.714 ± 0.022	11.2
$\rho^0(1450)$	1.066 ± 0.125	1.069 ± 0.045	1.7
$\rho(1700)$	-1.242 ± 0.223	-3.133 ± 0.290	1.3
$S-$Wave	48 points		62.4
$\sum$ FF (%)	102.6		
χ^2/ndof (range)	[1.74 - 1.45]		**FCN = 272898**

Table 13.8: Fit results from the baseline model plus $\rho(1700)$.

	$\omega(782)$	$\rho^0(770)$	$\rho^0(1450)$	$f_2(1270)$	$\rho(1700)$	$S-$wave
$\omega(782)$	0.09	-0.22	0.03	0.04	-0.02	0.00
$\rho^0(770)$		25.85	2.84	-0.38	-2.50	1.14
$\rho^0(1450)$			1.75	0.54	-1.34	0.64
$f_2(1270)$				11.17	-0.47	-0.73
$\rho(1700)$					1.30	-0.85
$S-$wave						62.44

Table 13.9: Interference fractions between amplitude components for the QMIPWA approach.

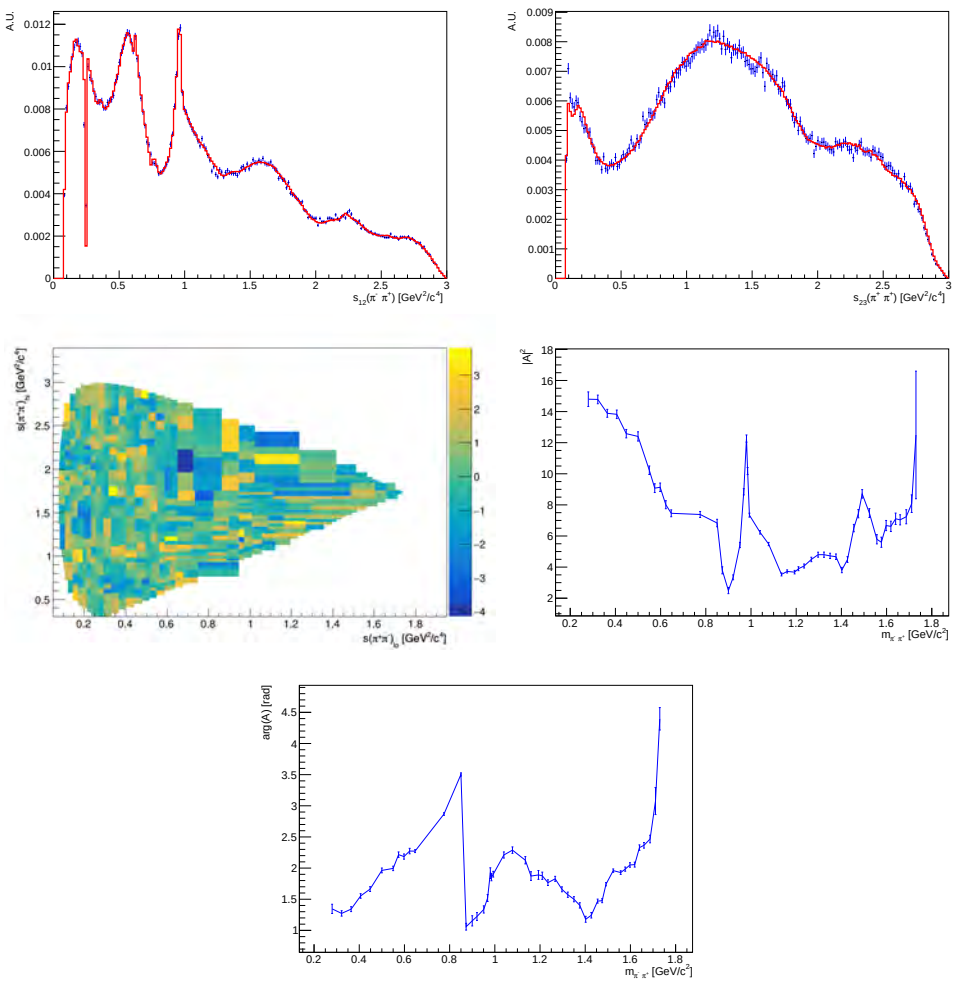

Figure 13.8: Fit projections from the baseline model plus $\rho(1700)$, extracted $S-$wave and residuals distribution.

Model PWA-1 plus Bose Einstein Correlation effect (BEC)

Resonance	**Real**	**Imaginary**	**Fit Fraction (FF)** (%)
$\rho^0(770)$	1 [fix]	0 [fix]	20.2
$\omega(782)$	-0.003 ± 0.001	-0.015 ± 0.001	0.1
$f_2(1270)$	-0.472 ± 0.032	-1.901 ± 0.029	10.8
$\rho^0(1450)$	1.483 ± 0.107	0.676 ± 0.098	1.6
BEC	9.664 ± 1.391	24.683 ± 1.476	38.1
$S-$Wave	48 points		40.4
$\sum$ FF (%)	111.3		
χ^2/ndof (range)	[1.69 - 1.41]		**FCN = 272833**

Table 13.10: Fit results from the baseline model plus the Bose Einstein correlation effect

	$\omega(782)$	$\rho^0(770)$	$\rho^0(1450)$	$f_2(1270)$	BEC	$S-$wave
$\omega(782)$	0.09	-0.19	0.04	0.04	-0.03	0.0
$\rho^0(770)$		20.23 1.65	-0.35	-3.94	6.09	
$\rho^0(1450)$			1.59	0.56	-2.26	2.03
$f_2(1270)$				10.81	-0.97	0.0
BEC					38.10	-8.29
$S-$wave						40.45

Table 13.11: Interference fractions between amplitude components for the QMIPWA approach.

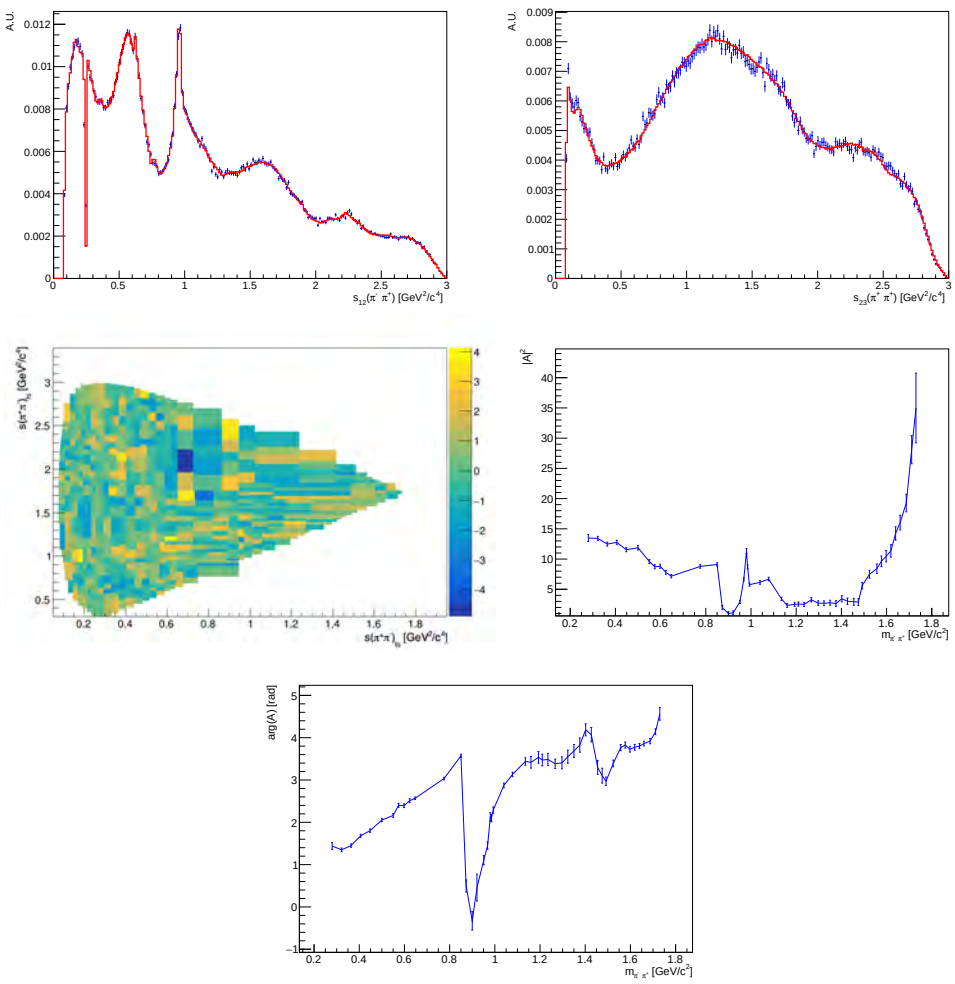

Figure 13.9: Fit projections from the baseline model plus the Bose Einstein correlation effect, extracted $S-$wave and residuals distribution.

Model PWA-1 with $\rho^0(770)$ mass and width free

Resonance	**Real**	**Imaginary**	**Fit Fraction (FF)** (%)
$\rho^0(770)$	1 [fix]	0 [fix]	25.1
$\omega(782)$	-0.004 ± 0.001	-0.012 ± 0.001	0.1
$f_2(1270)$	-0.562 ± 0.037	-1.642 ± 0.039	10.8
$\rho^0(1450)$	0.384 ± 0.113	1.240 ± 0.090	1.3
$S-$Wave	48 points		60.6
$m_{\rho^0(770)}$	778.703 ± 1.329 MeV/c^2		
$\Gamma_{\rho^0(770)}$	151.900 ± 2.284 MeV/c^2		
$\sum$ FF (%)	97.8		
χ^2/ndof (range)	[1.88 - 1.57]		**FCN = 272944**

Table 13.12: Fit results from the baseline model with $\rho^0(770)$ mass and width free.

	$\omega(782)$	$\rho^0(770)$	$\rho^0(1450)$	$f_2(1270)$	$S-$wave
$\omega(782)$	0.08	-0.22	0.0	0.04	0.02
$\rho^0(770)$		25.06	2.93	-0.55	-0.76
$\rho^0(1450)$			1.28	0.27	-0.22
$f_2(1270)$				10.80	-0.42
$S-$wave					60.64

Table 13.13: Interference fractions between amplitude components for the QMIPWA approach.

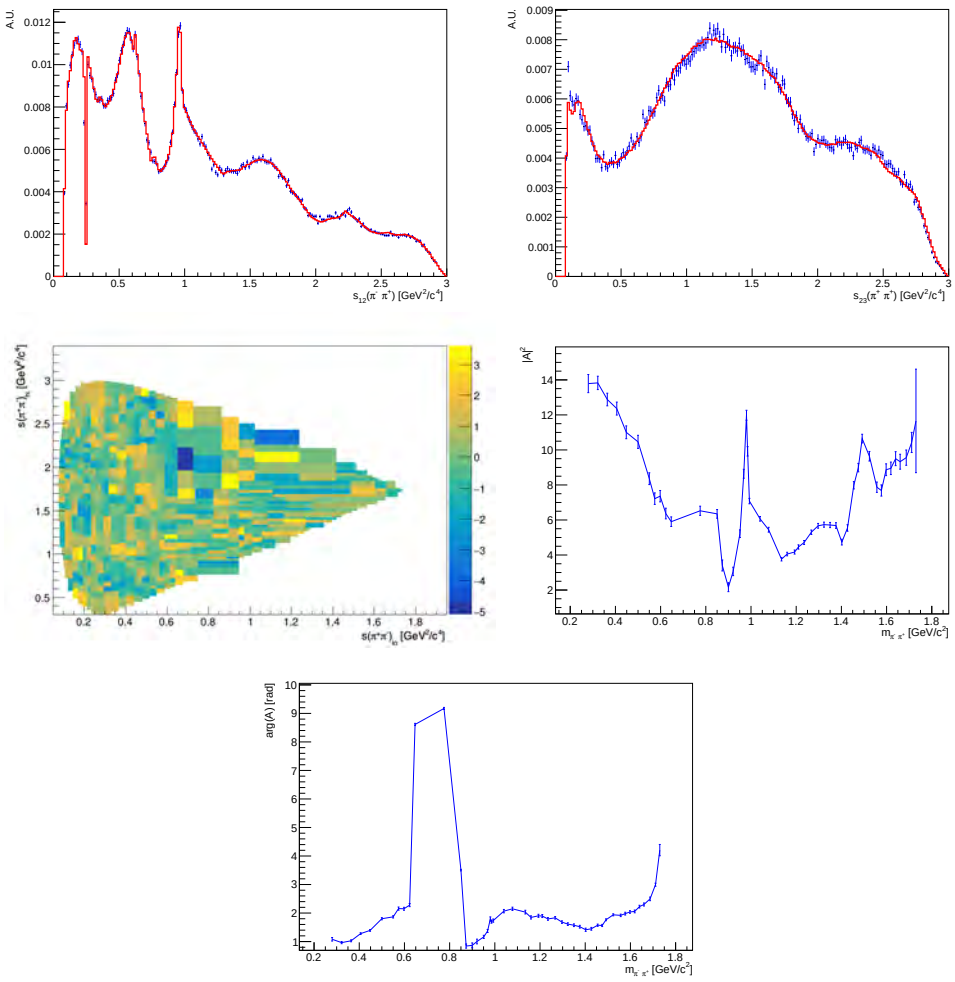

Figure 13.10: Fit projections from the baseline model with $\rho^0(770)$ mass and width free, extracted $S-$wave and residuals distribution.

Bibliography

[1] PARTICLE DATA GROUP. **Chin. Phys. C**. Review of particle physics, journal, v.40, 2016.

[2] HANNEKE, D.; HOOGERHEIDE, S. F. ; GABRIELSE, G. **Physical Review A**. Cavity control of a single-electron quantum cyclotron: Measuring the electron magnetic moment, journal, v.83, n.5, p. 052122, 2011.

[3] SAKHAROV, A. D. **Journal of Experimental and Theoretical Physics Letters (JETP Letters)**. Violation of CP invariance, C asymmetry, and baryon asymmetry of the universe, journal, n.5, p. 24–27, 1967.

[4] LHCB COLLABORATION AAIJ, R.; BETETA, C. A.; ADEVA, B.; ADINOLFI, M.; AIDALA, C. A.; AJALTOUNI, Z.; AKAR, S.; ALBICOCCO, P.; ALBRECHT, J.; ALESSIO, F. ; OTHERS. **Physical review letters**. Observation of CP violation in charm decays, journal, v.122, n.21, p. 211803, 2019.

[5] AAIJ, R.; ADEVA, B.; ADINOLFI, M.; ADROVER, C.; AFFOLDER, A.; AJALTOUNI, Z.; ALBRECHT, J.; ALESSIO, F.; ALEXANDER, M.; ALI, S. ; OTHERS. **Physics Letters B**. Search for CP violation in the decay $D^+ \to \pi^-\pi^+\pi^+$, journal, v.728, p. 585–595, 2014.

[6] E791 COLLABORATION :AITALA, E.; AMATO, S.; ANJOS, J.; APPEL, J.; ASHERY, D.; BANERJEE, S.; BEDIAGA, I.; BLAYLOCK, G.; BRACKER, S.; BURCHAT, P. ; OTHERS. **Physical Review Letters**. Experimental evidence for a light and broad scalar resonance in $D^+ \to \pi^-\pi^+\pi^+$ decay, journal, v.86, n.5, p. 770, 2001.

[7] FOCUS COLLABORATION LINK, J.; YAGER, P.; ANJOS, J.; BEDIAGA, I.; GÖBEL, C.; MACHADO, A.; MAGNIN, J.; MASSAFFERRI, A.; DE MIRANDA, J.; PEPE, I. ; OTHERS. **Physics Letters B**. Dalitz plot analysis of D_s^+ and D^+ decay to $\pi^+\pi^-\pi^+$ using the K-matrix formalism, journal, v.585, n.3-4, p. 200–212, 2004.

[8] CLEO COLLABORATION BONVICINI, G.; CINABRO, D.; DUBROVIN, M.; LINCOLN, A.; ASNER, D.; EDWARDS, K.;

NAIK, P.; BRIERE, R.; FERGUSON, T.; TATISHVILI, G. ; OTHERS. **Physical Review D**. Dalitz plot analysis of the $D^+ \to \pi^-\pi^+\pi^+$ decay, journal, v.76, n.1, p. 012001, 2007.

[9] LEADER, E.; PREDAZZI, E. **An introduction to gauge theories and modern particle physics**. Cambridge University Press, 1996.

[10] SALAM, A.; WARD, J. C. **Phys. Lett.** Electromagnetic and weak interactions, journal, v.13, p. 168–171, 1964.

[11] WEINBERG, S. **Physical review letters**. A model of leptons, journal, v.19, n.21, p. 1264, 1967.

[12] GLASHOW, S. L. **Nuclear Physics**. Partial-symmetries of weak interactions, journal, v.22, n.4, p. 579–588, 1961.

[13] GELL-MANN, M. **Il Nuovo Cimento (1955-1965)**. The interpretation of the new particles as displaced charge multiplets, journal, v.4, n.2, p. 848–866, 1956.

[14] NISHIJIMA, K. **Progress of Theoretical Physics**. Charge independence theory of v particles, journal, v.13, n.3, p. 285–304, 1955.

[15] AAD, G.; ABAJYAN, T.; ABBOTT, B.; ABDALLAH, J.; KHALEK, S. A.; ABDELALIM, A. A.; ABDINOV, O.; ABEN, R.; ABI, B.; ABOLINS, M. ; OTHERS. **Physics Letters B**. Observation of a new particle in the search for the Standard Model Higgs boson with the ATLAS detector at the LHC, journal, v.716, n.1, p. 1–29, 2012.

[16] CHATRCHYAN, S.; KHACHATRYAN, V.; SIRUNYAN, A. M.; TUMASYAN, A.; ADAM, W.; AGUILO, E.; BERGAUER, T.; DRAGICEVIC, M.; ERÖ, J.; FABJAN, C. ; OTHERS. **Physics Letters B**. Observation of a new boson at a mass of 125 GeV with the CMS experiment at the LHC, journal, v.716, n.1, p. 30–61, 2012.

[17] KOBAYASHI, M.; MASKAWA, T. **Progress of theoretical physics**. CP-violation in the renormalizable theory of weak interaction, journal, v.49, n.2, p. 652–657, 1973.

[18] CABIBBO, N. **Physical Review Letters**. Unitary symmetry and leptonic decays, journal, v.10, n.12, p. 531, 1963.

[19] WOLFENSTEIN, L. **Physical Review Letters**. Parametrization of the Kobayashi-Maskawa matrix, journal, v.51, n.21, p. 1945, 1983.

[20] CHAU, L.-L. **Physics Reports**. Quark mixing in weak interactions, journal, v.95, n.1, p. 1–94, 1983.

[21] CABIBBO, N.; MAIANI, L. **Physics Letters B**. Two-body decays of charmed mesons, journal, v.73, n.4-5, p. 418–422, 1978.

[22] FAKIROV, D.; STECH, B. **Nuclear Physics B**. F-and D-decays, journal, v.133, n.2, p. 315–326, 1978.

[23] ELLIS, J.; GAILLARD, M. K. ; NANOPOULOS, D. V. **Nuclear Physics B**. On the weak decays of high-mass hadrons, journal, v.100, n.2, p. 313–328, 1975.

[24] BURAS, A. J.; GÉRARD, J.-M. ; RÜCKL, R. **Nuclear Physics B**. 1n expansion for exclusive and inclusive charm decays, journal, v.268, n.1, p. 16–48, 1986.

[25] WILSON, K. G. **Physical Review**. Non-lagrangian models of current algebra, journal, v.179, n.5, p. 1499, 1969.

[26] WILSON, K. G.; ZIMMERMANN, W. **Communications in mathematical physics**. Operator product expansions and composite field operators in the general framework of quantum field theory, journal, v.24, n.2, p. 87–106, 1972.

[27] ZIMMERMANN, W. **Normal products and the short distance expansion in the perturbation theory of renormalizable interactions**. In: QUANTUM FIELD THEORY, p. 278–309. Springer, 2000.

[28] WATSON, K. M. **Physical Review**. Some general relations between the photoproduction and scattering of π mesons, journal, v.95, n.1, p. 228, 1954.

[29] HANHART, C. **Amplitude analysis for mesons and baryons: Tools and technology**. In: AIP CONFERENCE PROCEEDINGS, volume 1735, p. 020015. AIP Publishing LLC, 2016.

[30] PATRIGNANI, C.; OTHERS. **Chin. Phys. C**. Review of Particle Physics, 2016-2017, journal, v.40, n.10, p. 100001. 1808 p, 2016.

[31] OLLER, J. A. **A Brief Introduction to Dispersion Relations: With Modern Applications**. Springer, 2019.

[32] DE MELLO, C. G. B. **Estudo da Contribuiçao nao ressonante em decaimentos hadrônicos do méson D em três corpos**. 1999. PhD thesis - Tese de Doutorado, CBPF.

[33] DALITZ, R. H. **Phil. Mag. Ser.7**. On the analysis of τ-meson data and the nature of the τ-meson, journal, v.44, p. 1068–1080, 1953.

[34] BYCKLING, E.; KAJANTIE, K. Particle kinematics, journal, 1973.

[35] AKHMETSHINA, R.; ANASHKINA, E.; ARBUZOVB, A.; AULCHENKOA, V.; BANZAROVA, V. S.; BARKOVA, L.; BARUA, S.; BASHTOVOYA, N.; BONDARA, A.; BONDAREVA, D. ; OTHERS. **arXiv hep-ex/0112031**. Measurement of $e^+e^- \rightarrow \pi^+\pi^-$ cross section with CMD-2 around ρ-meson, journal.

[36] AITALA, E.; AMATO, S.; ANJOS, J.; APPEL, J.; ASHERY, D.; BANERJEE, S.; BEDIAGA, I.; BLAYLOCK, G.; BRACKER, S.; BURCHAT, P. ; OTHERS. **Physical review letters**. Dalitz plot analysis of the decay $D^+ \rightarrow K^-\pi^+\pi^+$ and indication of a low-mass scalar $K\pi$ resonance, journal, v.89, n.12, p. 121801, 2002.

[37] VAN BEVEREN, E.; RIJKEN, T.; METZGER, K.; DULLEMOND, C.; RUPP, G. ; RIBEIRO, J. **Zeitschrift für Physik C Particles and Fields**. A low lying scalar meson nonet in a unitarized meson model, journal, v.30, n.4, p. 615–620, 1986.

[38] OLLER, J. A.; OSET, E. **Nuclear Physics A**. Chiral symmetry amplitudes in the $S-$wave isoscalar and isovector channels and the σ, $f_0(980)$, $a_0(980)$ scalar mesons, journal, v.620, n.4, p. 438–456, 1997.

[39] KAMIŃSKI, R.; LEŚNIAK, L. ; LOISEAU, B. **Physics Letters B**. Three channel model of meson-meson scattering and scalar meson spectroscopy, journal, v.413, n.1-2, p. 130–136, 1997.

[40] SCHECHTER, J. **International Journal of Modern Physics A**. Isobar rescattering model and light scalar mesons, journal, v.20, n.27, p. 6149–6158, 2005.

[41] ACHASOV, N.; SHESTAKOV, G. **Physical Review D**. $\pi\pi$ scattering S wave from the data on the reaction $\pi^-p \rightarrow \pi^0\pi^0n$, journal, v.67, n.11, p. 114018, 2003.

[42] BOITO, D.; DEDONDER, J.-P.; EL-BENNICH, B.; ESCRIBANO, R.; KAMIŃSKI, R.; LEŚNIAK, L. ; LOISEAU, B. **Physical Review D**.

Parametrizations of three-body hadronic B-and D-decay amplitudes in terms of analytic and unitary meson-meson form factors, journal, v.96, n.11, p. 113003, 2017.

[43] BOITO, D.; DEDONDER, J.-P.; EL-BENNICH, B.; LEITNER, O. ; LOISEAU, B. **Physical Review D**. Scalar resonances in a unitary π π S-wave model for $D^+ \to \pi^+\pi^-\pi^+$, journal, v.79, n.3, p. 034020, 2009.

[44] HANHART, C. **Physics Letters B**. A new parameterization for the pion vector form factor, journal, v.715, n.1-3, p. 170–177, 2012.

[45] DAUB, J.; HANHART, C. ; KUBIS, B. **Journal of High Energy Physics**. A model-independent analysis of final-state interactions in $\bar{B}^0_{d/s} \to j/\psi\pi\pi$, journal, v.2016, n.2, p. 9, 2016.

[46] BOITO, D.; ESCRIBANO, R. **Physical Review D**. $k\pi$ form factors and final state interactions in $D^+ \to K^-\pi^+\pi^+$ decays, journal, v.80, n.5, p. 054007, 2009.

[47] OMNÈS, E. **Il Nuovo Cimento (1955-1965)**. On the solution of certain singular integral equations of quantum field theory, journal, v.8, n.2, p. 316–326, 1958.

[48] LEES, J.; POIREAU, V.; TISSERAND, V.; TICO, J. G.; GRAUGES, E.; PALANO, A.; EIGEN, G.; STUGU, B.; BROWN, D.; KERTH, L. ; OTHERS. **Physical Review D**. Precise measurement of the $e^+e^- \to \pi^+\pi^-(\gamma)$ cross section with the initial-state radiation method at babar, journal, v.86, n.3, p. 032013, 2012.

[49] ABLIKIM, M.; ACHASOV, M.; AI, X.; ALBAYRAK, O.; ALBRECHT, M.; AMBROSE, D.; AMOROSO, A.; AN, F.; AN, Q.; BAI, J. ; OTHERS. **arXiv:1507.08188**. Measurement of the $e^+e^- \to \pi^+\pi^-$ cross section between 600 and 900 MeV using initial state radiation, journal, 2015.

[50] GARDNER, S.; O'CONNELL, H. B. **Physical Review D**. Rho-omega mixing and the pion form factor in the timelike region, journal, v.57, n.5, p. 2716, 1998.

[51] AMBROSINO, F.; ARCHILLI, F.; BELTRAME, P.; BENCIVENNI, G.; BINI, C.; BLOISE, C.; BOCCHETTA, S.; BOSSI, F.; BRANCHINI, P.; CAPON, G. ; OTHERS. **Physics Letters B**. Measurement of σ ($e^+e^- \to \pi^+\pi^-$) from threshold to 0.85 GeV^2 using initial state radiation with the KLOE detector, journal, v.700, n.2, p. 102–110, 2011.

[52] EVANS, L.; BRYANT, P. **Journal of instrumentation**. LHC machine, journal, v.3, n.08, p. S08001, 2008.

[53] MARCASTEL, F. C. **Cern's accelerator complex**. Technical report, 2013.

[54] ALICE COLLABORATION; AAMODT, K. ; OTHERS. **S08002**. The ALICE experiment at the CERN LHC. jinst 3, journal, p. 1748–0221, 2008.

[55] AAD, G.; BUTTERWORTH, J.; THION, J.; BRATZLER, U.; RATOFF, P.; NICKERSON, R.; SEIXAS, J.; GRABOWSKA-BOLD, I.; MEISEL, F.; LOKWITZ, S. ; OTHERS. **Jinst**. The ATLAS experiment at the CERN large hadron collider, journal, v.3, p. S08003, 2008.

[56] ADOLPHI, R.; OTHERS. **Jinst**. The CMS experiment at the CERN LHC, journal, v.803, p. S08004, 2008.

[57] ALVES JR, A. A.; ANDRADE FILHO, L.; BARBOSA, A.; BEDIAGA, I.; CERNICCHIARO, G.; GUERRER, G.; LIMA JR, H.; MACHADO, A.; MAGNIN, J.; MARUJO, F. ; OTHERS. **Journal of instrumentation**. The LHCb detector at the LHC, journal, v.3, n.08, p. S08005, 2008.

[58] SCHUKRAFT, J. **Philosophical Transactions of the Royal Society A: Mathematical, Physical and Engineering Sciences**. Heavy-ion physics with the ALICE experiment at the CERN large hadron collider, journal, v.370, n.1961, p. 917–932, 2012.

[59] ATLAS COLLABORATION. AAD, G.; ABBOTT, B.; ABDALLAH, J.; ABDINOV, O.; ABELOOS, B.; ABEN, R.; ABOUZEID, O.; ABRAHAM, N.; ABRAMOWICZ, H. ; OTHERS. **Journal of High Energy Physics**. Measurements of the Higgs boson production and decay rates and constraints on its couplings from a combined ATLAS and CMS analysis of the LHC pp collision data at $\sqrt{s} = 7$ and 8 TeV, journal, v.2016, p. 1–113, 2016.

[60] KHACHATRYAN, V.; SIRUNYAN, A.; TUMASYAN, A.; ADAM, W.; BERGAUER, T.; DRAGICEVIC, M.; ERÖ, J.; FRIEDL, M.; FRÜHWIRTH, R.; GHETE, V. ; OTHERS. **The European Physical Journal C**. Precise determination of the mass of the Higgs boson and tests of compatibility of its couplings with the standard model predictions using proton collisions at 7 and 8 tev, journal, v.75, n.5, p. 212, 2015.

[61] BARTON, A.; BEATTIE, M.; BOUHOVA-THACKER, E. V.; DEARNALEY, W.; FOX, H.; GRIMM, K. A. T.; HENDERSON, R. C. W.; HUGHES, G.; JONES, R. W. L.; KARTVELISHVILI, V. ; OTHERS. **European Physical Journal C: Particles and Fields**. Study of the spin and parity of the Higgs boson in diboson decays with the ATLAS detector, journal, v.75, n.10, 2015.

[62] GERSHON, T.; NEEDHAM, M. **Comptes Rendus Physique**. Heavy flavour physics at the LHC, journal, v.16, n.4, p. 435–447, 2015.

[63] LHCB COLLABORATION. **International Journal of Modern Physics A**. LHCb detector performance, journal, v.30, n.07, p. 1530022, 2015.

[64] SJÖSTRAND, T.; MRENNA, S. ; SKANDS, P. **Computer Physics Communications**. A brief introduction to PYTHIA 8.1, journal, v.178, n.11, p. 852–867, 2008.

[65] AAIJ, R.; AFFOLDER, A.; AKIBA, K.; ALEXANDER, M.; ALI, S.; APPLEBY, R.; ARTUSO, M.; BATES, A.; BAY, A.; BEHRENDT, O. ; OTHERS. **Journal of Instrumentation**. Performance of the LHCb vertex locator, journal, v.9, n.09, p. P09007, 2014.

[66] LHCB COLLABORATION. **LHCb magnet: Technical design report**. Technical report, 2000.

[67] LHCB COLLABORATION; OTHERS. **Journal of Instrumentation**. Measurement of the track reconstruction efficiency at LHCb, journal, v.10, n.02, p. P02007, 2015.

[68] LHCB COLLABORATION. **Inner tracker technical design report**. Technical report, CERN-LHCC-2002-029, 2002.

[69] LHCB COLLABORATION. **Outer tracker technical design report**. Technical report, CERN-LHCC-2001-029, 2001.

[70] LHCB COLLABORATION. **Journal of Instrumentation**. Performance of the LHCb outer tracker, journal, v.9, n.01, p. P01002–P01002, jan 2014.

[71] LHCB COLLABORATION; OTHERS. **CERN/LHCC**. LHCb RICH technical design report, journal, v.37, n.3, 2000.

[72] ADINOLFI, M.; RINELLA, G. A.; ALBRECHT, E.; BELLUNATO, T.; BENSON, S.; BLAKE, T.; BLANKS, C.; BRISBANE, S.; BROOK, N.; CALVI, M. ; OTHERS. **The European Physical Journal C**. Performance of the LHCb RICH detector at the LHC, journal, v.73, n.5, p. 2431, 2013.

[73] LHCB COLLABORATION; OTHERS. **CERN/LHCC**. LHCb calorimeters technical design report, journal, v.36, p. 2000, 2000.

[74] ARCHILLI, F.; BALDINI, W.; BENCIVENNI, G.; BONDAR, N.; BONIVENTO, W.; CADEDDU, S.; CAMPANA, P.; CARDINI, A.; CIAMBRONE, P.; VIDAL, X. C. ; OTHERS. **Journal of Instrumentation**. Performance of the muon identification at LHCb, journal, v.8, n.10, p. P10020, 2013.

[75] ALVES JR, A. A.; ANDERLINI, L.; ANELLI, M.; NOBREGA, R. A.; AURIEMMA, G.; BALDINI, W.; BENCIVENNI, G.; BERUTTI, R.; BIZZETI, A.; BOCCI, V. ; OTHERS. **Journal of Instrumentation**. Performance of the LHCb muon system, journal, v.8, n.02, p. P02022, 2013.

[76] LHCB COLLABORATION. **LHCb muon system: Technical Design Report**. Technical Design Report LHCb. Geneva: CERN, 2001.

[77] AAIJ, R.; ALBRECHT, J.; ALESSIO, F.; AMATO, S.; ASLANIDES, E.; BELYAEV, I.; VAN BEUZEKOM, M.; BONACCORSI, E.; BONNEFOY, R.; BRARDA, L. ; OTHERS. **Journal of Instrumentation**. The LHCb trigger and its performance in 2011, journal, v.8, n.04, p. P04022, 2013.

[78] ALBRECHT, J.; GLIGOROV, V.; RAVEN, G.; TOLK, S. ; OTHERS. **Performance of the LHCb high level trigger in 2012**. In: JOURNAL OF PHYSICS: CONFERENCE SERIES, volume 513, p. 012001. IOP Publishing, 2014.

[79] CLEMENCIC, M.; CORTI, G.; EASO, S.; JONES, C.; MIGLIORANZI, S.; PAPPAGALLO, M.; ROBBE, P.; COLLABORATION, L. ; OTHERS. **The LHCb simulation application, Gauss: design, evolution and experience**. In: JOURNAL OF PHYSICS: CONFERENCE SERIES, volume 331, p. 032023. IOP Publishing, 2011.

[80] CORTI, G.; CHARPENTIER, P.; CLEMENCIC, M.; CLOSIER, J.; COUTURIER, B.; KREPS, M.; MATHE, Z.; O'HANLON, D.; ROBBE,

P.; ROMANOVSKY, V. ; OTHERS. **How the Monte Carlo production of a wide variety of different samples is centrally handled in the LHCb experiment**. In: JOURNAL OF PHYSICS: CONFERENCE SERIES, volume 664, p. 072014. IOP Publishing, 2015.

[81] LANGE, D. J. **Nuclear Instruments and Methods in Physics Research Section A: Accelerators, Spectrometers, Detectors and Associated Equipment**. The EvtGen particle decay simulation package, journal, v.462, n.1-2, p. 152–155, 2001.

[82] GEANT4 COLLABORATION. **Nucl. Instrum. Meth. A**. GEANT4–a simulation toolkit, journal, v.506, n.25, p. 0, 2003.

[83] GEANT4 COLLABORATION; OTHERS. **IEEE Trans. Nucl. Sci**. J. allison et al., Geant4 developments and applications, journal, v.53, n.270, p. 43, 2006.

[84] JACOBSSON, R. **Performance of the LHCb detector during the lhc proton runs 2010–2012**. In: 2012 IEEE NUCLEAR SCIENCE SYMPOSIUM AND MEDICAL IMAGING CONFERENCE RECORD (NSS/MIC), p. 1479–1486. IEEE, 2012.

[85] **Luminosity: Taking a closer look at lhc**. `http://lhc-closer.es/taking_a_closer_look_at_lhc/0.luminosity`. Accessed: 2020-02-05.

[86] FOLLIN, F.; JACQUET, D. **arXiv:1410.3667**. Implementation and experience with luminosity levelling with offset beam, journal, 2014.

[87] ALVES JR, A. A. E. A. **The LHCb detector at the LHC. jinst, 3 (s08005), 2008**.

[88] PUIG, A. **LHCb PUB**. The LHCb trigger in 2011 and 2012, journal, v.046, 2014.

[89] ALBRECHT, J.; GLIGOROV, V.; RAVEN, G.; TOLK, S. ; OTHERS. **Performance of the LHCb high level trigger in 2012**. In: JOURNAL OF PHYSICS: CONFERENCE SERIES, volume 513, p. 012001. IOP Publishing, 2014.

[90] GLIGOROV, V. V.; WILLIAMS, M. **Journal of Instrumentation**. Efficient, reliable and fast high-level triggering using a bonsai boosted decision tree, journal, v.8, n.02, p. P02013, 2013.

[91] SJÖSTRAND, T.; MRENNA, S. ; SKANDS, P. **Journal of High Energy Physics**. PYTHIA 6.4 physics and manual, journal, v.2006, n.05, p. 026, 2006.

[92] POWELL, A. **PoS**. Particle identification at LHCb, journal, p. 020, 2010.

[93] PIVK, M.; LE DIBERDER, F. R. **Nuclear Instruments and Methods in Physics Research Section A: Accelerators, Spectrometers, Detectors and Associated Equipment**. splot: A statistical tool to unfold data distributions, journal, v.555, n.1-2, p. 356–369, 2005.

[94] ROE, BYRON P, E. A. **Nuclear Instruments and Methods in Physics Research Section A: Accelerators, Spectrometers, Detectors and Associated Equipment**. Boosted decision trees as an alternative to artificial neural networks for particle identification, journal, v.543, n.2-3, p. 577–584, 2005.

[95] HOECKER, A.; SPECKMAYER, P.; STELZER, J.; THERHAAG, J.; VON TOERNE, E.; VOSS, H.; BACKES, M.; CARLI, T.; COHEN, O.; CHRISTOV, A. ; OTHERS. **arXiv physics/0703039**. TMVA-toolkit for multivariate data analysis, journal, 2007.

[96] VERKERKE, W.; KIRKBY, D. **The RooFit toolkit for data modeling**. In: STATISTICAL PROBLEMS IN PARTICLE PHYSICS, ASTROPHYSICS AND COSMOLOGY, p. 186–189. World Scientific, 2006.

[97] SKWARNICKI, T. **A study of the radiative cascade transitions between the upsilon-prime and upsilon resonances**. Technical report, 1986.

[98] LATHAM, T. **The Laura++ Dalitz plot fitter**. In: AIP CONFERENCE PROCEEDINGS, volume 1735, p. 070001. AIP Publishing LLC, 2016.

[99] HERNDON, D. J.; SÖDING, P. ; CASHMORE, R. J. **Physical Review D**. Generalized isobar model formalism, journal, v.11, n.11, p. 3165, 1975.

[100] FLEMING, G. N. **Physical Review**. Recoupling effects in the isobar model. i. general formalism for three-pion scattering, journal, v.135, n.2B, p. B551, 1964.

[101] ZEMACH, C. **Physical Review**. Three-pion decays of unstable particles, journal, v.133, n.5B, p. B1201, 1964.

[102] ZEMACH, C. **Physical Review**. Use of angular-momentum tensors, journal, v.140, n.1B, p. B97, 1965.

[103] ZEMACH, C. **Physical Review**. Determination of the spins and parities of resonances, journal, v.140, n.1B, p. B109, 1965.

[104] BLATT, J. M.; WEISSKOPF, V. F. **Theoretical nuclear physics**. Courier Corporation, 1991.

[105] BOHM, A. R.; SATO, Y. **Physical Review D**. Relativistic resonances: their masses, widths, lifetimes, superposition, and causal evolution, journal, v.71, n.8, p. 085018, 2005.

[106] FLATTE, S. M. **Phys. Lett. B**. Coupled-channel analysis of the $\pi\eta$ and $\bar{K}K$ systems near $\bar{K}K$ threshold, journal, v.63, n.CERN-EP-PHYS-76-8, p. 224–227, 1976.

[107] COLLABORATION AND OTHERS, B. **Phys. Lett. B**. Resonances in $J/\psi \to \varphi\pi^+\pi^-$ and φK^+K^-, journal, v.607, p. 243, 2005.

[108] OLLER, J. A. **Physical Review D**. Final state interactions in hadronic d decays, journal, v.71, n.5, p. 054030, 2005.

[109] PELÁEZ, J. R. **Physics Reports**. From controversy to precision on the sigma meson: a review on the status of the non-ordinary $f_0(500)$ resonance, journal, v.658, p. 1–111, 2016.

[110] GOUNARIS, G. J.; SAKURAI, J. J. **Phys. Rev. Lett.** Finite-width corrections to the vector-meson-dominance prediction for $\rho \to e^+e^-$, journal, v.21, p. 244–247, Jul 1968.

[111] CHEN, Y.-H.; YAO, D.-L. ; ZHENG, H.-Q. **Communications in Theoretical Physics**. A study of ρ-ω mixing in resonance chiral theory, journal, v.69, n.1, p. 50, 2018.

[112] **W. m. dunwoodie, *Omega-rho Mixing Parametrization*.** `https://www.slac.stanford.edu/~wmd/omega-rho_mixing/omega-rho_mixing.note`, note = Accessed: 2020-02-07.

[113] RENSING, P. E. **Single electron detection for SLD CRID and multi - pion spectroscopy in K- p interactions at 11-GeV/c**. 1993. PhD thesis - SLAC.

[114] LHCB COLLABORATION ;AAIJ, R.; ADEVA, B.; ADINOLFI, M.; AFFOLDER, A.; AJALTOUNI, Z.; AKAR, S.; ALBRECHT, J.; ALESSIO, F.; ALEXANDER, M.; ALI, S. ; OTHERS. **Physics Letters B**. Measurement of the cp-violating phase β in $B^0 \to J/\psi\pi^+\pi^-$ decays and limits on penguin effects, journal, v.742, p. 38–49, 2015.

[115] LHCB COLLABORATION, AAIJ, R.; ADEVA, B.; ADINOLFI, M.; AFFOLDER, A.; AJALTOUNI, Z.; AKAR, S.; ALBRECHT, J.; ALESSIO, F.; ALEXANDER, M.; ALI, S. ; OTHERS. **Phys. Rev. D**. Dalitz plot analysis of $B^0 \to \overline{D}^0\pi^+\pi^-$ decays, journal, v.92, p. 032002, Aug 2015.

[116] LHCB COLLABORATION:AAIJ, R.; ABELLÁN BETETA, C.; ADEVA, B.; ADINOLFI, M.; AIDALA, C. A.; AJALTOUNI, Z.; AKAR, S.; ALBICOCCO, P.; ALBRECHT, J. ; OTHERS. **Phys Rev D**. Amplitude analysis of the $B^+ \to \pi^+\pi^+\pi^-$ decay, journal, v.101, p. 012006, Jan 2020.

[117] BEDIAGA, I.; FREDERICO, T. ; LOURENÇO, O. **Physical Review D**. CP violation and CPT invariance in $B^{\pm}$ decays with final state interactions, journal, v.89, n.9, p. 094013, 2014.

[118] PELÁEZ, J. R.; YNDURAIN, F. J. **Physical Review D**. Pion-pion scattering amplitude, journal, v.71, n.7, p. 074016, 2005.

[119] NEBREDA, J.; PELAEZ, J. ; RIOS, G. **Physical Review D**. Chiral extrapolation of pion-pion scattering phase shifts within standard and unitarized chiral perturbation theory, journal, v.83, n.9, p. 094011, 2011.

[120] BUGG, D. **Physics Letters B**. Comments on the σ and κ, journal, v.572, n.1, p. 1 – 7, 2003.

[121] CHUNG, S.; BROSE, J.; HACKMANN, R.; KLEMPT, E.; SPANIER, S. ; STRASSBURGER, C. **Annalen der Physik**. Partial wave analysis in K-matrix formalism, journal, v.507, n.5, p. 404–430, 1995.

[122] DALITZ, R.; TUAN, S. **Annals of Physics**. The phenomenological representation of k-nucleon scattering and reaction amplitudes, journal, v.10, n.3, p. 307 – 351, 1960.

[123] WIGNER, E. P. **Phys. Rev.** Resonance reactions and anomalous scattering, journal, v.70, p. 15–33, Jul 1946.

[124] AITCHISON, I. **Nuclear Physics A**. The K-matrix formalism for overlapping resonances, journal, v.189, n.2, p. 417–423, 1972.

[125] O'HANLON, D. **Studies of CP-violation in charmless three-body b-hadron decays**. Springer, 2018.

[126] ANISOVICH, V.; SARANTSEV, A. **Physics Letters B**. K-matrix analysis of the (ijpc= 00++) amplitude in the mass region up to 1550 mev, journal, v.382, n.4, p. 429–440, 1996.

[127] ADLER, S. L. **Physical Review**. Consistency conditions on the strong interactions implied by a partially conserved axial-vector current. ii, journal, v.139, n.6B, p. B1638, 1965.

[128] LINK, J.; YAGER, P.; ANJOS, J.; BEDIAGA, I.; CASTROMONTE, C.; MACHADO, A.; MAGNIN, J.; MASSAFFERRI, A.; DE MIRANDA, J.; PEPE, I. ; OTHERS. **Physics Letters B**. The $K^-\pi^+$ S-wave from the $D^+ \to K^-\pi^+\pi^+$ decay, journal, v.681, n.1, p. 14–21, 2009.

[129] BEDIAGA, I.; DE MIRANDA, J. M. **Physics Letters B**. Phase motion in the scalar low-mass $\pi\pi$ amplitude in $D^+ \to \pi^-\pi^+\pi^+$ decay, journal, v.633, n.2-3, p. 167–172, 2006.

[130] AITALA, E.; AMATO, S.; ANJOS, J.; APPEL, J.; ASHERY, D.; BANERJEE, S.; BEDIAGA, I.; BLAYLOCK, G.; BRACKER, S.; BURCHAT, P. ; OTHERS. **Physical Review D**. Model-independent measurement of S-wave $K^-\pi^+$ systems using $D^+ \to K\pi\pi$ decays from Fermilab E791, journal, v.73, n.3, p. 032004, 2006.

[131] MIZOGUCHI, T.; BIYAJIMA, M. **arXiv:2003.00427**. Analysis of Bose-Einstein correlation at 7 TeV by LHCb collaboration based on stochastic approach, journal, 2020.

[132] KHACHATRYAN, V.; SIRUNYAN, A.; TUMASYAN, A.; ADAM, W.; BERGAUER, T.; DRAGICEVIC, M.; ERÖ, J.; FABJAN, C.; FRIEDL, M.; FRUEHWIRTH, R. ; OTHERS. **Journal of High Energy Physics**. Measurement of bose-einstein correlations in pp collisions at $\sqrt{s} = 0.9$ and 7 TeV, journal, v.2011, n.5, p. 29, 2011.

[133] KHACHATRYAN, V.; SIRUNYAN, A. M.; TUMASYAN, A.; ADAM, W.; BERGAUER, T.; DRAGICEVIC, M.; ERÖ, J.; FABJAN, C.; FRIEDL, M.; FRUEHWIRTH, R. ; OTHERS. **Physical review letters**. First measurement of bose-einstein correlations in proton-proton collisions at $\sqrt{s} = 0.9$ and 2.36 TeV at the LHC, journal, v.105, n.3, p. 032001, 2010.